Micromechanical and statistical studies of twinning in hexagonal metals: application to magnesium and zirconium

Pierre-Alexandre Juan

To cite this version:

Pierre-Alexandre Juan. Micromechanical and statistical studies of twinning in hexagonal metals: application to magnesium and zirconium. Other. Université de Lorraine, 2015. English. NNT : 2015LORR0336 . tel-01752219

HAL Id: tel-01752219
https://hal.univ-lorraine.fr/tel-01752219v1

Submitted on 29 Mar 2018

UNIVERSITÉ
DE LORRAINE

École doctorale Emma

Micromechanical and statistical studies of twinning in hexagonal metals : application to magnesium and zirconium
Études micromécaniques et statistiques du maclage dans les métaux hexagonaux : application au magnésium et zirconium

THÈSE

présentée et soutenue publiquement le 15 décembre 2015

pour l'obtention du

Doctorat de l'Université de Lorraine

(Spécialité: Mécanique des Matériaux)

par

Pierre-Alexandre Juan

Composition du jury

Directeur de thèse:	Stéphane Berbenni, Directeur de Recherche CNRS, LEM3, Université de Lorraine
Codirecteur de thèse:	Laurent Capolungo, Professeur, Georgia Institute of Technology
Rapporteurs :	Teresa María Pérez Prado, Directrice de Recherche, IMDEA Materials Laurent Delannay, Professeur, Université Catholique de Louvain
Examinateurs :	Edgar Rauch, Directeur de Recherche CNRS, SIMAP, Université de Grenoble Lazslo Toth, Professeur, LEM3, Université de Lorraine

Laboratoire d'Etude des Microstructures et de Mécanique des Matériaux — UMR 7239

Mis en page avec la classe thesul.

Remerciements

Je souhaiterais tout d'abord exprimer ma plus sincère gratitude à mes directeurs de thèse, Dr. Berbenni et Dr. Capolungo, pour tous leurs conseils et tout leur soutien. Je m'estime chanceux d'avoir eu l'opportunité de travailler sous leur supervision pendant toutes ces années. Je souhaite également remercier Dr. Pérez Prado, Dr. Delannay, Dr. Rauch et Dr. Tóth pour avoir accepté de faire partie de mon jury. Je garde de ma soutenance un excellent souvenir.

Le doctorat me permit par ailleurs de collaborer avec d'incroyables scientifiques que sont Dr. Pradalier, Dr. Tomé, Dr. McCabe et Dr. Barnett. Je tiens à les remercier pour tous les enseignements qu'ils ont pus me prodiguer.

Je remercie également les membres de l'administration de l'Université de Lorraine pour leur aide et sympathie. Je ne peux pas ne pas mentionner mes camarades de laboratoire dont j'ai apprécié la compagnie tout au long de mon doctorat et dont certains sont devenus des amis très proches. Je leur souhaite la meilleure des réussites dans leurs carrières futures.

Et enfin, j'aimerais remercier ma famille et mes amis pour leur soutien constant et indéfectible. Je leur dédie cette thèse.

Sommaire

Table des figures

Résumé

En préambule de ce résumé, je souhaiterais insister sur le fait que le travail rapporté dans ce manuscrit est le fruit de diverses collaborations intervenues à différents moments de mon doctorat tant en France qu'aux Etats-Unis.

Concernant les modèles micromécaniques introduits chapitre II, je suis, avec l'aide de mes directeurs de thèse, Dr. Berbenni et Dr. Capolungo, à l'origine de l'intégralité de leur développement et programmation. Dr. Tomé a eu la gentillesse de partager avec nous la dernière version du code EPSC, développée à Los Alamos National Laboratories, à partir de laquelle nous avons implémenté les nouvelles relations de localisation correspondant au schéma DI-EPSC. Leur implémentation a nécéssité une profonde adaptation du code initial. Les discussions avec Dr. Tomé et Dr. Barnett qui ont suivi le développement de cette nouvelle approche micromécanique à double inclusion ont permis l'enrichissement de l'étude.

Le chapitre III est principalement dédié à la description d'un nouveau logiciel de visualisation et d'analyse de cartographies EBSD pour matériaux hexagonaux, capable de reconnaître n'importe quel type de macle et d'extraire une "myriade" de données microstructurales, enregistrées au sein d'une base de données SQL. Le développement de l'outil est à mettre au crédit de Dr. Pradalier, professeur de Computer Sciences à Georgia Tech Lorraine, à l'origine du choix de la théorie des graphes pour la construction de l'outil. Pour ma part, je me suis chargé de vérifier les résultats obtenus à partir de ce dernier et de proposer les adaptations et améliorations nécéssaires pour rendre le logiciel plus ergonomique et plus intelligible aux membres de la communauté de la mécanique de la matière. J'ai également rédigé un code fortran qui a permis de générer tous les résultats de l'étude statistique présentée au chapitre IV et réalisée à partir des cartographies EBSD de zirconium que Dr. McCabe a eu l'amabilité de partager avec nous .

La double étude portant sur les macles à faible facteur de Schmid ainsi que sur les doubles macles d'extension au sein de l'alliage de magnésium AZ31 a été menée avec l'aide de Dr. Shi (post-doctorant au LEM3 de 2013 à 2015 dans le cadre du projet ANR Magtwin). Ma participation a consisté à réaliser les différents essais mécaniques de compression monotone et séquentielle permettant l'observation de ces macles aux caractéristiques particulières et le développement de la partie théorique du modèle micromécanique à double inclusion en élasticité hétérogène anisotrope avec "eigenstrains". Le travail relaté dans ce manuscrit a ainsi profité de l'interaction avec tous ces chercheurs que je remercie vivement pour m'avoir permis d'élargir mon spectre de connaissances de la sorte.

Les matériaux polycristallins à structure hexagonale compacte ont, depuis les années 1960, été l'objet de beaucoup d'intérêt. L'engouement que des métaux tels que le magnésium, le zirconium, le rhénium, le titane, ..., ont pu susciter et suscite toujours s'explique par l'ampleur et l'extrême variété de leurs applications. Une attention plus particulière est portée, au sein de cette thèse, sur le magnésium et le zirconium. Les propriétés de ce dernier, à savoir une excellente résistance à la corrosion, une grande pénétrabilité des neutrons lents, la conservation de ses propriétés à haute température ainsi qu'une bonne ductilité font du zirconium, et plus particulièrement de ses formes

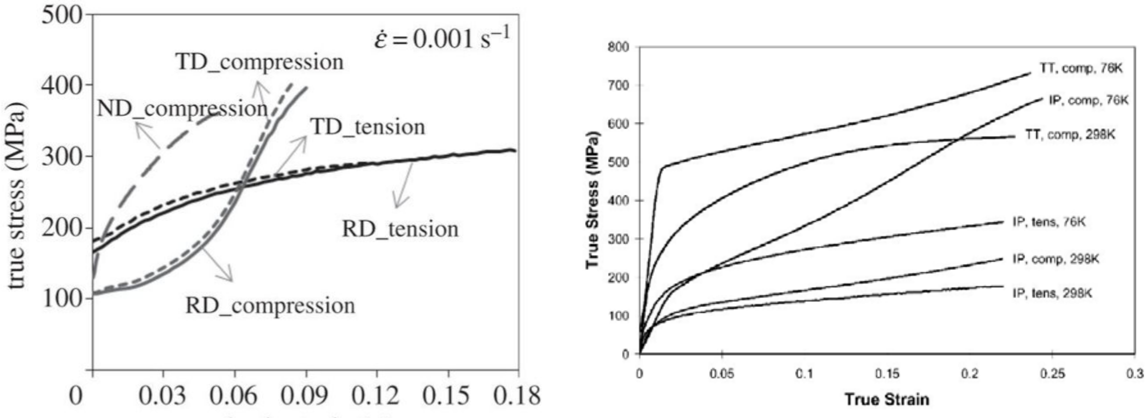

(a)

(b)

FIGURE 1 – (a) Comparaison des courbes contrainte-déformation en traction et compression de Mg AZ31B laminé [1] et (b) comparaison de la réponse mécanique du Zr pur laminé pour différentes températures et trajets de chargement [2]. Traction et compression apparaissent, respectivement, dans la légende sous la forme de "tens" et "comp". Les abréviations "TT" et "IP" signifient, quant à elles, "through-thickness compression" et "in-plane compression", à savoir "compression dans le sens de l' épaisseur" et "compression dans le plan".

alliées, un métal très utilisé en tant que gaine de combustible et matériau de tuyauterie dans les réacteurs nucléaires de génération III et IV. Le magnésium et ses différents alliages ont, quant à eux, fortement intéressé l'industrie automobile qui, par souci d'alléger les voitures, est toujours à la recherche de nouveaux matériaux plus légers mais aux modules de Young spécifiques élevés. Ainsi, depuis des décennies, des pièces de magnésium moulées ont été utilisées comme éléments structurels. En revanche, sa mise en forme, ainsi celle que des autres métaux hexagonaux, implique de déformer de façon irréversible le matériau. Or, la déformation plastique, dont les caractéristiques clé sont la limite d'élasticité, le durcissement et la ductilité, est fortement anisotropique pour le magnésium, le zirconium et leurs alliages respectifs. La Figure 1 montre les courbes de contrainte-déformation obtenues expérimentalement à partir d'éprouvettes composées d'alliage de Mg AZ31 et de Zr laminés et chargées en tension et compression selon différentes directions ainsi qu'à des températures différentes. Il apparaît clairement que température et direction de chargement ont tous deux un effet très important sur la réponse mécanique du matériau, rendant la prédiction de cette dernière beaucoup plus complexe. Les difficultés rencontrées lors la mise en forme de tôles métalliques faites de matériaux hexagonaux limitent sensiblement leurs potentielles applications.

L'accommodation de la déformation et la relaxation des contraintes au sein des matériaux hexagonaux résultent de l'activation, simultanée ou non, de modes de glissement et de maclage. Le glissement se caractérise par le déplacement de dislocations et l'interaction entre celles appartenant aux différents systèmes et modes de glissement. A contrario, le maclage se caractérise, quant à lui, par la nucléation, au sein des grains, de sous-volumes, appelés macles, dont la réorientation du réseau peut être décrite au moyen d'une symétrie spéculaire par rapport à un plan invariant, bien classiquement dénommé plan de maclage. La compréhension de la déformation plastique des métaux hexagonaux est donc particulièrement ardue au vu de la très grande variété des modes

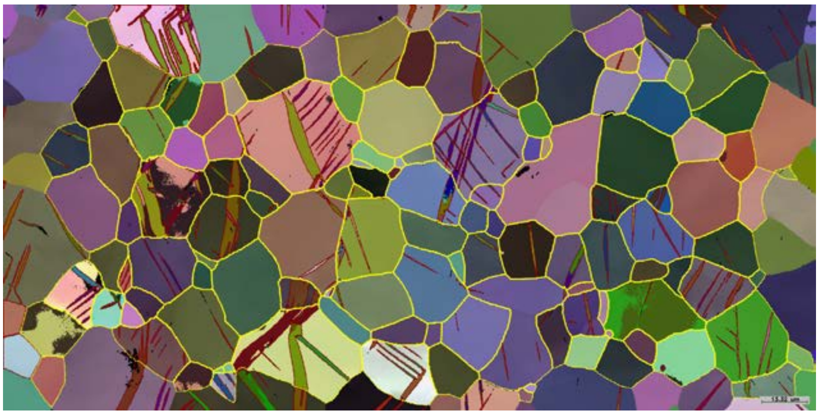

FIGURE 2 – Exemple de cartographie EBSD obtenu à partir d'un échantillon de Zr pur laminé chargé en compression dans le sens de son épaisseur. Cette cartographie fut traitée par le logiciel lequel sera plus longuement décrit chapitre 3.

,

de déformation pouvant être activés. A titre d'exemple, trois modes de glissement et deux de maclage ont été observés expérimentalement dans du magnésium pur tandis que quatre modes de maclage et trois de glissement l'ont été dans le zirconium. En outre, la plasticité ne se limite pas aux phases parent puisqu'intervenant très fréquemment au sein même des macles sous la forme de glissement et de maclage secondaire.

TABLE 1 – Modes de maclage dans le Zr

Mode de maclage	Plan de maclage K_1	Direction de maclage η_1	Angle de désorientation δ (°)
T_1	$\{1012\}$	$<1011>$	85.2
T_2	$\{11\bar{2}1\}$	$<\bar{1}\bar{1}26>$	34.9
C_1	$\{11\bar{2}2\}$	$<11\bar{2}\bar{3}>$	64.2
C_2	$\{10\bar{1}1\}$	$<10\bar{1}\bar{2}>$	57.1

En général, chaque mode de déformation actif impacte non seulement la réponse mécanique du matériau mais aussi l'évolution de sa texture. Les conséquences d'un tel phénomène s'observent sur les courbes de contrainte-déformation macroscopiques, présentées sur la Figure 1. Ainsi, les courbes correspondant à la compression de Mg AZ31 (Figure 1a) selon les directions transversale et normale à la direction de laminage sont similaires à bien des courbes de contrainte-déformation observées avec d'autres métaux. Cependant, la courbe de forme sigmoïdale obtenue dans le cas d'une compression le long de la direction de laminage est bien plus singulière. Les mêmes observations s'appliquent au zirconium (Figure 1b). La Figure 1b révèle, par ailleurs, l'influence très prononcée de la température sur le durcissement des métaux hexagonaux en présentant côte à côte les courbes de contrainte-déformation macroscopiques obtenues suite à la compression du spécimen selon l'une des directions du plan, à températures ambiante et cryogénique. En effet, alors que la courbe représentant la compression à température ambiante est "typique" d'une déformation dominée par le glissement, celle obtenue suite à la compression effectuée à température cryogénique est clairement de forme sigmoïdale. De telles variations ne peuvent s'expliquer que par l'activation et la compétition existant entre les différents modes de glissement et de maclage.

Par conséquent, la compréhension et la prédiction précise du comportement mécanique des métaux hexagonaux requièrent l'étude et la prise en compte de trois types distincts d'interaction que sont les interactions glissement/glissement (1), glissement/macle (2) et macle/macle (3). Le très générique terme « interaction macle/macle »englobe des phénomènes tels que le maclage secondaire mais également les jonctions macle-macle, présentées sur la Figure 2. En parallèle de ces trois problèmes fondamentaux dont il ne fait nul doute qu'ils soient étroitement liés à l'état des contraintes internes au sein des phases parent et macle, il est primordial d'accroître notre savoir concernant les mécanismes de nucléation et de croissance associés au maclage. Ce sont ces différentes problématiques qui motivèrent ce travail de thèse dont la méthodologie et les résultats clé sont résumés dans les paragraphes ci-après.

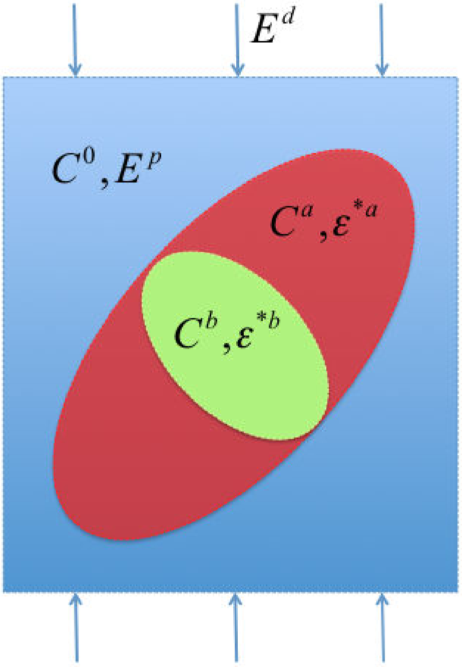

FIGURE 3 – Représentation schématique du problème élastique hétérogène avec "eigenstrains", dues aux maclages primaire et secondaire.

L'étude portant sur le développement des contraintes internes au cours du processus de maclage se fit tout d'abord faite à l'aide d'une nouvelle approche micromécanique basée sur une topologie à double inclusion et le recours au théorème de Tanaka-Mori. Cette approche fut déclinée en deux modèles dont le premier consista en un schéma de Tanaka-Mori élasto-statique pour milieux élastiques hétérogènes avec incompatibilités plastiques. Ce premier modèle, appliqué dans un premier temps au Mg pur puis à l'alliage de Mg AZ31B, fut initialement développé pour étudier l'évolution des contraintes internes dans les phases parent et macle lors de maclage primaire et secondaire. Bien que limité au cas d'élasticité anisotrope hétérogène, les résultats suggèrent que les niveaux de contraintes internes moyennées au sein des macles sont suffisants pour induire de la plasticité dans ces dernières. Par ailleurs, en raison de la forte différence d'orientation existant entre le parent et la macle, l'élasticité hétérogène semble être ce qui impacte le plus les contraintes internes, tant au niveau de leurs valeurs que de leurs signes. L'étude révèle également, dans le cas du maclage primaire, la forte dépendance de l'état de contrainte de la macle vis à vis de la forme de la phase parent.

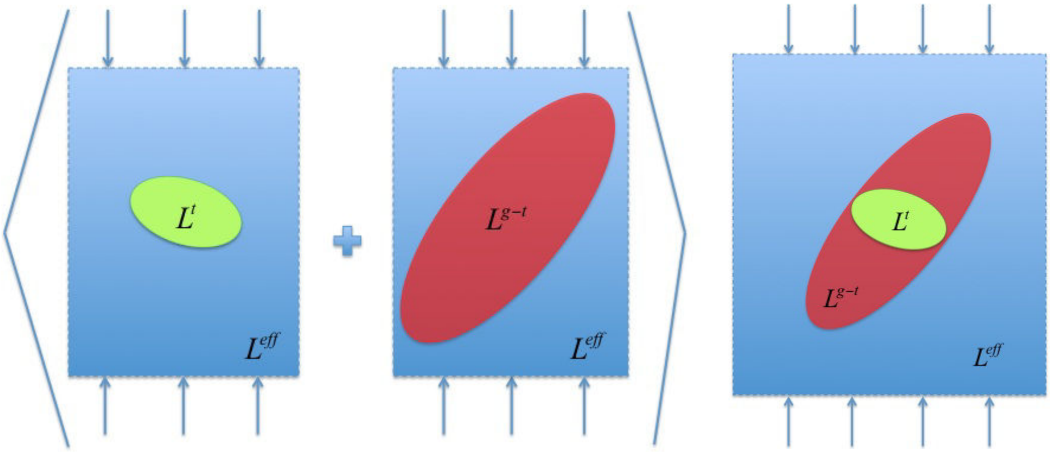

(a) (b)

FIGURE 4 – Représentation schématique du problème élasto-plastique telle que modélisé dans le modèle auto-cohérent élasto-plastique classique (dont l'abrv́iation anglaise est "EPSC") (a) et dans le nouveau modèle auto-cohérent élasto-plastique á double inclusion développé dans cette thése et appelé DI-EPSC.

Fort de ces résultats, un second modèle fut développé, appelé modèle élasto-plastique autocohérent à double inclusion, consistant en une extension du schéma élasto-statique précédemment introduit à l'élasto-plasticité ainsi qu'aux milieux polycristallins. A l'instar du premier modèle, le résultat original de Tanaka-Mori est utilisé pour dériver les nouvelles relations de concentration liant les champs de déformation moyens des macles et des grains maclés au champ de déformation macroscopique. Tous les grains, maclés ou non, sont considérés comme faisant partie intégrante du milieu homogène équivalent dont les propriétés mécaniques effectives sont calculées à l'aide d'une procédure auto-cohérente itérative implicite et non-linéaire, appélée modèle DI-EPSC. Contrairement aux modèles élasto-plastiques existants qui assimilent les phases parent et macle à des inclusions ellipsoïdales indépendantes, les nouvelles relations de concentration tiennent compte du couplage direct existant entre ces dernières. La comparaison des résultats obtenus avec le nouveau modèle DI-EPSC avec ceux provenant du modèle classique EPSC ainsi que ceux issus de l'expérience aboutit à trois résultats significatifs. Le premier consiste en la conclusion qu'une reproduction exacte des effets latents induits par le maclage permet de prédire l'influence de la plasticité sur le durcissement et sur le taux de durcissement se produisant dans les macles. Le second réside en l'observation que les nouvelles relations de concentration génèrent des distributions de déformation en cisaillement plus éparses. Enfin, le troisième résultat est la mise en exergue de l'influence de l'état de contrainte initiale de la macle, lors de sa nucléation, sur la réponse mécanique du matériau.

Par ailleurs, il apparut que la majeure partie des instabilités numériques rencontrées, au cours de cette étude, provenait du choix de la matrice de durcissement. En effet, bien que cette dernière fût positive semi-définie, le schéma auto-cohérent se serait avéré bien plus stable si elle avait été définie strictement positive. Cependant, une telle hypothèse va à l'encontre d'une récente étude qui montra que certaines valeurs propres associées à la matrice de durcissement du Mg pur

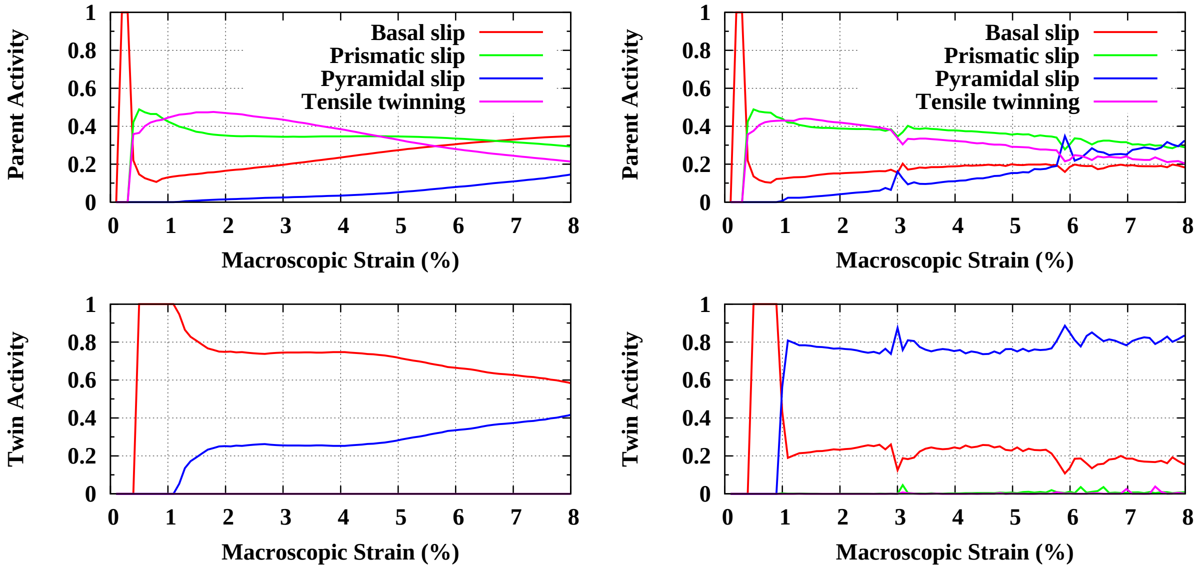

(a) (b)

Figure 5 – Activités plastiques moyennées des systèmes de déformation principaux de glissement et de maclage au sein des phases macle et parent obtenues à partir de (a) EPSC et du (b) DI-EPSC.

peuvent être négatives. Par conséquent, le moyen le plus simple de contourner une telle difficulté, inhérente à l'algorithme EPSC, est soit d'opter pour une matrice définie strictement positive soit d'utiliser des schémas visco-plastiques ou élasto-visco-plastiques.

Afin de traiter les cartographies EBSD et d'en extraire des statistiques relatives au maclage, et ce de façon automatique, un nouveau logiciel d'analyse EBSD, reposant sur les théories des graphes et structures de groupe et les quaternions, fut développé. Les quaternions permettent de calculer facilement les désorientations entre pixels et groupes de pixels de même orientation. L'utilisation de la théorie des graphes et des structures de groupe rend possible l'identification des grains, la reconnaissance des phases macle et l'extraction des statistiques.

Le logiciel se distingue des versions commerciales existantes en combinant visualisation et analyse automatisée du micrographe. L'interface graphique intégrée permet un accès direct et immédiat aux données relatives à la microstructure et au maclage ; elle autorise également l'utilisateur à corriger ou compléter, si nécessaire, l'analyse réalisée par le logiciel. Toutes les données, aussi bien brutes que traitées, sont sauvegardées au sein d'une base de données relationnelle. Il est, par conséquent, possible d'accéder à l'intégralité des paramètres expérimentaux, données microstructurelles et statistiques sur le maclage via de simples requêtes SQL. La base de données rend également possible la quantification systématique de l'influence d'un très grand nombre de paramètres. La construction et l'intégration d'une telle base de données au sein même du logiciel sont, en plus de l'interface graphique interactive, autant de fonctionnalités que les autres outils d'analyse actuels n'ont pas.

Bien qu'initialement développé pour analyser des micrographes de Zr et de Mg, les capacités du logiciel ne se limitent pas à ces deux métaux hexagonaux. En effet, son algorithme est à

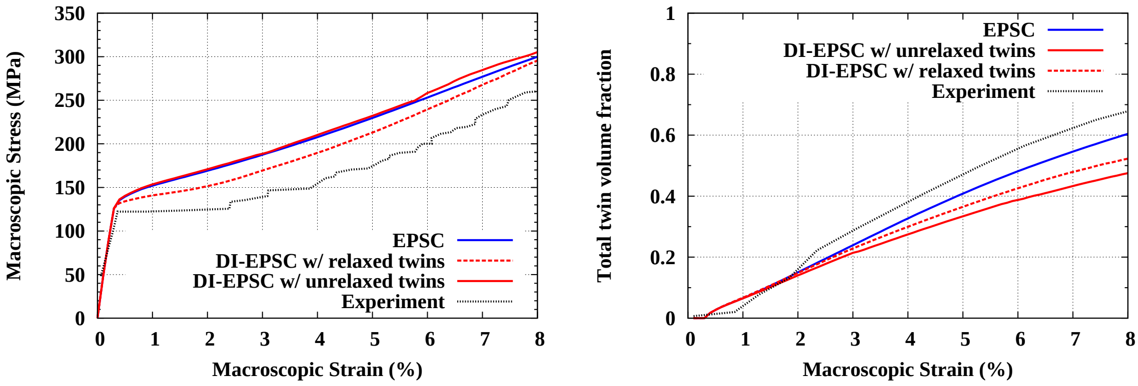

(a) (b)

FIGURE 6 – (a) comparaison des courbes contrainte-déformation macroscopiques prédites par l'EPSC et le DI-EPSC avec celle obtenue expérimentalement et (b) évolution de la fraction volumique totale de macle au sein du polycristal.

même d'identifier n'importe quel type de macle à condition que l'utilisateur renseigne dans le logiciel la valeur du ratio c/a ainsi que les désorientations théoriques correspondant aux différents systèmes de maclage potentiellement actifs. Pour l'analyse d'autres structures cristallographiques, l'utilisateur devra, en outre, modifier les paramètres de maille ainsi que les quaternions de symétrie.

Les deux premières études statistiques furent effectuées à partir de cartographies EBSD de Mg AZ31 laminé dans le but d'expliquer l'activation de macles d'extension $\{10\bar{1}2\}$ à faible facteur de Schmid et la nucléation de double macles d'extension $\{10\bar{1}2\}$-$\{10\bar{1}2\}$. La première étude révéla que les macles d'extension $\{10\bar{1}2\}$ ayant un faible facteur de Schmid ne représentent que 6,8% de toutes les macles observées. S'appuyant uniquement sur des lois constitutives déterministes, les modèles polycristallins tels qu'EPSC ou EVPSC (modèle élasto-visco-plastique) ne peuvent être capables de justifier de l'activation de telles macles. En raison de leur faible apparition, l'influence de ces dernières sur la réponse mécanique du matériau demeure a fortiori très limitée. La deuxième étude montra, quant à elle, que les double macles d'extension $\{10\bar{1}2\}$-$\{10\bar{1}2\}$ obéissent, en général, à la loi de Schmid. Elle révéla également que considérer les variations d'énergie interne induites par l'apparition de telles macles à partir d'un modèle micromécanique à double inclusion, même simplifié, permet de prédire de façon précise quelles sont les variantes susceptibles d'être activées. L'étude établit aussi que de telles macles restent extrêmement rares et ont un effet négligeable sur les propriétés mécaniques du matériau.

En parallèle de ces deux études, une troisième fut menée, cette fois, sur du Zr pur afin de discuter des influences respectives (i) des jonctions macle-macle entre macles de première génération, (ii) de la taille de grain, (iii) de l'orientation cristallographique sur la nucléation et la croissance de macle. Les échantillons furent baignés dans l'azote liquide et chargés en compression selon l'une des directions du plan ainsi que le long de la normale au plan dans le but de favoriser, respectivement, la formation de macles d'extension T_1 et de compression C_1. Les abréviations T_1, T_2 et C_1 réfèrent aux macles de type $\{10\bar{1}2\}$, $\{11\bar{2}1\}$ et $\{11\bar{2}2\}$. Cette étude est la première à établir la pertinence statistique des jonctions macle-macle. Six types

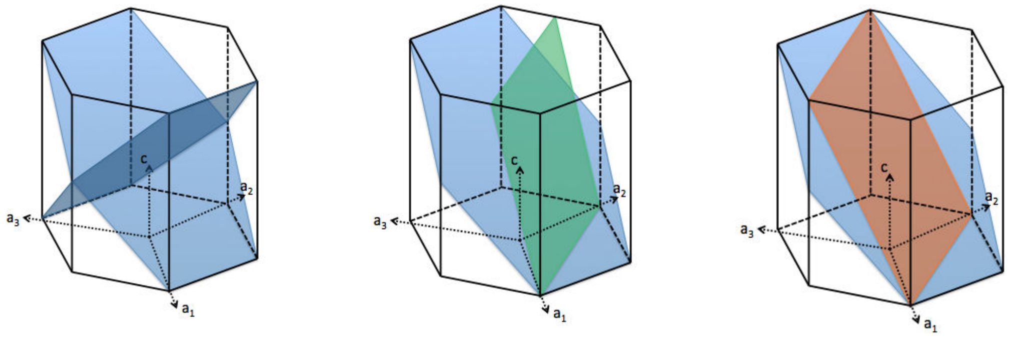

(a) $T_1 - T_1$ type 1 (b) $T_1 - T_2$ type 1 (c) $T_1 - C_1$ type 1

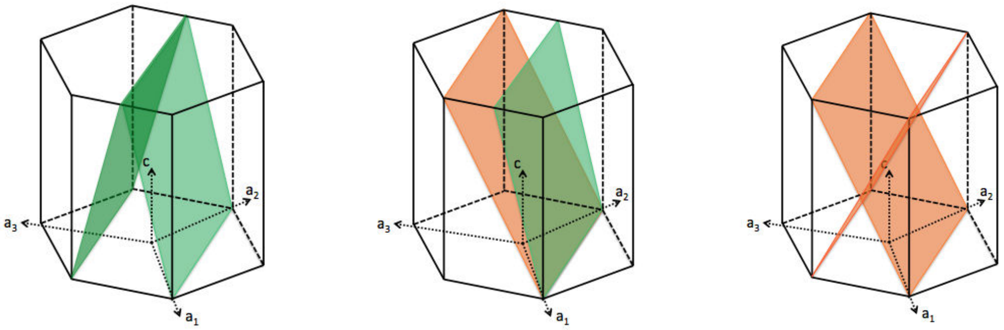

(d) $T_2 - T_2$ type 1 (e) $T_2 - C_1$ type 1 (f) $C_1 - C_1$ type 1

FIGURE 7 – Représentation graphique d'exemples de jonctions macle-macle observées dans les cartographies EBSD de Zr.

de jonctions macle-macle, à savoir $T_1 - T_1$, $T_1 - T_2$, $T_1 - C_1$, $T_2 - T_2$, $T_2 - C_1$ et $C_1 - C_1$, furent observés. Les jonctions macle-macle se produisant entre macles de même mode, et plus particulièrement entre celles appartenant aux deux modes les plus actifs, sont très fréquentes et ne peuvent donc pas être négligées. Selon le trajet de chargement considéré, ces dernières peuvent représenter plus de la moitié de toutes les jonctions observées. La comparaison des épaisseurs de macles apparues dans des grains ne contenant qu'une seule macle avec celles des macles appartenant à des grains comprenant plusieurs macles révèle que les jonctions macle-macle entravent la croissance des macles. En outre, seules les macles appartenant au mode de maclage prédominant semble être fortement affectées par l'orientation cristallographique du grain ainsi que par la direction de chargement. Ces différences peuvent probablement être expliquées par la présence de niveaux de contraintes très localisés permettant la nucléation de n'importe quel type de macle. En accord avec de précédentes études, il est apparu également que la probabilité de nucléation de macle et le nombre moyen de macles par grain maclé augmentent avec la taille de grain.

En termes de perspectives, la continuation logique de cette thèse consiste en 1) une intégration plus aboutie des capacités de post-traitement du logiciel EBSD et en 2) le développement et l'implémentation dans le DI-EPSC de modèles stochastiques de nucléation de macle qui prendraient en considération les données statistiques des récentes études. Par ailleurs, en multipliant les mesures EBSD sur plus d'échantillons de Mg et de Zr, chargés monotoniquement et cycliquement selon des directions variées à différentes températures et vitesses de chargement, il serait alors possible pour la modélisation micromécanique de prendre en considération une quantité précieuse de données statistiques.

Chapitre 1

Introduction and state-of-the-art

Sommaire

Polycrystalline materials with hexagonal close-packed crystal structure -hereafter h.c.p.- have been the subject of worldwide interest dating back to the late 1960s. Such is motivated by the broad range of applications of h.c.p. metals such as magnesium, zirconium, titanium, zinc, cadmium, beryllium, rhenium, cobalt, etc. Focus is placed here on the cases of pure zirconium and magnesium and some of their alloys (with emphasis on AZ31B Mg alloy). Zirconium has an ideal thermal neutron scattering cross-section, good ductility and resistance to corrosion and is therefore extensively used, in an alloyed form (e.g. Zircalloy), as cladding and piping material in generation 3 and 4 nuclear reactors[2, 12, 13, 14, 15]. Magnesium and its alloys on the other hand, have great potential for lightweithing applications [16] -particularly for the automotive industry- as they exhibit high specific Young's modulus. As a result, cast magnesium alloys have, over the past decade, been increasingly used as structural components. The use of sheets of h.c.p. metals for part production necessarily relies on forming operations in which the metal will be necessarily deformed irreversibly.

Plastic deformation -with key characteristics such as strength, hardening, ductility- is highly anisotropic both in pure Mg, Zr and most of their alloys. Figure 1.1 depicts experimentally measured stress-strain curves of rolled AZ31B Mg and clock-rolled high-purity Zr loaded in tension and compression along different directions and, in the case of Zr, at different temperatures. It is clearly shown here that a change in temperature or in loading direction can have a significant effect on the materials yield stress, strain hardening rate and ductility. As a result, sheet forming of h.c.p. materials remains a rather delicate task that largely limits their use in sheet forms.

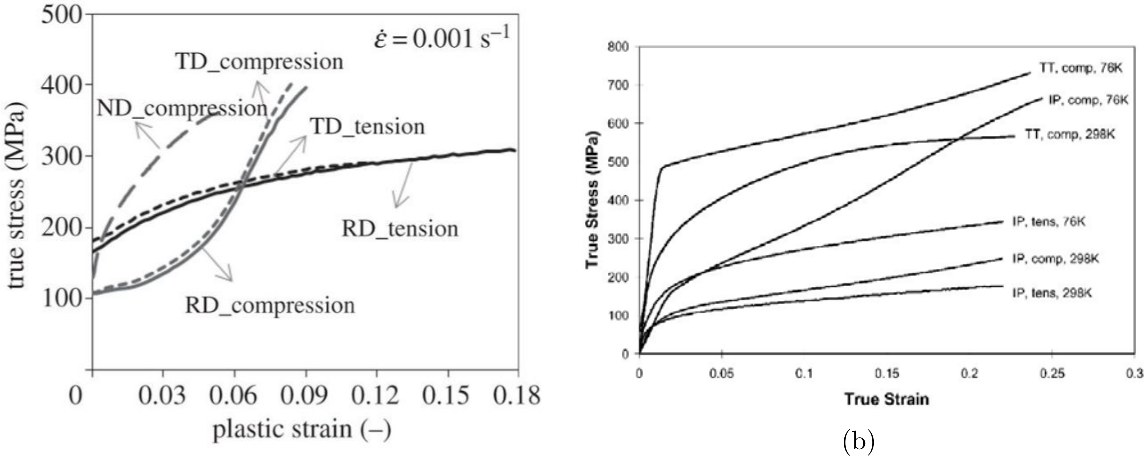

(a)

(b)

FIGURE 1.1 – (a) comparison of tension and compression stress-strain curves of rolled AZ31B Mg alloy [1] and (b) comparison of mechanical responses of clock-rolled high-purity Zr for various loading directions and temperatures [2]. Tension and compression are denoted by "tens" and "comp", respectively. Abbreviations "TT" and "IP" stand for "through-thickness" and "in-plane", respectively.

1.1 Motivation and Objectives

In h.c.p. metals [17, 18, 19, 20], strain accommodation and stress relaxation may result from the activation of either slip, twinning or both. Slip is characterized by the motion and interaction of dislocations belonging to different slip systems and possibly slip modes. On the other hand twinning is a sensibly different irreversible deformation mode characterized by the nucleation of sub-volumes within grains, i.e. twin domains, exhibiting a mirror symmetry reorientation of the lattice with respect to a specific plane, the twinning plane. Understanding plastic deformation in h.c.p. metals is particularly complex as a result of the large variety of possibly active deformation modes. For example, three active slip and two twinning modes can be found in pure magnesium while four twinning modes and three slip modes have been experimentally observed in pure zirconium. In addition, plasticity can also be activated within twin domains by means of secondary slip or of double twinning.

In general, the relative contribution and activity of each deformation mode will have an effect on both the mechanical response but also on the texture change in the material. The consequence of this can be appreciated by observing the macroscopic stress-strain curves displayed in Figure 1.1. For example, the macroscopic stress-strain curves of a rolled AZ31B Mg alloy loaded along the transverse and normal directions shown in Figure 1.1a are similar to many other metal stress-strain curves. However, the sigmoidal macroscopic stress-strain curve corresponding to the compression along the rolling direction is significantly different. The same observation applies for Zr (Figure 1.1b). Figure 1.1b also shows that temperature may strongly influence the hardening response of h.c.p. metals. It is observed that when compressed along one of the in-plane directions at both room and liquid nitrogen temperatures, the macroscopic stress-strain curve obtained is in one case typical of slip dominated deformation while in the other case the curve is clearly sigmoidal. Such variations in the mechanical responses can only result from the activation and the competition of many and diverse deformation mechanisms.

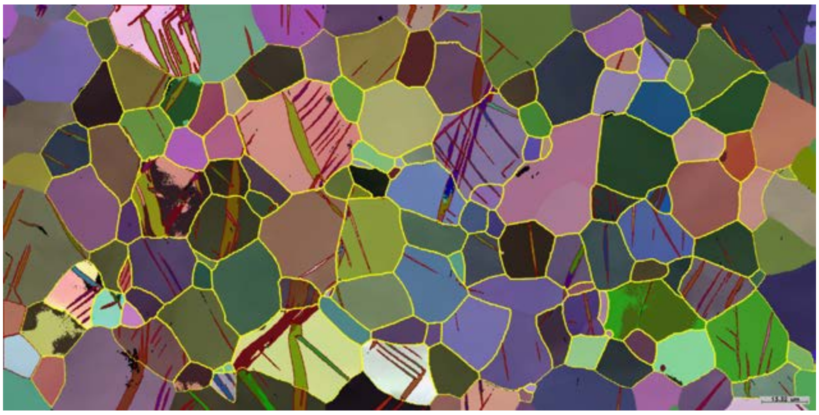

FIGURE 1.2 – EBSD scan example of a clock-rolled Zr specimen loaded in compression along the through-thickness direction. These scans were processed using the software presented in Chapter 3.

Consequently, accurately understanding and predicting the behavior of h.c.p. metals requires that we study and take into account three distinct interaction types : (1) slip/slip interactions, (2) slip/twin interactions, and (3) twin/twin interactions. The term twin-twin interaction is very general and includes phenomena such as secondary or double twinning and twin-twin junctions whose examples are displayed by Figure 1.2. In parallel to these three key fundamental problems, and acknowledging that slip/twin and twin/twin interactions will necessarily be largely driven by the internal stress state within twin domains -for example activation of secondary slip is clearly dependent on the internal stress within the twin- one must also gain an understanding of the growth and nucleation mechanisms associated with twinning [21, 22, 23]. These topics are briefly discussed in what follows so as to motivate the work to be presented in upcoming chapters.

Twinning : key experimental results

Twin domains form via the nucleation and glide of twinning partial dislocations on the twinning plane [24, 25]. The shear induced by the propagation of those dislocations reorients the lattice in such a way that the parent and twin lattices are symmetric with respect to either the twinning plane or the plane normal to both the twinning direction and the twinning plane [18, 26, 27, 28, 29]. Following nucleation, twin thickening occurs by the subsequent nucleation and propagation of twinning dislocations along planes parallel and adjacent to the faulted plane. Because motion and nucleation of twinning partial dislocations are sign sensitive, most of constitutive models for h.c.p. materials [30, 31, 32, 33] rely on positiveness and magnitude of resolved shear stresses (RSS) on the twinning plane in the shear direction to determine when a twin nucleates and grows. However, recent experimental studies [34, 35] based on EBSD measurements clearly show that twins nucleate at grain boundaries, crack tips, ledges and other interface defects where stresses are highly localized. Twin nucleation can be considered as a random event as it strongly depends on the presence of defects within the material. These studies suggest that the stress levels required for the nucleation and growth of twins are different. Consequently, knowledge of internal stresses in the parent phases is absolutely necessary for predicting twinning activity.

Using a three-dimensional X-ray diffraction technique, Aydiner et al. [36] performed in-situ measurements of the evolution of full strain and stress averaged tensors within both the twin and parent phases as the twin nucleated and grew. The authors revealed that the two nucleated twin variants were those with the highest averaged resolved shear stresses projected on the twinning plane along the twinning direction. Because the experimental study was limited to solely one grain, results about twin nucleation cannot be considered as statistically representative, but they still prove that internal stresses and twinning incidence are related. They also showed that stress magnitudes in the parent and twin phases are drastically different, while one could expect intuitively that, at least at the onset of twinning, both twin and parent phases have the same stress state. The initial stress state within the twin domain is particularly relevant because the latter influences the rate of hardening, the hardening and, hence, the activation of secondary slip in the twin phase. In addition, at large strains, the twinned volume becomes significant compared to the total volume, and stresses in the twin phases directly impact the macroscopic stress levels of the material. Until now, polycrystalline models based on deterministic approaches to deal with twin nucleation and homogenization techniques were capable of accounting for inter-granular interactions [37, 38, 39, 40, 41, 42, 43, 44, 45, 46, 47, 48, 49, 50] but were incapable of quantifying the influence of parent-twin interactions without fitting model parameters or adding an artificial stress correction term [4].

Slip/slip interactions : towards a comprehensive understanding

While this is not the main subject of the present thesis, slip system interactions are briefly discussed here for the sake of completeness. Taylor [20] elegantly proved that any polycrystalline material is able to undergo homogeneous deformation without producing cracks if five independent slip systems can be activated. The potentially active slip systems in h.c.p. metals are basal, prismatic and pyramidal first or second order [51, 52]. More recent works [53, 54] showed that five independent slip systems are not always necessary. For example, Hutchinson [54] observed that inelastic deformation can result from the activation of only four linearly independent slip systems without pyramidal slip. Regardless, during slip dominated plasticity, all slip systems necessarily interact. From the constitutive modeling standpoint all such interactions are usually grouped in self and latent hardening matrix. These are expected to capture the collective behavior of dislocations as they interact with one another. Ideally one should thus accurately render each unit process associated with each dislocation interaction event that can potentially lead to junction formation, unzipping, repulsion and crossed states.

Discrete dislocation dynamics (DDD) can largely provide answers to those questions. In DDD, dislocation lines are discretized and dislocation motion is predicted by solving an overdamped equation of motion for each dislocation segment (or node depending on the numerical strategy chosen). Then junction formation can be predicted by enforcing conservation of the Burgers vector as well as the maximum dissipation. Recently, latent hardening coefficients resulting from slip/slip interactions were computed from DDD by Bertin et al. [55] for pure magnesium. The authors showed that basal/pyramidal slip interactions are particularly strong. This can be of prime importance, as it suggests that such interactions could be detrimental to the material's ductility. Note however in the work cited above, some of the key fundamental aspects remain to be treated, as the nature and specifics associated with <c+a> dislocations on the second order pyramidal plane are subject to debate [56].

Slip/twin interactions : recent progress

Slip/twin interactions occur at the twin interface as a slip dislocation intersects and possibly dissociates onto the twinning interface. The nature of the reaction between slip and twinning dislocations depends on the geometry of the reaction at stake (i.e. incoming dislocation Burgers vector, character, etc.). In his review of deformation modes in h.c.p. metals [52], Yoo described to a high level of detail the specific crystallographic reactions that can result from slip/twin interactions. While of great interest, the study was necessarily limited to geometrical and elementary energetic considerations. In particular transition states describing dislocation core effects were disregarded. Provided that accurate atomistic pair potentials can be found/developped, these limitations can be circumvented by means of atomistic simulations such as those conducted in a series of pioneering studies by Serra and Bacon [57, 24, 58]. The authors revealed the complexity of the unit processes involved. For example, it was shown that a screw "basal" dislocation can easily cross a $\{10\bar{1}2\}$ twin boundary, while an edge basal dislocation will dissociate on the twin boundary and could generate surface disconnections.

Such simulations are ideal to understand and describe the different mechanisms but are limited to a few dislocations. Later on, the reactions described in the above were rationalized in a constitutive model that suggested that slip assisted twin growth resulting from the continuous generation of steps by means of slip/twin interactions was an unlikely candidate for explaining the rapid growth rate of tensile twins. In parallel, Fan et al. [59] used three-dimensional DDD to study the interactions between slip dislocations and $\{10\bar{1}2\}$ tension twin boundaries. It was found, as expected that twins have a stronger influence on hardening (in the sense of limiting slip) than grain boundaries. However, their results cannot be directly implemented in constitutive laws. This shortcoming serves as a motivation for developing novel micromechanical models allowing researchers to capture, albeit in a coarse fashion, these effects.

Twin/twin interactions : motivating theoretical and experimental results

Twin/twin interactions and secondary twinning are also suspected to have significant effect on microstructure evolution and internal stress developments during plasticity. Regarding twin-twin interactions, the crystallography associated with the different twinning partial dislocations that can occur was discussed in general in work by Cahn [18] on depleted uranium. In the specific case of h.c.p. materials the literature is quite scarce. One must acknowledge recent work [60, 61, 62] based on EBSD and TEM measurements investigated the nature of $\{10\bar{1}2\}$-$\{10\bar{1}2\}$ twin-twin junctions and their influence on twin nucleation and twin propagation rates. It was suggested that twin-twin junctions could hinder twin growth while favoring nucleation. However, these studies are limited to one type of twin-twin junction and rely on the observation of only a few single twinned grains such that they are not necessarily statistically representative. The question remaining is that of the need for accounting for these interactions in constitutive models. Micromechanical multi-inclusion models exist [63, 64] but have never been applied or adapted to treat this type of problem.

Secondary twinning, also called double twinning, is another interesting problem as several experimental studies [65, 66] have proposed connections between the activation of such processes and fracture. An experimental study performed by Martin et al. [67] from Mg EBSD scans revealed that activated double twin variants were those that either required the least strain accommodation within the parent domain or obeyed the Schmid's law. However, the latter study neither discussed the statistical relevance of secondary twinning nor quantified its influence on the mechanical response.

1.2 Crystallography of h.c.p. metals

In the Miller-Bravais indexing system, the hexagonal crystal structure as shown in Figure 1.3 is defined with respect to four axes or vectors denoted by $\mathbf{a_1}$, $\mathbf{a_2}$, $\mathbf{a_3}$ and $\mathbf{c}$, respectively. Vectors $\mathbf{a_1}$, $\mathbf{a_2}$, $\mathbf{a_3}$ lie in the lower basal plane. Angles formed by vector pairs ($\mathbf{a_1}$,$\mathbf{a_2}$), ($\mathbf{a_2}$,$\mathbf{a_3}$) and ($\mathbf{a_3}$,$\mathbf{a_1}$) are all equal to $2\pi/3$ radians. The c-axis is perpendicular to basal planes and, hence, to vectors $\mathbf{a_1}$, $\mathbf{a_2}$ and $\mathbf{a_3}$. The magnitude is the same for all vectors $\mathbf{a_i}$ with $i = \{1, 2, 3\}$ but differs from

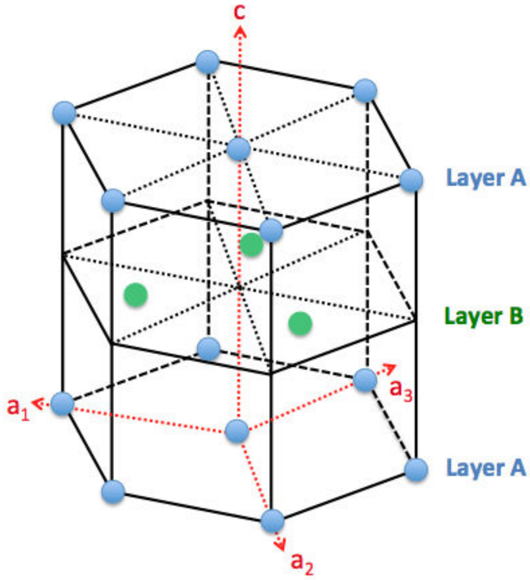

FIGURE 1.3 – Schematic representation of a hexagonal structure containing three primitive unit cells. Atoms are represented by blue hard spheres.

the magnitude of vector $\mathbf{c}$. The norm of vectors $\mathbf{a_i}$ corresponds to the distance between two neighboring atoms lying in the same atomic layer. The magnitude of the vector $\mathbf{c}$ represents the distance between two atomic layers of same type. Using other words, it represents the distance separating the lower part from the upper part of a hexagonal cell. Atom positions, directions and planes can be expressed from vectors $\mathbf{a_1}$, $\mathbf{a_2}$, $\mathbf{a_3}$ and $\mathbf{c}$. However, it is also possible to only use vectors $\mathbf{a_1}$, $\mathbf{a_2}$ and $\mathbf{c}$ since $\mathbf{a_3} = -(\mathbf{a_1} + \mathbf{a_2})$. The hexagonal structure as shown in figure 1.3 contains 3 unit cells consisting of atom arrangements made of two tetrahedra facing upwards. For example, by representing atoms with hard spheres, the first of the 3 unit cells shown in Figure 1.3 includes atoms located at coordinates (1,0,0), (0,0,0), (1/2,1/2,0), (2/3,1/3,1/2), (1,0,1), (0,0,1) and (1/2,1/2,1). An unit cell is composed of 7 atoms. Each atom lying in layers A, i.e. blue spheres, is shared with 2 other unit cells. The atom belonging to layer B is not shared with any other unit cell. As a result, the coordination number of an elementary hexagonal unit cell is 2. If all atoms contained in an unit cell are equidistant, then the axial ratio $\gamma = c/a$ is equal to $\sqrt{8/3} \sim 1.633$. This value is never reached with pure materials at room temperature and pressure but metals such as magnesium and cobalt exhibit axial ratios which are very close, e.g. 1.623 for both of them [17]. At room pressure and temperature conditions, axial ratios of pure h.c.p. metals are included between 1.56 (i.e. beryllium) and 1.89 (i.e. cadmium) [17]. Hexagonal intermetallic phases with a γ ratio equal to $\sqrt{8/3}$ have also been produced [68]. Note that the value of γ is function of temperature and pressure.

Figure 1.4 displays important planes and directions in h.c.p. metals. They correspond to planes and directions of either slip or twinning systems that will be mentioned further.

1.3 Crystallography of twinning in h.c.p. metals

Hall [26] and Cahn [18] were the first to present a detailed analysis of deformation twinning crystallography in h.c.p. materials. Shortly after, Kiho [69, 70] and Jawson and Dove [71, 72, 73]

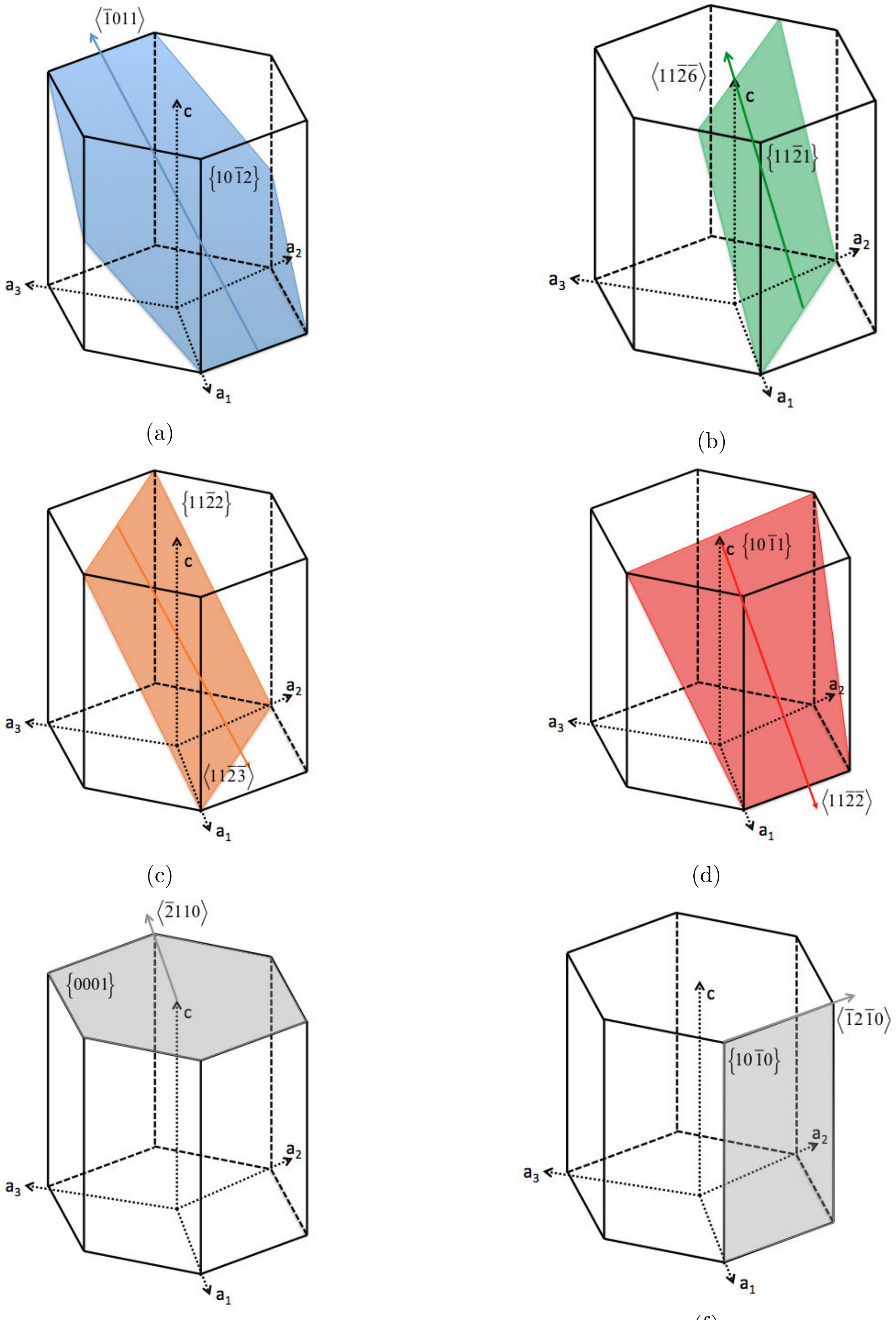

(a) (b) (c) (d) (e) (f)

FIGURE 1.4 – Schematic representation of the main crystallographic planes and directions in h.c.p. structures.

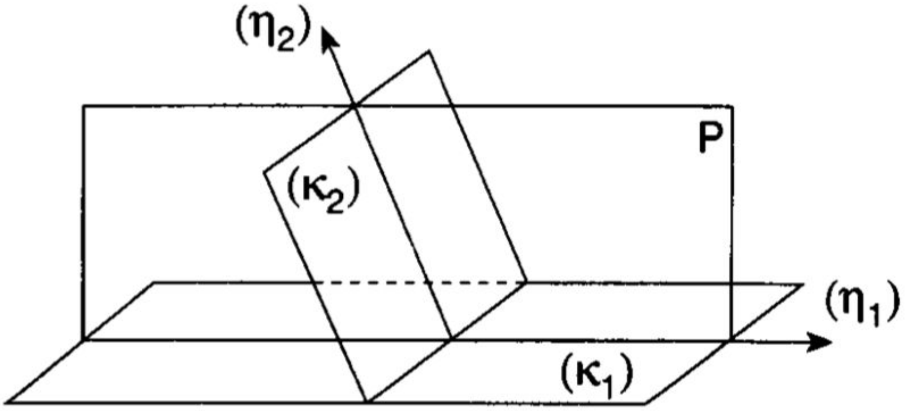

FIGURE 1.5 – Schematic representation of the twinning plane, K_1 and its conjugate, K_2, the twinning shear direction, η_1, and its conjugate, η_2, and the plane of shear, P [3].

developed theories aimed at predicting the activation of twinning modes. Their theories rely on the assumption that activated twinning systems are the ones that minimize both the twinning shear magnitude and shuffles. In 1965, Bilby and Crocker [27] reviewed and generalized the works previously mentioned. They provided the most complete analysis of shuffling processes and a very rigorous treatment of the orientation relationships and of the division of atomic displacements into shear and shuffles. Till now, their theory, referred to as the Bilby-Crocker theory or the classical crystallographic theory of deformation twinning in the following, remains the reference. Bevis and Crocker [28, 29] extended the theory to the case of non-classical twins. The objective of the present paragraph is to present the main aspects of deformation twinning crystallography and introduce the principal twinning modes in h.c.p. metals.

A deformation twin consists of a region of a grain that underwent a homogeneous shape deformation in such a way that the twinned domain has exactly the same crystalline structure as the parent domain but a different orientation. Consequently, deformation twinning consists in a homogeneous shape deformation but does not induce volume variation. Because parent and twin phases remain in contact, the deformation undergone by the twinned region must be an invariant plane shear strain. A twinning mode can be completely characterized by two planes and two directions. These planes and directions correspond to the invariant and unrotated plane, denoted by K_1, the second invariant but rotated plane of the simple shear, K_2, the twinning shear direction, η_1, and the direction, η_2, resulting from the intersection of the plane of shear P, perpendicular to both K_1 and K_2, with K_2 (Figure 1.5). The plane K_1 is called the composition or twinning plane. Even if four elements characterize a twinning mode, knowing only either K_1 and η_2 or K_2 and η_1 is sufficient to completely define a twinning mode. The conjugate of a given twinning mode is also described by planes K_1', K_2' and directions η_1', η_2' such that $K_1' = K_2$, $K_2' = K_1$, $\eta_1' = \eta_2$, $\eta_2' = \eta_1$ and the magnitude of the twinning shear, s, is the same. K_2 and η_2 are then called the reciprocal twinning plane and reciprocal twinning direction, respectively.

The four orientation relations of the classical crystallographic theory of twinning are :

- 1) reflexion in K_1,
- 2) rotation of π about η_1,
- 3) reflexion in the plane normal to η_1,

- 4) rotation of π about the normal to K_1.

Because hexagonal structures are centro-symmetric, lattices obtained with relations (1) and (4) are identical. The same observation can be made with relations (2) and (3). It is then natural to classify into three types of twins. Type 1 and type 2 twins correspond to twins whose lattices can be obtained from relations (1)-(4) and (2)-(3), respectively. The third type of twins includes all twins for which twin lattices can be reproduced by using any of the four classical orientation relations. Note that relations (2) and (4) are particularly convenient for expressing Rodrigues vectors and hence quaternions associated with twinning of types 2 and 1, respectively. Another way to differentiate twins of type 1 and 2 consists in looking at the rationality of indices of K_1, K_2, η_1 and η_2. Twins of type 1 are twins for which indices of K_1 and η_2 are rational while twins of type 2 are those for which K_2 and η_1 are rational. In the case of compound twins, all K_1, K_2, η_1 and η_2 indices are rational. Geometrical considerations explaining the rationality or non-rationality of Miller indices of planes K_1, K_2 and directions η_1, η_2 are detailed in Bilby and Crocker [27] and reminded by Christian and Mahajan [3]. Other twinning orientation relations are theoretically possible and have been investigated by Bevis and Crocker [28, 29] Referred to as non-classical twins, they will not be studied in the present document.

Denoting by $\mathbf{u_1}$, $\mathbf{u_2}$ and $\mathbf{u_3}$ basis vectors associated with the hexagonal cell and using Einstein convention and Christian et al. notations [3], unit vectors parallel to the η_1 direction, the η_2 direction and the normal to the twinning plane can be written as $\mathbf{l} = l_i u_i$, $\mathbf{g} = g_i u_i$ and $\mathbf{m} = m_i u_i$, respectively. As a result, if K_1 and η_2 are known, the shear direction η_1 is expressed as follows :

$$\eta_{\mathbf{1}} = s\mathbf{l} = 2(\mathbf{m} - (\mathbf{g}.\mathbf{m}^{-1})\mathbf{g}) \tag{1.1}$$

The magnitude of the twinning shear is given by :

$$s^2 = 4((\mathbf{g}.\mathbf{m})^{-2} - 1) \tag{1.2}$$

Consequently, the deformation gradient tensor associated with deformation twinning is expressed as

$$\mathbf{F} = \mathbf{I} + s(\mathbf{l} \otimes \mathbf{n}) \tag{1.3}$$

with $\mathbf{I}$, the identity tensor.

The case of $\{10\bar{1}2\}$ twins is particularly interesting because the twinning shear s becomes null when $\gamma = \sqrt{3}$, and shear direction reverses as γ passes through this value. As a result, $\{10\bar{1}2\}$ twins can be either tensile or compressive, depending on the axial ratio magnitude.

However, the simple application of the previously described shear is not sufficient to reorient the crystal lattice in such a way that atoms belonging to the twinned region face their image in the parent phase with respect to the mirror symmetry plane. Additional atomic displacements are then necessary to produce the twin structure from the sheared parent structure. These atomic displacements, which relate the twin lattice sites to the parent lattice sites, are called lattice shuffles. Consider a primitive lattice vector $\mathbf{w}$ parallel to the direction η_2. The magnitude of its projection along the normal to the twinning plane is equal to qd where q is an integer denoting the number of lattice planes K_1 of spacing d crossed by $\mathbf{w}$. Atom displacements are repeated in each successive group of q planes. Bilby and Crocker [27] showed that, in the case of twinning of type 1, lattice points lying in the planes $p = q/2$ and $p = q$ are sheared directly to their final

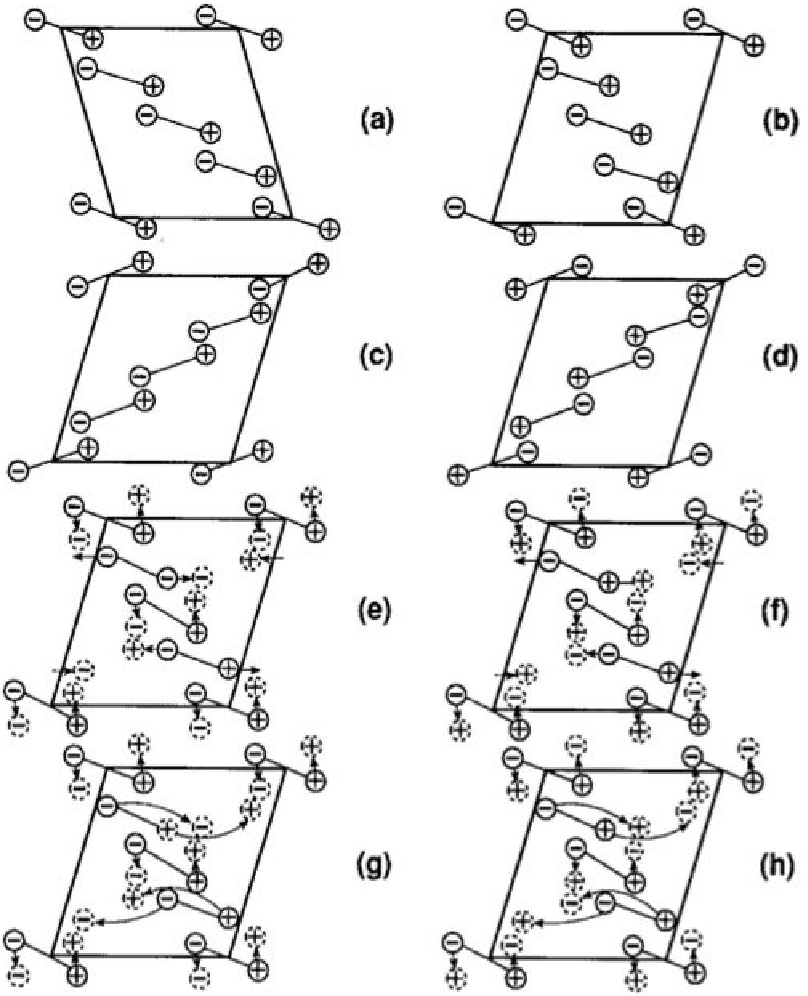

FIGURE 1.6 – Schematic representation of possible lattice shuffles for double lattice structures when $q = 4$. (a) Parent structure ; (b) sheared parent ; (c) type 1 twin ; (d) type 2 twin ; (e) possible type 1 shuffle ; (f) possible type 2 shuffle ; (g) alternative type 1 shuffle ; (h) alternative type 2 shuffle [3].

TABLE 1.1 – List of observed twinning modes in h.c.p. metals

K_1 {}	K_2 {}	η_1 <>	η_2 <>	s -	q -	Observed in
$10\bar{1}2$	$\bar{1}012$	$10\bar{1}\bar{1}$	$\bar{1}01\bar{1}$	$(\gamma^2-3)/3\gamma$	4	Mg, Ti, Co, Zr, Zn, Be
$10\bar{1}1$	$10\bar{1}\bar{3}$	$10\bar{1}\bar{2}$	$30\bar{3}2$	$(4\gamma^2-9)/4\sqrt{3}\gamma$	8	Mg, Ti
$11\bar{2}1$	0001	$11\bar{2}\bar{6}$	$11\bar{2}0$	$1/\gamma$	2	Re, Ti, Zr, Co
$10\bar{1}\bar{3}$	$10\bar{1}1$	$30\bar{3}2$	$10\bar{1}2$	$(4\gamma^2-9)/4\sqrt{3}\gamma$	8	Mg
i	i	i	i	$(4\gamma^4-21\gamma^2+36)^{1/2}/4\sqrt{3}\gamma$	-	Mg
$11\bar{2}2$	$11\bar{2}\bar{4}$	$11\bar{2}\bar{3}$	$22\bar{4}3$	$2(\gamma^2-2)/3\gamma$	2	Re, Ti, Zr, Co

positions, i.e. twin positions, if q is even. Regarding twinning of type 2, another parameter q^* has to be introduced. It corresponds to the number of K_2 planes crossed by a primitive lattice vector parallel to the twinning shear direction η_1. It is been proven that no shuffles are required when $q^* = 1$ and $q^* = 2$. In short, any crystalline structure containing more than one atom per unit primitive cell will undergo lattice shuffling during twinning deformation when $q = 4$. Examples of possible shuffling mechanisms are presented in Figure 1.6. Moreover, Table 1.1 lists most of the twinning systems observed in h.c.p. materials. Note that except a very rare twinning system observed in Mg by Reed-Hill [74], all twinning modes listed in Table 1.1 are compound.

Very early, Kiho [69, 70] and Jaswon et al. [71, 72, 73] developed models aimed at predicting the activation of twinning systems. These models are based on the simple assumption that activated twin systems are those inducing the least amount of shear and the smallest lattice shuffles. Bilby and Crocker [27] generalized them and suggested that a newly-formed twin has the following properties :

- 1) small twinning shear magnitude,
- 2) its formation required simple lattice shuffles, i.e. shuffles with a small value of q,
- 3) lattice shuffles induced by its nucleation have a small magnitude,
- 4) if large shuffles are necessary, they should be parallel to the twinning shear direction η_1.

In general, criteria (1) and (2) are sufficient to predict the predominant twinning modes. Criteria (3) and (4) are particularly useful to choose between a twin mode and its conjugate. However, they cannot be used to predict the nucleation and growth of twins at the grain scale. For example, they are not capable of predicting if a given strain will be accommodated by a large twin or by several small twins of same mode. More recently, El Kadiri et al. [75] derived the analytical expressions of all possible shuffles and shears for any compound twin in h.c.p. metal. Their purpose was to propose a generalized crystallographic framework capable of determining the twinning dislocations that can be formed for each twinning system. Their theory recovered the expressions of all twinning dislocations previously identified from the admissible interfacial defect theory developed by Serra et al. [57, 24, 76] and discussed hereafter. Their calculations enabled the identification of all planes subject to shear exclusively and those subject to both shear and shuffling for any non elementary twinning dislocation. Regarding the $\{11\bar{2}2\}$ and $\{10\bar{1}2\}$ twinning modes, the authors demonstrated that the smallest deviation from the stacking sequence is exactly repeatable with an order equal to 7 and 2, respectively. They also revealed that twinning disconnection with a step height equal to multiple interplanar spacings does not necessarily require shuffles within intermediate planes to operate in the twinning direction. Aware that some of the terms used to describe El Kadiri's results have not been defined yet, this discussion can be seen as a transition or an early introduction to the next paragraph.

1.4 Nucleation and growth of twins

1.4.1 Twinning dislocations and twin interfaces

A disconnection in a coherent rational twin boundary has a stress field similar to the one associated with a dislocation. This explains why the term of twinning dislocation was used when first discussed by Vladimirskij [77], Frank and Van der Merwe [78] in the late 40's. The equivalent Burgers vector of a disconnection, also called step, of height h can be expressed as follows :

$$\mathbf{b_t} = hs\frac{\eta_\mathbf{1}}{\|\eta_\mathbf{1}\|} \tag{1.4}$$

where s denotes the unit twinning shear magnitude and η_1, the twinning shear direction. In cases where h is equal to the spacing d of the lattice planes parallel to K_1, the twinning dislocation is called the elementary twinning dislocation. Moreover, since the elastic energy is proportional to the square of the Burgers vector magnitude, steps with heights equal to multiples of d tend to dissociate spontaneously into elementary twinning dislocations. However, when parent and twin lattices do not coincide, an elementary twinning dislocation might be energetically unfavorable. As shown by Thompson and Millard [79], lattice shuffles also imply that the interface structure repeats at every q lattice planes parallel to K_1 if q is odd and at every $q/2$ if q is even. As a result, Burgers vectors, $\mathbf{b_{t,odd}}$ and $\mathbf{b_{t,even}}$, corresponding to twinning dislocations for which q is odd and even, respectively, can be expressed such that :

$$\mathbf{b_{t,odd}} = qds\frac{\eta_\mathbf{1}}{\|\eta_\mathbf{1}\|} \tag{1.5}$$

$$\mathbf{b_{t,even}} = \frac{1}{2}qds\frac{\eta_\mathbf{1}}{\|\eta_\mathbf{1}\|} \tag{1.6}$$

These twinning dislocations are referred to as zonal twinning dislocations.

Regarding the nature of twinning dislocations, they can be of edge, screw or mixed type. Twinning dislocations have most of the properties of ordinary lattice dislocations. As explained by Christian and Mahajan [3], they can glide along the interface plane when a shear stress is applied. A twin can be represented as a series of twinning dislocation loops whose diameter inversely increases with the vicinity of the central plane of the twin. Then, while expansion of existing dislocation loops engenders diameter increase, formation of new dislocation loops results in an increase of the twin thickness. The motion of zonal dislocations along along free-defect planes parallel to K_1 is responsible for twin growth or shrinkage. The dislocation is then said to be glissile. In reality, short and long-range interactions with point, line, surface defects slow down or even block the displacement of the twinning dislocation. Such interactions can be considered as friction stresses. The lattice resistance is a kind of Peierls-Nabarro force whose magnitude strongly depends on the type of atomic bonding and hence on the structure of the dislocation core. Twinning dislocation cores were first assumed to be similar to lattice dislocation cores, i.e. quite narrow. However, experiments and simulation revealed that the size of twinning dislocation cores varies a lot with the material. For example, twinning dislocation cores observed in zirconia are very narrow and its corresponding Peierls stress is very high, while for many metals, dislocation cores may extend over several atomic planes and may be opposed to a relatively small Peierls stress.

In addition, the dissociation of zonal dislocations into elementary twinning dislocation lowers the elastic energy but increases the surface energy. Elementary dislocations, products of the dissociation, have parallel Burgers vectors. As a result, because of repulsive forces, they will tend to separate. Note that the dissociation process of zonal dislocations into elementary dislocations is very similar to the one corresponding to the dissociation of lattice dislocations into partials dislocations [80].

Thompson and Millard [79] established that the only stable twinning dislocation for the $\{10\bar{1}2\}$ twinning mode is the zonal dislocation of double step height with the following Burgers vector

$$\mathbf{b_t} = \frac{3-\gamma^2}{3+\gamma^2}\boldsymbol{\eta_1} \tag{1.7}$$

Its magnitude is then equal to

$$\|\mathbf{b_t}\| = \frac{3-\gamma^2}{\sqrt{3+\gamma^2}}a \tag{1.8}$$

Atomistic simulations performed by Serra et al. [57] with two-body potentials revealed that the width of these zonal dislocations is sensitive to the used potential.

Regarding the $\{11\bar{2}2\}$ twinning mode, the zonal dislocation corresponding to the twinning features presented in Table 1.1 has a step height equal to three interplanar spacing of K_1 planes and the following Burgers vector

$$\mathbf{b_t} = \frac{\gamma^2-2}{3(\gamma^2+1)}\boldsymbol{\eta_1} \tag{1.9}$$

whose magnitude is

$$\mathbf{b_t} = \frac{\gamma^2-2}{\sqrt{\gamma^2+1}}a \tag{1.10}$$

Due to the high value of q, i.e. $q = 6$, many lattice shuffles are expected to occur. Serra et al. [24] considered three different shuffle models and observed that the energy and the width of the twinning dislocation were not really affected by the type of shuffle but were sensitive to the atomic potential used.

No lattice shuffle occurs with $\{11\bar{2}1\}$ twinning. As a result, the twinning dislocation associated with this twinning mode is an elementary dislocation whose the Burgers vector and the Burgers vector magnitude are, respectively,

$$\mathbf{b_t} = \frac{1}{3\sqrt{4\gamma^2+1}}\eta_1 \tag{1.11}$$

and

$$\|\mathbf{b_t}\| = \frac{1}{\sqrt{1+4\gamma^2}}a \tag{1.12}$$

The most observed twinning dislocations in $\{10\bar{1}1\}$ twin interfaces in Mg and Ti are such that their step height is equal to $4d$, with d the interplanar distance between K_1 lattice planes. Their corresponding Burgers vector and Burgers vector magnitude have the following expressions :

$$\mathbf{b_t} = \frac{4\gamma^2-9}{4\gamma^2+3}\eta_1 \tag{1.13}$$

and

$$\|\mathbf{b_t}\| = \frac{\sqrt{2}(4\gamma^2 - 9)}{\sqrt{3}\sqrt{4\gamma^2 + 3}} a \tag{1.14}$$

In order to minimize the interfacial energy, all twinning dislocations mentioned in the above may dissociate into dislocations whose Burgers vectors are smaller in magnitude.

The energetic stability of twin interfaces is a very pertinent discrimination criterion for investigating the likelihood of twinning modes. Using different two-body potentials, Serra and Bacon [57, 24] thoroughly investigated the main twin interface structures in pure h.c.p. materials, i.e. $\{10\bar{1}2\}$, $\{11\bar{2}1\}$, $\{10\bar{1}1\}$ and $\{11\bar{2}2\}$ twins. As shown in Table 1.1, all these twin modes were observed experimentally in h.c.p. materials. Simulations revealed that classical twinning dislocations having both a relatively small $\|\mathbf{b}\|$ and h have smaller line energies in $\{10\bar{1}2\}$ and $\{11\bar{2}1\}$ interfaces than in $\{11\bar{2}2\}$ interfaces. The only stable equilibrium configuration found for the $\{10\bar{1}2\}$ twin interface is such that parent and twin lattices are mirror images, and the interface plane results from the coalescence of two adjacent atomic planes into a corrugated $\{10\bar{1}2\}$ plane. Moreover, Xu et al. [81] also showed that prismatic/basal interfaces which exhibit a low interface energy play an important role in the growth of $\{10\bar{1}2\}$ twins. The relaxed structure of the $\{10\bar{1}1\}$ is very similar to the one computed for $\{10\bar{1}2\}$ twins, since the stable interface consists of a $\{10\bar{1}1\}$ plane generated after the coalescence of two separate atomic planes. Regarding the $\{11\bar{2}2\}$ twin interface, atomistic simulations reveal that the interface, as well as all lattice planes parallel to K_1, is perfectly flat.

1.4.2 Mechanisms involved in nucleation and growth of twins

Twin formation can be decomposed into three steps. The first step is the nucleation, consisting of the formation of a small twin nucleus. The second step is named propagation and corresponds to the phase during which dislocation loops expand very quickly in all directions contained within the twinning plane. At the end of the second step, the newly-formed twin is flat and wide. The last step in the development of a twin, referred to as the growth step, consists of the thickening of the twin. Mechanisms involved in both nucleation and growth are detailed in the following.

In theory, twins may nucleate homogeneously or heterogeneously. Homogeneous nucleation consists in the formation of a small twin in a defect free region under the influence of an applied stress. Homogeneous nucleation implies that there exists a critical resolved shear stress (CRSS), also called theoretical strength of the material, such that when the resolved shear stress on the twinning plane in the twinning direction reaches or exceeds the critical stress, a twin forms. Theoretical works of Orowan [82], Price [83, 84, 85], Lee and Yoo [86, 87] show that twins may nucleate homogeneously if the applied resolved shear stress on the twinning plane is very high and if both the surface and strain energies are very small. As a consequence, homogeneous nucleations seem to be very unlikely. Experimental results obtained by Bell and Cahn [88, 89] as well as Price [83, 84, 85] are in agreement with the previous conclusion. Bell and Cahn [88, 89] observed that twins appeared at much higher stress levels in "almost" defect-free h.c.p. single crystals than they did in less perfect crystals. Carrying out in situ measurements on specimens in a scanning electron microscope, Price [83, 84, 85] found that the stresses required to initiate twinning were an order of magnitude higher than those usually measured on "regular" macroscopic specimens. Therefore, Bell et al. [88, 89] and Price [83, 84, 85] all agreed with the conclusion that twinning is initiated by some defect configuration.

As opposed to homogeneous nucleation, heterogeneous nucleation consists of a defect-assisted twin formation. Heterogeneous nucleation is usually modeled via the dissociation of some dislocation into a single or multi-layered stacking fault [90]. The resulting stacking fault, bounded by partial dislocations belonging to the parent crystal, is then the defect responsible for twin nucleation.

There are other ways for twins to form. These are called pole or cross-slip source mechanisms which enable a single twinning dislocation to move through successive K_1 planes. Derived from the general theory developed by Bilby [91], Cottrell-Bilby [92] and Thompson-Millard [79] introduce the concept of a pole mechanism in b.c.c and h.c.p. materials, respectively. The pole mechanism was described by Bilby and Christian [93] as follows. Consider a lattice dislocation in a parent crystal with a Burgers vector $\mathbf{b_a}$. The same dislocation has after crossing the twin interface, a Burgers vector $\mathbf{b_b}$. The two Burgers vectors are assumed to be related by the twinning shear such that $\mathbf{b_b} = \mathbf{S}\mathbf{b_a}$. As a result, the glide of the dislocation leaves a step in the interface of height equal to the projection of the Burgers vector $\mathbf{b_a}$ along the normal to the twinning plane, i.e. $h = \mathbf{b_a}.\mathbf{m}$ with $\mathbf{m}$ an unit vector normal to K_1. This step is a twinning dislocation whose Burgers vector is $\mathbf{b_t} = \mathbf{b_b} - \mathbf{b_a}$. Consequently, each point crossed by the initial lattice dislocation along the twin interface is the junction of three dislocation lines. Bilby called the junction point a "generating node". The twinning dislocation associated with such a configuration is said to be a pole dislocation. Other more elaborate illustrations of pole mechanisms involving the dissociation of a pole dislocation into partial and sessile dislocations have been detailed and explained by authors such as Cottrell-Bilby [92], Venables [94] and Hirth and Lothe [95].

Similar to nucleation, both homogeneous and heterogenous growth mechanisms have been and are still being investigated in the literature. However, in contrast to homogeneous nucleation, which is very unlikely, homogeneous growth is possible. Homogeneous growth corresponds to repeated homogeneous nucleation of twinning dislocations on K_1 lattice planes to form new twin layers. Twin thickening may also occur by random accumulation of nucleated faults or by heterogeneous nucleation of steps at defect loci or by pole or cross-slip mechanism.

1.5 Twinning in constitutive and polycrystalline modeling

Polycrystalline models accounting for twinning rely either on the use of the finite element method (FEM), such as recently done in work by Izadbakhsh et al. [96] [96, 97], or on the use of the Green operator techniques and Eshelbian micromechanics [97]. The latter can be applied in the form of a mean field approach (e.g. self-consistent methods) or of a full-field via the use of the Fast Fourier Transform (FFT) method originally proposed by Moulinec and Suquet [98, 99]. In both cases of full-field methods based on the FEM and the FFT, current models accounting for twin activity do not effectively reorient the crystal within the twin domain such that second generation twinning and secondary slip is necessarily predicted to a lesser accuracy. On the contrary, mean field self-consistent polycrystalline models, in which domain reorientation is straightforward, have been used in a large body of work to predict the effect of twinning on strain hardening and microstructure evolution [100, 101, 31].

A simple way to deal with the crystallographic reorientation induced by twinning consists in (1) initially representing the polycrystal with a finite set of orientations with given volume fractions and (2) reorienting an entire crystal when the effective twin fraction is larger than a critical value. This type of approach was originally proposed in early work by Van Houtte [102] in which a Monte Carlo type method was employed to allow for twin reorientation [102]. In the same spirit, Tomé et al. [100] developed the "Predominant Twin Reorientation" (PTR) scheme. This last scheme, in which an entire grain is reoriented at once and in which solely the most active twin system is accounted for in terms of crystallographic reorientation, necessarily leads to imprecision in the prediction of texture development. To overcome these limitations, an alternative method, referred to as the "Volume Fraction Transfer" (VFT) scheme was proposed [100, 101]. The polycrystal is represented as a finite set of fixed orientations, weighted by volume fractions. As deformation proceeds, the weights of the orientations evolve to reproduce the nucleation and growth of twins. The VFT scheme provides an accurate description of the texture development in the case of twinning, but does not allow for a direct coupling or for a direct connection between the parent and the twin domains.

More recently, Proust et al. [31, 32] developed the "Composite Grain" (CG) model from the PTR scheme. In the CG model, when a critical twin volume fraction is reached, new grains are created with an orientation corresponding to that of the twin domain. The shape of newly formed domains is fixed by a parameter such that the multi-lamellar aspect of twinning -yielding to relatively flat ellipsoidal twins- is respected. From the point of view of micromechanics, the newly formed twinned domains are either treated as new grains to be embedded in the homogeneous reference medium or can be artificially coupled to the parent phase by imposing traction continuity across the interface. Although the coupled CG approach may appear to be more a realistic description of the geometry and traction continuity conditions associated to twinning, it is to be noted that enforcing traction continuity on the mean field within the parent and twin domains is unlikely to be appropriate when the twin fraction is not small. When applied to the case of pure polycrystalline magnesium in an elasto-plastic self-consistent scheme, it is found that the CG model cannot accurately reproduce the evolution of internal strains concomitant to twinning activity.

Typically these approaches suffer from two limitations. First, they do not account explicitly for the direct mechanical interaction between parent and twin or between twin and neighboring grains. Second, they do not consider the stresses induced by the shear transformation inside the twin domain. These essentially limit the accuracy or correspondence with full-field methods of the predicted stress state in the twin domain both at the onset of twinning and when plasticity has occurred. Most models use the average stress in the parent and resolve it on the twin plane so as to quantify the driving force associated with twin growth. More recent approaches considered both the stress states in the parent and twin domains [103, 104]. However, at a fine continuum mechanics scale, the stress of interest is the one acting at the interface between the twin and the parent. Experiments [36, 105] reveal that those resolved shears could be very different. High energy X-ray diffraction in-situ measurements by Aydiner et al. [36] revealed that substantial backstresses develop within twin domains during the activation of $\{10\bar{1}2\}$ tensile twins. As such, the accuracy of predictions of secondary slip and second-generation twin activities in polycrystals is limited. The latter is typically observed in magnesium alloys AM30, where tensile twins of the $\{10\bar{1}2\}$ type develop within compressive twins of the $\{10\bar{1}1\}$ type [67, 65]. In recent EBSD measurements performed by Martin et al. [67], it was shown that out of the six possible second generation twin variants two are observed far more frequently. To date, no clear explanation of the phenomenon exists, but strain accommodation in twin domains inside both primary twin and parent phases is likely to play a significant role [67].

To remedy the first limitation, related to the direct coupling between the parent and twin domains, an alternative mean field approach still based on a 1-site self-consistent model for elasto-plastic polycrystals "EPSC" but including twins as new "child grains" embedded in the HEM (Homogeneous Equivalent Medium) was proposed [4]. Continuity conditions were enforced across the parent/twin interface. The traction continuity constraint is appropriate at the onset of twinning at the twin/parent interface. However, as it is enforced on mean stresses within the parent and twin phase, it is unlikely to be accurate when the twin has reached a significant volume. For the initial state of the twin domain, Clausen et al. [4] proposed to impose an initial twin volume fraction and hence an initial plastic shear for the twin system once twinning is activated. Clausen et al. [4] also showed that better agreement with experimental data could be obtained by introducing a back-stress term at the constitutive level in an ad-hoc fashion within the twin phase. The motivation there was essentially to reduce the stress within the twin domain at the onset of twinning so as to match elastic strains measured by neutron diffraction. An alternate route has also been proposed, in which, rather than first computing the plastic shear in the parent phase on the twinning plane and then reorienting a twin domain, one first creates a twin domain and then imposes an eigenstrain in the domain. In the work of Lebensohn et al. [106] , this method was used in a purely elastic two-phase model. Although limited to a purely elastic accommodation, these models lead to much reduced or even null stress states in the twin domain. The eigenstrain-based approach [107] was also used in full field elasto-plastic studies using finite element and fast Fourier transform methods.

Rendering such complex physical phenomena in view of performing virtual material characterization is complicated due to the local nature of nucleation events. The vast majority of polycrystalline models use deterministic criteria to predict nucleation events. However, the scale at which nucleation occurs is typically lower than the resolution scale of FFT or FEM based full field simulations such that connections with the atomistic structure of grain boundaries in terms of degrees of freedom and defect content are missing. To overcome such limitations, probabilistic twinning models accounting for the statistical nature of twin nucleation have been developed [108, 34]. Clearly these approaches rely on the gathering of rigorous statistical data from experimental studies. In Capolungo et al. [109] and Beyerlein et al. [110], an automated twin detection tool capable of detecting the presence and geometry of twins from Electron Backscatter Diffraction (EBSD) measurements was used to that end. These works clearly delineate a path towards both directly embedding experimental into constitutive models and generating datasets for model validation. Yet, the studies were limited to microstructures with relatively well organized twin structures and considered only one twin mode at a time. Indeed, automatically extracting microstructural data and twinning statistics such as grain size, grain orientation, number of twins per grain or modes and variants of twins is particularly complex because of the diversity of twinning modes, the multiplicity of certain twins and the complex morphologies one can introduce following complex or arbitrary loading [8, 111].

1.6 Scope of the thesis

Focused on twinning in h.c.p. metals, the present PhD thesis is dedicated to the study of internal stress development, the investigation and the quantification of the relative contributions of parent/twin and twin/twin interactions on the mechanical behavior and the microstructure evolution during deformation twinning. Particular attention will be drawn to magnesium and zirconium. The thesis is then organized in the following manner :

Chapter 2 introduces a new micromechanical approach based on a double inclusion topology and the use of the Tanaka-Mori theorem. A first elasto-static model in heterogeneous elastic media with eigenstrains is developed and applied to the case of first and second generation twinning in a Mg single twinned grain. A second model, referred to as the double-inclusion elasto-plastic self-consistent scheme (DI-EPSC), is then derived. The DI-EPSC scheme consists of an extension of the first model to the case of elasto-plastic media and polycrystalline materials. Applied to an initially extruded Mg AZ31alloy, its predictions will be compared to those obtained by Clausen et al. [4].

Chapter 3 aims at introducing a new EBSD analysis software developed for automated twinning statistics extraction and based on graph theory and quaternion algebra. Prior to presenting this new automated twin recognition tool, the chapter will briefly describe scanning electron microscopes, give the historical perspectives of the EBSD technique and review the basic concepts of electron diffraction and diffraction pattern analysis.

Chapter 4 is dedicated to the identification of statistically representative data associated to nucleation and growth of twins from three studies carried out from Mg AZ31 alloy and pure Zr EBSD scans. The first two studies performed on Mg AZ31 alloy are focused on the determination and explanation of activation criteria for low Schmid factor $\{10\bar{1}2\}$ tensile twins and successive $\{10\bar{1}2\}$-$\{10\bar{1}2\}$ double extension twins. The last statistical analysis performed on Zr discusses the statistical relevance of twin-twin junctions and their influence on nucleation and growth of twins.

Finally, chapter 5 summarizes the main results of the presented work and presents possible further developments and studies.

Chapitre 2

Study of the influence of parent-twin interactions on the mechanical behavior during twin growth

Sommaire

The present chapter focuses on the influence of parent/twin interactions on the mechanical behavior of polycrystalline Mg. A numerically efficient mean-field Eshelbian based micromechanical model is proposed to address the problem. The general idea is based on the use of the Tanaka-Mori scheme [112, 50] which is first extended to the case of heterogeneous elasticity [113] and then further extended to the case of elasto-plasticity [114]. Prior to that a few key foundations of Eshelbian micromechanics are recalled [115].

The following convention is used throughout the rest of the paper. Fourth-order tensors will be denoted with capital Latin characters, second-order tensors will be denoted with Greek characters and vectors will be denoted with lower case Latin characters. Einstein summation convention is used for the sake of brevity. Finally, when contracted notations (e.g. " :" denotes a doubly contracted product) are used, non-scalar variables will be noted in bold. The symbol "," denotes a spatial derivative.

2.1 The inclusion problem

2.1.1 Field equations and thermodynamics

In pioneering work, Eshelby [115] analytically determined the local strain and stress tensors in an inhomogeneous inclusion containing an eigenstrain and embedded in an infinite elastic homogeneous medium (Figure 2.1). The temperature of the medium is assumed to be constant, i.e. there is no thermal strain. Dynamics effects and body forces are neglected. Denoting $\mathbf{r}$ the position vector in the medium V, the equilibrium condition without body force and acceleration is expressed as the divergence of the Cauchy stress tensor denoted by σ :

$$\nabla.\sigma(\mathbf{r}) = 0 \tag{2.1}$$

The compatibility equation on the total distortion,β,is given by :

$$\beta(\mathbf{r}) = \nabla\mathbf{u}(\mathbf{r}) \tag{2.2}$$

where $\mathbf{u}$ is the displacement vector. In the small deformation approximation, the total strain and rotation tensors, respectively denoted with ϵ and ω, are related to the total distortion as follows :

$$\beta(\mathbf{r}) = \epsilon(\mathbf{r}) + \omega(\mathbf{r}) \tag{2.3}$$

with,

$$\epsilon(\mathbf{r}) = \frac{1}{2}\left[\nabla\mathbf{u}(\mathbf{r}) + \nabla^t\mathbf{u}(\mathbf{r})\right] \tag{2.4}$$

$$\omega(\mathbf{r}) = \frac{1}{2}\left[\nabla\mathbf{u}(\mathbf{r}) - \nabla^t\mathbf{u}(\mathbf{r})\right] \tag{2.5}$$

As previously mentioned, a spatially varying eigenstrain, denoted with superscript *, is imposed in the medium. The eigenstrain is a non-elastic stress-free strain -as per Eshelby- that can physically represent a phase transformation, a pre-strain, a thermal strain and a strain [50]. In the small perturbation hypothesis, the total strain is written as the sum of the elastic strain and of the eigenstrain.

$$\epsilon(\mathbf{r}) = \epsilon^{\mathbf{el}}(\mathbf{r}) + \epsilon^*(\mathbf{r}) \tag{2.6}$$

In a linear elastic homogeneous medium, the constitutive relation is simply given by :

$$\sigma(\mathbf{r}) = \mathbf{C^0} : \left[\epsilon(\mathbf{r}) - \epsilon^*(\mathbf{r})\right] \tag{2.7}$$

where $\mathbf{C^0}$ is the homogeneous reference elastic modulus tensor.

The traction and displacement boundary conditions, on ∂V_σ and ∂V_u respectively, are the following :

$$\mathbf{u^d} = \left(\mathbf{E} + \mathbf{\Omega}\right)\mathbf{r} \tag{2.8}$$

$$\mathbf{t^d} = \sigma.\mathbf{n} \tag{2.9}$$

where $\mathbf{E}$ and $\mathbf{\Omega}$ represent the macroscopic strain and rotation tensors imposed to the surface ∂V_u, respectively, and $\mathbf{n}$ is the vector normal to traction surface, ∂V_σ.

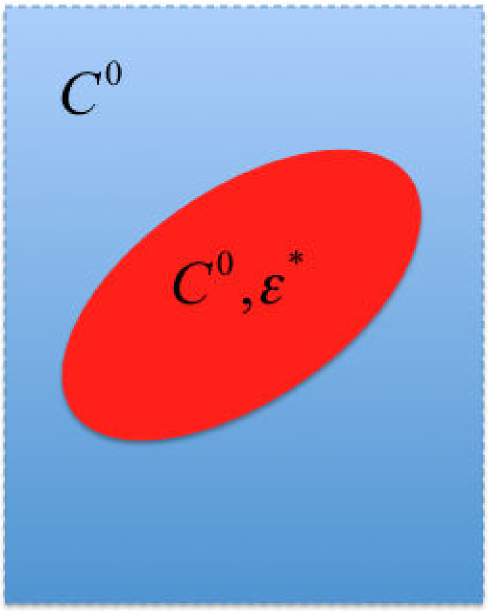

FIGURE 2.1 – Schematic representation of the original inclusion elastic problem containing one ellipsoidal inclusion V_Ω with prescribed eigenstrain ϵ^*. The dashed lines of the signify that the inclusion is embedded in an infinite elastic medium. The inclusion and the matrix have the same elastic modulus $\mathbf{C^0}$.

Using the minor symmetry of the elastic modulus of h.c.p. materials and accounting for strain compatibility, the constitutive equation can be written as follows :

$$\sigma(\mathbf{r}) = \mathbf{C^0} : [\nabla \mathbf{u}(\mathbf{r}) - \epsilon^*(\mathbf{r})] \tag{2.10}$$

After introducing the constitutive law into the balance equation, one obtains the so-called Navier type equation for the homogeneous problem considered here :

$$\mathbf{C^0} : \nabla.\nabla \mathbf{u}(\mathbf{r}) + \mathbf{f}^*(\mathbf{r}) = 0 \tag{2.11}$$

where $\mathbf{f}^*$, representing the virtual body forces due to the incompatibility, ϵ^*, is given by :

$$\mathbf{f}^*(\mathbf{r}) = -\mathbf{C^0} : \nabla.\epsilon^*(\mathbf{r}) \tag{2.12}$$

The static elastic Green's function $G^\infty_{ij}(\mathbf{r} - \mathbf{r}')$ corresponds to the displacement at point $\mathbf{r}$ in direction i due to the application of a unit body force applied at $\mathbf{r}'$ in the j direction. Consequently, the solution for the present problem is the product of the static Green function, $\mathbf{G}^\infty$, and the virtual body force vector, $\mathbf{f}^*$:

$$\mathbf{u}(\mathbf{r}) = \int_{-\infty}^{\infty} \mathbf{G}^\infty(\mathbf{r} - \mathbf{r}').\mathbf{f}^*(\mathbf{r}')\mathbf{dV_{r'}} \tag{2.13}$$

The static elastic Green function satisfies the following equation :

$$C^0_{ijkl} G^\infty_{km,lj}(\mathbf{r} - \mathbf{r}') + \delta_{\mathbf{im}}\delta(\mathbf{r} - \mathbf{r}') = \mathbf{0} \tag{2.14}$$

where δ_{im} is the kronecker symbol and $\delta(\mathbf{r}-\mathbf{r}')$ the three-dimensional Dirac delta function. Eq. 2.14 corresponds to the Navier equation after multiplying its terms by the Green function, performing two integrations by parts and simplifying the resulting equation by consideration of the boundary conditions [50].

The Helmholtz free energy density, denoted Φ and corresponding to the portion of the internal energy available for doing work in an isothermal process, is expressed as an integral of the volume density of elastic energy, W_{el}, on the volume of the medium, V [116, 117].

$$\Phi(\mathbf{E},\epsilon^*) = \frac{1}{2V}\int_V \sigma(\mathbf{r}) : \epsilon^{\mathbf{el}}(\mathbf{r})dV \tag{2.15}$$

After development and use of the Gauss theorem, the surface terms appear in the expression of Φ :

$$\Phi(\mathbf{E},\epsilon^*) = \frac{1}{2V}\int_{\partial V} \sigma(\mathbf{r})\mathbf{u}(\mathbf{r}).\mathbf{n}dS - \frac{1}{2V}\int_V \sigma(\mathbf{r}) : \epsilon^{\mathbf{el}}(\mathbf{r})dV \tag{2.16}$$

By considering the boundary conditions (Eqs. 2.8- 2.9), Φ becomes :

$$\Phi(\mathbf{E},\epsilon^*) = \frac{1}{2V}\int_{\partial V_\sigma} \mathbf{t^d}.\mathbf{u}dS + \frac{1}{2V}\int_{\partial V_u} \sigma(\mathbf{r})\mathbf{u^d}.\mathbf{n}dS - \frac{1}{2V}\int_V \sigma(\mathbf{r}) : \epsilon^*(\mathbf{r})dV \tag{2.17}$$

If only perturbation fields due to microstructural inhomogeneities fields are studied, the internal part of the Helmholtz free energy density reduces to :

$$\Phi^{\text{int}} = -\frac{1}{2V}\int_V \sigma(\mathbf{r}) : \epsilon^*(\mathbf{r})dV \tag{2.18}$$

2.1.2 Eshelby's solution

The exact solution to this boundary problem is given by the Lippman-Schwinger-Dyson,s type integral equations [118, 45] recalled here :

$$\epsilon(\mathbf{r}) = \mathbf{E^d} + \int_{-\infty}^{\infty} \mathbf{\Gamma}^{\infty,\mathbf{s}}(\mathbf{r}-\mathbf{r}') : \mathbf{C^0} : \epsilon^*(\mathbf{r}')dV_{r'} \tag{2.19}$$

where $\mathbf{\Gamma}^{\infty,\mathbf{s}}$ corresponds to the symmetric modified Green tensor

$$\Gamma^{\infty,s}_{ijkl}(\mathbf{r}-\mathbf{r}') = -\frac{1}{2}\left(G^{\infty}_{ik,jl}(\mathbf{r}-\mathbf{r}') + G^{\infty}_{jk,il}(\mathbf{r}-\mathbf{r}')\right) \tag{2.20}$$

Outside the inclusion, with volume V_Ω, the eigenstrain tensor is null. Considering a uniform eigenstrain tensor in V_Ω, the integral equation becomes :

$$\epsilon(\mathbf{r}) = \mathbf{E^d} + \int_{V_\Omega} \mathbf{\Gamma}^{\infty,\mathbf{s}}(\mathbf{r}-\mathbf{r}')dV_{r'} : \mathbf{C^0} : \epsilon^* \tag{2.21}$$

To simplify notations, uniform vectors or tensors are replaced by their values such that one writes for example $\epsilon^*(\mathbf{r}) = \epsilon^*$ when $\mathbf{r} \in V_\Omega$. Finally, the exact solution of this inclusion problem is given by :

$$\epsilon(\mathbf{r}) = \mathbf{E^d} + \mathbf{P}^{\mathbf{V_\Omega}}(\mathbf{r}) : \mathbf{C^0} : \epsilon^* \tag{2.22}$$

where the fourth-order tensor $\mathbf{P}^{\mathbf{V}_{\boldsymbol{\Omega}}}(\mathbf{r})$ denotes the so-called polarized Hill's tensor. It is expressed as the integral over the inclusion volume of the symmetric modified Green tensor :

$$\mathbf{P}^{\mathbf{V}_{\boldsymbol{\Omega}}}(\mathbf{r}) = \int_{V_\Omega} \boldsymbol{\Gamma}^{\infty,\mathbf{s}}(\mathbf{r}-\mathbf{r}')dV_{r'} \tag{2.23}$$

Similarly, the final expression of the rotation tensor ω is :

$$\omega(\mathbf{r}) = \boldsymbol{\Omega}^{\mathbf{d}} + \int_{V_\Omega} \boldsymbol{\Gamma}^{\infty,\mathbf{a}}(\mathbf{r}-\mathbf{r}')dV_{r'} : \mathbf{C}^{\mathbf{0}} : \epsilon^{*} \tag{2.24}$$

where $\boldsymbol{\Gamma}^{\infty,\mathbf{a}}$ corresponds to the anti-symmetric modified Green tensor whose expression is :

$$\Gamma^{\infty,s}_{ijkl}(\mathbf{r}-\mathbf{r}') = -\frac{1}{2}\left(G^{\infty}_{ik,jl}(\mathbf{r}-\mathbf{r}') - G^{\infty}_{jk,il}(\mathbf{r}-\mathbf{r}')\right) \tag{2.25}$$

Eshelby's tensor, $\mathbf{S}^{\mathbf{0}}$, is defined as the double dot product between Hill's polarized tensor and the fourth-order elastic stiffness tensor :

$$\mathbf{S}^{\mathbf{0}}(\mathbf{r}) = \mathbf{P}^{\mathbf{V}_{\boldsymbol{\Omega}}}(\mathbf{r}) : \mathbf{C}^{\mathbf{0}} \tag{2.26}$$

The fourth-order tensor $\mathbf{P}^{\mathbf{V}_{\boldsymbol{\Omega}}}(\mathbf{r})$ is uniform inside the inclusion Ω. As a result, $\mathbf{S}^{\mathbf{0}}$, ϵ and σ are also uniform when $\mathbf{r} \in V_\Omega$. The final expressions of the strain and stress tensors, inside and outside the inclusion, result from the combined use of intermediary results and newly-introduced notations :

— when $\mathbf{r} \in V_\Omega$,

$$\epsilon(\mathbf{r}) = \mathbf{E}^{\mathbf{d}} + \mathbf{S}^{\mathbf{0}} : \epsilon^{*} \tag{2.27}$$

$$\sigma(\mathbf{r}) = \mathbf{C}^{\mathbf{0}} : \mathbf{E}^{\mathbf{d}} + \mathbf{C}^{\mathbf{0}} : \left(\mathbf{S}^{\mathbf{0}} - \mathbf{I}\right) : \epsilon^{*} \tag{2.28}$$

— when $\mathbf{r} \notin V_\Omega$,

$$\epsilon(\mathbf{r}) = \mathbf{E}^{\mathbf{d}} + \mathbf{S}^{\mathbf{0}}(\mathbf{r}) : \epsilon^{*} \tag{2.29}$$

$$\sigma(\mathbf{r}) = \mathbf{C}^{\mathbf{0}} : \mathbf{E}^{\mathbf{d}} + \mathbf{C}^{\mathbf{0}} : \mathbf{S}^{\mathbf{0}}(\mathbf{r})s : \epsilon^{*} \tag{2.30}$$

2.2 A generalized Tanaka-Mori scheme in heterogeneous elastic media with plastic incompatibilities.

In this paragraph, a Lippman-Schwinger type equation is derived for microstructures with heterogeneous elasticity (due to twin reorientation) and plastic incompatibilities (eigenstrains due to the shearing in different types of twin domains). This is done by generalizing the original work of Tanaka and Mori [112, 50], initially developed in the case of homogeneous elasticity. This scheme aims at predicting the development of internal stresses within twin and parent domains during the growth of first and second-generation twins. The proposed method considers a static configuration for an elastic medium with eigenstrains. It allows computation of the values and evolutions of internal stresses in a double inclusion of ellipsoidal shape -mimicking the geometry of a twin domain contained in either a parent phase or a primary twin- with inclusion shape, relative shape and volume fraction.

2.2.1 Elasto-static Tanaka-Mori scheme

Generalized Tanaka-Mori scheme

This sub-paragraph presents both the twinning topology considered and the key steps in the derivation of a Generalized Tanaka-Mori scheme. Consider two ellipsoidal inclusions V_b and V_a such that $V_1 \subset V_2$ with elastic moduli $\mathbf{C^b}$ in V_b and $\mathbf{C^a}$ in the sub-domain $V_a - V_b$ (Figure 2.2). Both inclusions are embedded in an infinite matrix with reference elastic stiffness $\mathbf{C^0}$ and subjected to traction and displacement boundary conditions.

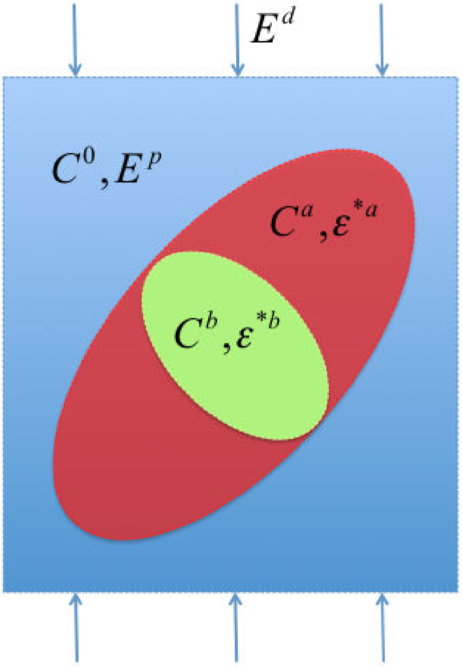

FIGURE 2.2 – Schematic representation of the heterogeneous elastic problem containing two ellipsoidal inclusions V_b and V_a (with $V_1 \subset V_2$) with prescribed eigenstrains ϵ^{*b} in V_b and ϵ^{*a} in sub-region $V_a - V_b$ and distinct elastic moduli $\mathbf{C^b}$ in V_b and $\mathbf{C^a}$ (in sub-region $V_a - V_b$). The two inclusions are embedded in an infinite elastic medium, with elastic modulus $\mathbf{C^0}$, containing an overall uniform plastic strain, $\mathbf{E^p}$. The second-order tensor $\mathbf{E^d}$ represents the imposed macroscopic strain.

Such a geometry can yield a geometrical representation of both the first generation twin, i.e. volume V_b is null and volume V_a represents the first generation twin, and the second-generation twin with V_a and V_b representing the first and second generation twins, respectively. In order to represent the shear deformation induced by twinning, two uniform eigenstrains, denoted with ϵ^{*b} and ϵ^{*a}, are respectively introduced in inclusion V_b and in the sub-region $V_a - V_b$. Another uniform plastic strain, denoted by the second-order tensor $\mathbf{E^p}$, is introduced in the sub-domain $V - V_a$ in order to model the macroscopic plastic strain undergone by the specimen during mechanical testing (Figure 2.2).

Following the same steps as for the inclusion problem, the Navier type equation of this heterogeneous multi-inclusion problem is :

$$\mathbf{C^0} : \nabla . \nabla \mathbf{u}(\mathbf{r}) + \mathbf{f}^*(\mathbf{r}) = 0 \tag{2.31}$$

where the virtual body forces, represented by f_i^*, result from both heterogeneous elasticity and incompatibilities (eigenstrains), are expressed as follows :

$$\mathbf{f}^*(\mathbf{r}) = \nabla.(\delta\mathbf{C}(\mathbf{r}) : \epsilon(\mathbf{r}) - \mathbf{C}(\mathbf{r}) : \epsilon^*(\mathbf{r})) \tag{2.32}$$

The new Lippman-Schwinger-Dyson's type integral equations are then :

$$\epsilon(\mathbf{r}) = \mathbf{E^d} - \int_V \Gamma^{\infty,s}(\mathbf{r}-\mathbf{r}') : \left[\delta\mathbf{C}(\mathbf{r}') : \epsilon(\mathbf{r}') - \mathbf{C}(\mathbf{r}') : \epsilon^*(\mathbf{r}')\right] dV_{r'} \tag{2.33}$$

$$\omega(\mathbf{r}) = \mathbf{\Omega^d} - \int_V \Gamma^{\infty,a}(\mathbf{r}-\mathbf{r}') : \left[\delta\mathbf{C}(\mathbf{r}') : \epsilon(\mathbf{r}') - \mathbf{C}(\mathbf{r}') : \epsilon^*(\mathbf{r}')\right] dV_{r'} \tag{2.34}$$

$\theta_b(\mathbf{r})$ and $\theta_a(\mathbf{r})$ denote the characteristics functions associated to V_b and V_a, respectively. These functions are equal to the identity and null tensors inside and outside their corresponding volumes, respectively. The heterogeneous elastic properties and eigenstrains in the infinite body, V, can be expressed as spatially fluctuating fourth and second-order tensors, $\mathbf{C}(\mathbf{r})$ and $\epsilon^*(\mathbf{r})$, respectively :

$$\mathbf{C}(\mathbf{r}) = \mathbf{C^0} + \delta\mathbf{C}(\mathbf{r}) = \mathbf{C^0} + \left(\mathbf{C^a} - \mathbf{C^0}\right)\theta_a(\mathbf{r}) + \left(\mathbf{C^b} - \mathbf{C^a}\right)\theta_b(\mathbf{r}) \tag{2.35}$$

$$\epsilon^*(\mathbf{r}) = \mathbf{E^p} + (\epsilon^{*a} - \mathbf{E^p})\,\theta_a(\mathbf{r}) + \left(\epsilon^{*b} - \epsilon^{*a}\right)\theta_b(\mathbf{r}) \tag{2.36}$$

In order to simply the subsequent calculations, rewrite the expressions of $\mathbf{C}(\mathbf{r})$ and $\epsilon^*(\mathbf{r})$ in the following manner :

$$\mathbf{C}(\mathbf{r}) = \mathbf{C^0}\left(\mathbf{1} - \theta_a(\mathbf{r})\right) + \mathbf{C^a}\left(\theta_a(\mathbf{r}) - \theta_b(\mathbf{r})\right) + \mathbf{C^b}\theta_b(\mathbf{r}) \tag{2.37}$$

$$\epsilon^*(\mathbf{r}) = \mathbf{E^p}\left(\mathbf{1} - \theta_a(\mathbf{r})\right) + \epsilon^{*a}\left(\theta_a(\mathbf{r}) - \theta_b(\mathbf{r})\right) + \epsilon^{*b}\theta_b(\mathbf{r}) \tag{2.38}$$

Replacing the spatially varying elastic modulus and eigenstrain tensors by their expressions into the integral equation, one obtains the following expression of the strain field anywhere in the volume :

$$\begin{aligned}\epsilon(\mathbf{r}) = \mathbf{E^d} &- \int_{V-V_a} \mathbf{\Gamma}^{\infty,\mathbf{s}}(\mathbf{r}-\mathbf{r}') : \mathbf{C^0} : \mathbf{E^p} dV_{r'} \\ &- \int_{V_a-V_b} \mathbf{\Gamma}^{\infty,\mathbf{s}}(\mathbf{r}-\mathbf{r}') : \left[\left(\mathbf{C^a} - \mathbf{C^0}\right) : \epsilon(\mathbf{r}) - \mathbf{C^a} : \epsilon^{*a}\right] dV_{r'} \\ &- \int_{V_b} \mathbf{\Gamma}^{\infty,\mathbf{s}}(\mathbf{r}-\mathbf{r}') : \left[\left(\mathbf{C^b} - \mathbf{C^0}\right) : \epsilon(\mathbf{r}') - \mathbf{C^b} : \epsilon^{*b}\right] dV_{r'}\end{aligned} \tag{2.39}$$

Since $\lim\limits_{V\to\infty} \int_V \mathbf{\Gamma}^{\infty,\mathbf{s}}(\mathbf{r}-\mathbf{r}')dV_{r'} = \mathbf{0}$ and after rearrangement of the terms in the integrand, the strain field expression becomes :

$$\begin{aligned}\epsilon(\mathbf{r}) = \mathbf{E^d} &- \int_{V_a} \mathbf{\Gamma}^{\infty,\mathbf{s}}(\mathbf{r}-\mathbf{r}') : \left[\left(\mathbf{C^a} - \mathbf{C^0}\right) : \epsilon(\mathbf{r}) + \mathbf{C^0} : \mathbf{E^p} - \mathbf{C^a} : \epsilon^{*a}\right] dV_{r'} \\ &- \int_{V_b} \mathbf{\Gamma}^{\infty,\mathbf{s}}(\mathbf{r}-\mathbf{r}') : \left[\left(\mathbf{C^b} - \mathbf{C^a}\right) : \epsilon(\mathbf{r}') + \mathbf{C^a} : \epsilon^{*a} - \mathbf{C^b} : \epsilon^{*b}\right] dV_{r'}\end{aligned} \tag{2.40}$$

Regardless of the respective shape of both volumes, the strain field $\epsilon(\mathbf{r})$ given by Eq. 2.40 is not uniform. Exact solutions of Eq. 2.40 can be obtained via the use of the FFT method [98, 99] or of high order polynomial expansions of $\epsilon(\mathbf{r})$ [119]. To avoid the numerical difficulty associated with solving exactly the integral equation, and to proceed with realistic analytical derivations, the strains under the integral are assumed to be equal to their averages over these volumes, i.e. $\bar{\epsilon}^i = \frac{1}{V_i}\int_{V_i} \epsilon(\mathbf{r}) dV_r$ (with $i = \{a, b\}$).

$$\begin{aligned}\epsilon(\mathbf{r}) = \mathbf{E^d} - \int_{V_a} \mathbf{\Gamma}^{\infty,\mathbf{s}}(\mathbf{r}-\mathbf{r}') : \left[\left(\mathbf{C^a} - \mathbf{C^0}\right) : \bar{\epsilon}^a + \mathbf{C^0} : \mathbf{E^p} - \mathbf{C^a} : \epsilon^{*a}\right] dV_{r'} \\ - \int_{V_b} \mathbf{\Gamma}^{\infty,\mathbf{s}}(\mathbf{r}-\mathbf{r}') : \left[\left(\mathbf{C^b} - \mathbf{C^a}\right) : \bar{\epsilon}^b + \mathbf{C^a} : \epsilon^{*a} - \mathbf{C^b} : \epsilon^{*b}\right] dV_{r'} \quad (2.41)\end{aligned}$$

All uniform terms can then be extracted from the integrals.

$$\begin{aligned}\epsilon(\mathbf{r}) = \mathbf{E^d} - \int_{V_a} \mathbf{\Gamma}^{\infty,\mathbf{s}}(\mathbf{r}-\mathbf{r}') dV_{r'} : \left[\left(\mathbf{C^a} - \mathbf{C^0}\right) : \bar{\epsilon}^a + \mathbf{C^0} : \mathbf{E^p} - \mathbf{C^a} : \epsilon^{*a}\right] \\ - \int_{V_b} \mathbf{\Gamma}^{\infty,\mathbf{s}}(\mathbf{r}-\mathbf{r}') dV_{r'} : \left[\left(\mathbf{C^b} - \mathbf{C^a}\right) : \bar{\epsilon}^b + \mathbf{C^a} : \epsilon^{*a} - \mathbf{C^b} : \epsilon^{*b}\right] \quad (2.42)\end{aligned}$$

As with other mean-field models [31, 4], strain fields are supposed to be uniform inside the inclusions and equal to their average values over these ellipsoidal volumes. The average strain in the inclusion V_b is derived as follows :

$$\begin{aligned}\bar{\epsilon}^b = \mathbf{E^d} - \frac{1}{V_b}\int_{V_b}\int_{V_a} \mathbf{\Gamma}^{\infty,\mathbf{s}}(\mathbf{r}-\mathbf{r}') dV_{r'} dV_r : \left[\left(\mathbf{C^a} - \mathbf{C^0}\right) : \bar{\epsilon}^a + \mathbf{C^0} : \mathbf{E^p} - \mathbf{C^a} : \epsilon^{*a}\right] \\ - \frac{1}{V_b}\int_{V_b}\int_{V_b} \mathbf{\Gamma}^{\infty,\mathbf{s}}(\mathbf{r}-\mathbf{r}') dV_{r'} dV_r : \left[\left(\mathbf{C^b} - \mathbf{C^a}\right) : \bar{\epsilon}^b + \mathbf{C^a} : \epsilon^{*a} - \mathbf{C^b} : \epsilon^{*b}\right] \quad (2.43)\end{aligned}$$

where $\int_{V_b} \mathbf{\Gamma}^{\infty,\mathbf{s}}(\mathbf{r}-\mathbf{r}') dV_{r'}$ and $\int_{V_a} \mathbf{\Gamma}^{\infty,\mathbf{s}}(\mathbf{r}-\mathbf{r}') dV_{r'}$ are uniform because V_b and V_a are ellipsoidal inclusions and $\mathbf{r} \in V_b \subset V_a$ (following Eshelby [115]).

$$\begin{aligned}\bar{\epsilon}^b = \mathbf{E^d} - \int_{V_a} \mathbf{\Gamma}^{\infty,\mathbf{s}}(\mathbf{r}-\mathbf{r}') dV_{r'} : \left[\left(\mathbf{C^a} - \mathbf{C^0}\right) : \bar{\epsilon}^a + \mathbf{C^0} : \mathbf{E^p} - \mathbf{C^a} : \epsilon^{*a}\right] \\ - \int_{V_b} \mathbf{\Gamma}^{\infty,\mathbf{s}}(\mathbf{r}-\mathbf{r}') dV_{r'} : \left[\left(\mathbf{C^b} - \mathbf{C^a}\right) : \bar{\epsilon}^b + \mathbf{C^a} : \epsilon^{*a} - \mathbf{C^b} : \epsilon^{*b}\right] \quad (2.44)\end{aligned}$$

The average strain tensor in inclusion V_a is derived following the same procedure.

$$\begin{aligned}\bar{\epsilon}^b = \mathbf{E^d} - \frac{1}{V_a}\int_{V_a}\int_{V_a} \mathbf{\Gamma}^{\infty,\mathbf{s}}(\mathbf{r}-\mathbf{r}') dV_{r'} dV_r : \left[\left(\mathbf{C^a} - \mathbf{C^0}\right) : \bar{\epsilon}^a + \mathbf{C^0} : \mathbf{E^p} - \mathbf{C^a} : \epsilon^{*a}\right] \\ - \frac{1}{V_a}\int_{V_a}\int_{V_b} \mathbf{\Gamma}^{\infty,\mathbf{s}}(\mathbf{r}-\mathbf{r}') dV_{r'} dV_r : \left[\left(\mathbf{C^b} - \mathbf{C^a}\right) : \bar{\epsilon}^b + \mathbf{C^a} : \epsilon^{*a} - \mathbf{C^b} : \epsilon^{*b}\right] \quad (2.45)\end{aligned}$$

Since $\int_{V_a} \mathbf{\Gamma}^{\infty,\mathbf{s}}(\mathbf{r}-\mathbf{r}') dV_r$ is independent of $\mathbf{r}$, the order of integration in the second term of the previous equation can be changed according to the Tanaka-Mori theorem [112, 50].

$$\begin{aligned}\bar{\epsilon}^a = \mathbf{E^d} &- \frac{1}{V_a}\int_{V_a}\int_{V_a}\mathbf{\Gamma}^{\infty,\mathbf{s}}(\mathbf{r}-\mathbf{r}')dV_{r'}dV_r : \left[\left(\mathbf{C^a}-\mathbf{C^0}\right):\bar{\epsilon}^a+\mathbf{C^0}:\mathbf{E^p}-\mathbf{C^a}:\epsilon^{*a}\right]\\ &- \frac{1}{V_a}\int_{V_b}\int_{V_a}\mathbf{\Gamma}^{\infty,\mathbf{s}}(\mathbf{r}-\mathbf{r}')dV_r dV_{r'} : \left[\left(\mathbf{C^b}-\mathbf{C^a}\right):\bar{\epsilon}^b+\mathbf{C^a}:\epsilon^{*a}-\mathbf{C^b}:\epsilon^{*b}\right]\end{aligned}\tag{2.46}$$

Considering the Eshelby's result [115], $\int_{V_a}\mathbf{\Gamma}^{\infty,\mathbf{s}}(\mathbf{r}-\mathbf{r}')dV_r$ is uniform, because $V_b \subset V_a$, so that :

$$\begin{aligned}\bar{\epsilon}^a = \mathbf{E^d} &- \int_{V_a}\mathbf{\Gamma}^{\infty,\mathbf{s}}(\mathbf{r}-\mathbf{r}')dV_{r'} : \left[\left(\mathbf{C^a}-\mathbf{C^0}\right):\bar{\epsilon}^a+\mathbf{C^0}:\mathbf{E^p}-\mathbf{C^a}:\epsilon^{*a}\right]\\ &- \frac{V_b}{V_a}\int_{V_a}\mathbf{\Gamma}^{\infty,\mathbf{s}}(\mathbf{r}-\mathbf{r}')dV_r : \left[\left(\mathbf{C^b}-\mathbf{C^a}\right):\bar{\epsilon}^b+\mathbf{C^a}:\epsilon^{*a}-\mathbf{C^b}:\epsilon^{*b}\right]\end{aligned}\tag{2.47}$$

Similar to the inclusion problem, the following tensors $\mathbf{P^{V_i}}$ are defined from the volume integral of the symmetrized modified Green function :

$$\mathbf{P^{V_i}}(\mathbf{r}) = \int_{V_i}\mathbf{\Gamma}^{\infty,\mathbf{s}}(\mathbf{r}-\mathbf{r}')\mathbf{dV_{r'}}\tag{2.48}$$

with $i = \{a, b\}$.

Tensors $\mathbf{S^j}(\mathbf{V_i})$, with$j = \{0, a, b\}$ and $i = \{a, b\}$, are written as the double contracted product of the $\mathbf{P^{V_i}}$ tensors with the stiffness tensors, $\mathbf{C^j}$:

$$\mathbf{S^j_{V_i}} = \mathbf{P^{V_i}} : \mathbf{C^j}\tag{2.49}$$

As the inclusion shapes considered here are all ellipsoidal, both $\mathbf{P^{V_i}}$ and $\mathbf{S^j_{V_i}}$ are uniform when $\mathbf{r} \in V_i$. Clearly, the different tensors $\mathbf{S^j_{V_i}}$ are to be considered as Eshelby type tensors.

Consequently, the approximated average strain in the inclusion V_b is given by :

$$\begin{aligned}\bar{\epsilon}^b = \mathbf{E^d} - \mathbf{S^0}(\mathbf{V_a}):\mathbf{E^p} - \left[\mathbf{S^a}(\mathbf{V_a})-\mathbf{S^0}(\mathbf{V_a})\right]:\bar{\epsilon}^a - \left[\mathbf{S^b}(\mathbf{V_b})-\mathbf{S^a}(\mathbf{V_b})\right]:\bar{\epsilon}^b\\ + \left[\mathbf{S^a}(\mathbf{V_a})-\mathbf{S^a}(\mathbf{V_b})\right]:\epsilon^{*a}+\mathbf{S^b}(\mathbf{V_b}):\epsilon^{*b}\end{aligned}\tag{2.50}$$

And the approximated average strain in the inclusion V_a is given by :

$$\begin{aligned}\bar{\epsilon}^a = \mathbf{E^d} - \mathbf{S^0}(\mathbf{V_a}):\mathbf{E^p} - \left[\mathbf{S^a}(\mathbf{V_a})-\mathbf{S^0}(\mathbf{V_a})\right]:\bar{\epsilon}^a - \frac{V_b}{V_a}\left[\mathbf{S^b}(\mathbf{V_a})-\mathbf{S^a}(\mathbf{V_a})\right]:\bar{\epsilon}^b\\ + \frac{V_a-V_b}{V_a}\mathbf{S^a}(\mathbf{V_a}):\epsilon^{*a}+\frac{V_b}{V_a}\mathbf{S^b}(\mathbf{V_a}):\epsilon^{*b}\end{aligned}\tag{2.51}$$

Evaluation of the average strain in sub-region $V_a - V_b$ is of interest here. It can be obtained from Eqs. 2.50 and 2.51 through the following relationship :

$$\bar{\epsilon}^{V_a-V_b} = \frac{V_a}{V_a-V_b}\bar{\epsilon}^a - \frac{V_b}{V_a-V_b}\bar{\epsilon}^b\tag{2.52}$$

Equations 2.51 and 2.50 consist of an extension of the Tanaka-Mori observation to the case of a double- inclusion problem with heterogeneous elastic properties and eigenstrains. Finally, the expression of the two unknown averaged strains within each volume is obtained by solving the following system of equations :

$$\bar{\epsilon}^a = \mathbf{E^d} + \mathbf{\Delta S^{a-0}_{V_a}} : \bar{\epsilon}^a + \frac{V_b}{V_a}\mathbf{\Delta S^{b-a}_{V_a}} : \bar{\epsilon}^b + \mathbf{R_a} \tag{2.53}$$

$$\bar{\epsilon}^b = \mathbf{E^d} + \mathbf{\Delta S^{a-0}_{V_a}} : \bar{\epsilon}^a + \mathbf{\Delta S^{b-a}_{V_b}} : \bar{\epsilon}^b + \mathbf{R_b} \tag{2.54}$$

with,

$$\mathbf{\Delta S^{a-0}_{V_a}} = \mathbf{S^a(V_a)} - \mathbf{S^0(V_a)} \tag{2.55}$$

$$\mathbf{\Delta S^{b-a}_{V_a}} = \mathbf{S^b(V_a)} - \mathbf{S^a(V_a)} \tag{2.56}$$

$$\mathbf{\Delta S^{b-a}_{V_b}} = \mathbf{S^b(V_b)} - \mathbf{S^a(V_b)} \tag{2.57}$$

$$\mathbf{R_a} = \mathbf{S^0(V_a)} : \mathbf{E^p} + \frac{V_a - V_b}{V_a}\mathbf{S^a(V_a)} : \epsilon^{*a} + \frac{V_b}{V_a}\mathbf{S^b(V_a)} : \epsilon^{*b} \tag{2.58}$$

$$\mathbf{R_b} = \mathbf{S^0(V_a)} : \mathbf{E^p} + [\mathbf{S^a(V_a)} - \mathbf{S^a(V_b)}] : \epsilon^{*a} + \mathbf{S^b(V_b)} : \epsilon^{*b} \tag{2.59}$$

Solutions of Eqs. 2.53 and 2.54 are given by :

$$\bar{\epsilon}^b = \left(\left[\mathbf{I} + \mathbf{\Delta S^{b-a}_{V_b}}\right] - \frac{V_b}{V_a}\mathbf{\Delta S^{a-0}_{V_a}} : \left[\mathbf{I} + \mathbf{\Delta S^{a-0}_{V_a}}\right]^{-1} : \mathbf{\Delta S^{b-a}_{V_a}}\right)^{-1} : \left(\mathbf{E^d} + \mathbf{R_b}\right) \tag{2.60}$$

$$\bar{\epsilon}^a = \left[\mathbf{I} + \mathbf{\Delta S^{a-0}_{V_a}}\right]^{-1} : \left[\mathbf{E^d} - \frac{V_b}{V_a}\mathbf{\Delta S^{b-a}_{V_a}} : \bar{\epsilon}^b + \mathbf{R_a}\right] \tag{2.61}$$

Interestingly, the expressions of $\mathbf{\Delta S^{a-0}_{V_a}}$, $\mathbf{\Delta S^{b-a}_{V_a}}$, $\mathbf{\Delta S^{b-a}_{V_b}}$, $\mathbf{R_a}$ and $\mathbf{R_b}$ defined in Eqs. 2.55-2.59 show that the generalization of the Tanaka-Mori method introduces a coupling between the averaged strain fields in each volume. Moreover, with the five $\mathbf{S^j(V_i)}$ tensors introduced in Eq. 2.49, relative shape and volume fraction effects between both inclusions can be predicted. Note that solution of Eq. 2.50 is not trivial, as it requires inverting a general four-dimensional tensor. Tensors $\mathbf{S^j(V_i)}$ are obtained by use of a Gauss-Lobatto integration of Greens tensors in the Fourier space. This method is similar to that used in the viscoplastic self-consistent (VPSC) [101] and elasto-plastic self-consistent (EPSC) [120] schemes.

Using Hooke,s law, average stresses in V_b and $V_1 - V_2$ are given by :

$$\bar{\sigma}^b = \mathbf{C^b} : \left(\bar{\epsilon}^b - \epsilon^{*b}\right) \tag{2.62}$$

$$\bar{\sigma}^{V_a - V_b} = \mathbf{C^a} : \left(\bar{\epsilon}^{V_a - V_b} - \epsilon^{*a}\right) \tag{2.63}$$

The average stresses in V_a are given by :

$$\bar{\sigma}^a = \frac{V_b}{V_a}\bar{\sigma}^b + \frac{V_a - V_b}{V_a}\bar{\sigma}^{V_a - V_b} \tag{2.64}$$

As defined in the previous paragraph, the stored elastic energy per unit of volume is given by

$$\Phi = \frac{1}{2V}\int_V \sigma(\mathbf{r}) : \epsilon^{el}(\mathbf{r})dV_r \tag{2.65}$$

Applying now the Hill's result for heterogeneous elasto-plastic media [121, 122] to heterogeneous elastic matrix with plastic incompatibilities enables to derive a new closed form of the stored elastic energy density as follows :

$$\Phi = \frac{1}{2}\Sigma : \mathbf{E^d} + \Phi^{\text{int}} = \frac{1}{2}\Sigma : \mathbf{E^d} - \frac{1}{2V}\int_V \sigma(\mathbf{r}) : \epsilon^*(\mathbf{r})dV_r \tag{2.66}$$

where Σ and Φ^{int} denote the macroscopic stress tensor and the internal part of the free Helmholtz energy density resulting from plastic incompatibilities, respectively.

Both the macroscopic stress and plastic strain tensors are given by the two subsequent integral equations :

$$\Sigma = \frac{1}{V}\int_V \sigma(\mathbf{r})dV_r \tag{2.67}$$

$$\mathbf{E^p} = \frac{1}{V}\int_V \mathbf{B^t}(\mathbf{r}) : \epsilon^*(\mathbf{r})dV_r \tag{2.68}$$

with $\mathbf{B}$, a fourth-order concentration tensor linking the virtual local stress fields that would have existed if the medium remained purely elastic to the macroscopic stress [121, 122].

In the present case, the macroscopic strain tensor, $\mathbf{E^d}$, can be computed from the homogeneous medium elastic constants and the macroscopic stress applied in the following manner

$$\mathbf{E^d} = \left(\mathbf{C^0}\right)^{-1} : \Sigma + \mathbf{E^p} \tag{2.69}$$

Given the spatial expression of plastic incompatibilities (Eq. 2.36) and the mean-field approximation, the internal free energy density, Φ^{int}, can be rewritten as :

$$\Phi^{\text{int}} = -\frac{V - V_a}{V}\bar{\sigma}^{V-V_a} : \mathbf{E^p} - \frac{V_a - V_b}{V_a}\bar{\sigma}^{V_a-V_b} : \epsilon^{*a} - \frac{V_b}{V}\bar{\sigma}^b : \epsilon^{*b} \tag{2.70}$$

Because the medium is infinite, $\bar{\sigma}^{V-V_a}$ is assumed to be equal to Σ. Consequently,

$$\Phi^{\text{int}} = -\frac{V - V_a}{V}\Sigma : \mathbf{E^p} - \frac{V_a - V_b}{V_a}\bar{\sigma}^{V_a-V_b} : \epsilon^{*a} - \frac{V_b}{V}\bar{\sigma}^b : \epsilon^{*b} \tag{2.71}$$

Relationship with the classical Eshelby's results and Nemat-Nasser and Hori's solutions

Considering the particular case of an elastically homogeneous medium such that $\mathbf{C^b} = \mathbf{C^a} = \mathbf{C^0}$, Eq. 2.40 reduces to :

$$\begin{aligned}\epsilon(\mathbf{r}) = \mathbf{E^d} - \int_{V_a} \mathbf{\Gamma}^{\infty,\mathbf{s}}(\mathbf{r} - \mathbf{r}')dV_{r'} : \left(\mathbf{C^0} : \mathbf{E^p} - \mathbf{C^a} : \epsilon^{*a}\right)& \\ - \int_{V_b} \mathbf{\Gamma}^{\infty,\mathbf{s}}(\mathbf{r} - \mathbf{r}')dV_{r'} : \mathbf{C^0} : \left(\epsilon^{*a} - \epsilon^{*b}\right)&\end{aligned} \tag{2.72}$$

Then, the average strains in V_a and V_b also reduce to :

$$\bar{\epsilon}^a = \mathbf{E^d} + \mathbf{S^0}(\mathbf{V_a}) : \mathbf{E^p} + \frac{V_a - V_b}{V_a}\mathbf{S^0}(\mathbf{V_a}) : \epsilon^{*a} + \frac{V_b}{V_a}\mathbf{S^0}(\mathbf{V_a}) : \epsilon^{*b} \tag{2.73}$$

$$\bar{\epsilon}^b = \mathbf{E^d} + \mathbf{S^0}(\mathbf{V_a}) : \mathbf{E^p} + \left[\mathbf{S^0}(\mathbf{V_a}) - \mathbf{S^0}(\mathbf{V_b})\right] : \epsilon^{*a} + \mathbf{S^0}(\mathbf{V_b}) : \epsilon^{*b} \tag{2.74}$$

where $\mathbf{S^0}(\mathbf{V_i}) = \mathbf{P^{V_i}} : \mathbf{C^0}$ are the elastic tensors associated with $\mathbf{C^0}$ and V_i.

As expected Eqs. 2.73 and 2.74 correspond to the first extension of the Tanaka-Mori scheme observed by Hori and Nemat-Nasser [63] and Nemat-Nasser and Hori [64] .

Note that in the case of homogeneous elasticity, Eqs. 2.61 and 2.60 yield null values for $\mathbf{\Delta S_{V_a}^{a-0}}$, $\mathbf{\Delta S_{V_a}^{b-a}}$ and $\mathbf{\Delta S_{V_b}^{b-a}}$ so that these equations become respectively Eqs. 2.73 and 2.74. Similarly, if one considers the eigenstrain in $V_a - V_b$ to be null, the average strain in V_b reduces to Eshelby's solution to the inclusion problem :

$$\bar{\epsilon}^b = \mathbf{E^d} + \mathbf{S^0}(\mathbf{V_b}) : \epsilon^{*b} \tag{2.75}$$

2.2.2 Application to first generation tensile twinning in magnesium

For the present application, a slightly simplified version of the elasto-static Tanaka-Mori scheme, described in the above, is considered since the matrix does not contain an overall plastic strain incompatibility, $\mathbf{E^p}$. The local elastic stiffness tensors, associated to each inclusion/twin domain, are related to that of medium "0" by simple rotation operations. Note that, for the sake of consistency, all calculations need to be performed in a reference coordinate system chosen arbitrarily as that associated to the grain. As a result, the elastic moduli of the inclusions, expressed in the reference coordinate system, are given by :

$$C^c_{ijkl} = C^0_{mnpq} R^c_{im} R^c_{jn} R^c_{kp} R^c_{lq} \tag{2.76}$$

where $c = \{a, b\}$ and R^i is the rotation matrix representing the misorientation of the inclusion "i" (Figure 2.2). Note that these cumulative rotations may transform transversely isotropic tensors into anisotropic tensors.

The elastic constants of Magnesium expressed in the crystal reference frame are extracted from [123] and given, in GPa, by :

$$\mathbf{C^0} = \begin{pmatrix} 59.4 & 25.6 & 21.4 & 0 & 0 & 0 \\ 25.6 & 59.5 & 21.4 & 0 & 0 & 0 \\ 21.4 & 21.4 & 61.6 & 0 & 0 & 0 \\ 0 & 0 & 0 & 16.4 & 0 & 0 \\ 0 & 0 & 0 & 0 & 16.4 & 0 \\ 0 & 0 & 0 & 0 & 0 & 16.9 \end{pmatrix}$$

Twinning on the $\{10\bar{1}2\}$ planes is common to all h.c.p. materials. Because experimental measures of the development of internal strains within both a parent and a $\{10\bar{1}2\}$ twin phase are available for magnesium alloy AZ31 [36], the generalized Tanaka-Mori method presented previously is applied to this problem. Therefore, the misorientation between $V_a - V_b$, representing the original parent crystal, and the "unbounded" body, V, is set to zero and the eigenstrain in the sub-region $V_a - V_b$, ϵ^{*a}, is equal to the null tensor. In V_b, a non-zero eigenstrain - only the shear components along the axis e'_2 and e'_3 are non null - is prescribed in order to restore the twinning shear for which the unit magnitude is equal to 0.131 according to [17] . Clearly, the use of a homogeneous eigenstrain within the twin domain is an approximation of the strain state within the twin domain since all the twinning shear strain is effectively concentrated at the twin interface. Note that a similar approximation was made in Lebensohn et al. [101] to study twin nucleation in anisotropic materials. The local frame is associated to the twin domain : axis $\mathbf{e'_1}$, is perpendicular to the twinning shear direction, η_1, and lies in the undistorted plane, K_1, and axis $\mathbf{e'_2}$, is parallel to the twinning shear direction and lies too in the undistorted planeK_1 ; the third axis, $\mathbf{e'_3}$, along which thickening occurs, is the cross product of the first axis with the second one.

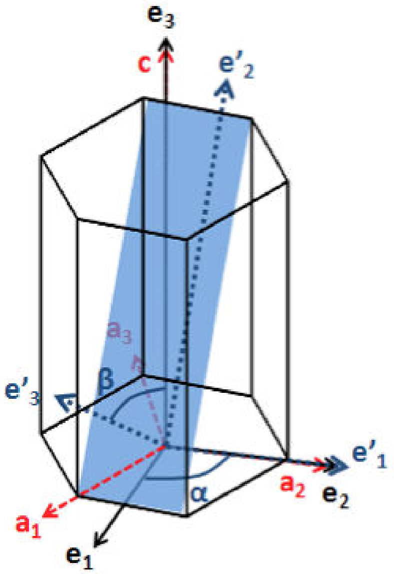

FIGURE 2.3 – Representation of the local coordinate system (e'_1, e'_2, e'_3) associated with the $\{10\bar{1}2\}$-tensile twinning. The reference coordinate system (e_1, e_2, e_3) associated to the crystal structure and the crystallographic coordinate system (a_1, a_2, a_3, c) are also shown.

The effect of both twin and grain shapes on the average internal stresses within each phase is studied first. In order to facilitate the understanding of relative shape effects in each inclusion (i.e. the parent grain and the twin phase), axes 1 and 2 of each ellipsoid have the same length. R denotes the aspect ratio of the ellipsoid length along axis 1 divided by that along axis 3 which corresponds to the axis of thickening. Therefore large values of R will denote flat ellipsoidal domains while R equal to 1 describes a perfectly spherical domain.

In order to isolate the effects of relative volume from the shape effects, the twin volume fractions are arbitrarily fixed here to 2.5 and 5 percent and R is varied in both the twin and parent domains. Figures 2.4a, 2.4b, 2.4c and 2.4d present the evolutions of the resolved shear stress on the twin system in the twin ((a) and (c)) (i.e. V_b) and in the parent ((b) and (d)) (i.e. $V_a - V_b$) domains, respectively, as a function of the ratio R_{twin}. Simulations are repeated for several initial grain shapes described with R_{parent}.

Figure 2.4 suggests several interesting shape effects. First, it is found, by comparison with the values of the resolved shear stresses (RSS) in the parent and twin domains that for some grain and twin shapes, the approach can predict the stress reversal, i.e. RSS of opposite signs in the twin and parent domain. This finding is in qualitative agreement with that experimentally measured in Aydiner et al. [36]. 3DXRD measurements showed that the difference in the RSS of the parent and twin domains depends on the twin volume fraction. For small twin volume fractions a stress reversal is observed. However, when the twin has reached a ”critical” size the stress reversal is no longer observed [36]. Interestingly it is found by comparison of Figures 2.4a and 2.4b that the relative shape effect between the parent and twin phases has a similar effect to that of the twin fraction discussed above. Namely, for a given parent shape, described by R_{parent}, an increase in R_{twin} (e.g. flattening of the twin phase) leads to an increase in the resolved shear stress in the parent phase. Such an increase can affect the sign of the RSS in the parent domain. As the RSS in the twin domain remains negative the relative shape effect shown here reveals that the occurrence of a stress reversal depends on the relative shape of the twin and parent phases.

Second, as otherwise predicted by the elementary solution to the inclusion problem proposed by Eshelby [115] and shown in Figure 2.4a, it is found that the parent grain shape has no effect on the stress state within the twin phase. Furthermore, it is found that at fixed relative volume fractions the magnitude of the RSS in the twin domain decreases with an increase in R_{twin}. In other words, internal stresses in the twin are the lowest in magnitude for a flat ellipsoidal twin and the highest for a spherical one. This is consistent with the experimentally observed twin shapes. Third, it is found that both the twin and grain shapes affect the stress state within the parent domain but in opposite directions. Namely, while increasing R_{twin} leads to an increase in the stress state within the parent grain, the same effect is produced by a decrease in R_{parent}. Note that the stress state within the twin phase is far more affected by relative shape effects than that in the parent domain (Figure 2.4b). Note also that the dependence is affected by the relative twin volume fraction.

Finally, comparing Figures 2.4a and 2.4c, corresponding to the two different twin fractions, shows that twin volume fraction only affects the magnitude of the stress states within each phase but not the trends associated with changes in the shape of the twin and parent domains. With this, it is to be concluded that in the range of twin fractions studied here, the orders of magnitude of the RSS in the parent and twin domains are different from a factor ≈ 100, while experimental measures do not exhibit such difference. It is to be expected that an elasto-plastic approach, as opposed to the purely elastic accommodation method as proposed here, will limit the stress state within the twin domains, as the magnitude of the elastic incompatibility could then be accommodated by plastic deformation modes. However, this is out the scope of the present work and will be the objective of a further study.

As experimental measures of back-stresses within the twin and parent domains showed that their magnitude evolves during growth [36], it is desired here to fictitiously and qualitatively reproduce growth of a twin in a parent grain by computing the evolution of the RSS in both phases for a fixed grain shape, with $R_{parent} = 3$, and a twin of increasing thickness. Initially, the twin is a flat ellipsoid with axes 1 and 2 such that the twin is spread on the entire surface available on the twin plane. Note here that as opposed to the previous case the simultaneous effects of both the shape and relative volume fraction effects are evaluated.

As shown in Figure 5, where symbols denote the experimentally measured RSS on the twin domains (reported from [36]), substantial changes in the backstresses are predicted during growth of the twin domain. However, since a purely elastic accommodation is used here, the magnitude

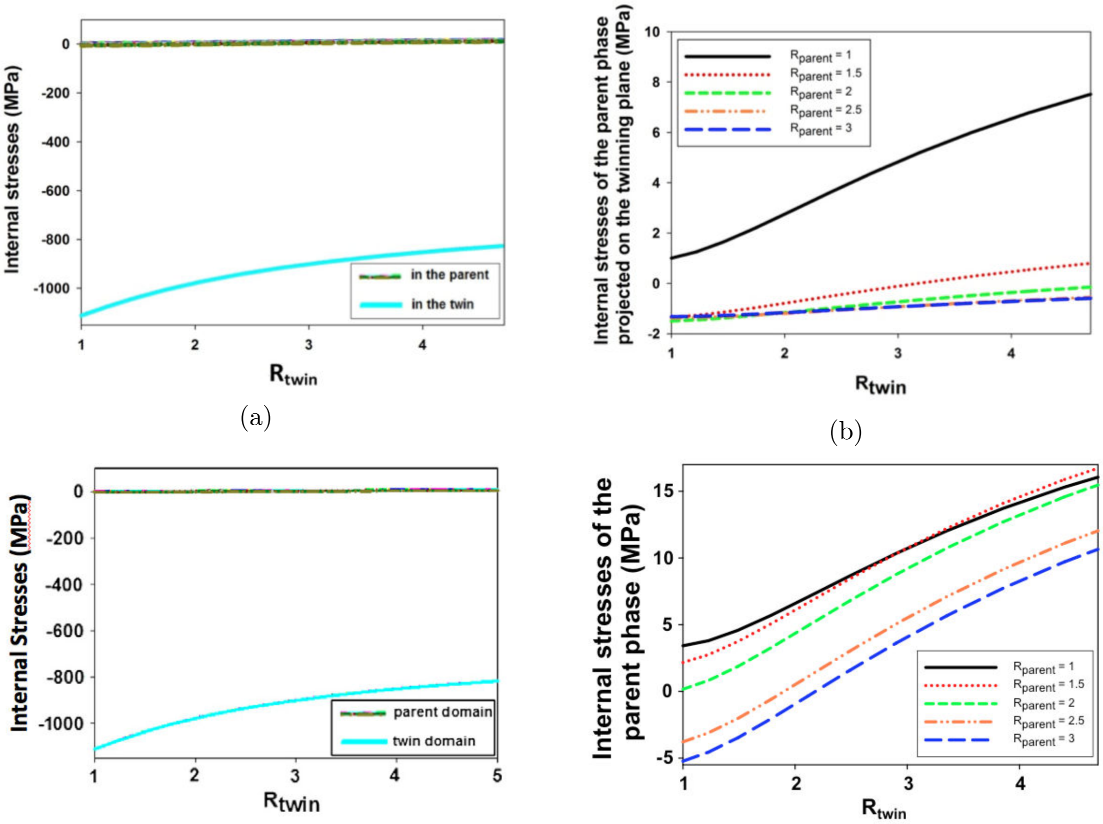

(a) (b)

(c) (d)

FIGURE 2.4 – (a and c) Mean internal stresses projected on the twinning plane in the twinning shear direction in both the twin phase and the parent phase as functions of R_{twin}, (b and d) Influence of R_{parent} on the mean internal stresses of the parent projected on the twinning plane. The twin volume fraction in the parent is 0.25 for (a) and (b) and 0.05 for (c) and (d).

of the stress reversal predicted is much larger than those measured at the level of plastic strains performed in Aydiner et al. [36]. On the contrary, as depicted in Figure 2.5, experimental measures indicate that the magnitude of the back-stresses vary little with twin growth. Therefore it is suggested, from comparison with experimental measures [36] that the elastic incompatibilities (evolving with twin shape and relative volume fraction effects) necessarily lead to an increase in plastic accommodation, via slip, during twin growth. This is likely to have a prominent role in the generation of the typically observed multi-lamellar twins, as the sequential nucleation of new twin lamellae allows for accommodation of elastic incompatibilities during twin growth.

Figure 2.5 exhibits the evolution with twin volume fraction and at a given parent geometry ($R_{parent} = 3$) of the internal stresses in the twin and parent domains. As revealed by 3DXRD experiments and shown in Figure 2.4, the RSS in the parent phase is of opposite sign, i.e. positive, with respect to that in the twin phase when the twin volume fraction is small. In Figure 2.5, the change of sign occurs at a twin volume fraction equal to 6% and R_{twin} equal to 2.3. For a twin volume fraction equal to 5%, and R_{twin} and R_{parent} respectively equal to 2.3 and 3, Figure 2.4d shows that the RSS in the parent domain is negative, whereas as shown in Figure 2.5 the RSS in the parent domain reaches zero when the twin volume fraction reaches 6%. This observation

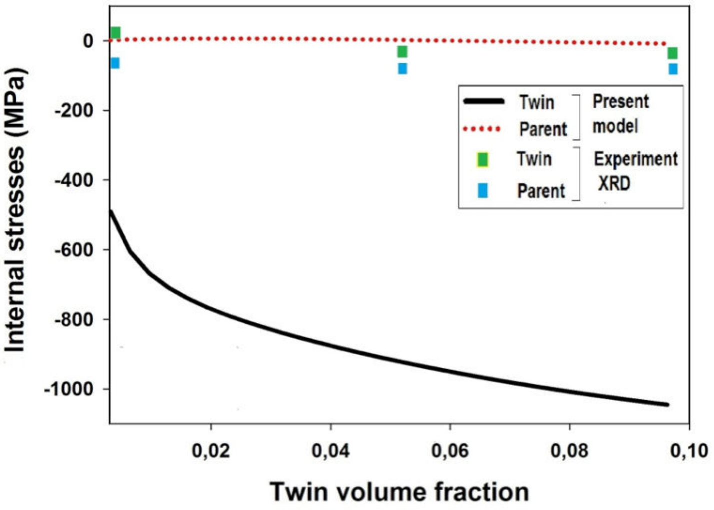

FIGURE 2.5 – Evolution of the mean internal stresses in both twin and parent phases projected on the twinning plane as a function of twin volume fraction. Lines refer to the model predictions while symbols denote measure data. The ellipsoid aspect ratio for the parent, R_{parent}, is set to 3.

underlines the consistency of the results presented in Figures 2.4 and 2.5.

The specificity of the present extension of the Tanaka-Mori scheme is the consideration of heterogeneous elasticity, the effect of which is to be discussed here. As discussed in the previous section, Nemat-Nasser and Hori [64, 63] dealt with problems in which two eigenstrains are placed in two overlapping inclusions. However, this scheme is limited to homogeneous elasticity. Hence, comparison of the two schemes allows for the investigation of the sole effect of elastic heterogeneity on the stress states in both parent and twin domains. Let us recall that, in the case of first generation twins, the eigenstrain in volume $V_a - V_b$ is null. Consequently, the mean stresses in the twin, obtained from the Hori and Nemat- Nasser schemes, correspond to Eshelby,s solution. In Figure 2.6, it is shown that elastic heterogeneity changes the trend of stress evolution considerably. This effect is especially appreciable for the internal resolved shear stress of the twin on the twinning plane. Indeed, one observes in Figure 2.6b that the solution using homogeneous elasticity does not capture the experimentally observed decrease of the RSS in the twin (Figure 2.5). However, Figure 2.6a shows that for small twin volume fractions, the present model and the Nemat-Nasser scheme display the same trend about mean internal stresses in the twin whereas, for larger twin volume fractions, the influence of heterogeneous elasticity becomes important and the two models evolve in opposite directions.

2.3 The Double Inclusion Elasto-Plastic Self-Consistent (DI-EPSC) scheme.

Encouraged by the promising results obtained with the approach introduced in the previous paragraph, the double inclusion elasto-plastic self-consistent scheme has then been developed. It consists of an adaptation of the EPSC model [120, 4] to consider the direct mechanical interaction

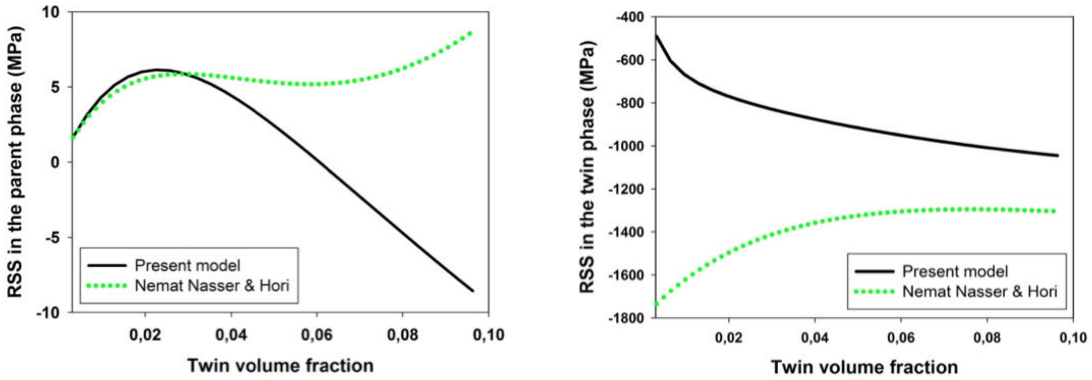

(a) (b)

FIGURE 2.6 – Resolved shear stresses - projected on the twinning plane and twin shear direction - of both the parent (a) and the twin (b) phases as functions of twin volume fraction. Solid lines and dashed lines refer to the present model and to the Nemat-Nasser and Hori's double inclusion scheme for homogeneous elasticity, respectively. The ellipsoid aspect ratio for the parent, R_{parent}, is set to 3.

between parent and twin phases during the development of intra-granular twins. With reference to the experimental and modeling results of Clausen et al. [4], the role of parent/twin interactions is examined especially regarding the predictions of internal strains and stresses within twin domains. The present section is organized as follows : in the first part is introduced the new double inclusion elasto-plastic self-consistent (DI-EPSC) scheme. Concentration relations for non-twinned grains, twin and parent domains are detailed and the single crystal plasticity model is descibed ; the second part is dedicated to the quantification of the impact of the topological coupling between the twin and parent phases on model predictions via the observation of latent effects induced by twinning and the comparison of results for an extruded and a randomly textured AZ31 alloy ; finally, in the third part, the authors show the influence of secondary slip on the material response and focus on how to model the twin stress states at the onset of twinning, studying two limit initial configurations where twins are either assumed to have the same stress state as the parent domain or to be fully relaxed.

2.3.1 DI-EPSC model

The idea to be mathematically derived in the following is to distinguish those grains not containing twins and those containing twin domains. In the self-consistent approach the polycrystal is represented as an ensemble of inclusions (i.e. grains containing or not containing twins) and the average strains and stresses within each domain are obtained from solving a specific inclusion problem yielding a concentration rule that relates the average local stress or strain fields to the macroscopic equivalents. Here in the case of grains not containing twins, the inclusion is assumed to be embedded in a homogeneous equivalent medium (HEM) with properties and mechanical response corresponding to those of the polycrystal. Such concentration laws are similar to that initially derived by Hill [40] and based on the work of Eshelby [115]. In the case of grains containing twins, new concentration relations are derived based on a double inclusion topology so called DI-EPSC in the following. Figure 2.7a presents the current uncoupled approach [4] while figure 2.7b presents the new coupled one.

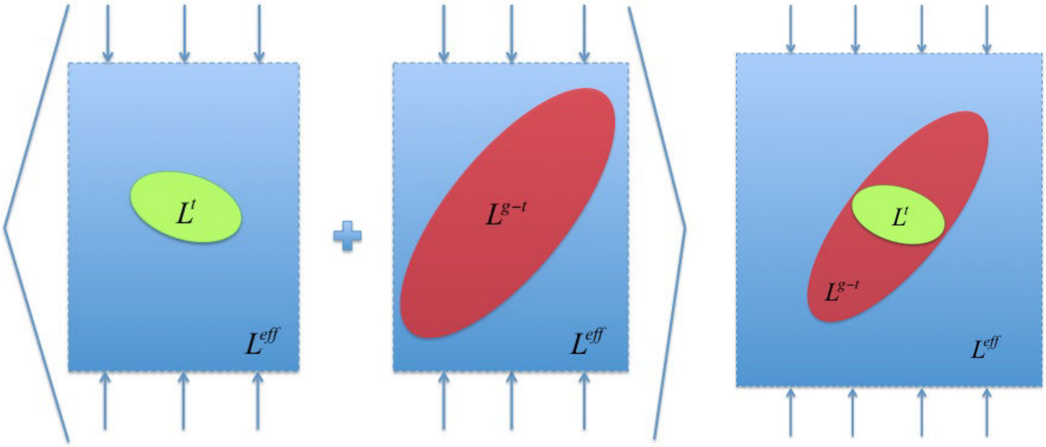

(a)

(b)

FIGURE 2.7 – Schematic representation of the elasto-plastic problem with twinning corresponding respectively to the uncoupled [4] (a) and coupled (present) (b) formulations. The dashed line signifies that inclusions V_t and V_{g-t} with tangent moduli L^t and L^{g-t} are embedded in an equivalent homogeneous medium with a tangent modulus L^{eff}

General equations

The fourth-order tensors L^{eff} and L^i denote the linearized tangent moduli of the HEM and of a given phase 'i' respectively. The latter may correspond to a non-twinned grain 'c', a twinned grain 'g', a twin domain 't' and a parent one 'g-t' associated with 'g'. The constitutive response of the HEM is thus given by :

$$\dot{\mathbf{\Sigma}} = \mathbf{L^{eff}} : \dot{\mathbf{E}} \tag{2.77}$$

where, $\dot{\mathbf{\Sigma}}$ and $\dot{\mathbf{E}}$ are respectively the macroscopic stress and strain rate tensors associated with the HEM. In similar fashion, the constitutive equation of crystal 'i' is expressed as follows :

$$\dot{\sigma}^{\mathbf{i}} = \mathbf{L^i} : \dot{\epsilon}^{\mathbf{i}} \tag{2.78}$$

where, $\dot{\sigma}^{\mathbf{i}}$ and $\dot{\epsilon}^{\mathbf{i}}$ denote the stress rate and strain rate tensors of crystal 'i', respectively. Concentration tensors then provide a link between the local and global mean fields. In the present formulation these are formally expressed as follows :

$$\dot{\epsilon}^{\mathbf{i}} = \mathbf{A^i} : \dot{\mathbf{E}} \tag{2.79}$$

$$\dot{\sigma}^{\mathbf{i}} = \mathbf{B^i} : \dot{\mathbf{\Sigma}} \tag{2.80}$$

Here $\mathbf{A^i}$ and $\mathbf{B^i}$ denote the strain and stress concentration tensors. These will be different whether or not the considered grain contains a twin domain. From homogeneous boundary conditions and average conditions, the overall mechanical response of the material is obtained by enforcing macro homogeneity conditions :

$$\dot{\mathbf{\Sigma}} =< \dot{\sigma^{\mathbf{i}}} > \tag{2.81}$$

$$\dot{\mathbf{E}} =< \dot{\epsilon^{\mathbf{i}}} > \tag{2.82}$$

Combining 2.81, 2.82 and 2.77, the overall tangent modulus is obtained self-consistently as follows :

$$\mathbf{L^{eff}} =< \mathbf{L^i} : \mathbf{A^i} >:< \mathbf{A^i} >^{-1} \tag{2.83}$$

Integral equation

Considering spatial fluctuations of linearized tangent moduli denoted $\delta\mathbf{L}$ with respect to a reference homogeneous medium denoted $\mathbf{L^0}$, the tangent modulus $\mathbf{L}$ decomposes as follows :

$$\mathbf{L}(\mathbf{r}) = \mathbf{L^0} + \delta\mathbf{L}(\mathbf{r}) \tag{2.84}$$

At any point $\mathbf{r}$ within the volume, the local constitutive equation is given by :

$$\dot{\sigma(\mathbf{r})} = \mathbf{L}(\mathbf{r}) : \dot{\epsilon}(\mathbf{r}) \tag{2.85}$$

Upon introducing Eq. 2.84 into Eq. 2.85 and enforcing both static mechanical equilibrium and compatibility of the total local strain, one obtains a Navier-type equation for the heterogeneous medium :

$$\nabla.\mathbf{L^0} : \nabla^s\dot{\mathbf{u}}(\mathbf{r}) + \mathbf{f}^*(\mathbf{r}) = \mathbf{0} \tag{2.86}$$

where, $\mathbf{f}^*$ represents the body forces resulting from the heterogeneity within the medium. $\nabla^s\dot{\mathbf{u}}$ denotes the displacement gradient.

$$\mathbf{f}^*(\mathbf{r}) = \nabla.(\delta\mathbf{L}(\mathbf{r}) : \dot{\epsilon}(\mathbf{r})) \tag{2.87}$$

A solution to this boundary value problem is given by the Lippman-Schwinger-Dyson-type integral equations. Following Lipinski and Berveiller [46], the strain field at any material point of position vector $\mathbf{r}$:

$$\dot{\epsilon}(\mathbf{r}) = \dot{\mathbf{E}} - \int_V \mathbf{\Gamma^{\infty,s}}(\mathbf{r} - \mathbf{r}') : \delta\mathbf{L}(\mathbf{r}') : \dot{\epsilon}(\mathbf{r}')dV_{r'} \tag{2.88}$$

where $\mathbf{\Gamma^{\infty,s}}(\mathbf{r} - \mathbf{r}')$ denotes the symmetric modified Green tensor, given by :

$$\Gamma^{\infty,s}_{ijkl}(\mathbf{r} - \mathbf{r}') = -\frac{1}{2}(G^{\infty,s}_{ik,jl}(\mathbf{r} - \mathbf{r}') + G^{\infty,s}_{jk,il}(\mathbf{r} - \mathbf{r}')) \tag{2.89}$$

Double inclusion geometry for twinned grains and mean field approximation

In the present case the geometry of the problem is as follows ; the twinned grain, embedded in the HEM, occupies a volume V_g that contains one single twin domain with volume V_t (such that $V_t \subset V_g$). Therefore the parent volume is given by $V_g - V_t$. The tangent moduli of the overall inclusion (i.e. twin and parent phase combined), the twin domain and the parent domains are given by $\mathbf{L^g}$, $\mathbf{L^t}$ and $\mathbf{L^{g-t}}$, respectively. Similarly, their volume fractions are denoted f_g, f_t and f_{g-t}. Let us introduce the characteristic functions $\theta^g(\mathbf{r})$ and $\theta^t(\mathbf{r})$ associated with V_g and V_t, respectively. These functions are either equal to the identity or to the null tensor inside and outside their corresponding volumes. Consequently, the spatially varying tangent modulus, $\delta\mathbf{L}(\mathbf{r})$, can be expressed as :

$$\delta\mathbf{L}(\mathbf{r}) = (\mathbf{L^{g-t}} - \mathbf{L^0})\theta^g(\mathbf{r}) + (\mathbf{L^t} - \mathbf{L^{g-t}})\theta^t(\mathbf{r}) \tag{2.90}$$

Note here that solely the stiffness tensors $\mathbf{L^t}$ and $\mathbf{L^{g-t}}$ are accessible via the constitutive law.

Introducing Eq. 2.90 into Eq. 2.88 one obtains an integral expression of the local strain increments :

$$\dot{\epsilon}(\mathbf{r}) = \dot{\mathbf{E}} - \int_{V_g} \mathbf{\Gamma}^{\infty,\mathbf{s}}(\mathbf{r} - \mathbf{r}') : (\mathbf{L^{g-t}} - \mathbf{L^0}) : \dot{\epsilon}(\mathbf{r}')dV_{r'} - \int_{V_t} \mathbf{\Gamma}^{\infty,\mathbf{s}}(\mathbf{r} - \mathbf{r}') : (\mathbf{L^t} - \mathbf{L^{g-t}}) : \dot{\epsilon}(\mathbf{r}')dV_{r'} \tag{2.91}$$

Such expression can also be solved exactly via the use of Fast Fourier transforms, or as proposed here can be approximated using the average strains in the different domains like e.g. in Berveiller et al. [45]. The volume average strain increment, denoted by $\dot{\epsilon}^{\mathbf{i}}$, within a volume V_i (with i=g, g-t, t) is defined as :

$$\dot{\epsilon}^{\mathbf{i}} = \frac{1}{V_i} \int_{V_i} \dot{\epsilon}(\mathbf{r})dV_r \tag{2.92}$$

Substituting the local strain increment by its expression (Eq. 2.91), the previously defined volume average strain increment becomes :

$$\begin{aligned} \dot{\epsilon}^{\mathbf{i}} = \dot{\mathbf{E}} &- \frac{1}{V_i} \int_{V_i} \int_{V_g} \mathbf{\Gamma}^{\infty,\mathbf{s}}(\mathbf{r} - \mathbf{r}') : (\mathbf{L^{g-t}} - \mathbf{L^0}) : \dot{\epsilon}(\mathbf{r}')dV_{r'}dV_r \\ &- \frac{1}{V_i} \int_{V_i} \int_{V_t} \mathbf{\Gamma}^{\infty,\mathbf{s}}(\mathbf{r} - \mathbf{r}') : (\mathbf{L^t} - \mathbf{L^{g-t}}) : \dot{\epsilon}(\mathbf{r}')dV_{r'}dV_r \end{aligned} \tag{2.93}$$

In the following, this last equation is applied to 'i'='g' or 't'. Because V_t and V_g are ellipsoidal and $V_t \subset V_g$, the order of integration in the computation of the averaged strain increment fields can be inverted according to the Tanaka-Mori theorem [112, 50]. In the present double inclusion topology, the strain increment $\dot{\epsilon}(\mathbf{r}')$ present in Eq. 2.91 interferes in subdomains 't' and 'g-t' and is not uniform neither in V_g nor V_t even in the case of ellipsoidal shape inclusions. However, an intuitive approximation used here considers the mean fields $\dot{\epsilon}^{\mathbf{g}}$ and $\dot{\epsilon}^{\mathbf{t}}$ defined by Eq. 2.92 .

One can introduce tensors $\mathbf{P^{V_i}}$ as the integral of the symmetrized modified Green function over volume V_i :

$$\mathbf{P^{V_i}}(\mathbf{r}) = \int_{V_i} \mathbf{\Gamma}^{\infty,\mathbf{s}}(\mathbf{r} - \mathbf{r}')dV_{r'} \tag{2.94}$$

Similarly, let us introduce tensors $\mathbf{S}^{\mathbf{j}}_{\mathbf{V_i}}$ as the double dot product of the $\mathbf{P}^{\mathbf{V_i}}$ tensors with the incremental stiffnesses $\mathbf{L}^{\mathbf{j}}$, with j=g, g-t, t, such that :

$$\mathbf{S}^{\mathbf{j}}_{\mathbf{V_i}} = \mathbf{P}^{\mathbf{V_i}} : \mathbf{L}^{\mathbf{j}} \tag{2.95}$$

Self-consistent solutions for twinned grains

In the case of ellipsoidal inclusions, tensors $\mathbf{P}^{\mathbf{V_i}}$ and $\mathbf{S}^{\mathbf{j}}_{\mathbf{V_i}}$ are uniform when $\mathbf{r} \in V_i$. Note the similarity between the expression of the $\mathbf{S}^{\mathbf{j}}_{\mathbf{V_i}}$ tensors and the Eshelby's tensor. Applying the self-consistent condition, i.e. $\mathbf{L}^{\mathbf{0}} = \mathbf{L}^{\mathbf{eff}}$, the strain increment solutions for the twin domains 't' and for the twinned grains 'g' - that include both the twin and the parent phases - are obtained as follows :

$$\dot{\epsilon}^{\mathbf{t}} = \dot{\mathbf{E}} - \mathbf{\Delta S}^{\mathbf{g-t}}_{\mathbf{V_g}} : \dot{\epsilon}^{\mathbf{g}} - \mathbf{\Delta S}^{\mathbf{t}}_{\mathbf{V_t}} : \dot{\epsilon}^{\mathbf{t}} \tag{2.96}$$

$$\dot{\epsilon}^{\mathbf{g}} = \dot{\mathbf{E}} - \mathbf{\Delta S}^{\mathbf{g-t}}_{\mathbf{V_g}} : \dot{\epsilon}^{\mathbf{g}} - \frac{f_t}{f_g} \mathbf{\Delta S}^{\mathbf{t}}_{\mathbf{V_g}} : \dot{\epsilon}^{\mathbf{t}} \tag{2.97}$$

with,

$$\mathbf{\Delta S}^{\mathbf{g-t}}_{\mathbf{V_g}} = \mathbf{S}^{\mathbf{g-t}}_{\mathbf{V_g}} - \mathbf{S}^{\mathbf{eff}}_{\mathbf{V_g}} \tag{2.98}$$

$$\mathbf{\Delta S}^{\mathbf{t}}_{\mathbf{V_t}} = \mathbf{S}^{\mathbf{t}}_{\mathbf{V_t}} - \mathbf{S}^{\mathbf{g-t}}_{\mathbf{V_t}} \tag{2.99}$$

$$\mathbf{\Delta S}^{\mathbf{t}}_{\mathbf{V_g}} = \mathbf{S}^{\mathbf{t}}_{\mathbf{V_g}} - \mathbf{S}^{\mathbf{g-t}}_{\mathbf{V_g}} \tag{2.100}$$

After some algebraic manipulations with the systems of equations 2.96 and 2.97, the concentration tensors in the twinned grains and in the twin domains, denoted $\mathbf{A}^{\mathbf{g}}$ and $\mathbf{A}^{\mathbf{t}}$ respectively, can be written as :

$$\mathbf{A}^{\mathbf{g}} = \left[\mathbf{I} + \mathbf{\Delta S}^{\mathbf{g-t}}_{\mathbf{V_g}} - \frac{f_t}{f_g} \mathbf{\Delta S}^{\mathbf{t}}_{\mathbf{V_g}} : (\mathbf{I} + \mathbf{\Delta S}^{\mathbf{t}}_{\mathbf{V_t}})^{-1} : \mathbf{\Delta S}^{\mathbf{g-t}}_{\mathbf{V_g}}\right]^{-1} : \left[\mathbf{I} - \frac{f_t}{f_g} \mathbf{\Delta S}^{\mathbf{t}}_{\mathbf{V_g}} : (\mathbf{I} + \mathbf{\Delta S}^{\mathbf{t}}_{\mathbf{V_t}})^{-1}\right] \tag{2.101}$$

$$\mathbf{A}^{\mathbf{t}} = \left[(\mathbf{I} + \mathbf{\Delta S}^{\mathbf{t}}_{\mathbf{V_t}})^{-1} : (\mathbf{I} - \mathbf{\Delta S}^{\mathbf{g-t}}_{\mathbf{V_g}} : \mathbf{A}^{\mathbf{g}})\right] \tag{2.102}$$

The average strain rate in the parent subdomains $V_g - V_t$ is estimated here using a simple averaging procedure :

$$\dot{\epsilon}^{\mathbf{g-t}} = \frac{1}{f_g - f_t} \left[f_g \mathbf{A}^{\mathbf{g}} - f_t \mathbf{A}^{\mathbf{t}}\right] : \dot{\mathbf{E}} \tag{2.103}$$

As a result, the associated concentration tensor, denoted $\mathbf{A}^{\mathbf{g-t}}$, is given by :

$$\mathbf{A}^{\mathbf{g-t}} = \frac{1}{f_g - f_t} \left[f_g \mathbf{A}^{\mathbf{g}} - f_t \mathbf{A}^{\mathbf{t}}\right] \tag{2.104}$$

Self-consistent solutions for non-twinned grains

In the case of non-twinned grains, tensors $\mathbf{A^c}$ and $\mathbf{B^c}$ are determined via use of Hill's classic self-consistent interaction law [40] :

$$\dot{\sigma}^{\mathbf{c}} - \dot{\mathbf{\Sigma}} = -\mathbf{L}^{\mathbf{eff}} : (\mathbf{S}^{\mathbf{c}-1} - \mathbf{I}) : (\dot{\epsilon}^{\mathbf{c}} - \dot{\mathbf{E}}) = -\mathbf{L}^{*,\mathbf{c}} : (\dot{\epsilon}^{\mathbf{c}} - \dot{\mathbf{E}}) \tag{2.105}$$

Here, $\mathbf{S^c}$, denotes Eshelby's tensor that depends on the grain shape and on the overall instantaneous elasto-plastic stiffness. $\mathbf{I}$, denotes the fourth-order identity tensor. $\mathbf{L}^{*,\mathbf{c}}$ is Hill's constraint tensor [40]. After simplification, the expression of the strain concentration tensor is given by the following equation :

$$\mathbf{A^c} = (\mathbf{L^c} + \mathbf{L}^{*,\mathbf{c}})^{-1} : (\mathbf{L^{eff}} + \mathbf{L}^{*,\mathbf{c}}) \tag{2.106}$$

It is noteworthy that setting $f_t = 0$ in Eq. 2.101 allows to retrieve us Eq. 2.106.

Single crystal constitutive model

The crystal plasticity constitutive model adopted here is based on Schmid's law for slip activity and on an extended Voce hardening law, which are briefly summarized in the following. Given a deformation system "s" (i.e. either slip or twin) of a phase "i" which may correspond to a non-twinned grain "c", a parent domain "g-t" or a twin domain "t" and denoting $\mathbf{m^s}$ the Schmidt tensor on system "s", the first consistency condition simply states that plasticity could occur if the resolved shear stress (RSS) on system "s" is equal to a critical resolved shear stress (CRSS) denoted τ^s as follows :

$$\mathbf{m^s} : \sigma^{\mathbf{i}} = \tau^s \tag{2.107}$$

The second condition states the necessity for the system "s" to remain on the yield surface during a deformation increment

$$\mathbf{m^s} : \dot{\sigma}^{\mathbf{i}} = \dot{\tau}^s \tag{2.108}$$

In addition, for any system "s", the plastic shear strain rate is necessarily positive.

$$\dot{\gamma}^s > 0 \tag{2.109}$$

In the case of slip, a negative shear strain rate corresponds to a positive shear strain rate on the opposite direction. Because twinning is considered as pseudo-slip, twin nucleation is controlled by the three conditions presented previously (Eqs. 2.107, 2.108 and 2.109). Moreover, a twin forms with exactly the same hardening parameters and variables (e.g. CRSS) as those of its parent domain. Then from purely kinematic considerations, the twin volume fraction evolves as follows :

$$\dot{f}^t = \frac{\dot{\gamma}^t}{s} \tag{2.110}$$

where $\dot{f}^t$ denotes the twin volume fraction increment, $\dot{\gamma}^t$ the shear strain increment on the twinning system of the parent phase and s the characteristic twinning shear ($s = 0.13$).

Note that the topology newly introduced does not allow twin multiplicity. The direct coupling between the parent and twin phases strongly decreases the damping and stabilizing effect of the HEM. The new topology makes twin and parent internal states and stiffnesses dependent on each other. Therefore, fulfilling consistency conditions for both domains in the same iteration becomes more difficult.

Following the tangent linearization of the material constitutive equations [40, 41, 120], the relation between the shear strain increment and the strain rate in crystal "c" is given by :

$$\dot{\gamma^s} = \mathbf{f^s} : \dot{\epsilon^i} \tag{2.111}$$

where,

$$\mathbf{f^s} = \sum_{s'} (X^{-1})^{ss'} \mathbf{m^{s'}} : \mathbf{C^i} \tag{2.112}$$

$\mathbf{C^c}$ is the elastic stiffness tensor and $(X^{-1})^{ss'}$ a square matrix with dimensions equal to the square of the number of active systems in the grain "c". It is expressed as :

$$X^{ss'} = \mathbf{m^s} : \mathbf{C^i} : \mathbf{m^{s'}} + V^s(\Gamma) h^{ss'} \tag{2.113}$$

The Voce hardening law is of the form

$$\tau^s = \tau_0^s + (\tau_1^s + \theta_1^s)(1 - exp(-\frac{\theta_0^s \Gamma}{\tau_1^s})) \tag{2.114}$$

And the hardening rate is given by :

$$\dot{\tau^s} = \sum_{s'} V^s(\Gamma) h^{ss'} \dot{\gamma^{s'}} \tag{2.115}$$

where $V^s(\Gamma)$ describes the hardening of slip system "s" with accumulated plastic strain Γ and $h^{ss'}$ describes the latent interactions between the different deformation systems :

$$\frac{\Delta\tau^s}{\Delta\Gamma} = V^s(\Gamma) = \theta_1^s + (\theta_0^s - \theta_1^s + \frac{\theta_0^s \theta_1^s \Gamma}{\tau_1^s}) exp(-\frac{\theta_0^s \Gamma}{\tau_1^s}) \tag{2.116}$$

τ_0^s, τ_1^s, θ_0^s and θ_1^s are hardening parameters presented in the following section.

Finally, the instantaneous single crystal stiffness is given by the following formula :

$$\mathbf{L^i} = \mathbf{C^i} : (\mathbf{I} - \sum_s \mathbf{m^s} \otimes \sum_{s'} (X^{-1})^{ss'} \mathbf{m^{s'}} : \mathbf{C^i}) \tag{2.117}$$

where the operator $\otimes$ is the tensor dyadic product.

Influence of initial twin stress state

From a modeling standpoint, the twinning transformation - inception and propagation of the twin - occurs out of equilibrium and at very fast rate leading to acoustic emission. It can thus be seen as an instantaneous process. From the physics standpoint, the twin/parent interaction strongly affects internal states within the parent and twin phases. Twin growth would tend to shear the parent domain in the twinning direction.

To model such a complex mechanism, two distinct assumptions can be considered. In the first case, in order to respect both quasi-static stress equilibrium in twinned grains before and after twin occurrence and overall stress equilibrium conditions, the assumption consists of imposing the parent stress state as initial twin stress state. Therefore, Cauchy stress tensor of parent and twin phases can be written, at the inception of the twin, as follows :

$$\sigma^{\mathbf{t}} = \sigma^{\mathbf{g-t}} \tag{2.118}$$

This assumption implies that stress in the parent is totally transmitted to the newly formed twin without accommodation. In the present paper, it will be referred to as the "unrelaxed initial twin stress state" estimate.

However, another assumption considers that twins initially behave like cracks (i.e. total stress relaxation). In order to do so, we chose an elementary case in which the twin is taken as stress free at inception. Mathematically, this corresponds to state in which the Cauchy stress tensor of the twin phase is initially equal to the null tensor :

$$\sigma^{\mathbf{t}} = \mathbf{0} \tag{2.119}$$

This assumption will be referred to as the "relaxed initial twin stress state" estimate. At the onset of twinning and only at that time step, such approach violates the global equilibrium but minimizes the local energy. At the time step following nucleation, stress equilibrium is naturally restored via use of the self-consistent scheme. In both cases, the twin is assumed to behave elastically at nucleation. Therefore, Hooke,s law is used to relate the initial elastic twin strain tensor to the twin domain stress tensor, which, under the assumption considered, is equal to either the parent domain stress tensor or the null tensor. The initial total strain is then expressed as the sum of the elastic twin strain and the plastic strain of the parent domain. Both approximations results will be analyzed and discussed further in this chapter.

2.3.2 Computational flowchart

The computational flowchart shows how and when tangent moduli and concentration tensors for non-twinned grains, twin and parent domains are numerically derived (see figure 2.8). In figure 2.8, subscripts "n" and "n-1" indicate the "self-consistency conditions" loop iteration considered. At each time step, a macroscopic strain increment is imposed. In order to return the macroscopic stress increment and to calculate the linearized tangent modulus of the HEM, the DI-EPSC code has to compute the local tangent modulus, the stress and strain tensors in all grains. Consequently, it has to deal with twinned and non-twinned grains.

Consider first the case of a non-twinned grain. At the beginning of a given self-consistent loop iteration, denoted by ”n” in the flowchart, all deformation systems fulfilling the first consistency condition (Eq. 2.107) are flagged as potentially active ; Cauchy stress tensors used in Eq. 2.107 have been computed at the previous self-consistent loop iteration, denoted by ”n-1”. From these potentially active systems, the instantaneous grain tangent modulus is estimated using Eq. 2.117. The latter is expressed as a function of the elastic stiffness tensor and the active slip systems. Mathematically, the individual contribution of a slip system ”s” is represented by the second-order tensor $\mathbf{f^s}$ (Eq. 2.112) whose formula depends on the inverse of the reduced square matrix X (Eq. 2.113), and hence on the Voce hardening rate, V (Eq. 2.116). The work of Hill [124] shows that to obtain a unique stress-rate corresponding to a given strain-rate it is sufficient that the matrix $V^s h^{ss'}$ be positive semi-definite and the elastic stiffness tensor be positive definite. All latent and self-hardening coefficients $h^{ss'}$ are equal to 1. Therefore, the hardening matrix $V^s h^{ss'}$ is not always symmetric, but all its eigenvalues are positive or zero. However, it would have been

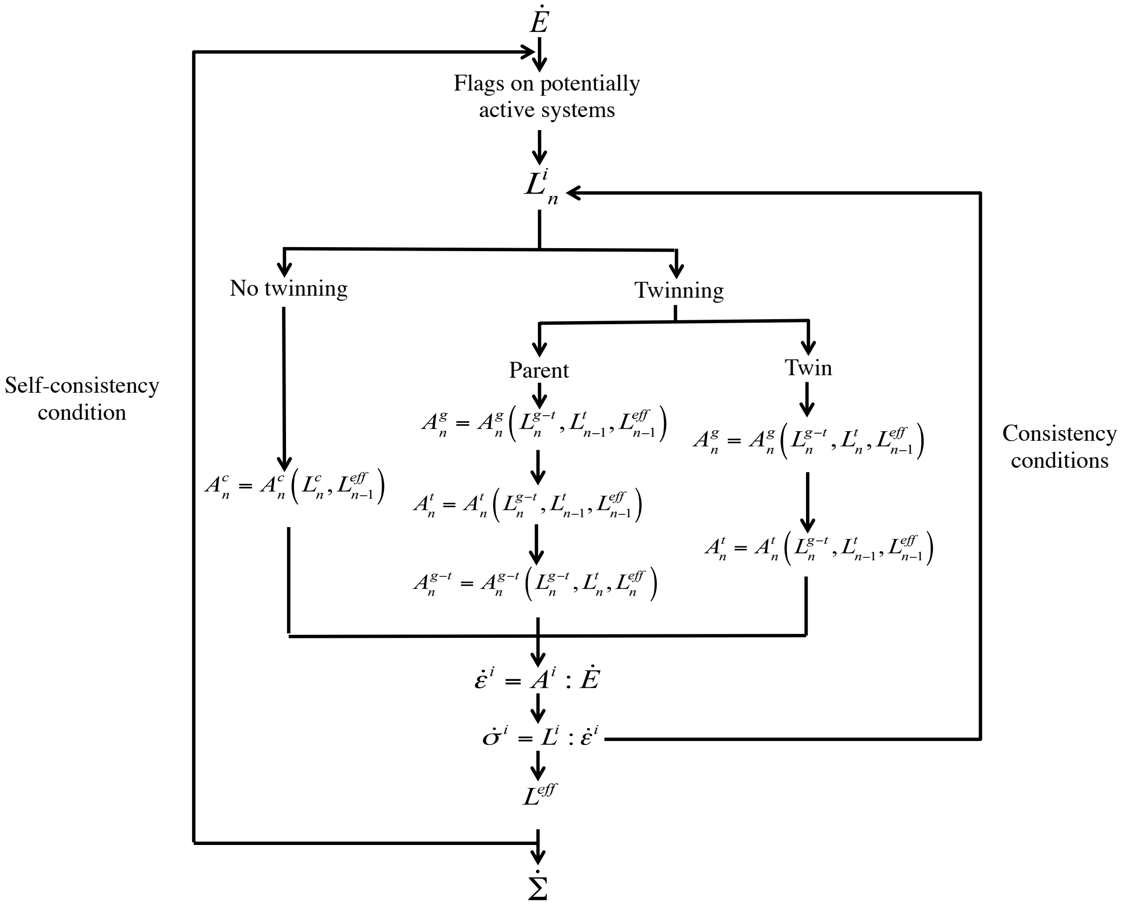

FIGURE 2.8 – Computational flowchart of the DI-EPSC scheme

physically incorrect to ignore the slip anisotropy. In addition, we observed numerically that the major symmetry of local tangent moduli is almost respected. Differences between symmetric non-diagonal components of tangent moduli greater than 1 MPa never exceeded 15.6%. Because the elastic stiffness tensor components are orders of magnitude larger than any hardening rate V, the symmetry of the elastic stiffness tensor dominates the tangent modulus. Then, internal strains and stresses are computed using the Hill's concentration relation (Eq. 2.106). The second consistency condition (Eq. 2.108) associated with a positive shear strain increment condition (Eq. 2.109) allows us to verify whether flagged systems are truly active. The tangent modulus, and the local strain and stress increments are computed and checked again until the fulfillment of these two conditions. The procedure used eliminates randomly one of the potentially active systems and re-iterate the calculation, until either all the systems considered give positive shear or until all have been eliminated, in which case the considered phase is assumed to be elastic. The latter is the case when simulating unloading using EPSC : in some grains the stress first 'slides back' along the yield surface, unloading plastic systems in succession, and eventually detaching from the yield surface. In other grains it detaches at the start of unloading, and goes from plastic to elastic state in one incremental step. Note here that, if the RSS exceeds the CRSS, the stress tensor is proportionally scaled to put it on the yield surface. However, this situation occurs very rarely. For non-twinned grains, there is no difference compared to the EPSC algorithm developed by [120].

Consider now the case of a twinned grain. The algorithm deals with parent and twin domains separately. Choice is made here to compute first the tangent moduli (Eq. 2.104) and stresses of the parent phases and then those of the twin phases (Eq. 2.102). As a result, in the case of parent domains, one must use the tangent moduli of the twin phases computed at the previous iteration. Such is not necessary when dealing with twin domains. It is found that this approach improves convergence. Once the computations on all grains have been performed, the overall tangent modulus from which the self-consistency condition checks the convergence is calculated using Eq. 2.83. The overall tangent modulus major symmetry is enforced numerically. If the self-consistency condition is fulfilled, the DI-EPSC code returns the macroscopic stress increment (Eq. 2.77).

2.3.3 Application to AZ31 alloy

Material parameters and initial textures

The AZ31 alloy studied here is composed of 3 wt% Al, 1 wt% Zn, with restrictions on the transition impurities Fe, Ni and Cu. As shown in Figure 2.9, both initially extruded and randomly textured materials are considered. Elastic constants, expressed in the crystal reference frame with Voigt notation, are given, in GPA, by $C_{11} = 59.75$, $C_{22} = 59.74$, $C_{33} = 61.7$, $C_{12} = 23.24$, $C_{13} = 21.7$, $C_{44} = 16.39$ and $C_{66} = 18.25$. In Mg alloys, basal slip $\{0001\}\ \langle 2\bar{1}\bar{1}0\rangle$, prism slip $\{10\bar{1}0\}\ \langle \bar{1}2\bar{1}0\rangle$, second-order pyramidal slip $\{2\bar{1}\bar{1}2\}\ \langle 2\bar{1}\bar{1}3\rangle$ and tensile twinning $\{10\bar{1}2\}\ \langle \bar{1}011\rangle$ are potential active systems. As shown previously, the present work uses an extended Voce law to describe hardening evolution [4]. The hardening parameters used in the present simulations are the same as those used in work by Clausen et al. [4] under the FIF assumption, which consists of assigning a finite volume fraction to the twins at nucleation. All values and parameters are presented in Table 2.1. In order to quantify the impact of the double inclusion topology, we did not re-fit hardening model parameters, and we removed the "backstress" correction added by Clausen et al. [4] at twin inception. Moreover, all latent hardening constants were assumed to be equal to 1.

Table 2.1 – CRSS and hardening parameters used in Voce hardening rule

Initial twin fraction	Deformation system	τ_0 (MPa)	τ_1 (MPa)	θ_0 (MPa)	θ_1 (MPa)
0.03	Basal	12	20	240	0
	Prism	60	20	240	0
	Pyramidal	100	117	2000	0
	Tensile twin	60	0	0	0

Latent effects induced by twinning

The DI-EPSC scheme introduces a more realistic topology for twinning where twins are directly embedded in parent domains. Note that latent is meant in a sense of capturing the effect of plasticity in the parent phase on hardening and hardening rates in the twin phase. All simulations presented in this paragraph consider the case of the extruded alloy. Only the unrelaxed

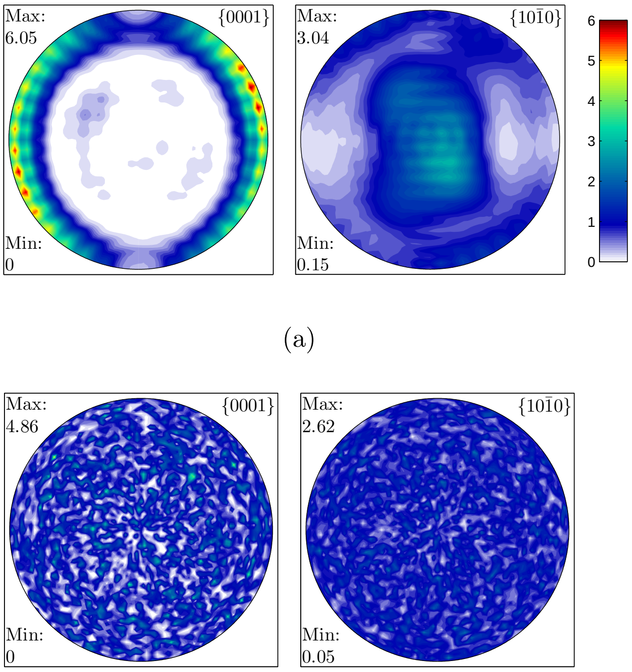

(a)

(b)

FIGURE 2.9 – Initial textures of (a) the extruded alloy (with the extrusion axis at the center of the pole figures) and (b) the randomly textured material

initial twin stress state estimate is used in this section. Figure 2.10a shows the macroscopic response of the material, loaded along its extrusion axis, obtained from mechanical loading, EPSC and DI-EPSC. The experimental stress-strain curve is characteristic of twinning-dominated compression with a plateau in the early stages of the deformation and then a progressive stress increase as twins grow and slip occurs in the twins [125]. As parameters are not fitted to the set of data, differences between experimental measures and macroscopic predictions are to be expected. In spite of the different topologies, the macroscopic stress-strain curves predicted by the DI-EPSC scheme and the EPSC scheme are nearly identical. However, Figure 2.10b, which describes the evolution of the total twin volume fraction in the polycrystal, reveals that the total twin volume fraction predicted by DI-EPSC is lower than the total twin volume fraction predicted by EPSC. Predicting similar overall mechanical response but different twin volume fractions necessarily implies significant differences in the calculation of internal stresses and the selection of active slip systems within the twin and parent domains.

Figure 2.11 presents slip and twinning system activities in both the parent and twin domains as predicted with the current and extended EPSC schemes. In both cases twinning occurs in the early stages of compression : at 1% strain, 80 % of the total number of twins have been created. Before twins appear, basal slip is the prevalent active slip system in the parent phase due to its low CRSS. Once twinning is activated, the activity of basal slip within the parent phase decreases strongly while prismatic slip followed by pyramidal slip are activated, consistent with predictions of Capolungo et al. [126]. Regardless of the topology used (i.e. EPSC vs DI-EPSC), similar responses in the parent phases are to be expected. Plasticity in the twin and twin domains

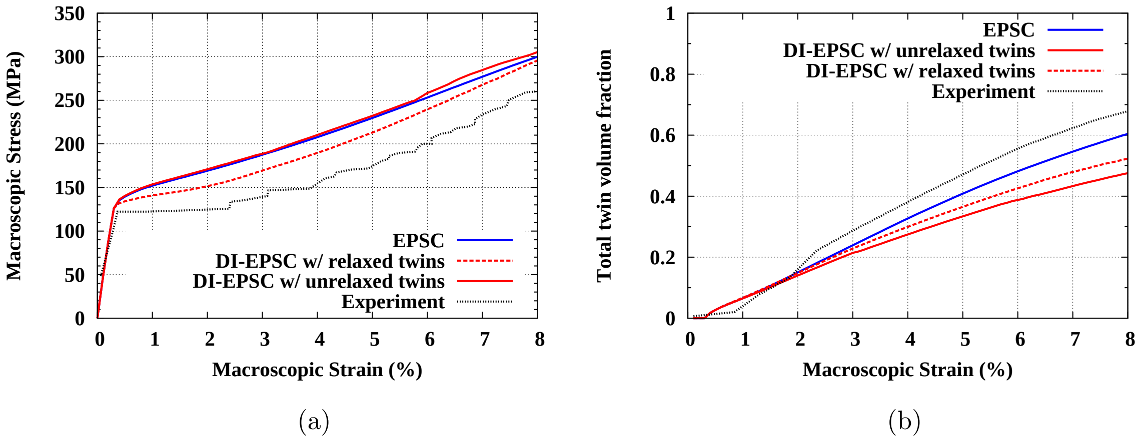

(a) (b)

FIGURE 2.10 – (a) comparison of macroscopic stress-strain curves from EPSC and DI-EPSC with experimental diffraction data and (b) evolution of the total twin volume fraction in the polycrystal.

morphology do not significantly affect the average stress state within the parent phase. Within the twin domains, though, the two approaches yield drastically different predictions of the slip system activity. At strains lower than 1%, basal slip is the predominant deformation mode in twins. This is to be expected as the twin orientation combined with the imposed stress state favors basal slip activation. However, as twins grow, the current model predicts that basal slip activity drops in favor of pyramidal slip. In spite of a CRSS nearly two times greater than that of prismatic slip CRSS and eight times that of basal slip CRSS, pyramidal slip is extensively activated within the parent and twin phases.

Adapting the micromechanical scheme to twinning topology directly enforces the twin/parent interaction and reveals another latent hardening effect that is generally described by single crystal plasticity models. Indeed, in comparing resolved shear stresses (RSS) projected on the twinning plane along twinning direction within twin and parent phases of an arbitrarily chosen twinned grain, one observes that the new DI-EPSC scheme predicts both a higher strain hardening rate and a higher RSS in the twin than the EPSC scheme (Figure 2.12). With the choice of hardening parameters associated with tensile twinning, hardening cannot occur on the twin system.

Although not shown here, the effect of grain morphology on slip system activities was studied. From the pioneering work of Tanaka and Mori [112], it is known that for homothetic inclusions, grain and twin shape have a negligible contribution. This can be seen in Eqs. 2.92-2.93 in which the Eshelby type tensors introduce the relative shape effects. When considering different parent and twin morphologies for twins and parents, via the Eshelby-type tensors, it is found that twin shape does not affect the stress state within the parent domains. However, it is found that ellipsoidal twin shapes tend to marginally increase the stress level within the twin domains but do not affect the selected slip systems. At the onset of twinning, twin volume fractions are too small for twin morphologies to influence internal stress and strain states. In the early stages of twin growth, volume fraction effects have a significant effect on local stress levels.

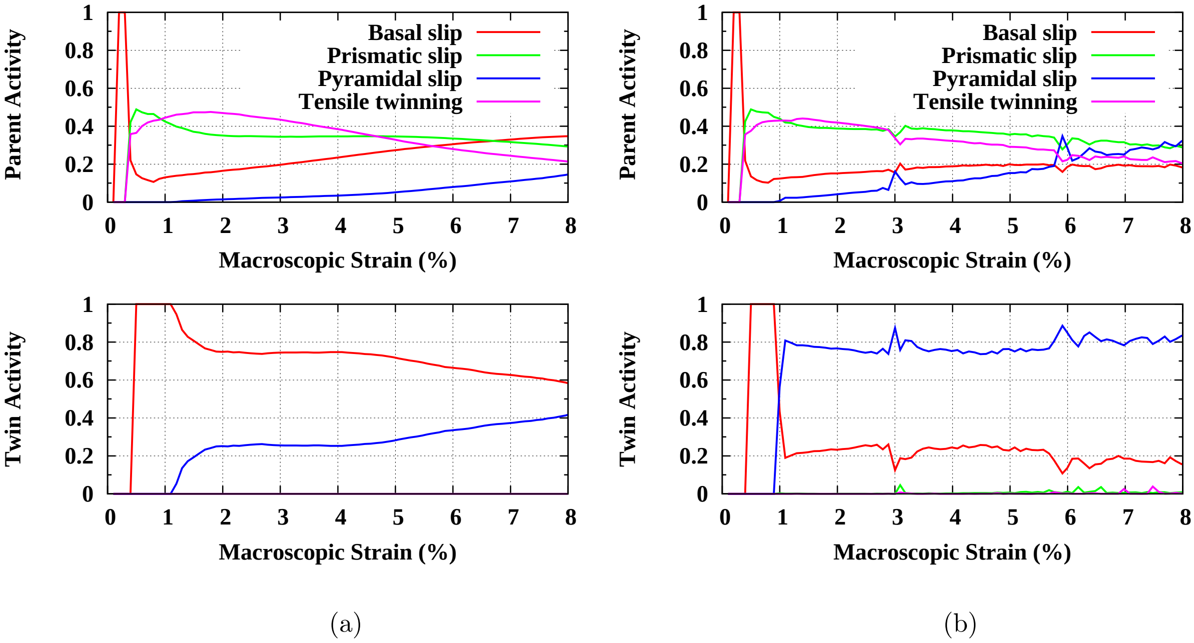

(a) (b)

FIGURE 2.11 – Averaged system activities within the parent and twin phases from (a) EPSC and (b) DI-EPSC

Interestingly, the direct coupling between parent and twin phases leads to far more scattered accumulated plastic strain distributions. Figure 2.13 shows both the total shear strain in each single twin and parent domain and the averaged total shear strain in the twin and parent domains as obtained from the DI-EPSC and the EPSC schemes. It appears that the standard deviation of the distribution of total accumulated shear strain in twin phases obtained from the new coupled approach is four times higher than that obtained from the previous uncoupled approach. This phenomenon is more visible in Figure 2.14, where total accumulated shear strain distributions derived from the DI-EPSC scheme are less evenly distributed compared to those predicted by the EPSC scheme. Bin size was optimized using the following formula : $w = 3.49Xn^{-1/3}$, where w denotes the bin width, X the standard deviation associated to total shear strains and n the number of twins. Note here that points corresponding to grains for which numerical stability cannot be guaranteed shall be disregarded. Nonetheless the predictions seem more representative, as they directly result from the concentration relations (Eqs. 2.93-2.95). However, shown in black symbols, the averaged total shear strains in twin domains seem to be insensitive to the new coupling, while the averaged total shear strains in parent domains is slightly decreased. That is precisely why, in spite of a higher strain hardening in twins and a smaller twinned volume, the DI-EPSC scheme predicts a macroscopic stress-strain curve nearly identical to that obtained from the EPSC scheme without the backtress correction.

Influence of initial texture

To test the coupling between the parent and twin phases in a more general way, i.e. with a broader spectrum of active slip and twinning systems, the case of an initially randomly textured AZ31 alloy is investigated. In this paragraph, we only consider simulations regarding the unrelaxed

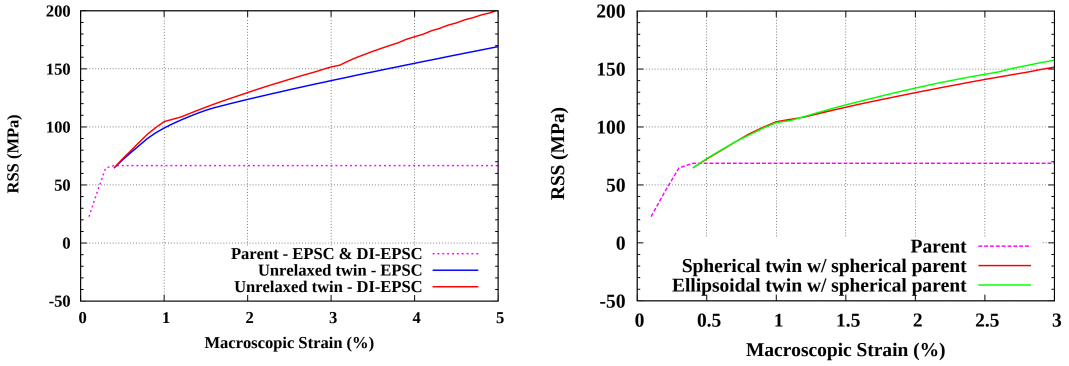

(a) (b)

FIGURE 2.12 – RSS projected on the twinning plane in the twinning direction within the parent and twin phases. (a) compares the DI-EPSC and EPSC results ; (b) compares internal stresses for different geometrical configurations for initially unrelaxed twins. Axis length ratios for ellipsoidal shapes are $a_1/a_2 = 1$ and $a_1/a_3 = 3$.

initial twin stress state estimate. Figure 2.14 shows that total shear strain distributions in twin phases derived from the DI-EPSC scheme are centered around a few peaks while they are more evenly distributed when derived from the EPSC scheme. The heavy centre of the DI-EPSC distributions is interpreted as resulting from the orientation of parent domains, which was initially favorable to an easy activation of twinning and secondary slip occurrence. As deformation occurs and plasticity develops, parent grain configurations change, and therefore plastic strain accommodation in the twin domains is affected as a direct result of the new concentration laws. Although not shown here, the diversity of grain orientations limits the number of parent grains favorably oriented for twinning and, hence, lowers the total twin volume fraction in the case of an initially non-textured material. In addition, Figure 2.13 reveals that initial texture has a marginal effect on the averaged total accumulated plastic strain in twin and parent domains because secondary slip and plastic strain accommodation are controlled by criteria which are independent of the initial texture. However, Figure 2.14 shows that plastic strain accommodation in both the parent and twin phases depends on the parent-twin interaction.

Moreover, even with an initial random texture, pyramidal slip remains the predominant active slip system in twins, but it is significantly less present compared to the first case with the extruded alloy (Figure 2.15).

Influence of initial twin stress state

Section 2.3.1.7 introduces the modeling challenges induced by twin inception and presents the two approximations that are used throughout the paper. The present section focuses now on analyzing and quantifying the influence of the initial twin stress state on the mechanical response of an extruded AZ31 alloy.

The evolution of RSS projected on the twinning plane along the twinning direction in the cases of initially relaxed and unrelaxed twins is shown in Figure 2.16. It reveals that, with initially relaxed twins, the strain hardening rate in the twin predicted by the DI-EPSC scheme is higher in

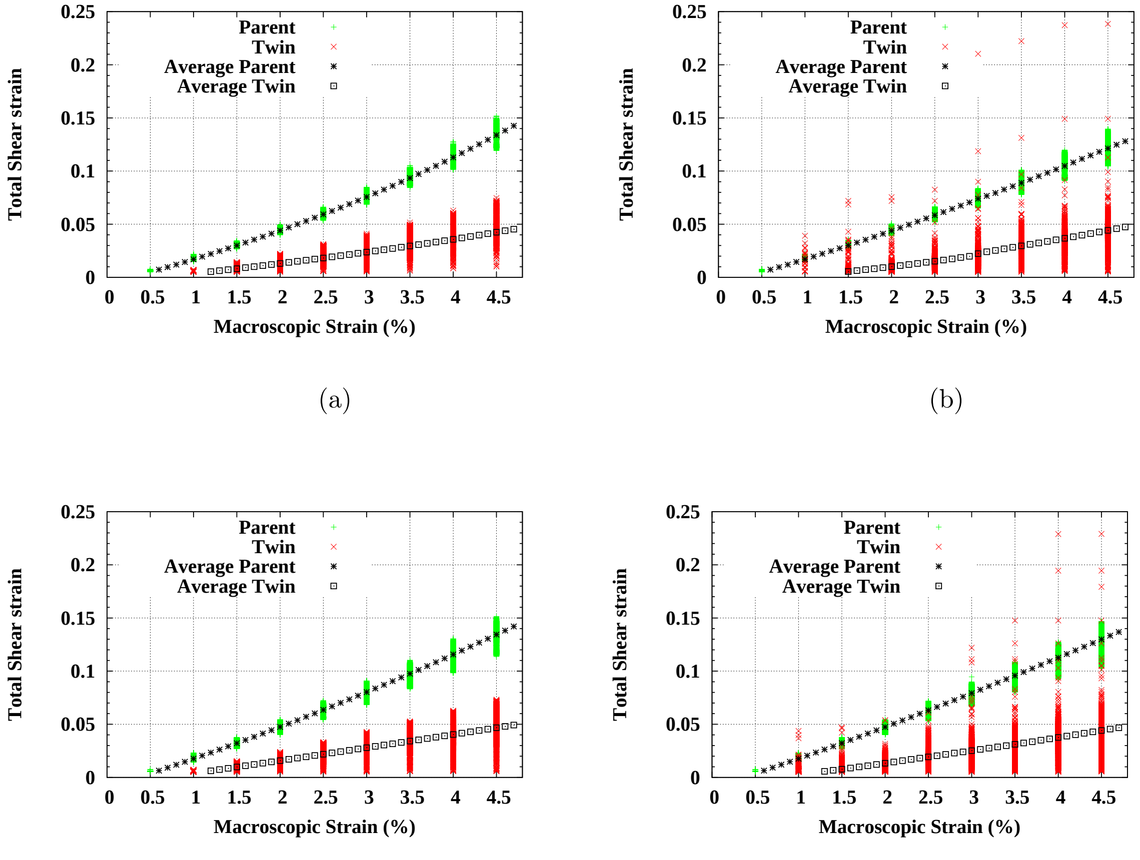

(a)

(b)

(c)

(d)

FIGURE 2.13 – Spread of total shear strains within the parent and twin phases from (a) EPSC and (b) DI-EPSC for an extruded alloy (c) EPSC and (d) DI-EPSC for an initially randomly textured alloy. Each cross represents the total shear strain for one single grain.

the first 3% of deformation and then stabilizes at a value close to the one observed with unrelaxed twins. However, the new coupled approach predicts both a higher strain hardening rate and a higher strain hardening in the twins regardless of the initial stress state of the twins. In addition, comparison with the predictions obtained from the EPSC model with initially relaxed and unrelaxed twins shows that the strain hardening rate in the twin domains is not solely controlled by the twin-parent interaction in the case of the DI-EPSC model or by the twin-HEM interaction in the case of the EPSC model. Strain hardening rate and, hence, hardening are strongly dependent on the considered initial twin stress state. In parallel, the total twin volume fraction tends to increase with relaxed twins (Figure 2.10b). As expected and shown in Figures 2.10a and 2.16, initially relaxed twins lower both global and local stress levels that become closer to experimental ones. In addition, the averaged pyramidal slip activity in each twin is significantly lowered as compared to the stress equilibrated case (Figure 2.17).

Note that imposing a null Cauchy stress tensor in the twin domain at the inception of twin is a lower bound case. Another way to account for the stress accommodation induced by twinning

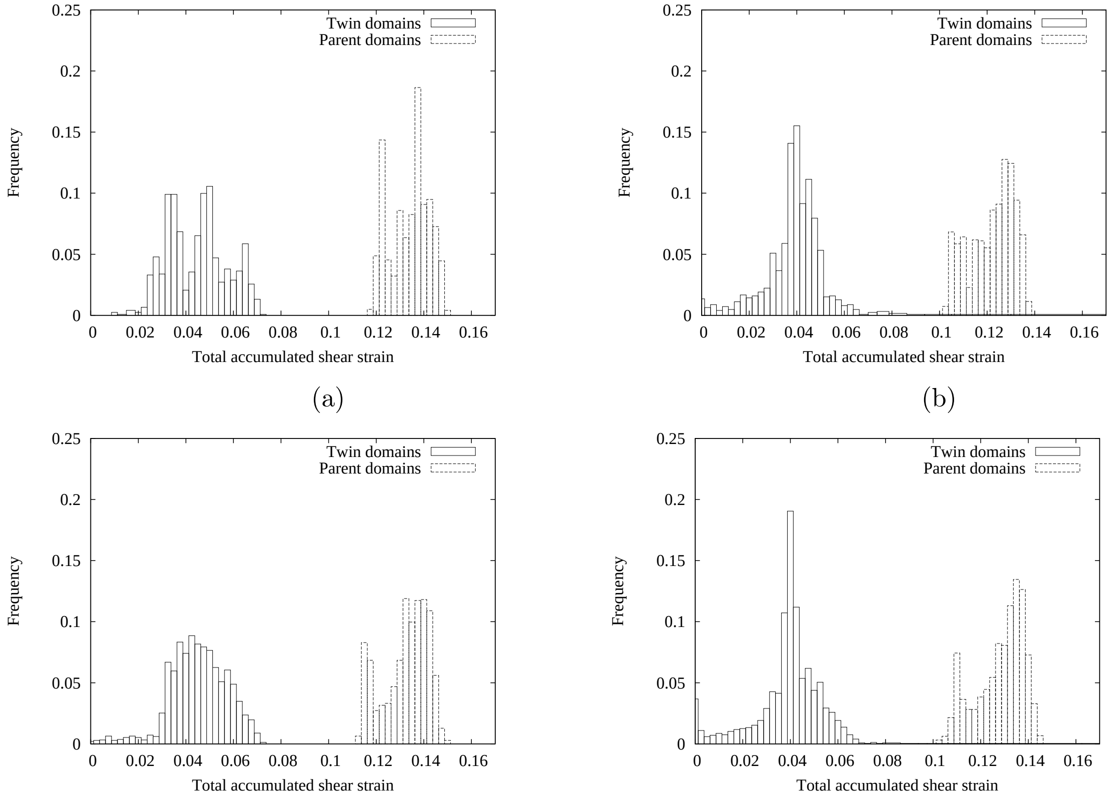

(a) (b)

(c) (d)

FIGURE 2.14 – Total shear strain distributions in parent and twin domains at 4.5% deformation obtained from (a) EPSC and (b) DI-EPSC in the case of the extruded AZ31 alloy and from (c) EPSC and (d) DI-EPSC in the case of the initially randomly textured AZ31 alloy.

consists of using an eigenstrain, representative of that due to the twinning shear, within the twin domain at the onset of twinning. However, considering both twinning as pseudo-slip in the parent phase and twinning shear as an eigenstrain within the twinning phase appears as mechanically redundant. Therefore an alternate approach would impose the eigenstrain within the twin domain and considers only slip as a deformation mechanism in the parent domain.

2.4 Conclusion

A new double inclusion micromechanical approach, generalizing the original Tanaka-Mori scheme, is introduced to study the evolution of internal stresses in both parent and twins during twin growth in h.c.p materials. A first elasto-static scheme in heterogeneous elastic media with plastic incompatibilities was derived. The model was shown to reduce to the Nemat-Nasser and Hori scheme as well as to the elementary inclusion problem of Eshelby in some peculiar situations (e.g. homogeneous elasticity) and was first applied to the case of pure Mg to reproduce the average internal resolved shear stresses in the parent and the twinning phases. While the first study is limited to anisotropic elasticity with eigenstrains representing the twinning shears, it is suggested that the magnitude of these backstresses is sufficient to induce plastic deformation within twin domains. Moreover, a detailed analysis of the model shows that the predominant effect

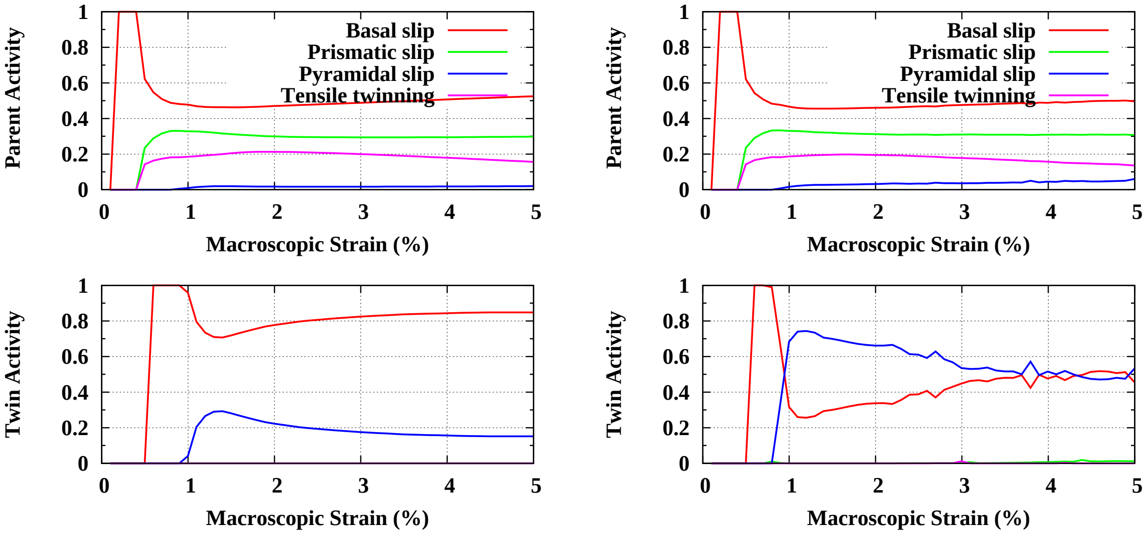

(a) (b)

FIGURE 2.15 – Averaged system activities within the parent and twin phases from (a) EPSC and (b) DI-EPSC for an initially randomly textured material

on the magnitude and the direction of backstresses is due to heterogeneous elasticity because of large induced misorientations between the parent and the twin domains. It is also found here that the stress state within twin domains is largely affected by the shape of the parent phase. Clearly, all results shown here are limited to static configurations and neglect internal variable evolutions. Nonetheless, it is suggested that application of the generalized Tanaka Mori scheme to mean-field self-consistent methods shall yield more accurate predictions of the internal state within twin domains for real polycrystalline hexagonal metals like magnesium and associated alloys.

Then, a second study investigated evolution of internal stresses and strains and plasticity within twin and parent domains of Mg alloys via a new double inclusion-based elasto-plastic self-consistent scheme (DI-EPSC) that used the original Tanaka-Mori result to derive new concentration relations that include average strains in twins and twinned grains (double inclusions). Then, twinned and non-twinned grains are embedded in an HEM with effective behavior determined in an implicit nonlinear iterative self-consistent procedure (called "DI-EPSC" model). Contrary to the existing EPSC scheme which only considers single ellipsoidal inclusions, new localization relations account for a direct coupling between parent and twin phases. Using the same hardening parameters as in [4], comparison between the EPSC, the DI-EPSC and experimental data leads to three main results with respect to twinning and associated plasticity mechanisms. First, it appears that, by introducing a new topology for twinning, latent effects induced by twinning in the parent phases are capable of predicting the influence of plasticity on hardening and hardening rates in the twin phases. Second, because twins are now directly embedded in the parent phases, new concentration relations lead to more scattered shear strain distributions in the twin phases. Twin stress states are strongly controlled by the interaction with their associated parent domains. Third, the study clearly shows the importance of appropriately considering the initial twin stress state at twin inception.

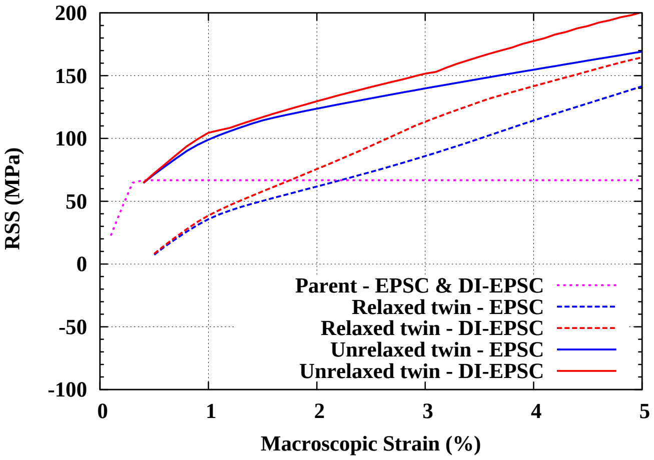

Figure 2.16 – RSS projected on the twinning plane in the twinning direction within the parent and twin phases and obtained from the EPSC and DI-EPSC models for both initially relaxed and unrelaxed twins.

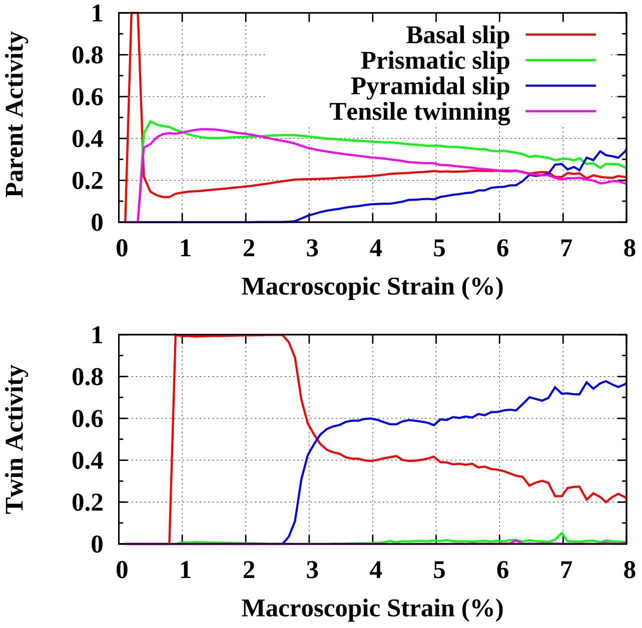

Figure 2.17 – Averaged system activities within the parent and twin phases from DI-EPSC when twins are assumed to be initially totally relaxed

Chapitre 3

Electron backscattered diffraction technique and automated twinning statistics extraction

Sommaire

The Electron Backscatter Diffraction (EBSD) technique is based on the collection of backscattered electrons and the indexing of Kikuchi diffraction patterns. EBSD scans provide a profusion of information regarding the texture, presence of grain boundaries, grain morphologies, nature and crystallographic orientation of the different phases present in the material, etc. The EBSD technique is then particularly interesting because it enables us to extract the possibility of extracting statistical information about the microstructure and automatically compute metrics that can be used to guide for models for example.

The present chapter introduces a new automated data collection numerical tool [127] that uses EBSD scans to generate statistical connections between twin features, microstructure and loading path. The first, second and third parts of this chapter describe the SEM microscopes, the EBSD technique and the basic concepts of electron diffraction and EBSD pattern analysis, respectively. The final section describes the newly developed graph theory-based automated twin recognition technique for EBSD analysis.

Figure 3.1 – Philips XL 30 F Orientation Imaging Microscopy System at Los Alamos National Laboratory, MST-6 (LANL web site).

3.1 Brief description of Scanning Electron Microscopes

In a scanning electron microscope, a beam of high energy electrons, emitted by either a thermoelectronic gun or a field emission gun (FEG), hits the sample. A system of electromagnetic lenses, also referred to as condensers, and coils enable the user to focus the beam and scan the whole surface of the sample. All incident electrons have a quasi parallel trajectory. Although it depends on the voltage chosen (between 0.1 kV and 30 kV), the diameter of the incident beam does not exceed a few nanometers.

When incident electrons penetrate into the sample, they interact both elastically (i.e. no energy loss) and inelastically with atoms and electrons present at or near the surface. These interactions result in the emission of secondary electrons (SE) (i.e., electrons produced by inelastic interactions of high energy electrons with valence electrons, causing the ejection of the electrons from their atomic orbitals), back-scattered electrons (BSE) (i.e. electrons produced by elastic interaction of high energy beam electrons with atom nuclei), characteristic X-rays and photons. Elastic scattering consists of the deviation of the electron trajectory by the nucleus of an atom without loss of energy. Because of the mass difference between the electron and the nucleus, energy transfers are negligible ; the energy loss induced by elastic scattering is smaller than 1 eV. But the deviation angle is important. As a result, backscattered electrons are assumed to have the same energy as beam electrons. It has also been shown that the number of backscattered electrons increases with the atomic number, Z. Depending on the input voltage and Z number, the penetration depth will vary from a few nanometers to 20-30 nanometers.

In contrast, inelastic scattering induces a progressive loss of energy due to transfers between high energy electrons and valence electrons belonging to the different atomic orbitals of specimen atoms. These high energy electrons can either be incident beam electrons, also called primary electrons, or back-scattered electrons. The excitation and the ionization of the sample atoms result

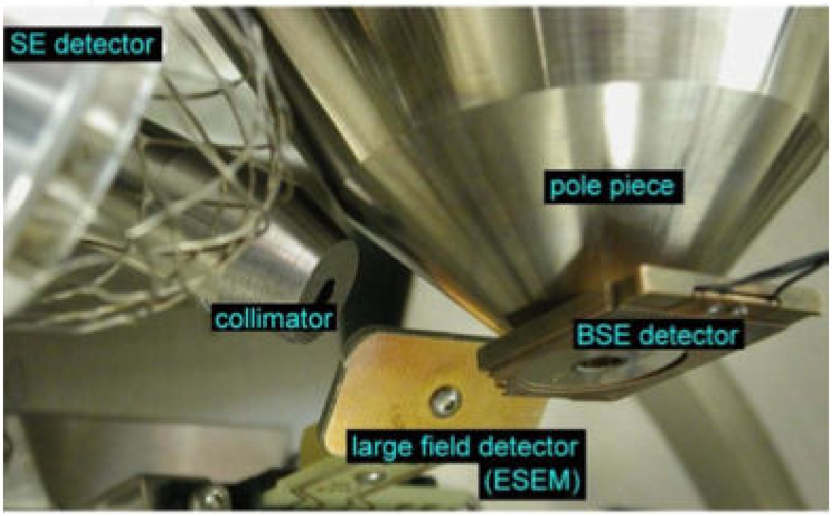

FIGURE 3.2 – Chamber of a Scanning Electron Microscope.

in the emission of secondary electrons with low deviation angle and low energy (0-50 eV), X-rays, Auger electrons and photons. Secondary electrons can also be produced after back-scattered electrons strike pole pieces or other solid objects located in the vicinity of the sample. They are emitted isotropically from the superficial layers of the specimen, e.g. the depth of these layers can either be a few nanometers in the case of metals or 20-30 nm in the case of non-conducting materials. The secondary emission yield, defined as the ratio of the secondary electrons to the number of primary electrons, increases when the energy, i.e. the voltage, of the beam electrons decreases. Lower primary energies induce slower incident electrons. Except for light atoms ($Z<20$), the second emission yield does not vary with atom mass. However, the secondary emission yield has to be corrected, since a signifiant part of the detected secondary electrons consists of backscattered electrons. In addition, the ionization of atomic orbitals close to the nucleus triggers the emission of characteristic X-rays and Auger electrons, as shown in Figure 3.3. Mechanisms involved in the emission of X-rays and Auger electrons that consist in electronic transitions between the ionized atomic orbital and external orbitals are aimed at leading the atom toward its state of equilibrium. Energy levels associated with the different types of electrons mentioned in this paragraph are graphically represented in Figure 3.4. Therefore, any standard SEM includes a secondary electron detector. However, it is common to equip scanning electron microscopes with back-scattered electron detectors and X-ray spectrometers, as shown in Figure 3.2.

Two types of electron guns exist, i.e. thermal electron guns and field emission guns. The first ones use either a heated tungsten wire or a lanthanum hexaboride crystal. Field emission guns can either be of the cold-cathode type using tungsten single crystal emitters or the thermally assisted Schottky type (Figure 3.1) using emitters made of zirconium oxide. While electrons are emitted from a tungsten thermal guns with voltages between 10 kV and 30 kV, field emission guns are capable of producing incident electron beams whose voltages are between about 0.1 kV and 30 kV. The choice of the electron gun type has to be based on the nature of the materials studied.

The resolution of a microscope can be defined as its ability to distinguish and separate very close "objects". Its resolution is altered by monochromatic and chromatic aberrations resulting from the geometry and the variation of the refractive index of lenses, respectively. In addition to aberrations, the resolution of an optical microscope is limited by the diffraction of light. Therefore,

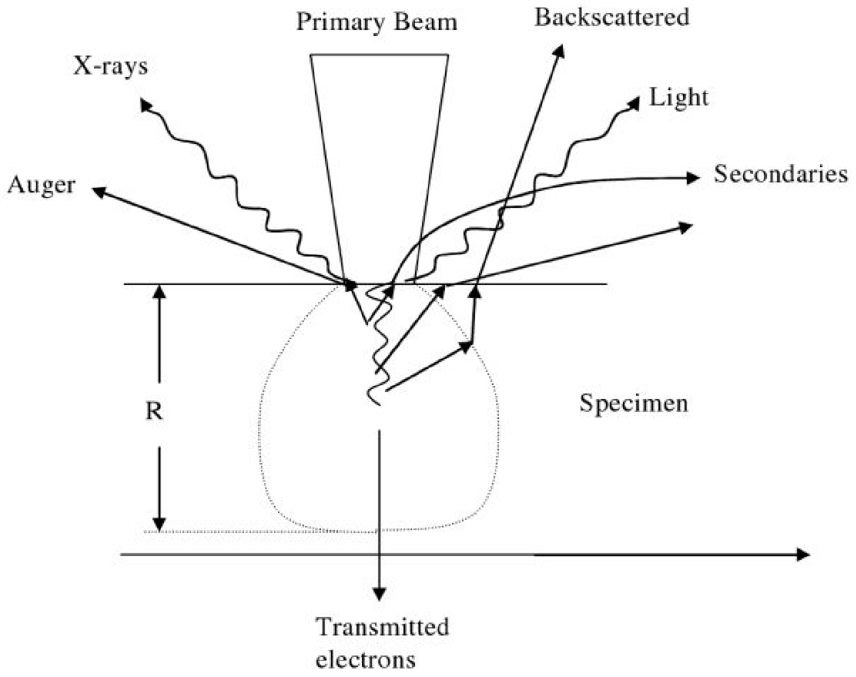

FIGURE 3.3 – Schematic representation of signals resulting from the interaction between primary electrons and atoms at or near the sample surface ; R denotes the depth of the interaction volume [5].

the image of a point through a lens is not another point but a diffracted disk, called Airy disk. The consequence of this phenomenon is that disks corresponding to the images of two distinct points may overlap. Abbe's theory states that the resolution limit of a microscope is proportional to the incident wavelength and inversely proportional to the refractive index of the medium. Consequently, decreasing the wavelength allows the resolution limit to improve and, hence, allows users to observe finer details. Using X-rays would then be ideal but they cannot be focused. However, it is possible to generate electron beams whose wavelengths are of the same order of magnitude as X-rays. In both transmission and scanning electron microscopes, electrons are focused by several electromagnetic lenses.

3.2 Historical perspectives of the Electron Backscatter Diffraction Technique

The origins of the EBSD technique date back to 1928 when Shoji Nishikawa and Seishi Kikuchi pointed a beam of 50 keV electrons on a cleavage face of calcite, inclined at 6° to the vertical [128, 129]. Backscattered electrons were collected on photographic plates positioned perpendicular to the primary beam at 6.4 cm behind and in front of the sample. Recorded patterns displayed black and white lines, as revealed by Figure 3.5. The existence of line pairs is due to multiple scattering and selective reflection. Figure 3.5 shows iron Kikuchi patterns corresponding to experiments performed by Boersch et al. in 1937 [6]. Boersch et al. [6] studied both transmission and backscatter diffraction patterns obtained from a wide variety of polished, etched and cleaved crystals such as NaCl, PbS, mica, quartz, etc. Both Boersch et al. [6] and Alam et al. [130] used

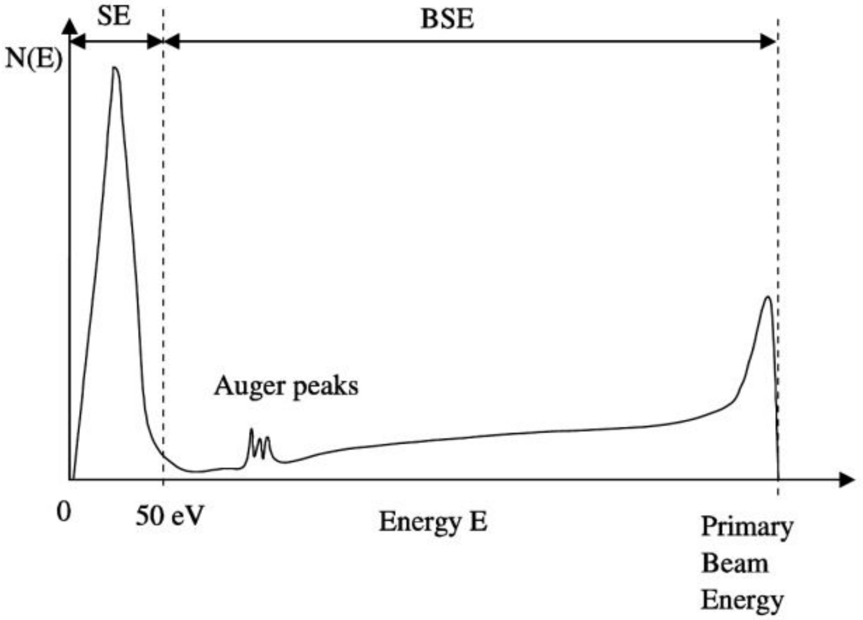

FIGURE 3.4 – Schematic representation of energy levels of electrons resulting from the interaction between primary electrons and atoms at or near the sample surface [5].

purpose-built vacuum chambers.

The first SEM commercial version, Stereoscan 1, was released by Cambridge Instrument Company in 1965. Its development started in 1948 and was initiated by Sir Oatley. About six months later, Jeol commercialized its first SEM. The commercial releases of the first SEM incredibly boosted research on both diffraction and material characterization resulting in three major discoveries in the decade following their introduction on the market : selected area channeling (SACP) by Joy et al. [131] at Oxford University, Kossel diffraction by Biggin and Dingley[132] at Bristol University and electron backscatter patterns (EBSP) by Venables and Harland [7] at the University of Sussex. Note that EBS patterns are nothing else than Kikuchi patterns. Venables and Harland [7] obtained them with a TV camera and phosphor screens. Moreover, Venables [133] found an easy way to locate the pattern center, defined as the shortest distance between the impact area where the electron beam hits the sample and the phosphore screen. To do so, Venables placed three spheres on the sample surface, whose projections appear elliptical on the pattern (Figure 3.6). The intersection point of the three major axes corresponds to the pattern center. In 1984, Dingley [134] developed and implemented an indexing algorithm capable of locating the pattern center numerically. In 1987, the first indexing software, based on Dingley's code, was released by Link Analytical, now Oxford Instruments. Dingley's model is still used now by current EBSD systems.

Five years later, Krieger-Lassen, Conradsen and Juul-Jensen [135] used the Hough transform, originally developed by Hough [136] in 1962 to track high energy particles, to automatically detect and identify Kikuchi bands. The use of the Hough transform allows the system to transform parallel bands into collections of points.

In 1993, Brent Adams [137], from Yale University, introduced the term "Orientation Imaging Microscopy" to describe the procedure that generates an orientation map. The technique consists

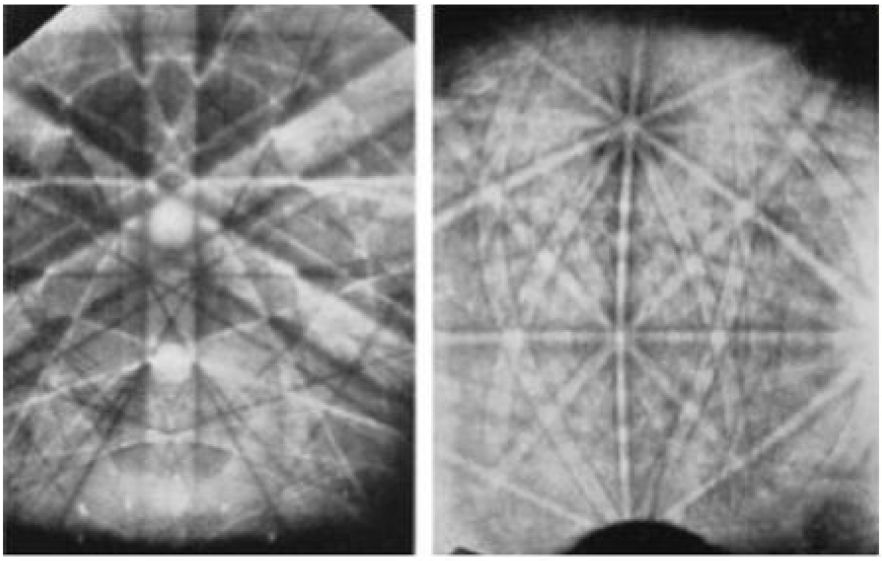

Figure 3.5 – Boersch (1937) Iron Kikuchi patterns [6, 5]

in representing pixels of similar orientation with an unique color. Adams and Dingley founded TexSEM Laboratory, alias TSL, to release their EBSD analysis system and chose Thermo Noran to distribute it. In 1999, EDAX purchased TSL, depriving Thermo Noran of their EBSD analysis system. Thermo Noran turned to Robert Schwarzer [138], from TU Clausthal, who developed its own system for orientation and texture measurements, and Joe Michael and Richard Goehner [139], from Sandia National Laboratory. Joe Michael and Richard Goehner were amongst the first to use EBSD for phase identification. There also existed another software, very popular amongst geologists, released by HKL Technologies and based on the work of Schmidt [140]. This software was widely used by scientists willing to study minerals because it included very efficient low-symmetry indexing algorithms. In April 2005, Oxford Instruments purchased HKL Technologies. Currently, both EDAX and Oxford Instruments continue to develop and sell their own EBSD analysis software.

3.3 Basic concepts of electron diffraction and diffraction pattern analysis

Regarding the technique itself, at each measurement point, the electron beam hits the sample surface, tilted about 70° with respect to the horizontal line and preliminarily polished. Primary accelerated electrons are either transmitted or reflected by the specimen atoms. The EBSD detector (Figures 3.2 and 3.8) collects low loss energy backscattered electrons.

Modern EBSD detectors are usually made of a phosphor screen, a compact lens to channel the electrons and low and high resolution CCD camera chips for fast and slow measurements, respectively. The impact of electrons with the phosphor screen produces light that is converted into an electric signal by the CCD camera chips. The different Kikuchi bands and the pattern center are then identified by using an optimized Hough transform and Dingley's method, respectively. From the pattern center and the Kikuchi bands, EBSP softwares are capable of identifying the crystallographic structure and the orientation of the region struck by the beam. This step is called

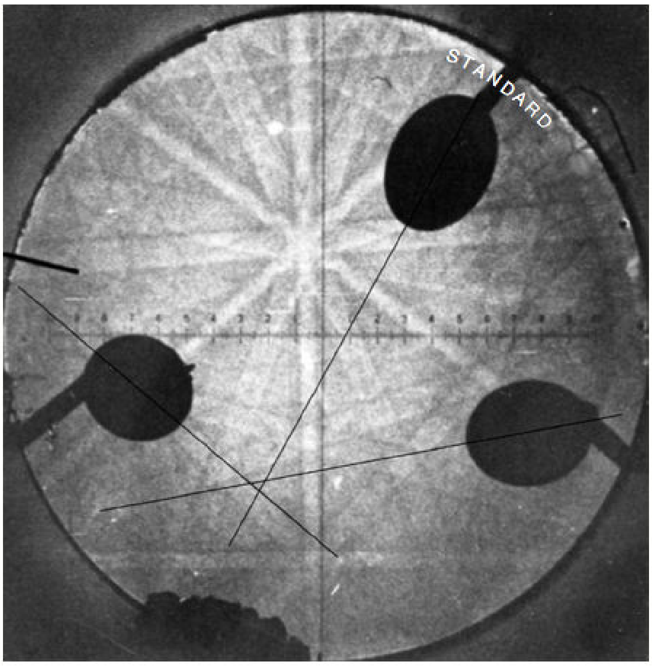

FIGURE 3.6 – Image of a Kikuchi pattern obtained by using a phosphor screen and a TV camera that illustrates the method developed by Venables [7] to locate the pattern center. Elliptical black shapes correspond to the projected shadows of the three spheres placed at the surface of the sample [5].

indexing and will be repeated for each Kikuchi pattern recorded by the CCD chips, i.e. for each measurement point. Note that samples are usually scanned following a square or hexagonal grid.

Electron diffraction techniques rely on the principle of wave-particle duality asserted by Louis de Broglie in 1925. According to this principle, a beam of accelerated electrons is a wave whose wavelength is proportional to the particle velocity. Wavelength and velocity are related by the following expression

$$\lambda = \frac{h}{p} = \frac{h}{\sqrt{2meV}} \tag{3.1}$$

where h denotes the Planck's constant, i.e. $6,626.10^{-34}$ J.s, p, the momentum of electrons, V, the potential used to accelerate the beam, m, the mass of an electron, i.e. $9.10938215.10^{-31}$ kg, and e, the elementary negative electric charge of an electron, i.e. $1.6021765.10^{-19}$ coulombs. This equation is the fundamental relationship of wave mechanics. In 1927, Davisson and Germer [141] verified de Broglie's relationship by observing diffracted electrons after a beam of 54 eV struck a single crystal of nickel.

The Bragg's condition for constructive interference is written as

$$2.d_{hkl}.sin\theta = n.\lambda \tag{3.2}$$

with d, the distance between two successive lattice planes whose family plane Miller indices are represented by (h, k,l) and n, an integer denoting the order of reflection. As shown by Figure

FIGURE 3.7 – Example of EBSD orientation map showing the undeformed microstructure of a high purity clock-rolled Zr specimen. Colors designate crystal orientations as indicated by the unit triangle in the bottom right-hand corner. The software used to generate this map is OIM Analysis [8].

3.9, the incident electron beam is diffracted at an angle 2θ. Thus θ is also the angle between the incident beam and the lattice planes.

While incident primary electrons have a narrow range of energies and directions, inelastic scattering undergone by backscattered electrons broadens the spectrum of energies. Momentum changes caused by both elastic and inelastic scattering cause electrons satisfying the Bragg's condition to scatter in all directions. Therefore, for a given plane {hkl}, electrons diffract in such a way that they form two cones located on each side of the plane. These cones are named Kossel cones, and they are shown by Figure 3.11. The projection of the two cones and the {hkl} plane on the viewing screen consists of three lines. However, since more electrons are scattered forward than sideways or backward, the projected line corresponding to the cone formed by the electrons that scattered forwards appears brighter than the one corresponding to the second cone. The "bright" and "dark" lines are referred to as the excess and deficit lines (Figure 3.10). The spacing of the pair of Kikuchi lines, i.e. the pair of lines formed by the excess and deficit lines, is the same as the spacing of the diffracted spots from the same plane. However, the position of Kikuchi lines is strongly dependent on the orientation of the specimen. Although not proved here, it can also be shown that Kikuchi lines associated with planes {hkl} and {-h-k-l} are parallel. Because each diffraction band represents a lattice plane, the intersections of these bands correspond to zone axes. If more than two diffraction bands intersect at a single spot, the latter is called a pole.

The width of the diffraction bands appearing on EBS patterns, denoted by w, is a function of both electron wavelength, λ, and the inter-planar spacing, d_{hkl}, and is then be expressed as

$$w = 2\sin^{-1}\frac{\lambda}{d_{hkl}} \tag{3.3}$$

As shown by Figure 3.12, the width can also be determined experimentally from two positions vectors, $\mathbf{r}$ and $\mathbf{r}'$, extending from the pattern center (PC) and intersecting the sides of the band

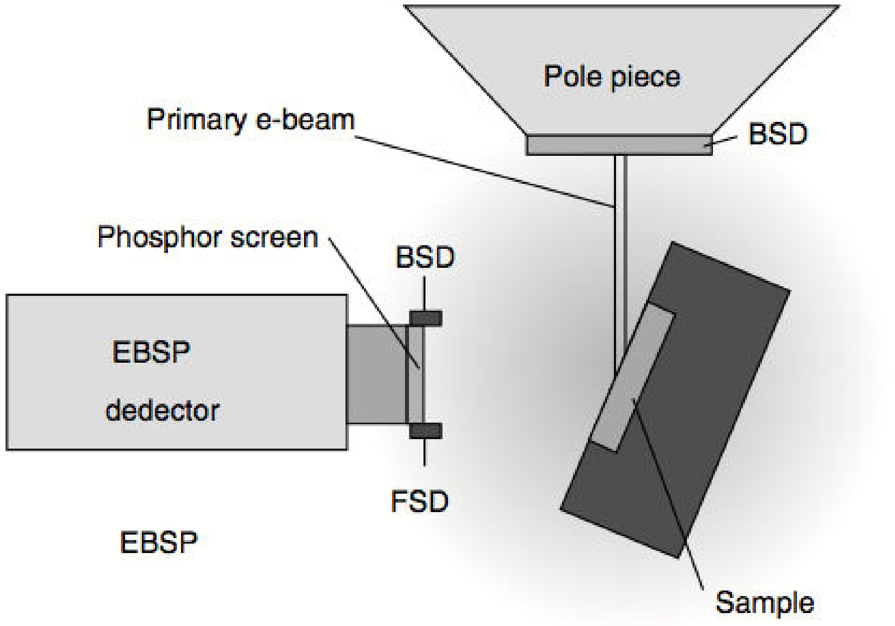

FIGURE 3.8 – Schematic representation of the chamber of a SEM equipped with an EBSD detector. The abbreviation BSD stands for backscattered detector [5].

at right angles :

$$w = tan^{-1}\frac{\mathbf{r}'}{z} - tan^{-1}\frac{\mathbf{r}}{z} \tag{3.4}$$

The angle between two bands can be computed directly from the phosphor screen (Figure 3.14). Denote by O the area struck by the electron beam and by points P and R the two points belonging to the two different diffraction bands. Vectors ($\mathbf{e_1^s}$,$\mathbf{e_2^s}$,$\mathbf{e_3^s}$) and ($\mathbf{e_1^c}$,$\mathbf{e_2^c}$,$\mathbf{e_3^c}$) are basis vectors associated with the sample and crystal frames, respectively. Consider unit plane normal

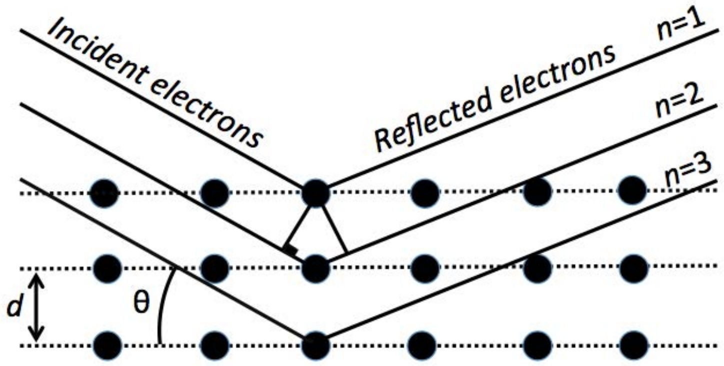

FIGURE 3.9 – Schematic representation of the Bragg's condition

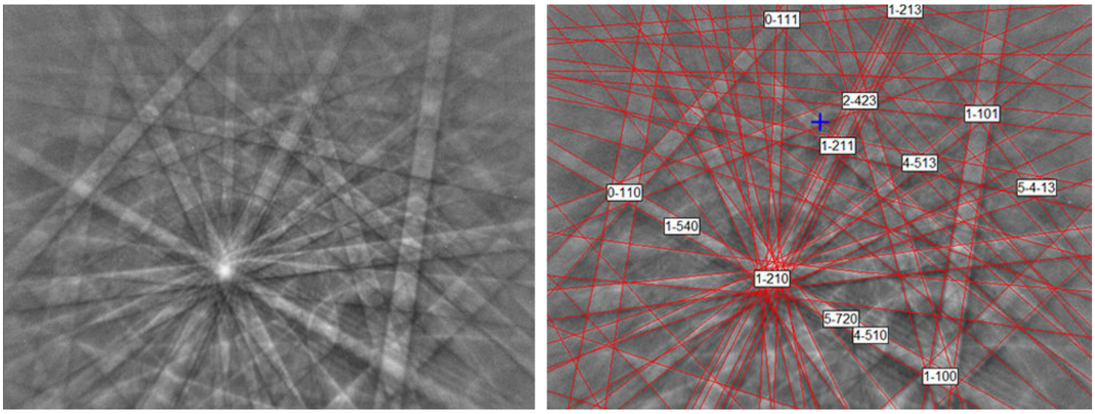

FIGURE 3.10 – Examples of Kikuchi patterns obtained from a h.c.p. material (Oxford Instrument)

vectors $\mathbf{n_1}$ and $\mathbf{n_2}$ expressed as follows in the specimen frame

$$\mathbf{n_1} = \frac{\vec{OP} \times \vec{OQ}}{\|\vec{OP} \times \vec{OQ}\|} \tag{3.5}$$

$$\mathbf{n_2} = \frac{\vec{OR} \times \vec{OS}}{\|\vec{OR} \times \vec{OS}\|} \tag{3.6}$$

As a result, the inter-planar angle, γ, is equal to the arccosine of the scalar product of the first and second unit plane normal vectors previously derived

$$\gamma = \cos^{-1}(\mathbf{n_1}.\mathbf{n_2}) \tag{3.7}$$

The main output of any EBSD analysis software is the texture file providing the lattice orientation associated with each pixel of the micrograph. A method for computing the lattice orientation was proposed by Wright et al. [10] and relies on the construction of a new set of vectors, ($\mathbf{e_1^t}$,$\mathbf{e_2^t}$,$\mathbf{e_3^t}$), expressed successively in the crystal and sample frames. Defined relative to the sample, their expressions are

$$\mathbf{e_1^{t,s}} = \mathbf{n_1} \tag{3.8}$$

$$\mathbf{e_2^{t,s}} = \frac{\mathbf{n_1} \times \mathbf{n_2}}{\|\mathbf{n_1} \times \mathbf{n_2}\|} \tag{3.9}$$

$$\mathbf{e_3^{t,s}} = \mathbf{e_1^{t,s}} \times \mathbf{e_2^{t,s}} \tag{3.10}$$

In the crystal frame, their expressions become

$$\mathbf{e_1^{t,c}} = \frac{(hkl)_1}{\|(hkl)_1\|} \tag{3.11}$$

$$\mathbf{e_2^{t,c}} = \frac{(hkl)_1 \times (hkl)_2}{\|(hkl)_1 \times (hkl)_2\|} \tag{3.12}$$

$$\mathbf{e_3^{t,c}} = \mathbf{e_1^{t,c}} \times \mathbf{e_2^{t,c}} \tag{3.13}$$

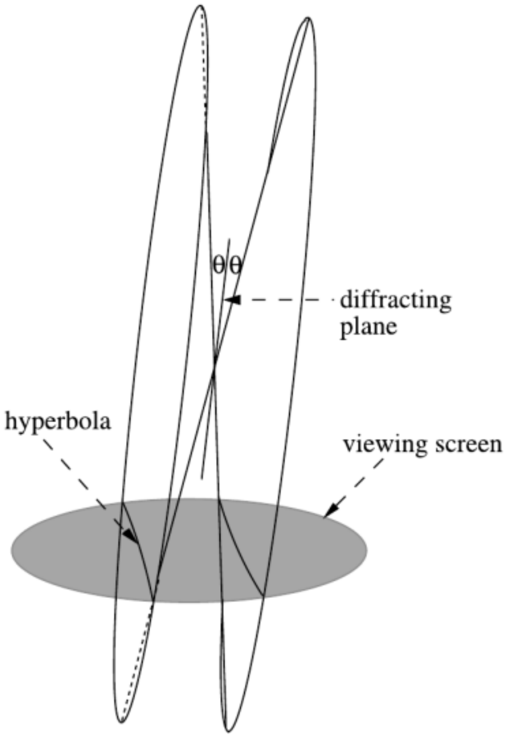

FIGURE 3.11 – Intersection of Kossel cones with the viewing screen [9]

where h_i, k_i and l_i with $i = \{1, 2\}$ are Miller indices of the plane i.

The direction cosines, g_{ij}, specify the lattice orientation and are written as

$$g_{ij} = g_{ij}^c g_{ij}^s \tag{3.14}$$

with,

$$g_{ij}^c = e_i^c . e_j^{t,c} \tag{3.15}$$

$$g_{ij}^s = e_i^{t,s} . e_j^s \tag{3.16}$$

The cosine value g_{ij} represents the rotation required to bring the coordinate frames of the sample and of the crystal lattice in coincidence. However, computation of cosine directions requires knowledge of the Miller indices corresponding to the different Kikuchi lines. Prior to presenting one of the possible indexing procedures, it is important and useful to introduce the reciprocal lattice.

The reciprocal lattice is a fictitious lattice consisting of the Fourier transform of the direct lattice. Denote ($\mathbf{u}$, $\mathbf{v}$, $\mathbf{w}$) and ($\mathbf{u}^*$, $\mathbf{v}^*$, $\mathbf{w}^*$) the two sets of basis vectors associated with the frames of the direct and reciprocal lattices, respectively. Therefore, any direction vector $\mathbf{d}$ can be expressed by using Miller indices as follows

$$\mathbf{d} = h\mathbf{u} + k\mathbf{v} + l\mathbf{w} \tag{3.17}$$

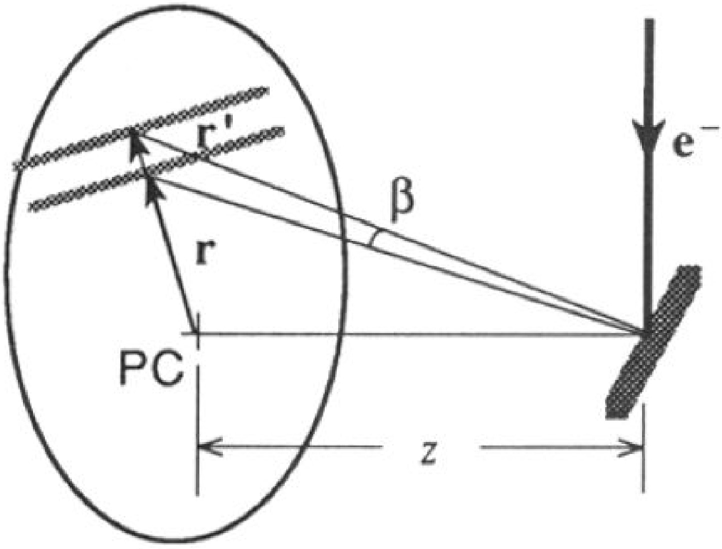

FIGURE 3.12 – Diagram for calculation of bandwidth angle [10]

Similarly, any direction vector passing through two nodes of the reciprocal lattices can be written as

$$\mathbf{d} = h * \mathbf{u}^* + k * \mathbf{v}^* + l * \mathbf{w}^* \tag{3.18}$$

such that

$$\|\mathbf{d}\| = \frac{1}{d_{h'k'l'}} \tag{3.19}$$

Vectors **u**, **v** and **w** are related to vectors $\mathbf{u}^*$ $\mathbf{v}^*$, $\mathbf{w}^*$ such that

$$\mathbf{u}^*.\mathbf{v} = \mathbf{u}^*.\mathbf{w} = \mathbf{v}^*.\mathbf{u} = \mathbf{v}^*.\mathbf{w} = \mathbf{w}^*.\mathbf{u} = \mathbf{w}^*.\mathbf{v} = 0 \tag{3.20}$$

and

$$\mathbf{u}.\mathbf{u}^* = \mathbf{v}.\mathbf{v}^* = \mathbf{w}.\mathbf{w}^* = 1 \tag{3.21}$$

Consequently, metric and orientational relations existing between the direct and reciprocal lattices are listed below :

- dimensions in the reciprocal lattice are equal to their inverse in the direct lattice ;
- the direction vector $\left[\text{hkl}\right]*$ is perpendicular to the plane (hkl) ;
- the direction vector $\left[\text{mnp}\right]$ is perpendicular to the plane (mnp)* ;
- $d_{hkl} = \frac{1}{\|\mathbf{n^*_{hkl}}\|}$;
- $d_{mnp*} = \frac{1}{\|\mathbf{n_{mnp}}\|}$.

The use of the reciprocal lattice simplifies many calculations such as, for example, the computation of the angle Φ formed by two reticular planes represented by their respective Miller indices $(h_1k_1l_1)$ and $(h_2k_2l_2)$ and expressed as

$$\Phi = \cos^{-1}\left(\frac{\mathbf{n^*_{h_1k_1l_1}}.\mathbf{n^*_{h_2k_2l_2}}}{\|\mathbf{n^*_{h_1k_1l_1}}\|.\|\mathbf{n^*_{h_2k_2l_2}}\|}\right) \tag{3.22}$$

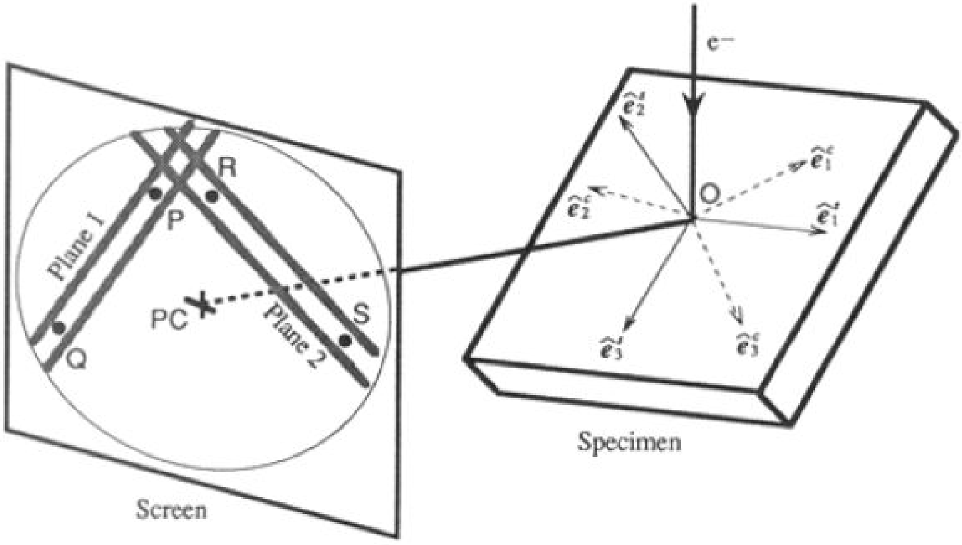

FIGURE 3.13 – Simplified and schematic representation of diffraction setup [10]

The reciprocal lattice also enables an easy computation of the zone axis of two intersecting planes. Its expression is given by the following relation

$$\mathbf{n_{mnp}} = \mathbf{n^*_{h_1k_1l_1}} \times \mathbf{n^*_{h_2k_2l_2}} \tag{3.23}$$

Moreover, each atom located within the interaction volume scatters incident electrons. The intensity of diffracted electrons in a given direction results from the sum of destructive and non-destructive interferences which are functions of the number of atoms, their nature and location. This dependence on the arrangement of the different atoms composing the unit cell is expressed via a factor called shape factor and usually denoted by $F(hkl)$

$$F(hkl) = \sum_{j=1}^{n} f_j \exp\big(2\pi i(hx_j + ky_j + lz_j)\big) \tag{3.24}$$

where f_j is the atomic diffusion factor of the j-th atom of coordinates (x_j,y_j,z_j). Therefore, the formula implies that a node in the reciprocal space does not exist if its associated factor F is null. The diffraction intensity $I(hkl)$ is strictly proportional to the structure factor and can be written as

$$I(hkl) = \kappa.F(hkl) \tag{3.25}$$

with κ a real constant.

Regarding the indexing of diffraction bands and spots, different methods exist and depend whether the material structure is known or not by the experimentalist. Assume for example a hexagonal crystal lattice. The procedure described hereafter is named the triplet indexing technique, or more simply the triplet method, because three vectors or three bands are used to obtain an unique orientation solution for both diffraction spots and bands. The first step consists of measuring the distances D_{hkl} between two diffraction spots symmetric with respect to the pattern center O. Figure 3.14 shows that the distance $D_{h_1k_1l_1}$ corresponds to the distance between points $P_1(h_1, k_1, l_1)$ and $P_1'(-h_1, -k_1, -l_1)$. Distances are then sorted by increasing order. The second step is the computation of inter-reticular distances from previously calculated distances that can be obtained by using the following formula

$$d_{hkl} = \frac{2Z\lambda}{D_{hkl}} \tag{3.26}$$

Since the material is known, inter-reticular distances can be compared to values listed in standard look-up tables with corresponding Miller indices, such as ASTM tables.

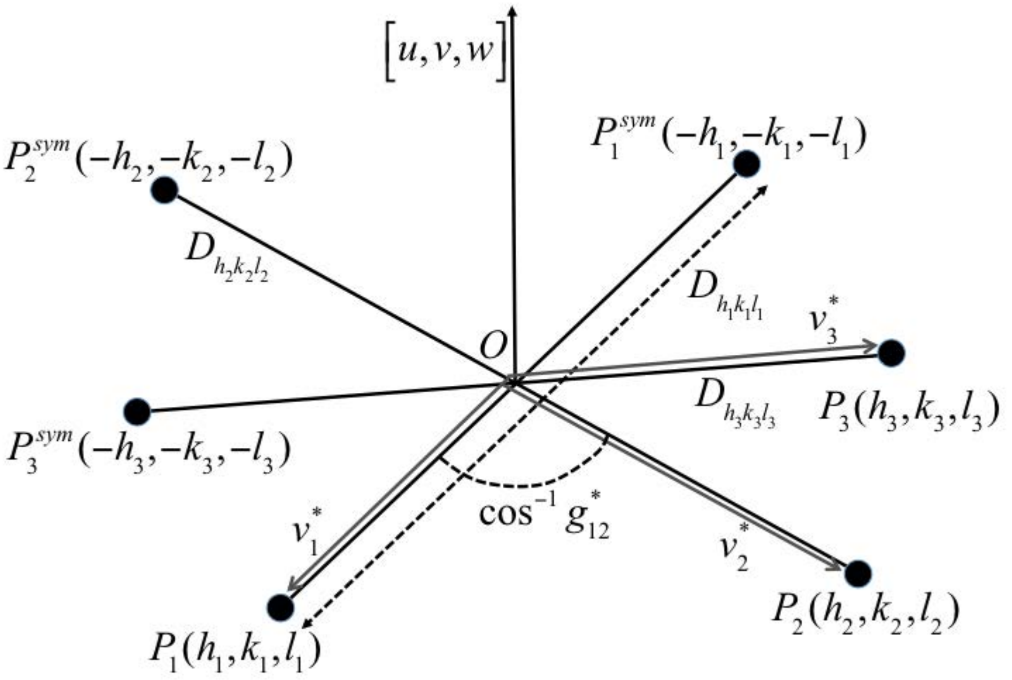

FIGURE 3.14 – Schematic representation of the triplet method for diffraction spot indexing

In the third step, we ensure that points have been indexed consistently, i.e. Miller indices of three diffraction spots $P_1(h_1, k_1, l_1)$, $P_2(h_2, k_2, l_2)$ and $P_3(h_3, k_3, l_3)$ can be related to each other such that $h_1 = h_2 + h_3$, $k_1 = k_2 + k_3$ and $l_1 = l_2 + l_3$. Denoting by $\mathbf{v*_1} = \vec{OP_1}$, $\mathbf{v*_2} = \vec{OP_2}$ and $\mathbf{v*_3} = \vec{OP_3}$, the cosine directions $g*_{ij}$ associated with vectors $\mathbf{v*_i}$ and $\mathbf{v*_j}$ are expressed as

$$g*_{ij} = \frac{\mathbf{v*_i}\mathbf{v*_j}}{\|\mathbf{v*_i}\|\|\mathbf{v*_j}\|} \tag{3.27}$$

The zone axis, displayed with Miller indices $\left[\text{uvw}\right]$ on Figure 3.14, can be derived from the cross product of two of the three vectors $\mathbf{v*_i}$ with $i = 1, 2, 3$. The method to deal with diffraction bands is exactly the same. One computes the angle between two bands. Knowing the structural data of the studied phase, angle values are then compared to those of look-up tables of inter-planar spacings and corresponding Miller indices. Theoretically, using only one triplet of bands is enough to obtain an unique orientation solution. However, because of experimental uncertainties and the presence of rogue bands, it is better to use multiple triplets.

3.4 A graph theory based automated twin recognition technique for Electron Back-Scatter Diffraction analysis

This section introduces a new EBSD data analysis and visualization software capable of automatically identifying twins and of extracting statistical information pertaining to the presence and geometrical features of twins in relationship with the microstructure. Twin recognition is performed via the use of several graph and group structures. Twin statistics and microstructural data are then classified and saved in a relational database. Software results are all accessible and can be easily corrected, if necessary, via the graphical user interface. Initially developed to identify twins in magnesium and zirconium, the numerical tool's architecture is such that only a minimum of changes is required to analyze other materials, h.c.p. or not. The first part of the section is dedicated to presenting and describing the method. The choice and the evaluation of features of the graphical user interface, as well as the construction of a relational database storing both microstructural information and twinning statistics, are discussed in the second part of the section.

3.4.1 Euler angles, quaternion rotation representations and their application to EBSD data

Euler angles and quaternion orientation and rotation representations

- Euler angles

An EBSD map can be seen as an image, e.g. a square or hexagonal array of measurement points, where each measurement point (or pixel) gives the crystal local orientation as a set of Euler angles following the Z-X-Z convention, denoted by (ϕ_1, Φ, ϕ_2). Crystal orientation can be obtained by applying the following rotation matrix to the basic crystal structure :

$$R(\phi_1, \Phi, \phi_2) = \begin{pmatrix} \cos\phi_1 & -\sin\phi_1 & 0 \\ \sin\phi_1 & \cos\phi_1 & 0 \\ 0 & 0 & 1 \end{pmatrix} \begin{pmatrix} 1 & 0 & 0 \\ 0 & \cos\Phi & -\sin\Phi \\ 0 & \sin\Phi & \cos\Phi \end{pmatrix} \begin{pmatrix} \cos\phi_2 & -\sin\phi_2 & 0 \\ \sin\phi_2 & \cos\phi_2 & 0 \\ 0 & 0 & 1 \end{pmatrix} \tag{3.28}$$

From a transformation perspective, the matrix $\mathbf{R}$, also more explicitly denoted by $\mathbf{R}_{\mathbf{c}}^{\mathbf{w}}$, corresponds to the transformation from the local crystal frame to the world frame. Conversely, the transformation from the world to the crystal will be denoted by $\mathbf{R}_{\mathbf{w}}^{\mathbf{c}}$. The rotation matrix $\mathbf{R}_{\mathbf{w}}^{\mathbf{c}}$ transforms the vector $\mathbf{v_c}$, initially expressed in the local crystal frame, into v_w, expressed in the world frame as following : $\mathbf{v_w} = \mathbf{R}_{\mathbf{w}}^{\mathbf{c}}\mathbf{v_c}$.

The matrix $\mathbf{R}$ is a representation of an element belonging to the algebraic group of 3D rotations, also called the Special Orthogonal group of dimension 3, $SO(3)$. This space is a group in the algebraic sense, meaning that it supports a multiplication operator, defines an inverse, i.e. the transpose of a rotation matrix, and a neutral element, i.e. the identity matrix.

- Rodrigues' formalism and quaternions

Other useful and well known representations of 3D rotations are the Rodrigues vector and unit quaternions. The Rodrigues vector is a vector whose length is proportional to the amplitude of a given rotation and whose direction is the axis around which the rotation is applied. Quaternions are a compact representation of a rotation of angle θ around an axis v with four values (w, x, y, z) where $w = \cos\frac{\theta}{2}$ and $(x, y, z) = \mathbf{v} \cdot \sin\frac{\theta}{2}$. By analogy with complex numbers, w is called the *real* part of the quaternion and $\mathbf{v}$ the imaginary part. When working with rotations, unit quaternions are preferred, i.e. $\sqrt{w^2+x^2+y^2+z^2}=1$. The advantage of quaternions lies in the existence of a multiplication operator allowing the preservation of the group structure while keeping the representation compact. In computer graphics, quaternions are frequently used because they allow an easy implementation of interpolated rotations between two rotations [142]. Note that well-known formulas exist for conversion between rotation matrices and quaternions.

In formal terms coming from differential geometry, extracting the Rodrigues representation from a quaternion or a rotation matrix is referred to as using the logarithmic map of the differential manifold [143]. Recovering the quaternion from the Rodrigues representation is the exponential map. Therefore, the relationship between a given Rodrigues vector, $\mathbf{r}$, and its equivalent quaternion, q, can be written as follows :

$$\mathbf{r} = \log q \text{ and } q = \exp \mathbf{r} \tag{3.29}$$

As a result, the amplitude of the rotation q, denoted by θ, can be expressed as the norm of $\log q$: $\theta = \|\log q\|$.

- Metrics

The $SO(3)$ group is not a vector space. As a consequence, the usual norm of the Euclidean space $\mathbb{R}^3$, i.e. $\sqrt{x^2+y^2+z^2}$, does not apply. A more appropriate norm consists in the amplitude of the rotation, θ. Therefore, the norm of a rotation represented by its quaternion q is defined as

$$\|q\|_{so} = \|\log q\| \tag{3.30}$$

Although the norm of a rotation is not directly used for EBSD map analysis, the resulting distance leads to a unified definition of disorientation. Therefore, the distance between two rotations represented by q_1 and q_2 is denoted by :

$$d(q_1,q_2) = \left\|\log\left(q_1^{-1}\cdot q_2\right)\right\| = \|q_1^{-1}\cdot q_2\|_{so} \tag{3.31}$$

Application to EBSD data

An EBSD map can be seen as a set of orientations and coordinates since three Euler angles are associated with each single pixel. In addition, the geometrical transformation induced by twinning is described via either the reflection of the lattice with respect to a specific plane or the π radian rotation of the lattice with respect to a given axis. As a result, quaternions and Rodrigues' formalism suit well for EBSD data processing, since they enable a relatively easy computation of disorientations, recognition and classification of the different phases or domains of the map.

- Disorientation

Disorientation is defined as the orientation difference between two entities. These entities can be grains, parent and/or twin phases or individual measurements. Consider now the case of two measurements points, represented by their quaternions $q_1 = q_w^{c1}$ and $q_2 = q_w^{c2}$. Both quaternions q_1 and q_2 correspond to a rotation from the sample to the local crystal frames. The amplitude of the disorientation between these two measurements, denoted by $\delta(q_1,q_2)$, can be expressed as $d(q_1,q_2) = \|q_1^{-1}\cdot q_2\|_{so}$. However, the actual disorientation consists in the rotation that needs to be applied to q_1 to transform it into q_2.

$$\delta(q_1,q_2) = q_2\cdot q_1^{-1} = q_w^{c2}\cdot (q_w^{c1})^{-1} = q_w^{c2}\cdot q_{c1}^{w} = q_{c1}^{c2} \tag{3.32}$$

The advantage of such a notation lies in the fact that δ includes both the amplitude and the axis of the rotation. The latter property will be particularly useful to recognize and identify mode and system of twins.

For the sake of consistency and taking advantage of quaternion properties, what follows systematically identifies the smallest positive rotation transforming q_1 into q_2 when computing the disorientation $\delta(q_1, q_2)$. For example, if the real part of $\delta(q_1, q_2)$ is negative, it implies that $|\frac{\theta}{2}| > \frac{\pi}{2}$ radians. In this case, $\delta(q_1, q_2)$ is then replaced by $-\delta(q_1, q_2)$ which corresponds to a rotation around the same axis but with an angle equal to $\theta + \pi$ radians. Note that the disorientation angle is now smaller than π radians in absolute value. In addition, the disorientation can be made positive since a quaternion representing a rotation of an angle θ around a vector v is equal to the quaternion corresponding to a rotation of an angle $-\theta$ around $-v$. These two choices lead to an unambiguous representation of quaternions that is helpful when comparing rotations to identify twins.

However, the disorientation measure, δ, ignores crystal symmetries. The hexagonal crystallographic structure is invariant by rotations around the c-axis by $k\frac{\pi}{3}$, $k \in I\!N$ and by π radian around any vector lying in the basal plane. Quaternions associated with symmetries around the c-axis and vectors lying in the basal plane are denoted by $q_x(k)$ and $q_z(k)$, respectively, and are expressed as follows :

$$q_x(k) = \exp\left(k\pi\vec{x}\right) \tag{3.33}$$

$$q_z(k) = \exp\left(k\frac{\pi}{3}\vec{z}\right) \tag{3.34}$$

The set of possible disorientations between q_1 and q_2, denoted by $\Delta(q_1, q_2)$, is then defined as :

$$\Delta(q_1, q_2) = \{q_z(j) \cdot q_x(i) \cdot \delta(q_1, q_2)\}_{i=0\ldots1, j=0\ldots5} \tag{3.35}$$

In the case of h.c.p. materials, $\Delta(q_1, q_2)$ contains 12 elements. The definition of the disorientation quaternion, $Diso(q_1, q_2)$, and its norm, $\|Diso(q_1, q_2)\|_{so}$, results from the definition of $\Delta(q_1, q_2)$. Their expressions are, respectively :

$$Diso(q_1, q_2) = \underset{q \in \Delta(q_1, q_2)}{\arg\min} \|q\|_{so} \tag{3.36}$$

$$\|Diso(q_1, q_2)\|_{so} = \min_{q \in \Delta(q_1, q_2)} \|q\|_{so} \tag{3.37}$$

The symmetry around any vector lying in the basal plane allows the disorientation with an angle θ greater than $\pi/2$ radian to be equivalent to a disorientation with an angle equal to $\theta - \pi$, smaller in magnitude. If $\theta - \pi$ is negative, the negative sign is removed by considering the rotation of $-(\theta - \pi)$ around the opposite rotation vector. Symmetries also imply that the norm of the disorientation quaternion, $\|Diso(q_1, q_2)\|_{so}$, is always in the range of 0 to $\pi/2$ radian.

- Classification of twinning relationships

As previously mentioned, a twin system can be completely defined by the indices of either the twinning plane, K_1, and η_2 or the second invariant plane, K_2, and the twinning shear direction, η_1. Planes K_1 and K_2 and vectors η_1 and η_2 are all invariant. Also, as per Chapter 1, the lattice reorientation induced by twinning of the first and second kinds can be described by a rotation of 180° about the normal to K_1 and the twinning shear direction, respectively. In the case of

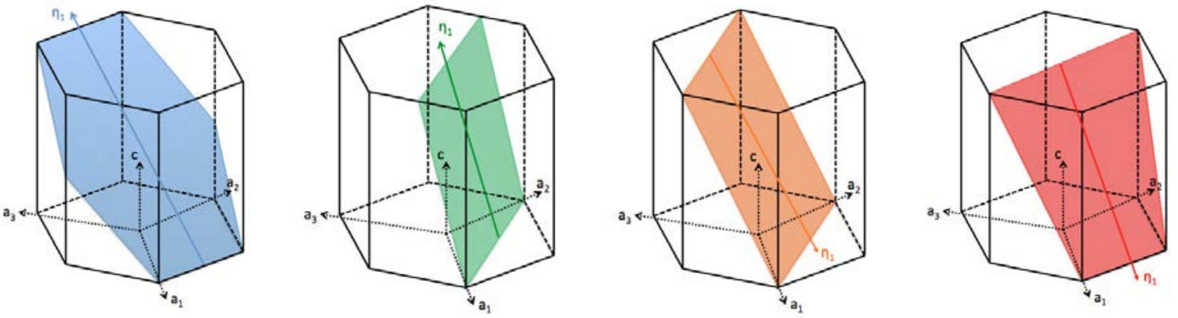

(a) T_1 - $(10\bar{1}2)$ (b) T_2 - $(11\bar{2}1)$ (c) C_1 - $(11\bar{2}2)$ (d) C_2 - $(10\bar{1}1)$

FIGURE 3.15 – Schematic representation of twinning modes observed in Zr Mg. Twins are represented via their twinning planes, K_1.

compound twins, these two rotations can be used to obtain the twin orientation from the parent one. Two tensile twinning modes, i.e $\{10\bar{1}2\}$ and $\{11\bar{2}1\}$, referred to as tensile 1 or T_1 and tensile 2 or T_2, respectively, and one compressive mode, i.e. $\{11\bar{2}2\}$, referred to as compressive 1 or C_1, are observed in high-purity clock-rolled Zr samples loaded along the through thickness and in-plane directions at 76K [144, 11]. Although not observed in our dataset, a second compressive mode, i.e. $\{10\bar{1}1\}$, referred to as compressive 2 or C_2, may appear. In Magnesium, only T_1 and C_2 are susceptible to nucleate and grow. T_1, T_2, C_1 and C_2 twins observed in Zr and Mg are all compound twins. Table 3.1 lists some of the twinning mode crystallographic properties such as twinning plane, disorientation angle, etc. The parameter γ denotes the c/a ratio, equal to 1.59 and 1.62 in Zr and Mg, respectively. Figure 3.15 shows a graphical representation of one of the six possible twin systems that can be activated for the four above mentioned twinning modes, .

TABLE 3.1 – Twinning modes in Zr

Twinning mode	Twinning plane K_1	Twinning direction η_1	Disorientation angle δ (°)
T_1	$\{10\bar{1}2\}$	$<\bar{1}011>$	85.2
T_2	$\{11\bar{2}1\}$	$<\bar{1}\bar{1}26>$	34.9
C_1	$\{11\bar{2}2\}$	$<11\bar{2}\bar{3}>$	64.2
C_2	$\{10\bar{1}1\}$	$<10\bar{1}\bar{2}>$	57.1

All twin modes considered correspond to compound twins [18]. As a result, the lattice reorientation that they induce can either be described by a rotation of π radians around the shear direction, η_1, or by a rotation of π radians around the normal to the twinning plane. In the case of h.c.p. structures, the expressions of disorientation quaternions representative of twinning relationships can be indexed by k, such that $k \in [1, 6]$, and written as follows :

$$q(k) = \exp\left[\pi \cdot \vec{\eta}(k)\right] \tag{3.38}$$

with,

$$\vec{\eta}(k) = \begin{bmatrix} cos\left[\alpha(k)\right] cos\left[\beta\right] \\ sin\left[\alpha(k)\right] cos\left[\beta\right] \\ sin\left[\beta\right] \end{bmatrix} \tag{3.39}$$

where,

— $\alpha(k) = \frac{(k-1)\pi}{3} - \frac{5\pi}{6}$ and $\beta = \arctan\left(\frac{\gamma}{\sqrt{3}}\right)$ for Tensile 1,

— $\alpha(k) = \frac{(k-3)\pi}{3}$ and $\beta = \arctan 2\gamma$ for Tensile 2,

— $\alpha(k) = \frac{k\pi}{3}$ and $\beta = \pi + \arctan\gamma$ for Compressive 1,

— $\alpha(k) = \frac{(k-1)\pi}{3} + \frac{\pi}{6}$ and $\beta = \pi + \arctan\left(\frac{2\gamma}{\sqrt{3}}\right)$ for Compressive 2.

Identifying the mode and system of a twin consists in finding the closest object to the disorientation q_{c1}^{c2} existing between the parent and twin phases in $\mathcal{T}$, defined as the set of possible twinning relationships within a given threshold $d_{\max}$:

$$\tau = \arg\min_{t\in\mathcal{T}} \delta\left(q_{c1}^{c2}, t\right) \quad \text{such that} \quad \left\|\delta\left(q_{c1}^{c2}, t\right)\right\|_{so} < d_{\max} \tag{3.40}$$

The set $\mathcal{T}$ contains 24 and 12 elements in the case of Zr and Mg, respectively. Note how easy it is for the software, and hence for the user, to switch from the analysis of a Zr EBSD map to a Mg EBSD scan. The only two differences lie in a change of the value of the c/a ratio and in a readjustment of the list of theoretical disorientation quaternions corresponding to the different potentially active twinning modes.

3.4.2 Identification of grains, parent and twin phases

In EBSD scans, non-twinned grains, parent and twin phases are contiguous areas with a consistent orientation. Therefore, detecting grains and twins consists of identifying and grouping contiguous and consistent areas. These operations will be performed following an approach similar to the "super-pixels" [145, 146] technique based on graph theory and commonly used in image analysis. The whole process of twin recognition and parent phase identification relies on one tool of graph theory, the extraction of connected parts, used five times at different levels, which is the extraction of connected parts.

Mathematically, a graph $\mathcal{G}$ is a pair of sets (V, E) containing vertices and edges, respectively. Two vertices are said to be connected when an edge links them. Vertices are usually designated by integers. It implies that the edge (i, j) connects vertex i to vertex j. A path between two vertices k and l corresponds to a sequence of edges and vertices reaching k from l, and reciprocally. A path is, by definition, non-directional. In addition, a subset $W \subset V$ is a connected part of $\mathcal{G}$ if, for all pairs of vertices (i, j), $i \in W$, $j \in W$, there exists a path in $\mathcal{G}$ between i and j. Extracting connected components is a well known problem in graph theory, for which efficient algorithms already exist [147]. The degree of complexity of the extraction of connected parts increases linearly with the number of vertices belonging to the graph.

Segmentation of the EBSD map into connected parts of consisted orientations

The first step in the EBSD analysis consists of grouping all measurement points of similar orientation into fragments. To this end, a first graph is built as follows : every measurement point is considered as a vertex and an edge between two neighboring pixels is created if the disorientation between them is smaller than a given threshold, e.g. 5 degrees. The type of measurement grid, i.e. square or hexagonal (Figure 3.16), affects the construction of the graph but does not have a significant influence on the extraction of connected parts.

In addition, assuming that edge disorientations follow a normal distribution, the thickness with which edges appear on screen is characterized by a weight, w, whose value depends on the

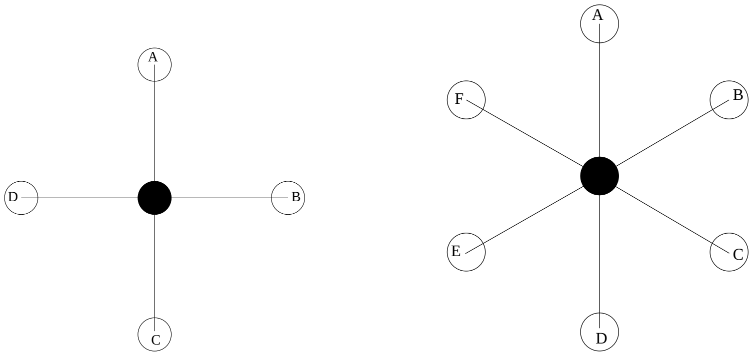

Figure 3.16 – Example of neighboring relationships encountered in EBSD data. On the left, when measurement points form a square grid, the pixel represented by the black disc has 4 neighbors represented by the white circles. On the right, when measurement points form an hexagonal grid, each measurement has 6 neighbors.

likelihood of the disorientation :

$$w(q_1, q_2) = e^{\frac{diso(q_1,q_2)^2}{L^2}} \tag{3.41}$$

where L is a threshold value. As a result, the smaller disorientation between two pixels, the more strongly is displayed their mutual edge. The edge color indicates the nature of the disorientation. For example, an edge between two points of similar orientation appears in white. But as shown in Figure 3.18, disorientations corresponding to tensile 1 and compressive 1 twinning relationships are displayed in green and red, respectively.

Moreover, some measurement points located in a few small areas exhibit a very low resolution, i.e. the software cannot determine their orientation. Then, a flood-filling algorithm [148] interpolates missing measurement points and associates them with their closest connected parts.

- Grouping of connected parts into grains

The second step in the analysis of an EBSD data is to group connected fragments of consistent orientation into grains. In a material free of twins or precipitates, this step is trivial, since every fragment corresponds to a grain. However, when twinning occurs, different configurations have to be considered. Figure 3.19 depicts the three most typical twinning configurations observed in Zr scans. Therefore, a second graph, referred to as the twinning graph, is generated at the level of connected fragments to group them into grains. Vertices are now connected fragments, and edges link two vertices in contact if the disorientation between them can be classified as a twinning relation. A connected component in this graph is a set of fragments all linked by known twinning relations. Hence, this set of fragments is very likely to be part of the same grain.

The construction of this graph relies on the measure of disorientation between two components of consistent orientation, i.e. connected parts. Three hypotheses have been taken into account to compute the disorientation between components :

- Measuring the disorientation along the connected part boundary. This hypothesis was discarded on the argument that the boundary is the hardest part to measure with the EBSD process and as such is the least reliable.
- Using the disorientation of the measurement at the barycenter of the connected part. This is simple enough, but can be incorrect if the barycenter happens to be a bad measurement spot, or even a point outside of the connected part if the latter is non convex.

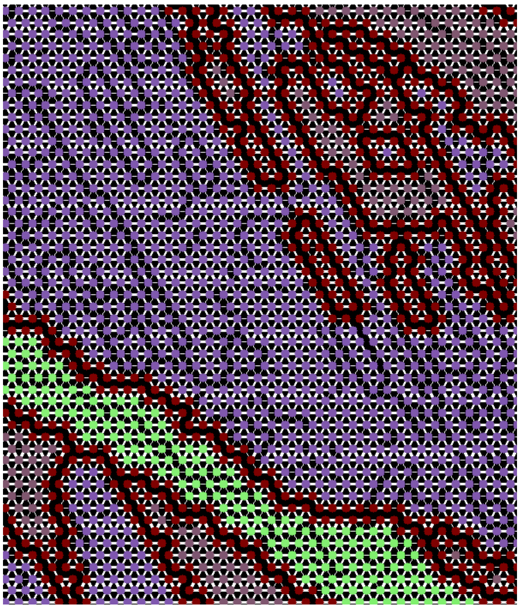

FIGURE 3.17 – Graph grouping measurement points of consistent orientation in connected parts. The colored circles correspond to EBSD measurement points, with the Euler angles mapped on the RGB cube and, white lines represent edges, whose thicknesses are proportional to the weight, w. Consequently, twins appear clearly as areas delineated by a black border where the edge weight becomes negligible.

— Computing the average orientation across the connected part. This is computationally more expensive and sensitive to continuous changes of orientation across the grain, but can be implemented in the most generic way.

The third hypothesis is the one chosen in the present work. However, because $SO(3)$ is not an Euclidean space, the closed-form expression of the average is incorrect. Consequently, a specific algorithm, similar to the one computing average of quaternions, is used to determine the average orientation of connected EBSD measurements. Consider a set of n EBSD measurement points represented as quaternions q_i, $i = 1..n$. Assume that the initial average, m_0 is equal to q_1, i.e. $m_0 = q_1$. The average orientation of a connected part is estimated iteratively by computing the following two equations :

$$\begin{aligned} e_k &= \frac{1}{n}\sum_{i=1}^{n} \log Diso(m_k, q_i) \qquad (3.42) \\ m_{k+1} &= m_k \cdot \exp e_k \qquad (3.43) \end{aligned}$$

The iteration stops when $\|e_k\|$ reaches a given threshold (5.10^{-4} in the present case). At this step, m_k corresponds to the best estimate of the connected part orientation. The construction of this second graph allows extraction of a significant amount of properties such as twin modes, twin systems, twin boundary lengths, the list of neighbors for each grain, the list of pixels belonging to grain borders, etc.

- Identification of parent phases

In twinned grains, parent phases are composed of one or several connected parts, as shown in Figure 3.19. Parent phases are then considered as sets of connected fragments of consistent

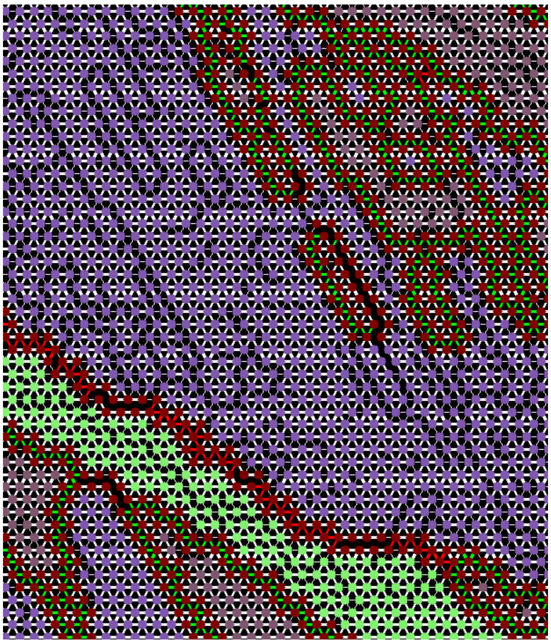

FIGURE 3.18 – Graph grouping measurement points of consistent orientation in connected parts with added twinning mode. Green and red edges linking border points, displayed in brown, indicate tensile and compressive twinning relations, respectively.

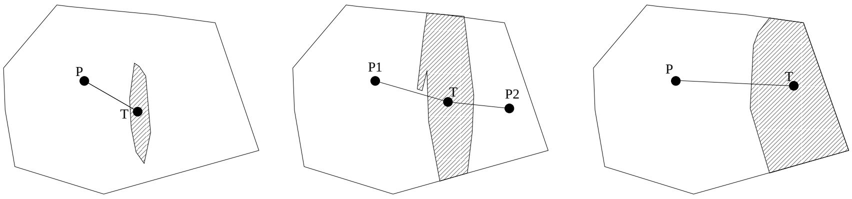

FIGURE 3.19 – Three sample cases of twinning : on the left a single twin T in the middle of its parent P ; in the middle, a twin going across its parent and separating it into two consistent part P1 and P2 ; on the right, a grain appearing as two consistent parts next to each others.

orientation. To build such sets of connected fragments, the software generates a third graph over the EBSD map. Vertices are now connected fragments and edges only link two connected fragments if they belong to the same grain and if they have a low respective disorientation. By construction, a connected component of this graph is a set of connected parts embedded in the same grain with consistent orientation. By default, the parent phase is identified as the set of orientation path occupying the largest part of the grain. In addition to the incorrect links, the user has also the possibility to correct the software in case a twin occupies more than half of the total grain area. Figures 3.20 and 3.21 show two parts of EBSD maps before and after edition of incorrect twinning relationships, respectively. Note that, as shown in figure 3.22, the software is still capable of recovering complex grain structures.

- Detection of higher order twins

A higher order twin is defined as a twin embedded in another. For example, a secondary and tertiary twin corresponds to a twin that nucleated in a primary and secondary twin, respectively. Depending on the material, the loading path and loading history, secondary twinning may occur.

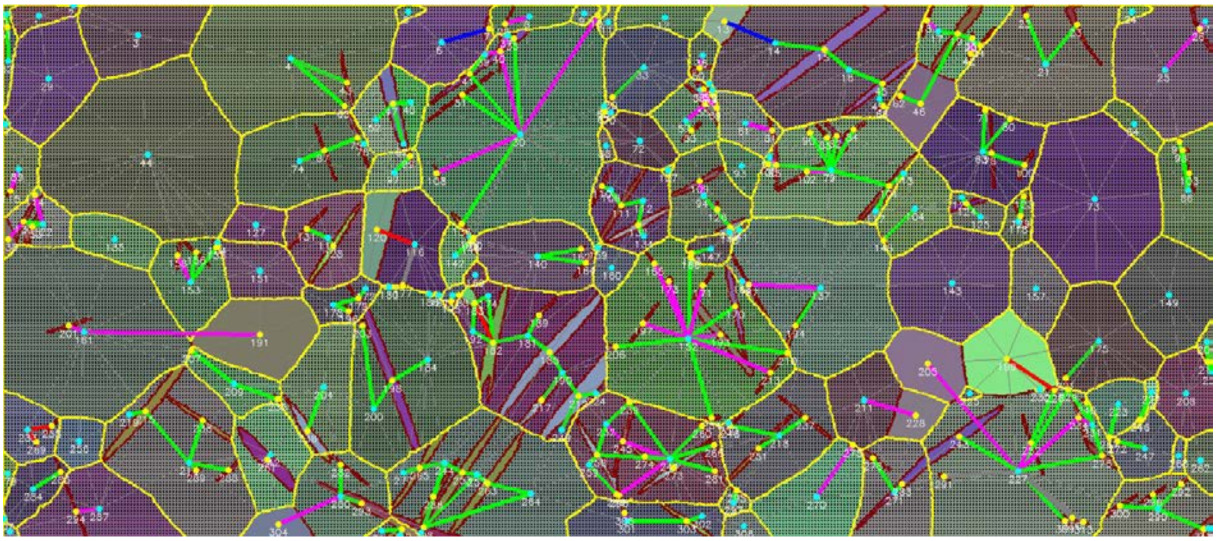

FIGURE 3.20 – Automatic output for a Zr EBSD map. The sample was cut from a high-purity clock-rolled Zr plate and loaded in compression along one of the in-plane directions up to 5% strain [11]. Yellow borders mark the grain joints, brown borders the twin joints. Green edges represent tensile 1 relation, magenta tensile 2, red compressive 1 and blue compressive 2.

For example, it has been observed by Martin et al. [67] in Mg and appears on scans of Zr samples loaded along the through-thickness direction [144]. Tertiary twinning is more unlikely and statistically irrelevant. However, the software is still capable of identifying tertiary and higher order twins if necessary. The identification of these twins relies on the graph of connected fragments used to build the grains. In this graph, a twin of order n has an edge (i.e. an identifiable twinning relation) with a $(n-1)^{th}$-order twin or parent, if $n-1=0$, but no identifiable relation with $(n-k)^{th}$-order twins, with $k>1$. An example of such a situation is seen in figure 3.23 where the orange secondary twin (marked with a blue dot in its center) is embedded in the gray twin (marked by a yellow dot). Although the orange twin shares a border with the parent phase, its disorientation with respect to the parent domain does not correspond to one of the previously detailed twinning relations.

The present definition of twinning order leads to a simple recursive implementation of higher-order twins. The initialization step consists of considering that all parent fragments previously identified are of twinning order 0. To find n^{th} order twins, all nodes, i.e. fragments, with a twinning order strictly lower than n are removed as well as all edges with one extremity corresponding to one of these nodes. The connected components of the resulting graph are twins of order n. If such a connected component contains several fragments, these fragments can be separated in groups of consistent orientation and identify the "parent" phase, i.e. n^{th}-order twin itself, as the largest one. All fragments not identified as the "parent" fragment correspond to twins of order greater than n. The result of this process applied to the case of secondary and ternary twinning is shown in figure 3.23 where the grey first-order twin (highlighted in cyan) has four secondary twins (in blue), one of which having a tertiary twin (in red).

The indirect benefit of detecting and tagging higher order twins lies in the fact that, because of their decreasing likelihood, they help the user to check the software results more rapidly.

- The particular case of "twin strips"

In a non-negligible number of cases, small twins appear as a strip of connected twins at the

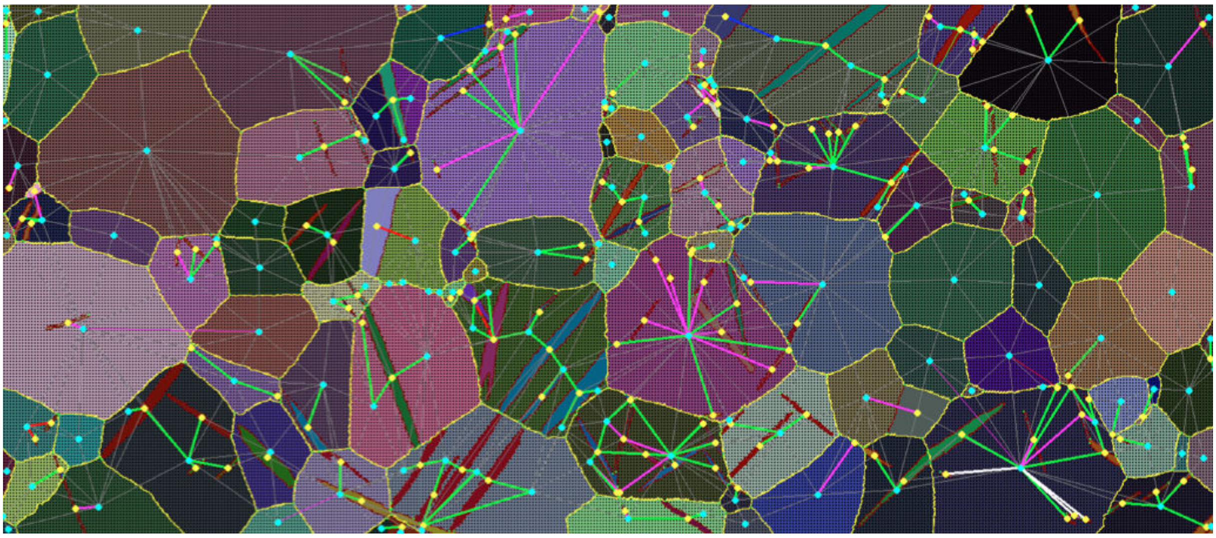

FIGURE 3.21 – Same map as Figure 3.20, but with manual edition of 4 incorrect links. The disabled links are displayed as thin edges.

outcome of the previous algorithm. This phenomenon occurs either when a very thin twin is separated in small objects because of the low resolution of a few EBSD measurement points or when a twin is divided into two parts by another twin. However, it is statistically relevant to be able to count these connected twins, also called "twin strips", as single twins. Two connected components are considered to belong to the same twin or twin strip if they meet the following five conditions :

- They are in the same grain.
- They have the same orientation, or the disorientation between the average orientation of both components is small. Typically, the same threshold is used as the one used to build connected components.
- The twin's ellipse main orientations (see sec. 3.4.2) are similar, for instance, less than 5 degrees apart.
- The sum of the twin half-lengths is within 20% of the distance between their centroid.
- The vector linking their centroids diverges by less than a few degrees from the twin's ellipse main orientation.

From these conditions, a fifth graph is generated in all grains. Vertices are connected fragments again, and edges link pairs of connected components fulfilling the previous 5 conditions. Consequently, the connected components with more than 1 vertex are twin strips. Figure 3.24 gives an example of the type of reconstruction obtained with this approach.

Examples of automatically extracted metrics and statistics

The following section illustrates the capabilities of the approach discussed above in terms of exploitable metrics.

- Area and Perimeter

The area of connected parts, i.e. grains, twins, parent phases, is obtained by multiplying the number of measurement points with the area corresponding to a single pixel. The area associated with a measurement point depends on the step size and the grid type (i.e., hexagonal or square).

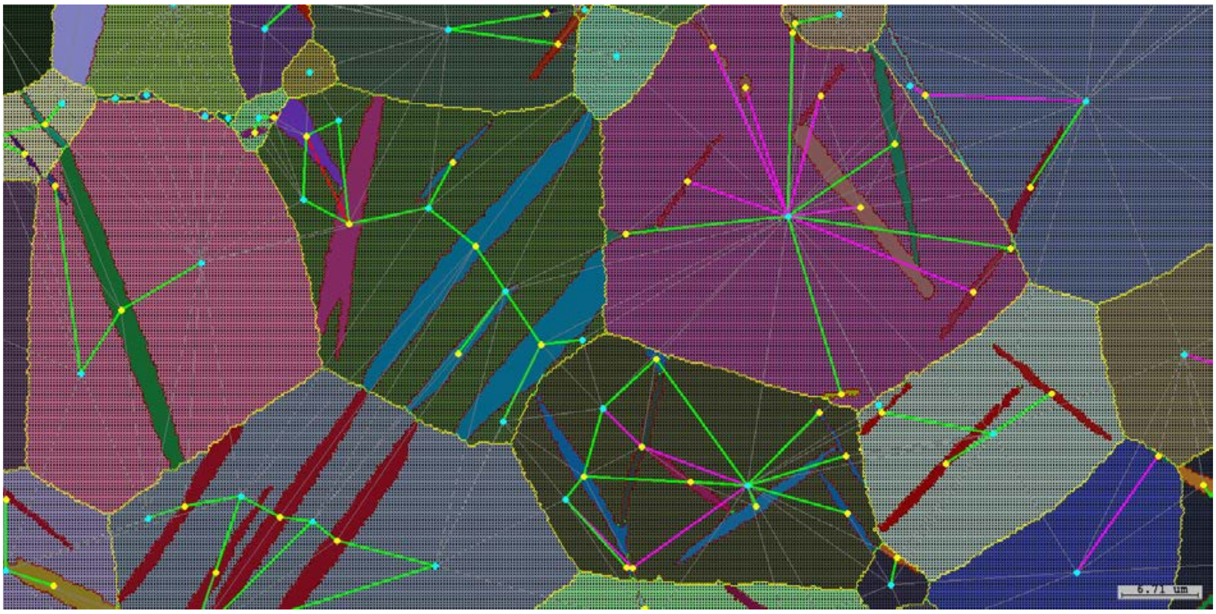

FIGURE 3.22 – Zoom on the map of Figure 3.20 to illustrate complex grain structures recovered by our software. The dashed line is a disorientation relation that matches a known relation (compressive 1) but is identified as irrelevant to the twinning process.

Similarly, grain boundary length is estimated by multiplying the number of measurement points located along the boundary by the inter-measurement length, associated, here, with the hexagonal grid.

- Grain Boundary Properties

Because the disorientations between every pair of measurement points or pair of connected fragments are identified, classified and saved, many statistics, such as, for example, grain boundary length and number of neighbors, are easily accessible and stored in the output database.

- Convexity

Visual observation of EBSD maps suggests that every grain or twin seems to be more or less convex. The degree of convexity of grains and twins can be quantified as follows. First, the convex hull of the object of interest is built by building the convex hull of all its joint points. The object can be either a grain or a twin. The convex hull is a convex polygon that encloses a set of 2D points[1]. The construction of the convex hull can be performed in $O(n \log n)$. Computing the area of such a polygon is a well defined geometric process. The degree of convexity can then be defined as the ratio of the area of the object to the area of its corresponding convex hull. The ratio is expected to be lower than 1 and the farther away from 1 it is, the less convex the object is.

This measure of convexity was implemented to refine the grain detection by identifying grains with a low convexity, trying to break edges in the connected fragment graph and recomputing the convexity of the resulting grains. If the overall convexity is improved, this edge is removed. Tests showed that this method is generally successful. However, the current automatic grain extraction method combined with the graphical user interface is efficient enough to not require the use of this refinement step in practice.

---

[1] The concept also extends to higher dimensions

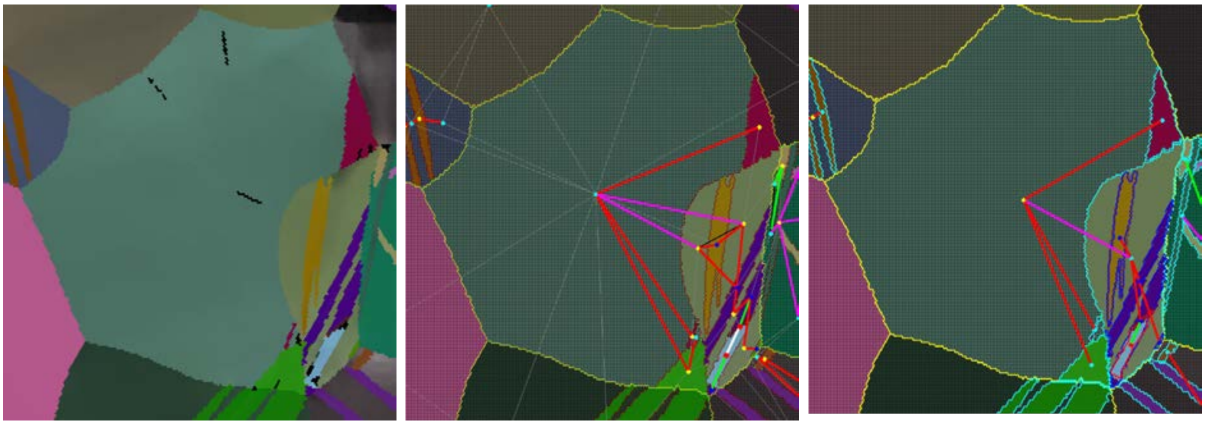

FIGURE 3.23 – Example of secondary and ternary twinning observed in an EBSD map of a high-purity clock-rolled Zr sample loaded in compression along the through-thickness direction up to 3% strain. This is shown using three different visualization modes (see appendix A) : raw mode (left), twinning editor mode (middle) and twinning statistics mode (right). The parent grain is surrounded in yellow, first order twins appear in cyan, secondary twins in blue and ternary or higher order twins in red.

-Twin shape and ellipsicity

The length and the thickness of twins are computed by estimating the 2D covariance of their constituent EBSD measurement points. The eigenvectors of the covariance matrix indicate the main directions of the twin. The apparent twin length is estimated to be equal to four times the square-root of the largest eigenvalue of its covariance matrix, and the apparent twin thickness is assumed to be equal to four times the square-root of the smallest eigenvalue. The orientation of the twin main axis is then given by the orientation of the largest eigenvectors of its covariance matrix, using the C function `atan2`. Both the true twin length and thickness can be computed in post-processing by multiplying them by the cosine of the angle between the twin plane and the normal to the sample [110, 111].

Comparing the ellipse area with the actual twin area computed from the number of measurement points contained in the twin allows estimation of the ellipsicity of a twin, defined as its departure from an idealized ellipse. Figure 3.25 depicts these ellipses and illustrates how the ellipsicity criterion highlights what the software identifies as "merged" twins. These "merged" twins are very likely co-zonal Tensile 1 twin variants. Considering co-zonal Tensile 1 variants have an ideal misorientation of 9.6 degrees and given the 5 degree tolerance used for twin variant recognition, the software is, in rare cases, not capable of distinguishing such twins. However, because of the level of precision of EBSD measurement, reducing the software tolerance for twin variant recognition, does not improve the results.

3.4.3 Graphical User Interface and Data availability

Graphical User Interface

To provide a quick and direct access to a large choice of metrics and statistics displayed on an EBSD map, the graphical user interface is aimed at allowing the user to check and correct, if

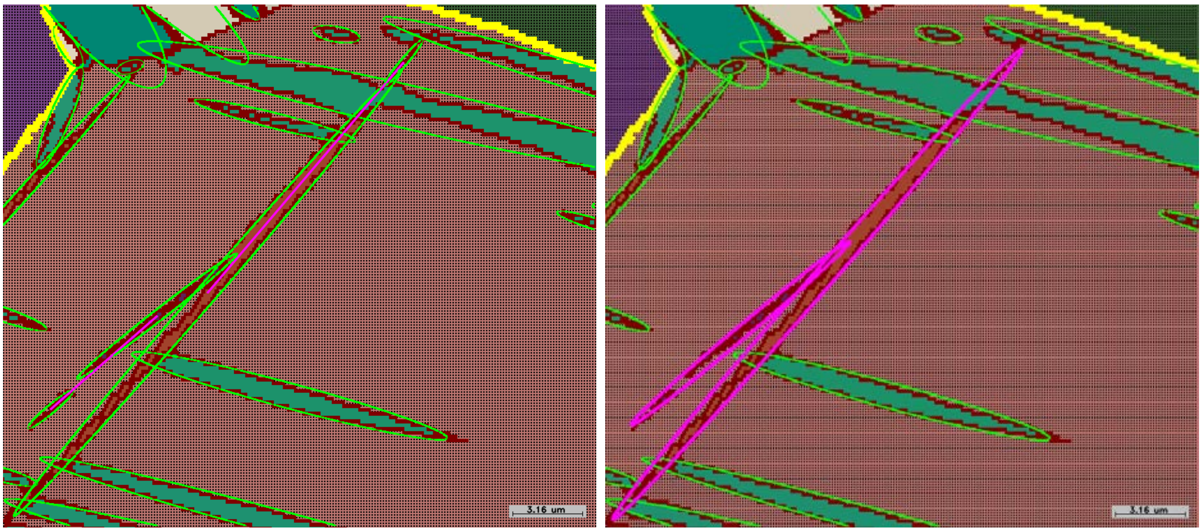

FIGURE 3.24 – Zoomed-in EBSD map of a high-purity clock-rolled Zr sample loaded in compression along one of the in-plane directions up to 10% strain. Left : detected component with their ellipses and twin-strip links in magenta ; right : reconstructed complete twin.

necessary, software results. Three types of situation require the intervention of the user. First, because of the random distribution of disorientations between neighboring grains, it is statistically likely that, for a few grains per map, the disorientation between adjacent grains matches a twinning relation. The user has the choice between either using the convexity option to refine the analysis performed by the map or simply deactivating manually the edge linking the parent to the mistaken twin. Second, in highly strained sample scans, orientation gradients can be significant, and the disorientation between two connected parts may be above the threshold to be flagged as a twinning relation. In such a case, the user can manually activate this twinning relation. Third, the parent is by default the largest connected component of the grain. However, twin phases may occupy the largest part of the grain and appear as the parent phase. Once again, this can be corrected manually by the user. This feature will be particularly useful when dealing with highly strained Mg samples. The result of such manual editions can be seen by comparing Figures 3.20 and 3.21.

Data availability

The analysis of an EBSD map generates a wealth of quantitative data about grains, twins and parent phases. However, different studies will not use the same EBSD data for the same purposes. This is why it is of primary importance to export data in a way that preserves all relations and does not make assumptions regarding what should or should not be stored.

To do so, the present software exports the data-structure extracted from the EBSD map analysis to a SQL database with the structure described in Figure 3.26. In practice, this is performed by using the SQLite library that implements a server-less database stored inside a single file. The advantage of such a relational database lies in the fact that it keeps all the information in a single file and allows the user to create aggregated statistics with simple SQL requests, as shown hereafter with requests 1 and 3, shown in Appendix A. For example, Request 1 generates a table containing features about twins, such as twinning modes (i.e. "twinning"),

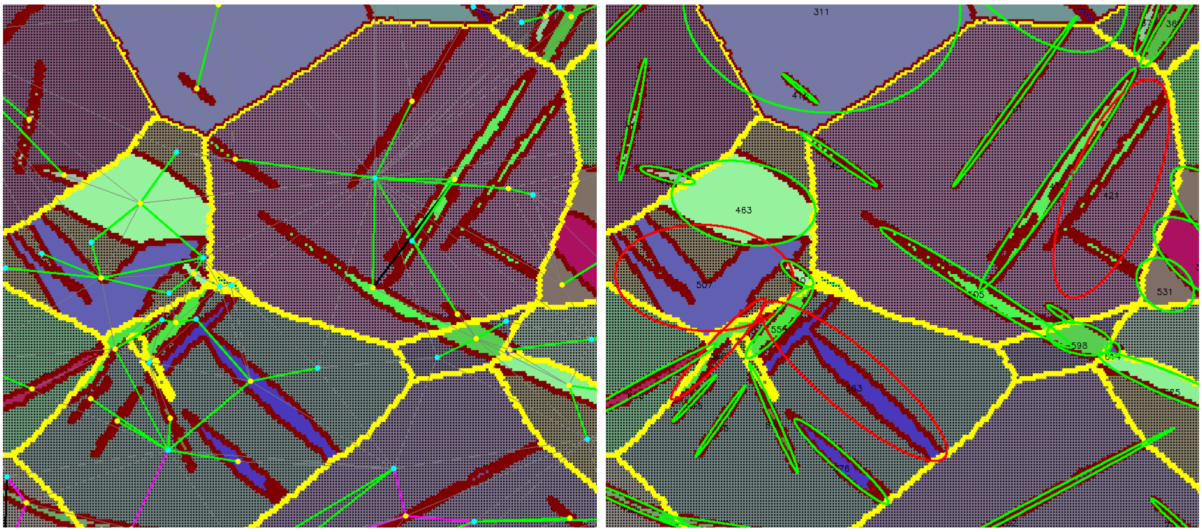

FIGURE 3.25 – EBSD map of a high-purity clock-rolled Zr sample loaded in compression along one of the in-plane directions up 10% strain. The top part shows the twinning relation identified. The right caption displays ellipses fitted to twins. Red ellipses correspond to low ellipsicity (below 70%). Low ellipsicity twins correspond here to merged orthogonal twins.

twin systems (i.e. "variant"), twin area (i.e. "area"), twin thickness (i.e. "thicknesse), quaternions corresponding to the average twin orientation (i.e. "qx", "qy", "qz", "qw"), etc. Request 3 was used to extract information about twin-twin junctions such as the modes and systems of intersecting twins. This request relies on the view created by Request 1 to generate the table containing twin characteristics. Matlab, C++ or Fortran codes can then process the tables generated by the SQL requests in order to extract statistics of interest. For example, the statistics about the influence of microstructure and twin-twin junctions on nucleation and growth of twins presented in the next chapter were computed from four tables only. Moreover, for the sake of keeping a record of experimental conditions, the database also stores constants and parameters used to construct this particular EBSD analysis.

3.5 Conclusion

In addition to a brief description of scanning electron microscopes, physical phenomena observed with electron diffraction and existing EBSD pattern analysis techniques and softwares, the present chapter introduces a new software for EBSD map automated analysis based on graph theory and quaternion algebra. Quaternions allow easy computation of disorientations between pixels and areas of consistent orientation. The subsequent use of graph and group structures allows grain identification, twin recognition and statistics extraction.

The newly introduced software is distinguished from pre-existing commercial softwares or academic codes by combining visualization with automated analysis of the EBSD map. The built-in graphical user interface enables an immediate and direct access to microstructural and twinning data such as orientation and size of twins and grains, mode and system of twins, but also allows the user to correct or complete, if necessary, the analysis performed by the software. In addition, all raw and processed data are saved in a relational database. Consequently, all experimental parameters, microstructural data and twinning statistics are easily accessible via

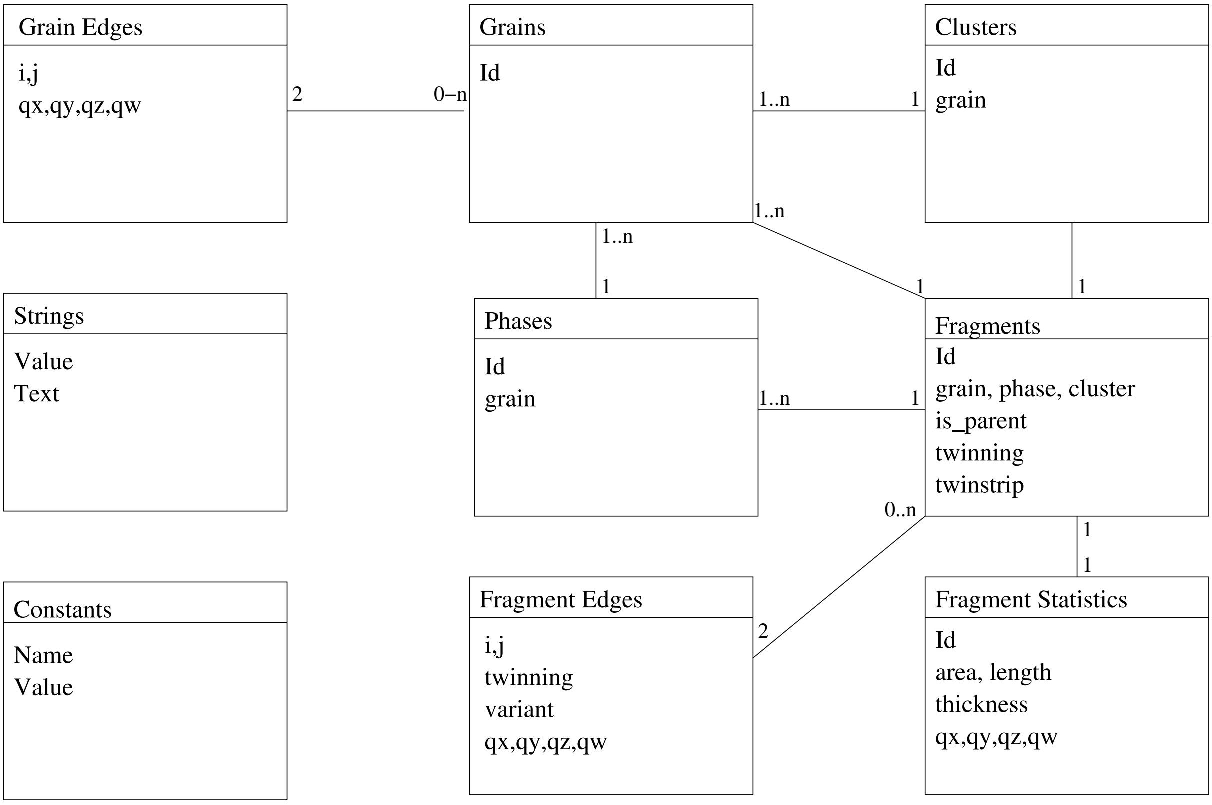

FIGURE 3.26 – Structure of the database used to store the EBSD analysis results. Boxes are database tables, edges with numbers indicates relations and the n-arity of these relations.

SQL requests. The database also enables the systematic quantification of the influence of a very large number of parameters. The constructions of such a database makes a significant difference compared to other pre-existing analysis tools.

Moreover, although the software was initially developed to perform statistical analyses on Mg and Zr scans, it is not limited to these two h.c.p. metals. Its algorithm is capable of identifying any twin occurring in h.c.p. materials on the condition that the user properly defines the c/a ratio and the theoretical disorientation quaternions corresponding to all potentially active twinning systems. For the analysis of other crystallographic structures, the user has to adapt the cell characteristics and modify the symmetry quaternions. For example, the authors are using the software for martensite identification, whose the crystallographic structure is tetragonal, in TRIP steels.

Chapitre 4

Identification of statistically representative data associated to nucleation and growth of twins

Sommaire

The objective of the present chapter is to provide new statistically representative data to establish relationships between the presence and size of twins and loading conditions, texture, etc. As shown in Chapter 2, from the micromechanical standpoint, one can -at the cost of relatively lengthy mathematical derivations- solve Eshelby type problems for relatively complex topologies. Similarly, constitutive models can be extended to reproduce the stochasticity associated with the nucleation of twins, double twins, etc. However, prior to resorting to such developments it is necessary to assess the statistical relevance of the phenomena to be modeled so as to distinguish between first and second order phenomena. In the present chapter, it is the objective to provide data by using the automated EBSD statistical analysis method presented in Chapter 3 to make such distinctions.

The following three phenomena will be studied : (1) nucleation and growth of "unlikely twins", (2) double extension twinning and (3) twin-twin junctions. Here "unlikely twins" refers to twin variants one would not expect to find in a given grain owing to its relatively poor orientation with respect to loading conditions. Both in the case of (1) and (2) current mean field models do not accurately reproduce these processes. The question at stake is that of the necessity of addressing this shortcoming. To this end a study will be performed on initially hot rolled AZ31 magnesium alloy [149, 150]. Regarding (3), so far the literature on twin/twin interactions has remained quite limited ; the objective is simply to assess whether twin-twin junctions do affect the selection of variants, and, more importantly, whether these have an effect at the macroscale on twin growth. This second study [11] will be performed on high purity Zr, as this material readily allows for the nucleation of four twin modes.

The present chapter is then organized such that its first part is dedicated to the formation of "unlikely twins" with a first sub-section about low Schmid factor tensile twins and a second one about successive double extension twins that can also be considered as another type of "unlikely twins". The two studies of "unlikely twins" include experimental, statistical and modeling results. The last part of the chapter is focused on the influence of microstructure and twin-twin junctions on the nucleation and growth of twins in Zr.

4.1 Preliminary notations and considerations

Because EBSD scans do not provide access to local stresses before unloading and sectioning, for classification purposes the geometric Schmid factors (SF) are computed from the inner product of the symmetric Schmid tensor and the normalized macroscopic stress tensor, such that $\|\Sigma\|^2 = \sum_{i=1}^{3}\sum_{j=1}^{3}\Sigma_{ij}^2 = 1$. In addition, similar statistics using the macroscopic stress for computations of distributions can be produced from the use of either full-field or mean field models. The symmetric Schmid tensor is defined as the symmetric part of the dyadic product between the Burgers vector and the normal vector to the deformation plane. For each twinned grain, the six possible twin variants of each twinning mode are classified in order of decreasing SF.

Low Schmid factor twins are here divided into two categories. The first type consists of twins with a negative Schmid factor. A twin is said to be a low Schmid factor twin of the second type when its Schmid factor is positive but lower than or equal to 0.3, and when the ratio of its Schmid factor to the highest twin variant Schmid factor possible in the considered twinned grain is lower or equal to 0.6. This ratio will be now referred to as the Schmid factor ratio.

4.2 Nucleation of "unlikely twins" : low Schmid factor twins and double twinning in AZ31 Mg alloy

4.2.1 Experimental set-up and testing conditions

The material used is initially hot-rolled AZ31 Mg with composition shown in table 4.1 and an initial grain size of 11.4 μm. The thick sheet was annealed at 400°C for 2 hours after rolling. Using XRD the initial pole figures of the material were measured. These are shown in Figure 4.4 where all three $\{0001\}$, $\{2\bar{1}\bar{1}0\}$ and $\{10\bar{1}0\}$ pole figures were recorded prior to and after loading. For the sake of brevity, the abbreviations RD, TD, and ND will stand for rolling, transverse and normal directions, respectively in the remaining of this chapter. As expected, prior to compression basal poles are centered around RD while the $\{10\bar{1}0\}$ and $\{2\bar{1}\bar{1}0\}$ poles are axi-symmetrically distributed about and perpendicular to RD. Using either a wheel saw or a diamond wire saw cubic samples with 10 mm edge length were cut from the as received plate. The diamond wire saw is preferred here, as it yields minimum changes on the microstructure during the cutting process (i.e. in particular it minimizes the number of twins induced by the cutting process).

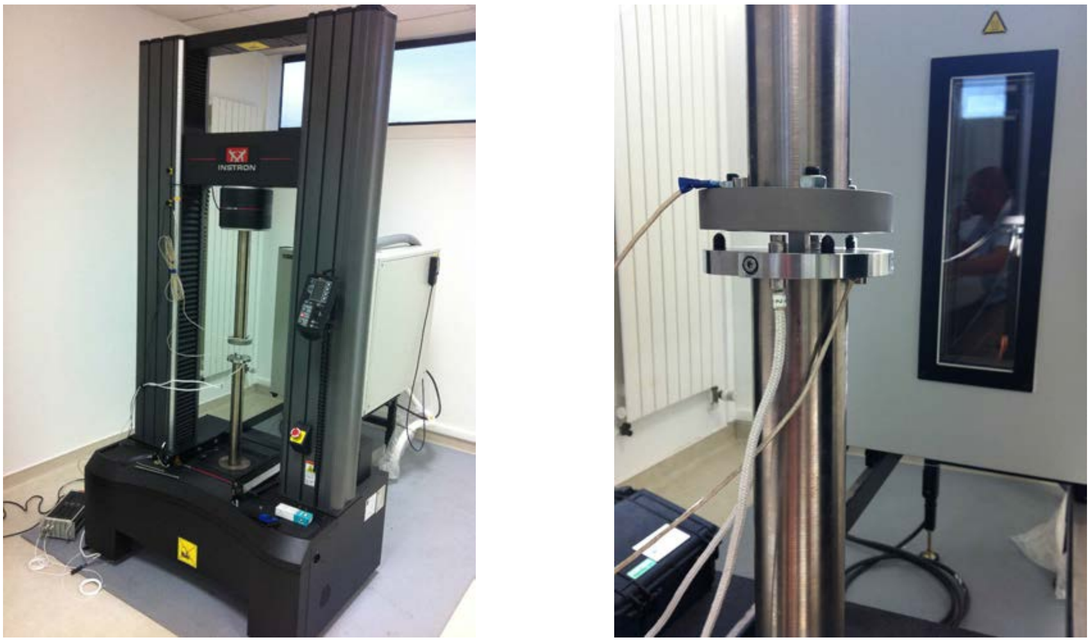

(a) (b)

FIGURE 4.1 – (a) Instron tensile-compression machine ; (b) Compression test at room temperature.

TABLE 4.1 – Chemical composition limits of AZ31B Mg alloy in $wt\%$

Al	Zn	Mn	Si	Cu
2.5-3.5	0.7-1.3	0.2 min	0.05 max	0.05 max
Ca	**Fe**	**Ni**	**Others**	**Mg**
0.04 max	0.005 max	0.005 max	0.30 max	balance

Two different testing conditions were defined to introduce low Schmid factor twins and secondary extension twins. In the first case, uniaxial compression was performed along the rolling direction up to 2.7% engineering strain. These tests were performed at room temperature with a strain rate of 10^{-3} s^{-1} (Figure 4.1). Clearly, a compressive load perpendicular to the basal poles is not expected to generate extension twins.

The second battery of tests aims to introduce, in a sequential fashion, $\{10\bar{1}2\}$-$\{10\bar{1}2\}$ double extension twins. To this end samples were subjected to more complex loading conditions. Three scenarios were considered ; three cubes were compressed along the rolling direction up to 1.8% strain ; three cubes were compressed along the transverse direction up to 1.8% strain and three cubes were compressed first along the rolling direction up to 1.8% strain and then compressed along the transverse direction up to 1.3% strain. Here too, the imposed strain rate was set to 10^{-3} s^{-1} (Figure 4.1). Table B.2 lists all test cases considered. It is expected here that the first loading path should initiate twinning and that the following compression enables the nucleation of secondary tensile twins.

TABLE 4.2 – Description of loading conditions

Sample Label	Loading Direction	Strain Rate (/s)	Temperature (K)
RD1	RD	0.001	25
RD2	RD	0.001	25
RD3	RD	0.001	25
TD2	TD	0.001	25
ND2	ND	0.001	75
ND3	ND	0.001	75
ND5	ND	0.1	25
ND6	ND	0.1	25
RD1TD1	RD thenTD	0.001	25
RD2TD2	RD thenTD	0.001	25
RD3TD3	RD thenTD	0.001	25

All tests were performed on the Instron 5985 floor testing machine shown in Figure 4.1. Its has a load capacity of 250 kN and a 1430 mm vertical test space. Tests were controlled with the software Bluehill III, and two LVDT capacitive sensors were used to measure displacement to an accuracy 0.4 μm. In Figure 4.1b, the two cylindrical devices correspond to the LVDT sensors, placed on each side of the cubic specimen and protected by three screws. In addition, teflon tape was used to minimize the effect of surface friction. As detailed in appendix B, the machine stiffness was systematically taken into account.

Following each compression, the samples were sectioned perpendicularly to the loading direction for microstructure analysis within the bulk. Sectioned faces were ground using SiC papers with grits from 2400 to 4000, and then were electrolytically polished in an electrolyte of 62.5% phosphoric acid and 37.5% ethanol at 3V for 30 seconds and then at 1.5V for 2 minutes at -15°C. A JEOL 6500F FEG SEM equipped with Channel 5 Analysis was used for EBSD measurements. Samples were scanned using a square grid with a step size of 0.1 μm and 0.3 μm for the first and second statistical analyses, respectively .

4.2.2 Mechanical behavior and microstructure evolutions

Figures 4.2 and 4.3 show the macroscopic stress-strain curves corresponding to specimens loaded in compression along RD, TD, ND and in compression along RD, followed by a second compression along TD. For compressions along RD and TD, the yield stress was approximately equal to 70 MPa. The inflection observed in the plastic region of the curves is typical of the activation of $\{10\bar{1}2\}$ tensile twins. As revealed by Proust et al. [32], the two deformation modes active in the matrix are basal slip and tensile twinning, with twinning increasing its contribution until about 3% strain while the basal slip activity decreases. At 5% strain, the total twinned volume is expected to occupy about 70% of the material volume.

This result is consistent with initial pole figures, showing that the initial texture of the material is not optimal for twinning activation when compressed along ND. Figure 4.3 reveals that after a first compression along RD the yield stress associated with compression along TD is no longer 70 MPa but approximately 115 MPa. Such a change can be explained by the presence of twin boundaries formed during the first compression, which act as barriers and

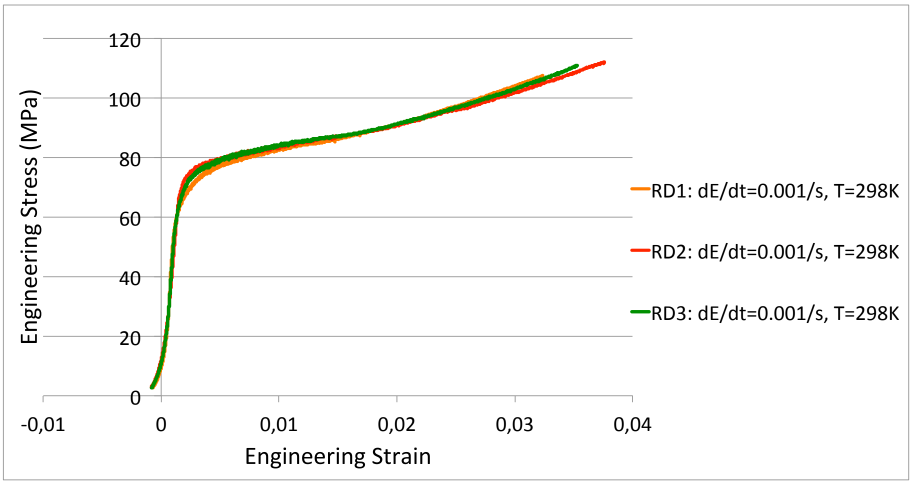

(a)

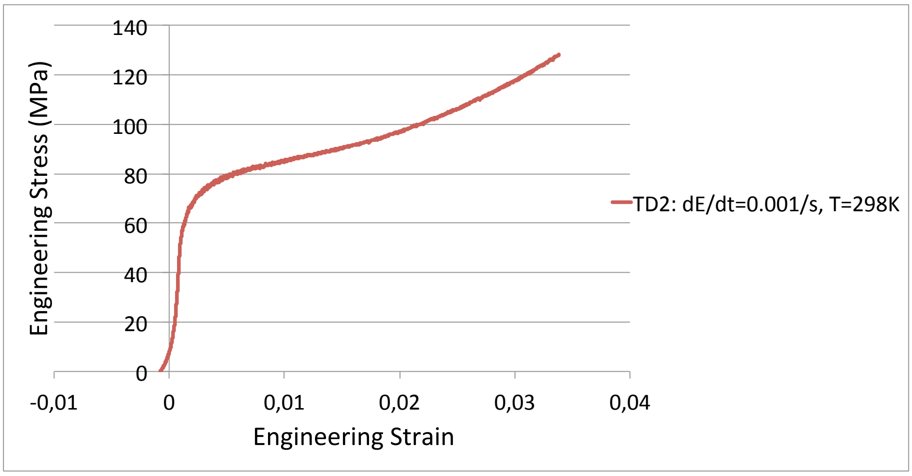

(b)

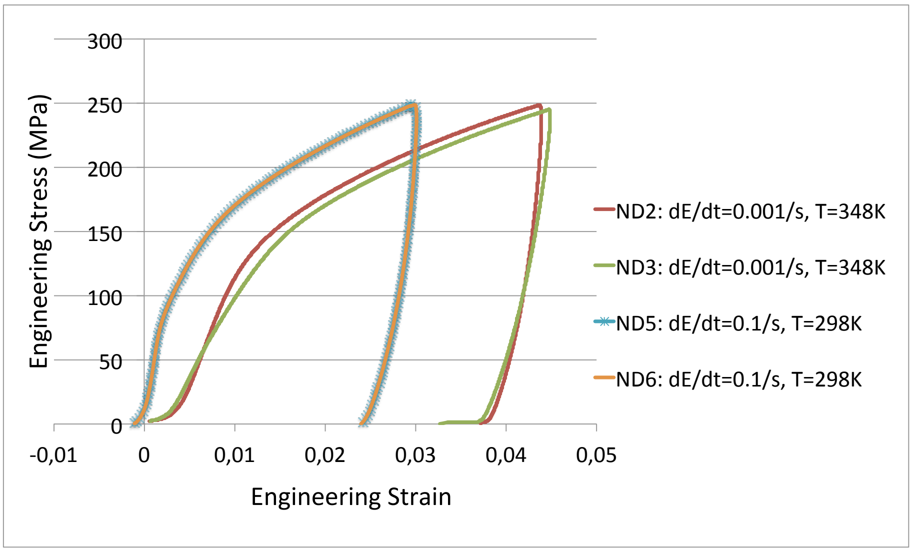

(c)

FIGURE 4.2 – Macroscopic stress-strain curves of specimens monotonically loaded in compression along RD (a), along TD (b) and along ND (c) at different temperatures and strain rates.

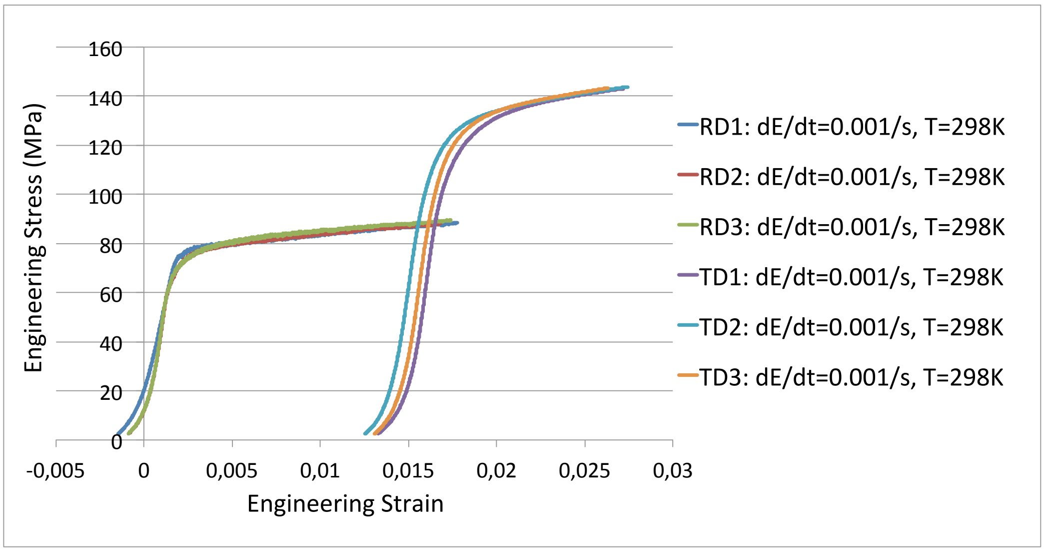

FIGURE 4.3 – Macroscopic stress-strain curves of specimens loaded in compression along the rolling direction followed by a second compression along the transverse direction.

prevent the glide of dislocations. Recent discrete dislocation dynamics simulations performed by Fan et al. [59] revealed that twin boundaries induce a stronger hardening than grain boundaries.

After uni-axial compression along TD and RD, basal poles move from the normal direction to the transverse and rolling directions, respectively. This texture change is due to the activation of tensile twinning, which induces a reorientation of the crystal lattice by 86.6°. As a result, a first compression along RD followed by a second compression along TD is expected to produce successive $\{10\bar{1}2\}$-$\{10\bar{1}2\}$ double extension twins.

Similarly, Figure 4.5 displays EBSD micrographs prior to compression, after compression along RD, and after compression along RD followed by a second compression along the TD.

4.2.3 Low Schmid factor $\{10\bar{1}2\}$ tensile twins

In this first study [149], a new type of selection criteria for low Schmid factor tensile twin variants based on strain compatibility considerations is proposed. The distinction is also made between tensile twins of groups 1 and 2, defined as twins intersecting the grain boundary and twins constituting a pair of cross-boundary twins, respectively.

The grain-by-grain analysis of 844 grains containing 2046 twins revealed that the Schmid factors of all twins range from -0.09 to a maximum value of 0.5. Twins with a negative Schmid factor represent 0.6% of all twins. Twins with a Schmid factor lower than 0.3 represent 23.4% of the total twin population. According to the definitions presented in the preliminary section, 127 twins can be deemed low SF twins, i.e. 26.6% of twins with a Schmid factor lower than 0.3 and 6.2% of all twins. As a result, low Schmid factor twins represent 6.8% of the total twin population. In addition, all twinned grains contain between 1 and 4 different twin variants. Twinned grains with 1, 2, 3 or 4 variants represent 62.6%, 30.3% and 7.1% of all twinned grains, respectively. The

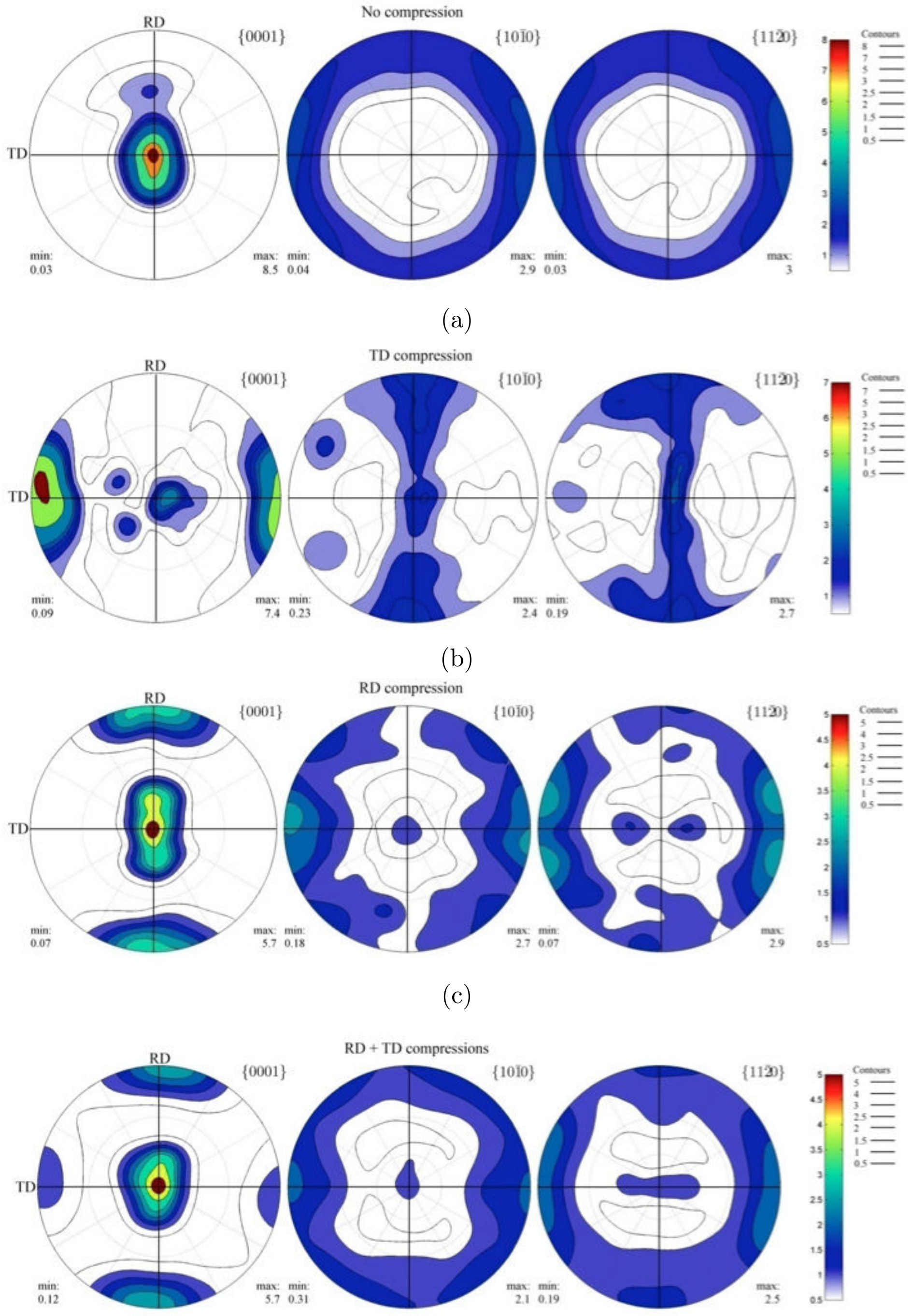

(a)

(b)

(c)

(d)

FIGURE 4.4 – (a) XRD $\{0001\}$, $\{2\bar{1}\bar{1}0\}$ and $\{10\bar{1}0\}$ pole figures of specimens before compression (a) and after compression along the transverse direction up to 4% strain (b), the rolling direction up to 1.8% strain (c) and along the rolling direction up to 1.8% strain and then along the transverse direction up to 1.3% strain (d).

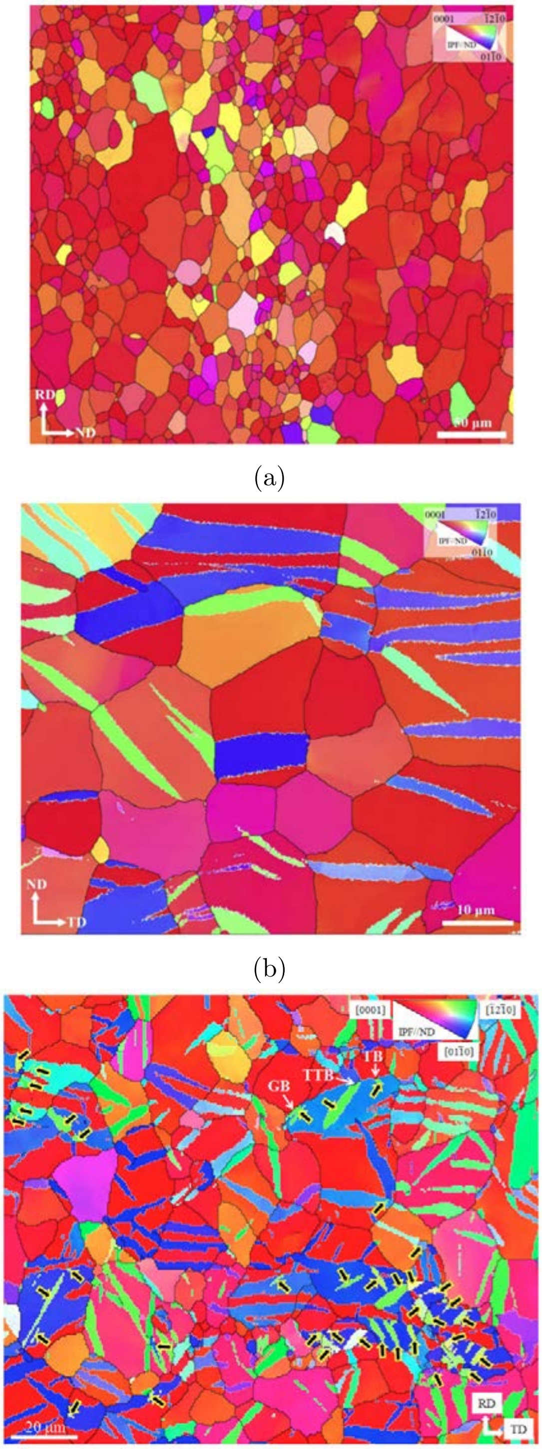

(a)

(b)

(c)

FIGURE 4.5 – (a) EBSD ND inverse pole figure micrograph of the specimen before compression along RD ; (b) Part of an EBSD orientation micrograph of a specimen compressed along the rolling direction up to 2.7% strain ; (c) EBSD orientation micrograph of a specimen successively loaded in compression along the rolling direction up to 1.8% strain and the transverse direction up to 1.3% strain. Black and yellow arrows indicate the presence of double extension twins.

analysis of twin Schmid factor revealed that the proportion of low Schmid factor per twinned grain increases with the number of activated twin variants. This was expected considering the second criterion defining a low positive Schmid factor.

As twinning participates significantly in plastic deformation, the relative contribution of twinning shears to the macroscopic strain tensor, ϵ, is here estimated from the normal components of stress-free distortion tensor of twins, E, expressed in the sample reference frame. The three coordinate axes of the sample reference frame are aligned with RD, TD and ND. The components of both the macroscopic strain and the distortion tensors along RD, TD and ND are denoted by ϵ_{RD}, ϵ_{TD}, ϵ_{ND} and e_{RD}, e_{TD}, e_{ND}, respectively. Since twinning does not involve any volume change, the trace of the twin distortion tensor is null. This implies that there exist six independent sign combinations for e_{RD}, e_{TD} and e_{ND}. These six combinations correspond to a new definition of twin variants. They are detailed, as well as their occurrence frequencies, in Table 4.3.

TABLE 4.3 – Classification of twins with respect to the sign of the normal components of the twin distortion tensor. The number of twins corresponding to each variant type and their occurrence frequency with respect to the total twin population are also indicated.

Variants	e_{RD}	e_{TD}	e_{ND}	Observed twins		Observed low SF twins	
				Number	%	Number	%
1	-	+	+	835	40.8	16	1.9
2	-	-	+	920	45.0	74	8.0
3	-	+	-	152	7.4	8	5.3
4	+	-	-	13	0.6	12	92.3
5	+	-	+	42	2.1	21	51.0
6	+	+	-	84	4.1	9	10.7

Table 4.3 reveals that low Schmid factor twins form more frequently in grains favoring the nucleation of twins producing an extension along the rolling direction, which is opposite to the strain induced by the compressive loading. The normal to the twinning plane's shear direction and the twinning plane normal can be written in a set of coordinate axes associated with the twin, i.e. reference axes are chosen parallel to the shear direction. The distortion tensor, $\mathbf{E^{tw}}$, corresponding to the deformation induced by twinning is then written as follows :

$$\mathbf{E^{tw}} = \begin{pmatrix} 0 & 0 & s \\ 0 & 0 & 0 \\ 0 & 0 & 0 \end{pmatrix}$$

with $s = 0.129$ [17].

The expression of the distortion tensor associated with a given tensile twin variant t and expressed in the reference frame of a potentially active deformation system, i, is denoted by $E^{t,i}$. As mentioned previously, two groups of low Schmid factor twins are here considered. Group 1 includes twins growing from the grain boundary. Group 2 contains twins forming a "cross-boundary" twin pair. Therefore, deformation systems i do not correspond to systems potentially active in the twinned grain but in the neighboring grain with which the observed low Schmid factor twin is in contact. The index i refers to basal slip, pyramidal slip, prismatic slip, tensile and compressive twinning systems. Then, in order to compare the characteristics of low Schmid factor twins in terms of strain accommodation with other tensile twin variants, the distortion tensor for each tensile twin variant t and for each of the 24 slip and twinning systems that could be activated in the neighboring grain was computed. This implied that, for each low Schmid factor twin, 144 different distortion tensors were calculated. The amount of strain to be accommodated by a given system i is assumed to be equal to the component e^i_{xz} of the distortion tensor $\mathbf{E^i}$, expressed in the reference frame of the system i. Therefore, the larger the component, the higher the ability of the system i to accommodate the twinning shear. It can also be interpreted as being a favorable factor for twin growth. This can be defined as a mean to approximate geometrical accommodation.

It resulted from data processing that group 1 low Schmid factor twins require the most accommodation through basal slip with the lowest CRSS and the least accommodation through pyramidal slip with the highest CRSS. It is also found that group 2 low Schmid factor twins require the least pyramidal slip or contraction twinning accommodations with high CRSS but the most accommodation through prismatic slip and tensile twinning. Note that CRSSs associated with prismatic slip and tensile twinning are both higher than the CRSS associated with basal slip and lower than CRSSs associated with pyramidal slip and compressive twinning.

4.2.4 Successive $\{10\bar{1}2\}$-$\{10\bar{1}2\}$ double extension twins

For the study of double extension twins, the total scanned area represents 0.82 mm^2. Therefore, 4481 grains were observed, none of them were in contact with the map border, as well as 11 052 primary tensile twins and 585 double extension twins. Further details are provided by Table 4.4. Note that double extension twins are 19 times less frequent than primary twins. In terms of twinned area, the difference is even more pronounced ; the total area occupied by secondary twins is 66 times smaller than the total area occupied by primary twins. EBSD scans performed on samples loaded in uniaxial compression along RD and TD did not contain any double extension twin. As a result, double extension twins only appear during the second compression along TD.

Table 4.4 – Main characteristics of grains, primary and secondary $\{10\bar{1}2\}$ tensile twins observed on EBSD maps of AZ31 Mg alloy specimens loaded in compression along RD and then along TD

Phase type	Number -	Area (x10^3 μm^2)	Area fraction (%)	Average diameter (μm)
Grains	4 481	823	100	16.34
Primary twins	11 052	230	27.94	5.24
Secondary twins	585	3.47	0.42	1.37

Considering crystal symmetries of hexagonal crystals, 6 $\{10\bar{1}2\}$ tensile twin variants and hence 36 $\{10\bar{1}2\}$-$\{10\bar{1}2\}$ double extension twin variants may be activated in Mg. However, based on the misorientation angle existing between the primary and secondary twins, these 36 variants can be grouped into 4 distinct sets, detailed in Table 4.5. The minimum angle associated with Group I twin variants is 0° because the twinning plane of the secondary twin coincides with the one of the primary twin. Over the 585 double extension twins experimentally observed, 383 were clearly identified, i.e. the difference between the theoretical misorientation angles of the two variants that best match the experimentally measured misorientation angle is smaller than 3°. Consequently, the study was limited to these 383 double extension twins.

TABLE 4.5 – Groups of possible double extension twins

Group	Axis-minimum angle pair	Number of variants
I	0°	6
II	$< 1\bar{2}10 >$ 7.4°	6
III	$< 0141\bar{4}1 >$ 60°	12
IV	$< 1\bar{7}80 >$ 60.4°	12

All identified secondary twins have a positive Schmid factor, and 78.1% of them have a Schmid factor greater than 0.3. Moreover, 95.8% of these secondary twins have a Schmid factor ratio, introduced in the previous sub-section, greater than 0.6 (Figure 4.6). As a result, activated tensile secondary twins have a relatively high Schmid factor compared to the Schmid factor of the other 5 potentially active tensile secondary twins.

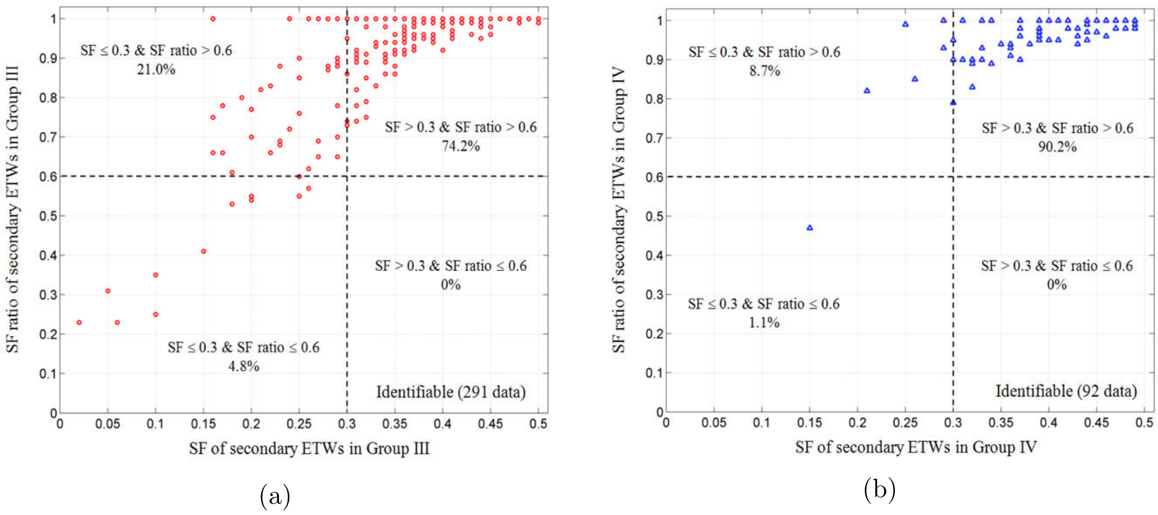

(a) (b)

FIGURE 4.6 – Scatter plots displaying the Schmid factor and Schmid factor ratio values of 291 Group 3 secondary twins (a) and 92 Group 4 secondary twins (b).

In addition, only 4.2% of the secondary twins can be qualified as "low Schmid factor" twins, as defined in the previous paragraph. The present study clearly shows that the activation of tensile secondary twins depends on both grain and primary twin orientations as well as loading direction. However, the Schmid factor analysis is not able to explain why 76.0% of secondary twins belong to Group III and 24.0% to Group IV. Schmid factors corresponding to variants of Group III and IV are always too close, i.e. their difference is lower than 0.05 in magnitude, to be meaningful and to be used as a selection criterion.

Elasto-static micromechanical analysis

In order to explain such a phenomenon, a simplified version of the elasto-static Tanaka-Mori scheme (Figure 4.7), described in the first section of Chaper 2, was developed. The simplification consists in assuming that the medium was homogeneous, isotropic and elastic. However, in addition to the simplifications induced by the assumption of homogeneous elasticity, considering an isotropic medium implies that the Eshelby type tensors, $\mathbf{S}(\mathbf{V_A})$ and $\mathbf{S}(\mathbf{V_B})$, can be expressed analytically [115, 50]. The purpose of the present analysis is the study of the variations of internal

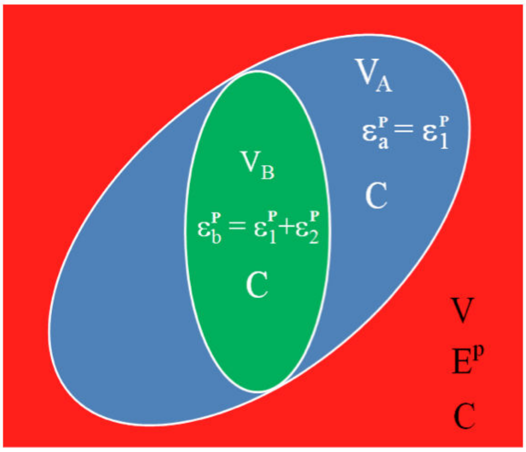

Figure 4.7 – Schematic representation of the simplified elasto-static Tanaka-Mori scheme. Second-order tensors $\mathbf{E}^\mathbf{p}$, $\epsilon_\mathbf{1}^\mathbf{p}$ and $\epsilon_\mathbf{2}^\mathbf{p}$ denote the macroscopic plastic strain imposed to the medium and plastic strains induced by primary and secondary twinning, respectively. The infinite matrix and primary and secondary tensile twins are represented by volumes $V - V_A$, $V_A - V_B$ and V_B, respectively. Second-order tensors $\epsilon_\mathbf{a}^\mathbf{p}$ and $\epsilon_\mathbf{b}^\mathbf{p}$ correspond to eigenstrains, modeling twinning shears induced by primary and secondary twinning, prescribed in inclusions $V_A - V_B$ and V_B, respectively. The homogeneous elastic tensor is denoted by the fourth-order tensor $\mathbf{C}$.

free energy induced by the formation of a tensile secondary twin. Twins are then represented by oblate inclusions embedded in an infinite homogeneous elastic medium. A uniform macroscopic plastic strain, $\mathbf{E}^\mathbf{p}$, is also introduced in the matrix in order to represent the deformation undergone by the specimen.

Double extension twin variants inducing the smallest change of elastic energy are assumed to nucleate preferentially. The change of elastic energy induced by the formation of the secondary twin is defined as the difference of free energies before and after secondary twinning, i.e. $\Delta\Phi = \Phi^{II} - \Phi^{I}$. Figure 4.8, and is expressed as follows :

$$\Delta\Phi = -\frac{V_B}{2V}\left[\Sigma : \epsilon_2^p + \mathbf{C} : \left([\mathbf{S}(\mathbf{V_A}) - \mathbf{I}] : [\epsilon_1^p : \epsilon_2^p + \epsilon_2^p : \epsilon_1^p - \mathbf{E}^\mathbf{p} : \epsilon_2^p] + [\mathbf{S}(\mathbf{V_B}) - \mathbf{I}] : \epsilon_2^p : \epsilon_1^p\right)\right] \tag{4.1}$$

where the second-order tensors ϵ_1^p and ϵ_2^p correspond to the plastic shear strains, assumed to be uniform, induced by primary and secondary twinning, respectively. They differ from ϵ_a^p and ϵ_b^p, defined as the uniform plastic strains present in inclusions $V_A - V_B$ and V_B, respectively. This explains why $\epsilon_a^p = \epsilon_1^p$ and $\epsilon_b^p = \epsilon_1^p + \epsilon_2^p$. Figures 4.8a and 4.8b show the evolution of the change of elastic energy normalized by the twin volume fraction V_B/V with respect to the applied stress and the secondary twin volume fraction, respectively. In the first case, the secondary twin volume fraction remains fixed and equal to 0.03 (Figure 4.8a) ; in the second case, the macroscopic stress, Σ^{TD}, is set to be equal to 100 MPa (Figure 4.8b). Figure 4.8a reveals that the change of free energy density is minimal with Group III double extension twin variants and maximal with Group II double twin variants. Figure 4.8b shows that the free energy density change associated with Group II double twin variants is the highest and increases rapidly with twin volume fraction. It also shows that, when the secondary twin volume fraction is greater than 0.03, the PV4-SV5 variant, belonging to Group III, exhibits the lowest normalized free energy variation and is then the most preferred energetically. Consequently, the variations of the internal free energy density

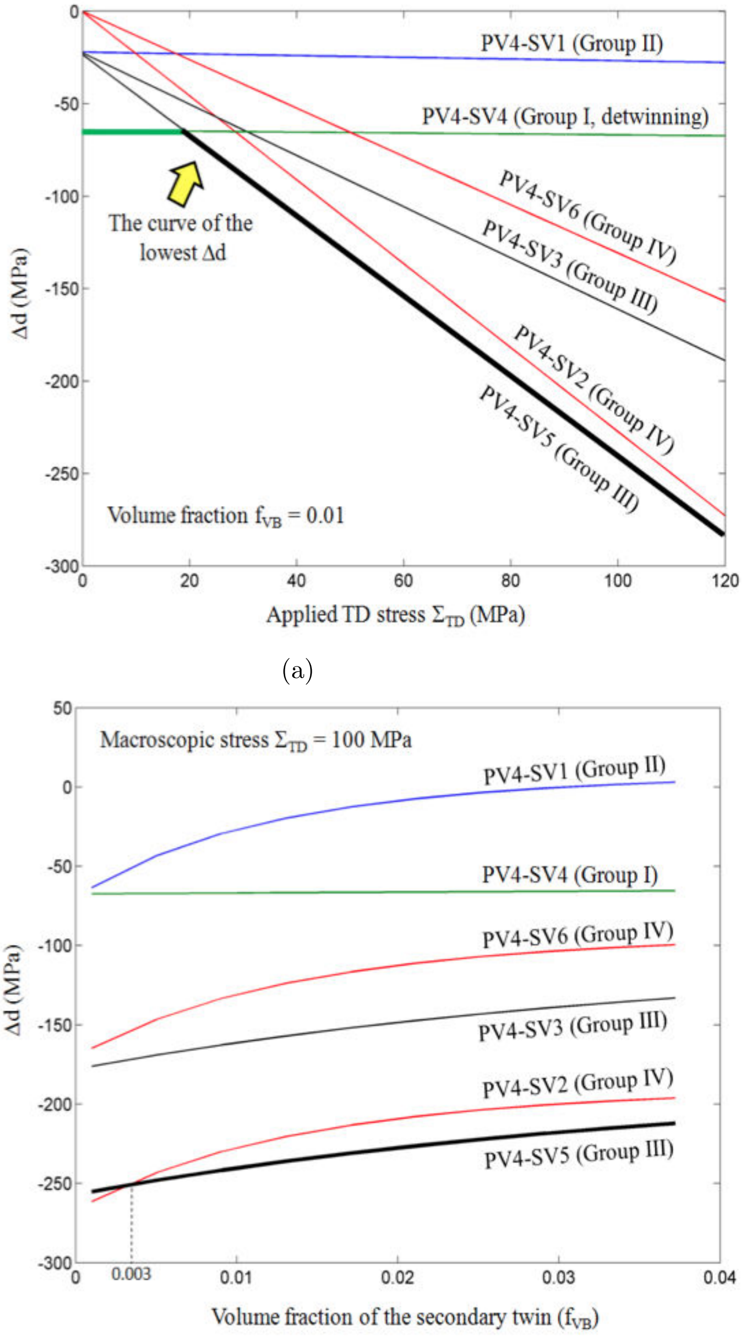

(a)

(b)

FIGURE 4.8 – Evolution of the change of elastic energy normalized by the twin volume fraction with respect to (a) the applied stress, Σ^{TD}, and (b) the secondary twin volume fraction, $f_{VB} = V_B/V_A$.

explain why Group III double twin variants are the most frequently observed and Group II double twin variants never observed. In addition, the comparison of predictions by the simplified double inclusion model and the classical Eshelby's scheme revealed that the classical single inclusion model derived by Eshelby is not capable of reproducing the trends obtained with the double inclusion model. Enforcing the topological coupling between the primary and secondary twins then appears as essential for accurate secondary twin activation predictions.

4.3 Probing for the latent effect of twin-twin junctions : application to the case of high purity Zr

4.3.1 Experimental set-up and testing conditions

The material used comes from a high-purity crystal bar Zr (<100 ppm) which was arc-melted, cast and clock-rolled at room temperature. Cuboidal samples were machined from the rolled plate and annealed at 823K for 1 hour. In the as-annealed state, grains are free of twins, equiaxed and have an average diameter equal to 17 μm. Specimens display a strong axisymmetric texture where basal poles are aligned within approximately 30 degrees of the through-thickness direction (Figure 4.9). Samples were deformed in an equilibrium liquid nitrogen bath at 76K in order to facilitate twin nucleation and loaded in compression along one of the in-plane directions to 5% strain (IP05) and along the through-thickness direction to 3% strain (TT03). Figure 4.10 shows the macroscopic stress-strain curves of cubes compressed along the through-thickness (TT) and in-plane (IP) directions.

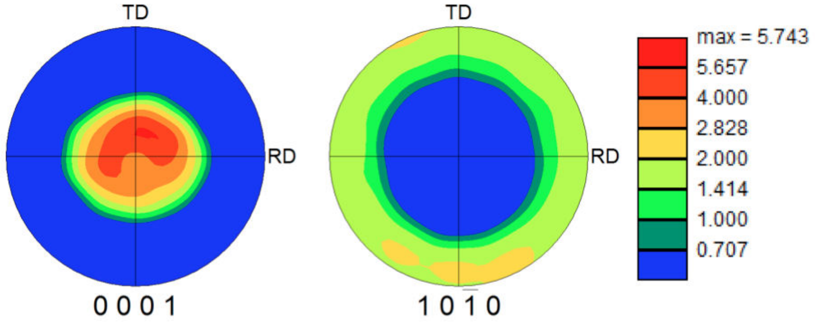

FIGURE 4.9 – Initial basal (0001) and prismatic (10-10) pole Figures of the clock-rolled high-purity zirconium studied in this work. The 3-axis is the through thickness direction of the plate.

Experimental data was collected from 10 and 4 (240 μm x 120 μm) scans at different locations on the same cross sectional area of the TT03 and IP05 samples (Figure 4.11), respectively. The section plane for TT03 analysis contains both the TT direction and IP direction, and the section plane for IP05 analysis contains the TT direction and the IP compression direction. Statistical data was obtained using the automated EBSD technique developed by Pradalier et al. [127]. The total analyzed area for TT03 and IP05 specimens is 205 736 μm^2 and 73 122 μm^2, respectively. Twins represent 9.1 % and 5.7 % of the total scanned area in the TT03 and IP05 samples, respectively. Incomplete grains bounded by scan edges are not considered in the statistical analyses.

Computing misorientations between measurement points and relying on graph theory analysis, the twin recognition EBSD software [127] is able to identify the four twin modes present in Zr

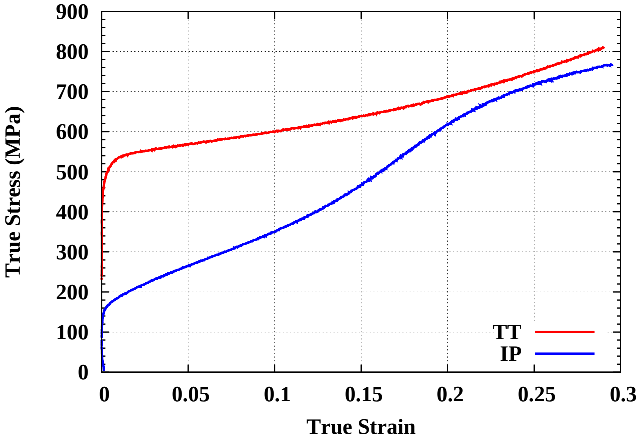

FIGURE 4.10 – Macroscopic stress-strain curves of high purity Zr samples loaded in compression along through-thickness (TT) and in-plane (IP) directions at 76K and 300K.

(Table 4.6). As highlighted by recent studies [144, 109], $\{11\bar{2}2\}$ compressive (C_1) twins and $\{10\bar{1}2\}$ tensile (T_1) twins are the most commonly observed twins in the TT03 and IP05 scans, with 74.4% and 81.7% respectively (Table 4.7). Table 4.7 also reveals that the second most active twinning modes are $\{10\bar{1}2\}$ (T_1) and $\{11\bar{2}1\}$ (T_2) in the TT03 and IP05 samples, respectively. In both cases, the second most active twin modes represent about 17% of the total number of twins. However, no $\{10\bar{1}1\}$ (C_2) twin was observed in the 14 scans.

TABLE 4.6 – Twinning modes in Zr. $\{10\bar{1}1\}$ (C_2) twins were not observed

Abbreviation	Twinning plane, K_1	Twinning direction, η_1	Misorientation (deg)
T_1	$\{1012\}$	$<1011>$	85.2
T_2	$\{11\bar{2}1\}$	$<\bar{1}\bar{1}26>$	34.9
C_1	$\{11\bar{2}2\}$	$<11\bar{2}\bar{3}>$	64.2
C_2	$\{10\bar{1}1\}$	$<10\bar{1}\bar{2}>$	57.1

Grain areas are directly calculated from the number of experimental points of the same orientation with a step size equal to 0.2 μm. As a result of the annealing treatment the grains are equiaxed. The grain area is computed by multiplying the number of measurement points that the grain contains by the area associated with a pixel, i.e. 0.1 μm^2. Grain diameter is estimated assuming a spherical grain. The software developed by Pradalier et al. [127] fits an ellipse to each twin. The measured twin thickness is defined as the minor axis of the ellipse. The true twin thickness is then estimated by multiplying the measured twin thickness by the cosine of the angle formed by the twin plane, K_1, and the normal to the sample surface [111, 110].

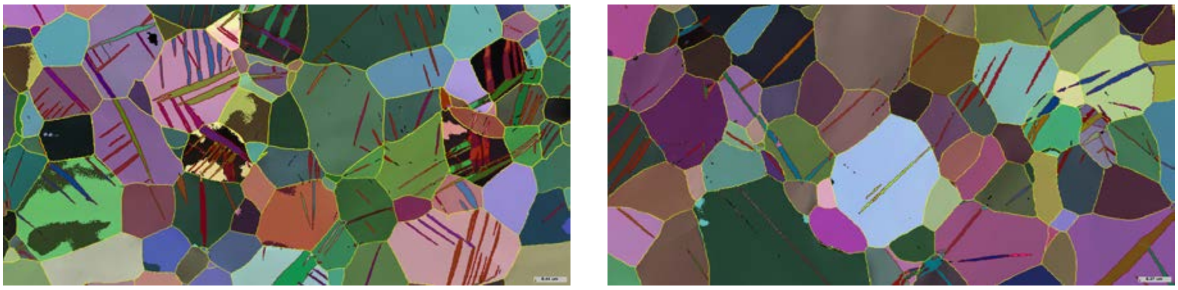

(a) (b)

Figure 4.11 – Examples of EBSD scans for specimens loaded in compression along the TT (a) and along one of the IP (b) directions.

Table 4.7 – Statistical data for twinned grains and twins in deformed TT03 and IP05 samples

Loading path	TT03		IP05	
Twin and grain type	Number	Frequency (%)	Number	Frequency (%)
All grains	1 200	-	361	-
Twinned grains	530	-	197	-
All twins	1 975	100.	514	100.
T_1 - $\{10\bar{1}2\}$	326	16.5	420	81.7
T_2 - $\{11\bar{2}1\}$	178	9.0	90	17.7
C_1 - $\{11\bar{2}2\}$	1471	74.5	3	0.58

While we can only detect fully formed twins with EBSD, their presence implies previous nucleation of such variant. To study twin nucleation, all grains (i.e. twinned and untwinned) that are not on the edge of the map are considered. Concerning twin growth, statistics are based on twinned grains solely. Figure 4.12 shows grain diameter and area distributions of specimens loaded along the TT and IP directions. Because the notion of "grain" is questionable for cases with very small numbers of measurement points, grains smaller than 4 μm^2 (i.e. 23 measurement points) are disregarded. In the following, data are represented as histograms. Histograms are consistent statistical tools capable of estimating density functions, but they do not directly address the issues of bias and variance. However, it is still possible to minimize the error introduced by the histogram representation. In the present article, bin sizes are estimated from Scott's formula : $w = 3.49\sigma.n^{-1/3}$ [151], where σ is an estimate of the standard deviation and n the number of elements considered, i.e. the total number of grains. The term $n^{-1/3}$ results from the minimization of the integrated mean squared error function. The main advantage of this expression lies in its insensitivity to the nature of the estimated density function (Gaussian, log normal, etc). Mean and standard deviation have been computed for area, diameter and SF distributions in TT03 and IP05 specimens. As a result, optimal bin widths for diameter, area and SF in TT03 samples are 63 μm^2, 2.5 μm and 0.06, respectively, and 112 μm^2, 4.1 μm and 0.06, respectively, in the case of IP05 maps. However, to be able to compare results obtained from both TT03 and IP05 maps, the same bin sizes have to be applied. In addition, we enforced the constraints that all distributions expressed with respect to diameter and area have the same number of subdomains and that every subdomain contains at least one element. Consequently, diameter and bin sizes used in the next histograms are 5.47 μm and 132 μm^2, respectively. To avoid empty columns, one grain larger than 1456 μm^2 observed in a TT03 scan was disregarded. Concerning distributions

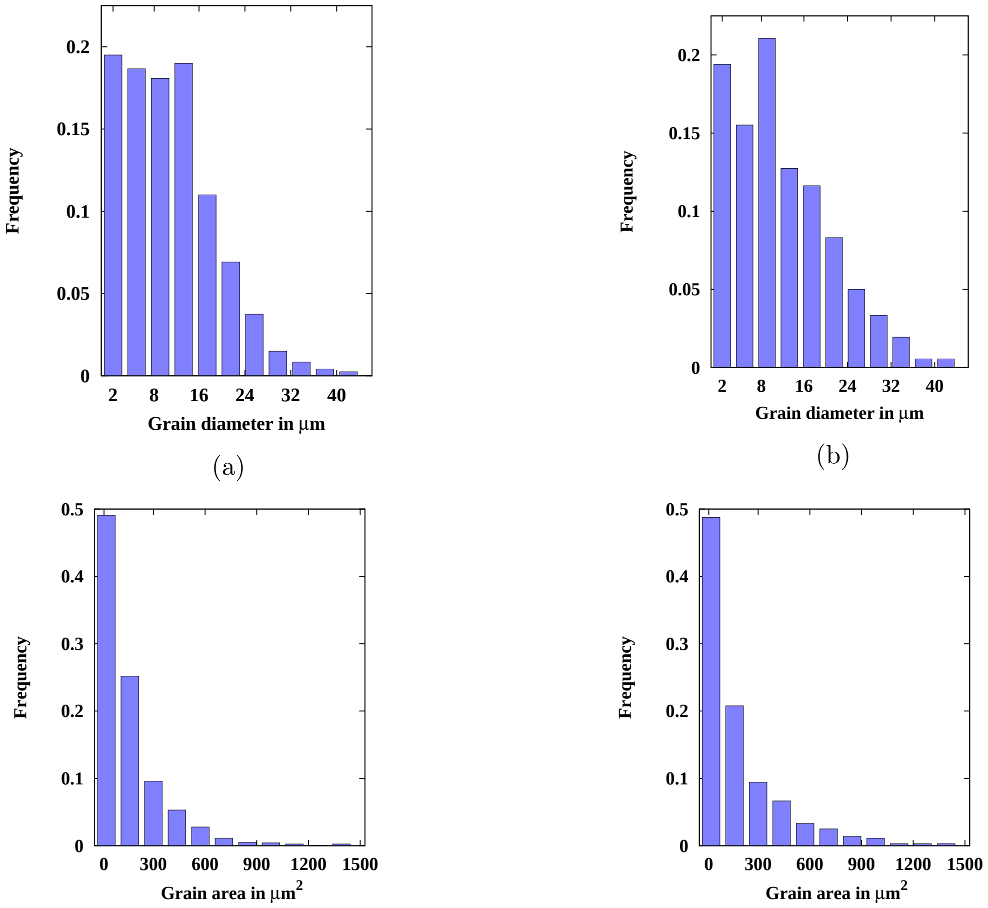

(a) (b)

(c) (d)

FIGURE 4.12 – Effective grain diameter (a,b) and grain area (c,d) distributions for TT03 (a,c) and IP05 (b,d) samples

plotted with respect to Schmid factor, the bin size was rounded down to 0.05 in order to obtain an exact integer number of subdomains between -0.5 and 0.5.

4.3.2 Twin-twin junctions statistics

This section is dedicated to the description of twin-twin junctions between first generation twins occurring in Zr. As mentioned in the previous section, 4 different twin modes are reported for Zr, which allows for 10 different junction modes. However, since only 3 twinning modes have been observed, 6 different twin-twin junction modes may occur. These are listed in Table 4.8. Depending on the twinning modes involved, each twin-twin junction mode contains 3 or 4 types. The distinction between the different twin-twin junction types is based on the value of the minimum angle formed by twin zone axes. The twin zone axis is here used to define the direction that is perpendicular to both the K_1 plane normal and the twinning shear direction, η_1. For example, 3 different types of T_1-T_1, T_1-T_1 and C_1-C_1 junctions exist : the first one corresponds to junctions between two twins sharing the same zone axis ; the second and third types correspond to junctions between twins for which the minimum angle formed by the two axes is equal to $2\pi/3$

and $\pi/3$ radians, respectively. In the case of $T_2 - C_1$ twin-twin junctions, 4 types of junctions are considered : 2 types corresponding to junctions between twins sharing the same zone axis and 2 other types for junctions between twins with non parallel zone axes. In the case of $T_1 - T_2$ and $T_1 - C_1$, 3 different types of junctions can be distinguished. None of them corresponds to junctions between twins with parallel zone axes. Minimum angles formed by twin zone axes are here equal to $\pi/6$, $\pi/2$ and $\pi/3$ rad. The 19 interaction modes and types observed in TT03 and IP05 scans are graphically represented in Figure 4.13.

Table 4.8 – Twin-twin junction frequencies for samples loaded in compression along the TT and IP directions

Loading path		TT03		IP05	
Type number	Twin-twin interaction type	Number -	Frequency (%)	Number -	Frequency (%)
1	$T_1 - T_1$	19	2.3	40	41.7
2	$T_1 - T_2$	49	5.9	50	52.1
3	$T_1 - C_1$	5	0.6	0	0.0
4	$T_2 - T_2$	12	1.4	6	6.2
5	$T_2 - C_1$	37	4.5	0	0.0
6	$C_1 - C_1$	709	85.5	0	0.0

The total number of twin-twin junctions observed in TT03 and IP05 scans is 833 and 96, respectively. Table 4.8 lists all possible twin-twin junctions modes in Zr, and, more relevant to this work, their observed occurrence frequencies. Frequencies are here defined as the ratio of the population of a given species to the overall population. Tables 4.7 and 4.8 show that in the case of specimens loaded along the through-thickness direction, whereby C_1 twins are most frequently observed, i.e. 74.5% of all twins, C_1 twins interact mostly with other C_1 twins. Furthermore, T_2 twins tend to interact with twins of different modes regardless the predominant mode since $T_2 - T_1$, $T_2 - C_1$ and $T_2 - T_2$ twin-twin junctions represent 5.9 %, 4.5 % and 1.4 % of all junctions appearing in TT03 maps and 52.1 %, 0 % and 6.2 % of all junctions observed in specimens loaded along the in-plane direction (IP05), respectively. In TT03 specimens, T_1 twins represent 16.5% of all twins (Table 4.7) but are only involved in 8.8% of all twin-twin junctions ; they also represent 31.4% of all twins embedded in single twinned grains (Table 4.9). Even when parent grains are suitably well oriented for T_1 twin nucleation, such as in the case of compression along the IP direction, $T_1 - T_1$ twin-twin junctions only represent 41.7% of all twin-twin junctions while T_2 twins, whose population is 4.7 times smaller, are involved in 58.3% of all twin-twin junctions. For both TT and IP specimens, the ratio of twins belonging to the most active twinning mode to the number of twins belonging to the second most active twinning mode is similar, i.e. 4.5 and 4.6, respectively. However, no statistical trend appears regarding the 3 types of twin-twin junctions that may occur between the first and second most active twinning modes.

Figure 4.14 shows twin-twin junction types for each mode whose frequency is greater than 4% in TT03 (Figures 4.14a, 4.14c, 4.14e) and IP05 (Figures 4.14b, 4.14d, 4.14f) scans. Notations are all detailed in the Appendix. Therefore, Figure 4.14c shows that, in the case of through thickness compression, 80 % of $C_1 - C_1$ twin-twin junctions correspond to the third type of junctions. Figure 4.14 also reveals that junctions between $T_1 - T_1$ twins with parallel zone axes, studied by Yu et al. [60, 62] in Mg single crystals, do not correspond to the predominant type of twin-twin junctions here. These results are purely qualitative, but they can be used as guidelines

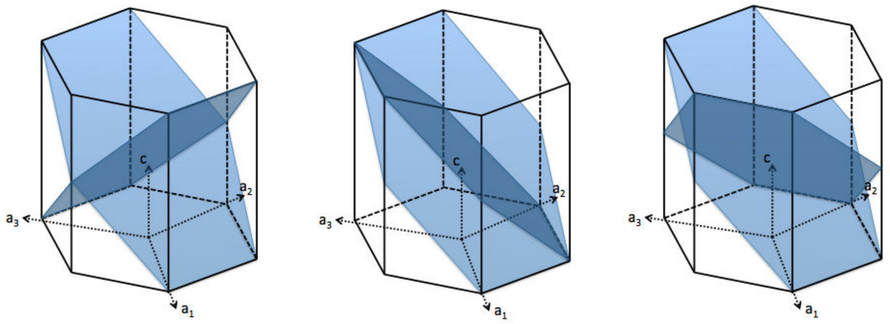

(a) $T_1 - T_1$ type 1 (b) $T_1 - T_1$ type 2 (c) $T_1 - T_1$ type 3

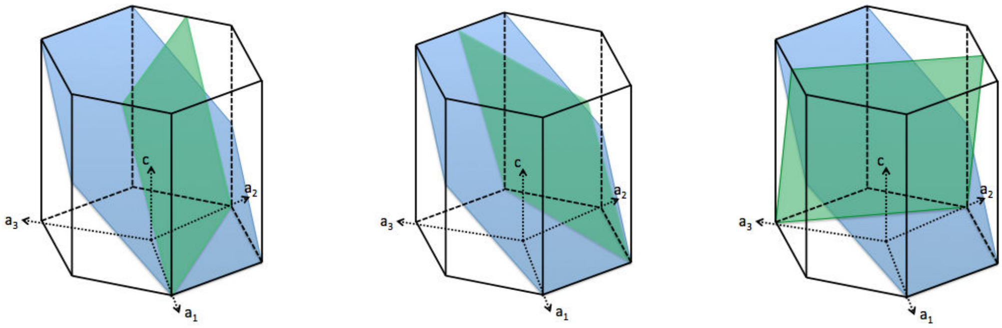

(d) $T_1 - T_2$ type 1 (e) $T_1 - T_2$ type 2 (f) $T_1 - T_2$ type 3

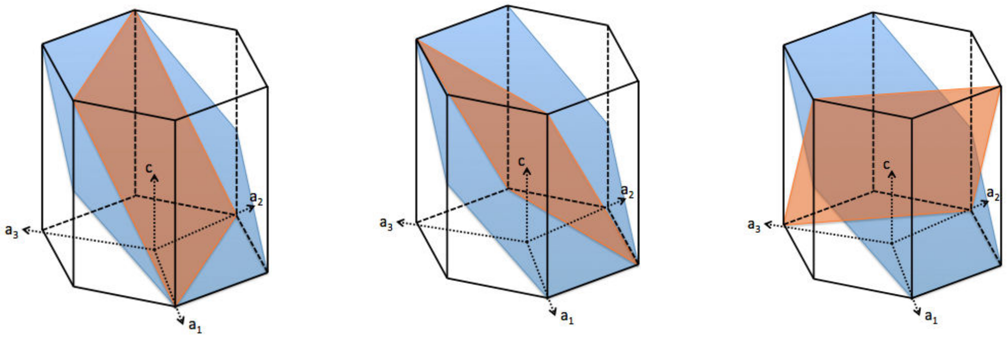

(g) $T_1 - C_1$ type 1 (h) $T_1 - C_1$ type 2 (i) $T_1 - C_1$ type 3

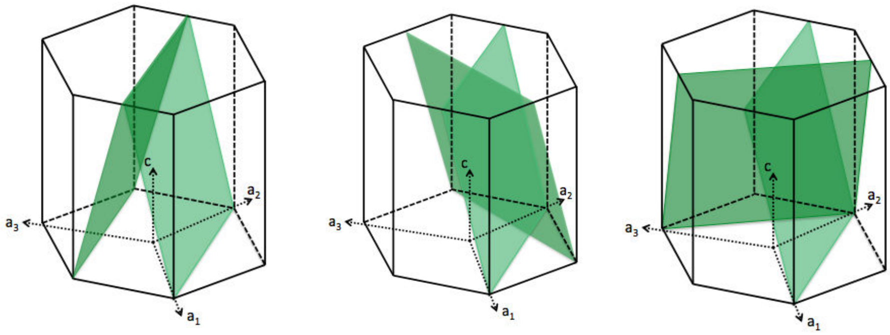

(j) $T_2 - T_2$ type 1 (k) $T_2 - T_2$ type 2 (l) $T_2 - T_2$ type 3

FIGURE 4.13 – Graphical representation of twin-twin junction modes and types observed in TT03 and IP05 Zr EBSD scans.

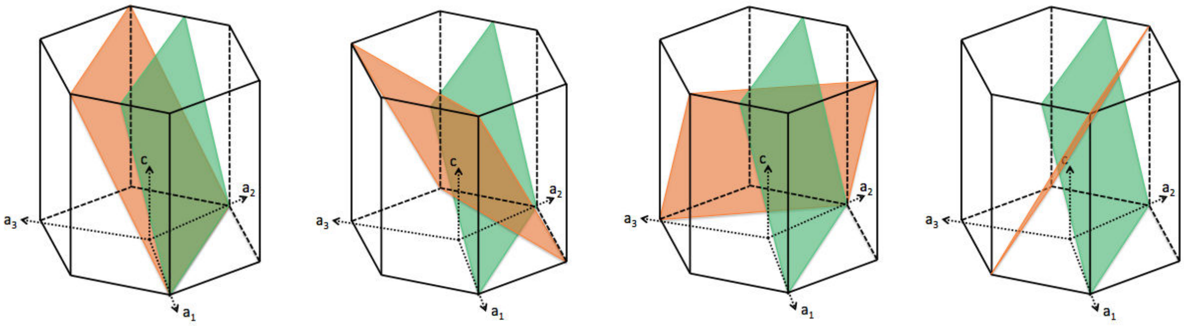

(m) $T_2 - C_1$ type 1 (n) $T_2 - C_1$ type 2 (o) $T_2 - C_1$ type 3 (p) $T_2 - C_1$ type 4

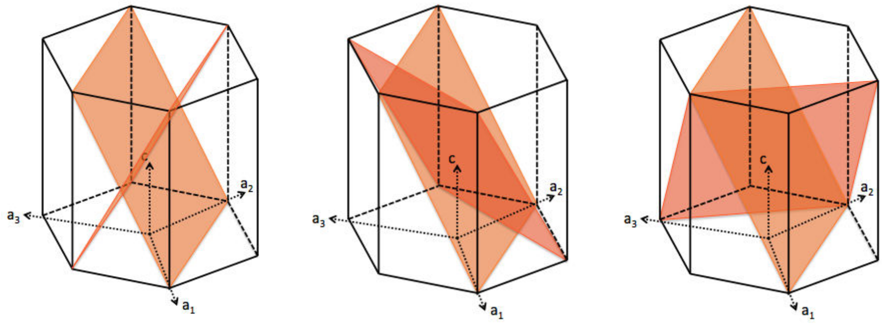

(q) $C_1 - C_1$ type 1 (r) $C_1 - C_1$ type 2 (s) $C_1 - C_1$ type 3

FIGURE 4.13 – Schematic representation of twin-twin junction modes and types observed in TT03 and IP05 Zr EBSD scans.

for molecular dynamic simulations by highlighting what types of twin-twin junctions should be considered for a given microstructure and loading path.

Influence of twin-twin junctions and grain-scale microstructural characteristics on twin nucleation and twin growth

The twinning process should be decomposed into three steps, starting with twin nucleation. This generally occurs at grain boundaries or local defects where internal stresses are highly concentrated. The second step corresponds to transverse propagation across the grain. Like a crack, the newly formed twin propagates very quickly until reaching another grain boundary or defect. Then, the third and last step is twin growth, consisting of twin thickening [152]. This section is dedicated to the study of statistics related to twin nucleation and twin growth. However, prior to any result, and as a complement to Table 4.7, Figures 4.15 and 4.18 present the distribution of twinning mode frequencies with respect to grain size and Schmid factor for specimens loaded along the TT and IP directions. Twinning mode frequencies are defined as the number of T_1, T_2 and C_1 twins contained in grains belonging to a given subdomain divided by the total population of twins. Notice that the larger number of twins associated with smaller grains should not be interpreted as a "reverse" Hall-Petch effect. Rather, it is a consequence of having a large number of small grains, as shown in Figure 4.12. Figures 4.12, 4.15 and 4.18 also indicate that certain bars are only representative of a few twins or a few grains. But, since most of statistics presented in this section rely on average values, the authors decided to not plot bars corresponding to averages performed over less than 3 twins and 3 twinned grains in histograms

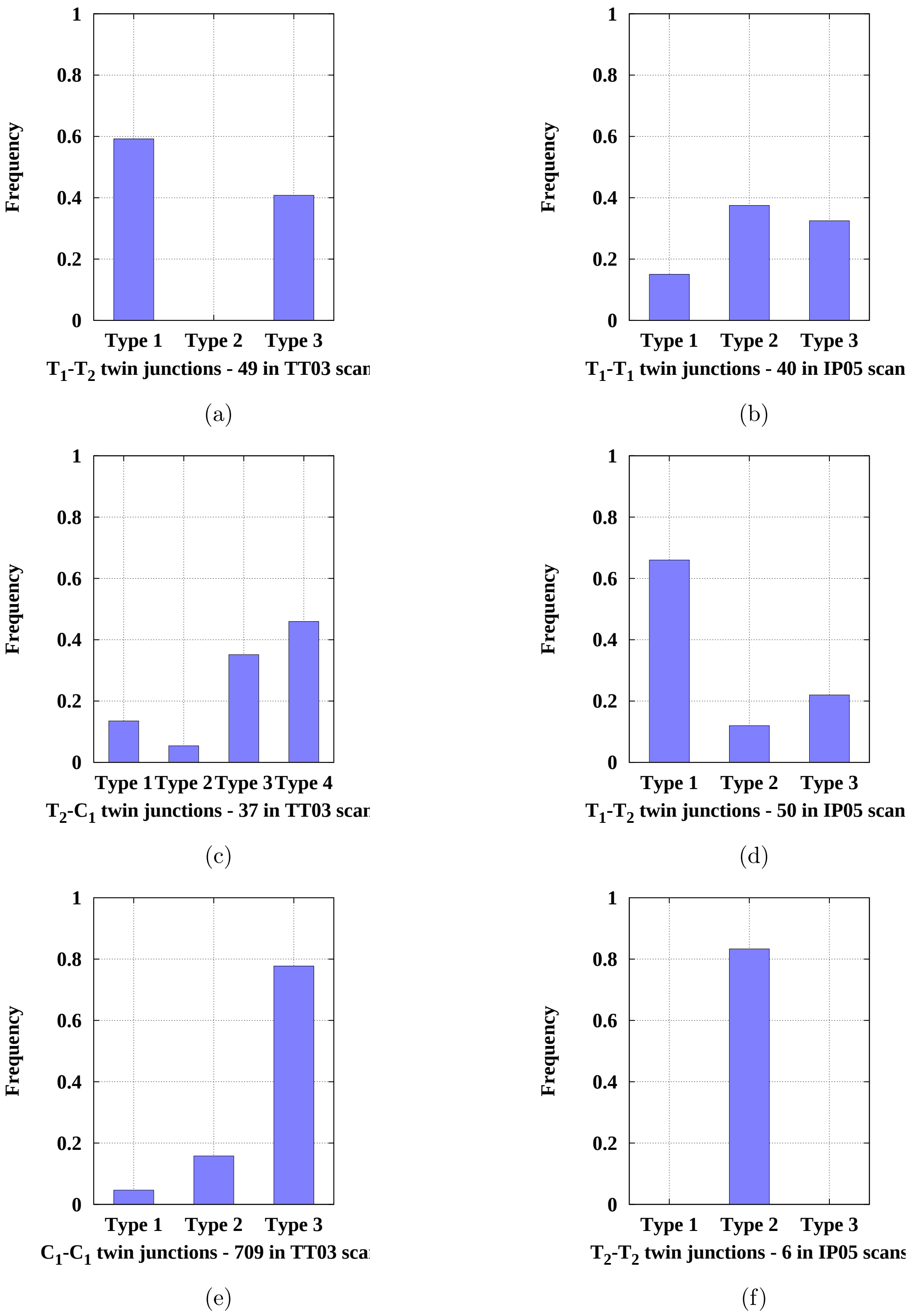

(a) (b)

(c) (d)

(e) (f)

FIGURE 4.14 – Modes and types of twin-twin junctions observed in EBSD scans of samples loaded along the TT-direction ((a),(c),(e)) and the in-plane directions ((b),(d),(f))

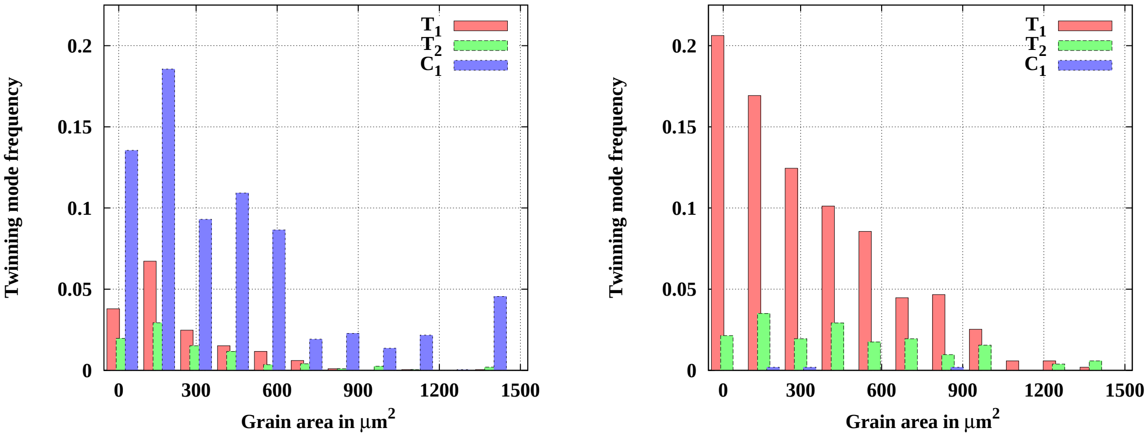

(a)

(b)

FIGURE 4.15 – Distribution of frequencies of T_1, T_2 and C_1 twins with respect to grain size in samples loaded along the TT (a) and the IP (b) directions.

displaying average twin thicknesses and average twin numbers per twinned grain, respectively.

Twin nucleation

Figure 4.16 shows the evolution of the fraction of twinned grains containing T_1, T_2 and C_1 twins as a function of grain area. Similar to previous statistical studies performed in Mg and Zr [109, 110], the present work also finds that twin nucleation can be correlated to grain size. However, Figure 4.16 not only establishes that the overall probability of twinning incidence increases with grain area but also differentiates the 3 cases corresponding to the different twinning modes observed in samples loaded in compression along the TT and IP directions. The influence of grain size on nucleation probability appears to be the strongest for C_1 and T_1 twins in TT03 and IP05 scans, respectively, since 100% of grains larger than 1060 μm^2 contain at least one twin of the predominant twinning mode while less than 50% of grains smaller than 136 μm^2 are twinned. In both TT03 and IP05 specimens, the effect of grain size on T_2 twin incidence is significant. The fraction of grains containing at least one T_2 twin increases rapidly and linearly with grain area, even if, in the case of samples compressed along the TT direction, T_2 does not correspond to the second most active twinning mode. Still note that about 10% of grains smaller than 136 μm^2 and 30% of grains larger than 664 μm^2 contain at least one T_1 twin in TT03 scans.

Figure 4.17 shows the distributions of the number of T_1, T_2 and C_1 twins per twinned grain with respect to grain size. While Figures 4.17a and 4.17b are histograms displaying averaged values, i.e. averaged numbers of twins, Figures 8c and 8d are scattergraphs displaying all values. Figures 4.17a and 4.17b clearly reveal that the average number of twins belonging to the predominant twinning mode increases with grain size. The phenomenon is more pronounced for C_1 twins in samples loaded in compression along the TT direction. However, the influence of grain size remains significant in the case of IP05 specimens : the average number of T_1 twins contained by grains whose areas are in the range [4 μm^2, 136 μm^2] and [534 μm^2, 664 μm^2] is equal to 1.5 and 4.9, respectively. This trend seems to change for grains larger than 928 μm^2. However, Figure 4.15b indicates that beyond 796 μm^2, averages are performed over fewer than 5 grains. The interest of

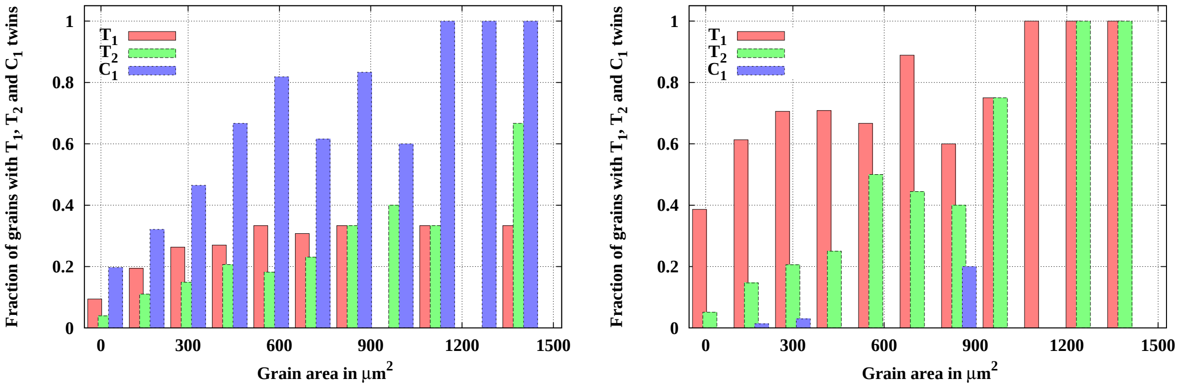

(a) (b)

FIGURE 4.16 – Distribution of the fraction of twinned grains containing T_1, T_2 and C_1 twins plotted with respect to twinned grain area for samples loaded along the TT (a) and the IP (b) directions.

Figures 4.17c and 4.17d lies in the observation that small grains can contain a very large number of twins. It also shows that the number of twins per twinned grain can vary significantly from one grain to another. However, EBSD scans are images of 2D sections. As a result, it is possible that small grains are actually bigger than they seem to be. This introduces a bias in grain size effect statistics.

TABLE 4.9 – Frequencies of twins contained in single twinned grains for TT03 and IP05 samples

Loading path	TT03		IP05	
Twin category	Number	Frequency (%)	Number	Frequency (%)
All single twinned grains	176	-	73	-
T_1	55	31.4	62	84.9
T_2	18	10.3	8	11.0
C_1	102	58.3	3	4.1

Nucleation of twins belonging to the predominant twinning mode is strongly controlled by grain orientation and macroscopic stress direction. As indicated by a classic Schmid factor analysis (Figure 4.18), 91% and 76% of C_1 and T_1 twins, respectively, have a Schmid factor greater than 0.25. Figure 4.19 also shows that 21% and 42% of C_1 and T_1 twins observed in specimens loaded along the TT and IP directions correspond to the 1^{st} Schmid factor variant, denoted by v_1, respectively. Regarding the activation of twins belonging to the second most active twinning mode, the dependence on grain orientation and loading direction is less obvious. The phenomenon is particularly striking in the case of T_1 twins in TT03 specimens since 55% of T_1 twins exhibit a negative Schmid factor (Table 4.10) and 26% of them correspond to either the 4^{th}, 5^{th} or 6^{th} variants. For T_2 twins observed in IP05 scans, 38% have a Schmid factor lower than 0.25, and 20% correspond to either the 4^{th}, 5^{th} or 6^{th} variants. Figure 4.18 and Table 4.10 also reveal that the proportion of T_2 twins with a negative Schmid factor remains low (i.e. 11% and 8% in the case of TT and IP compressions, respectively) irrespective of the loading direction. The activation of twins with negative SF is a result of using the macroscopic stress to define SF. In practice, this result is pointing at large local deviations from the macroscopic stress in the grains involved.

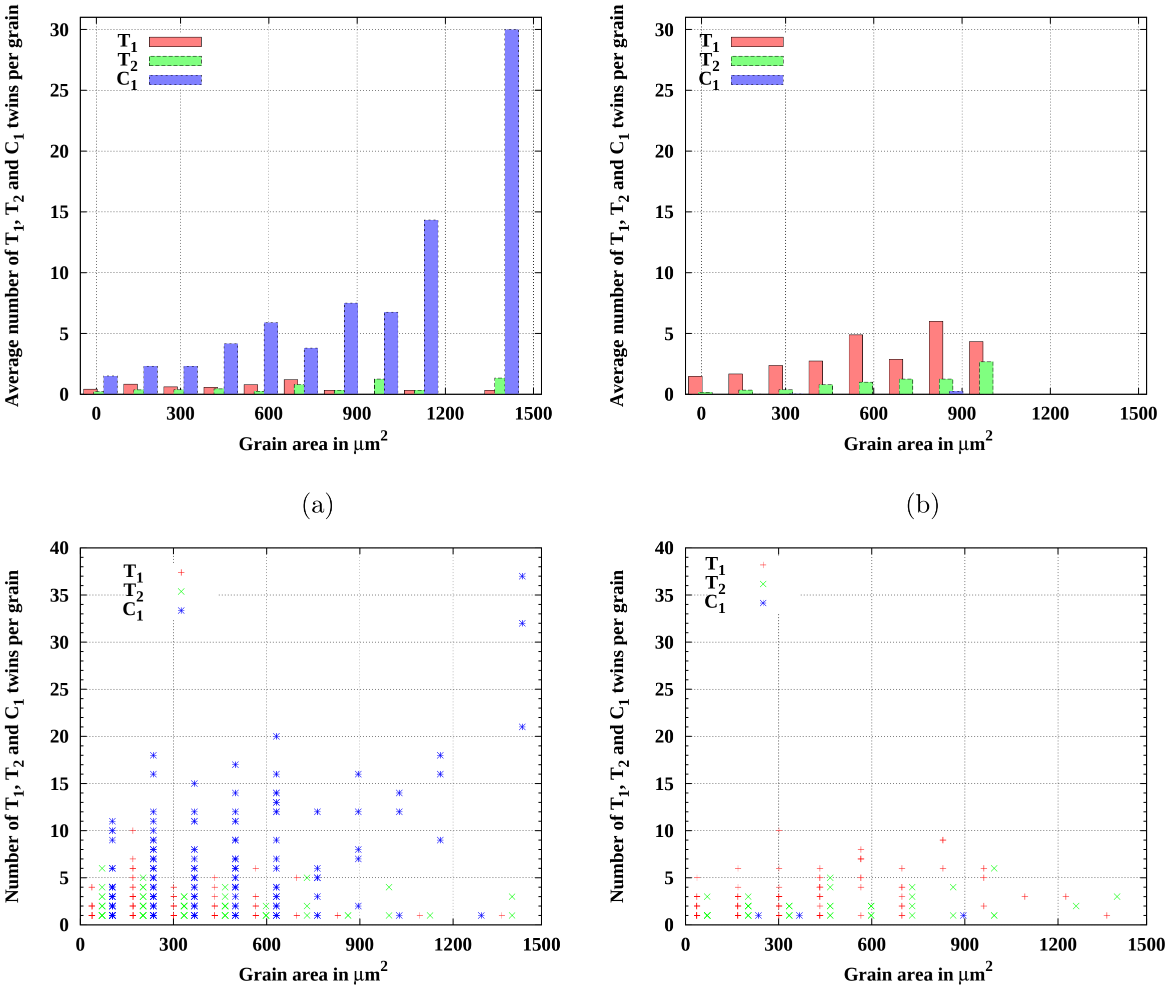

(a)

(b)

(c)

(d)

FIGURE 4.17 – Distribution of the number of T_1, T_2 and C_1 twins per twinned grain for TT03 (a) and IP05 (b) samples and scattergraphs displaying the number of C_1, T_2 and C_1 twins embedded in parent phases with respect to twinned grain area for TT03 (c) and IP05 (d) samples. Each cross represents one single twin. But because twin numbers are integers, many crosses overlap.

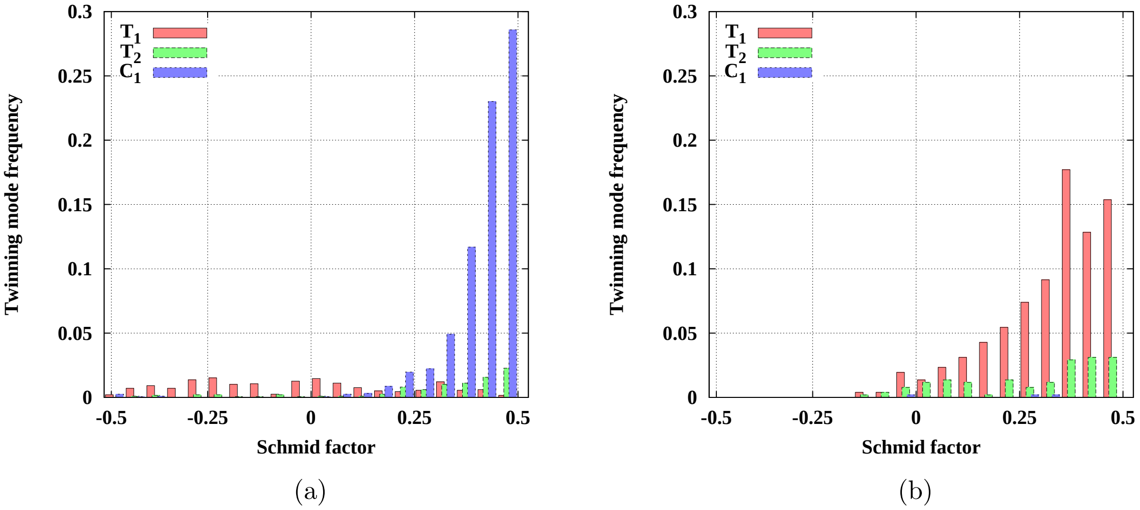

(a) (b)

FIGURE 4.18 – Distribution of SF values corresponding to twins activated in samples loaded along the TT-direction (a) and the IP-direction (b).

TABLE 4.10 – Twins with negative SF and their relative frequencies and twinned areas in TT03 and IP05 samples

Loading path		TT03			IP05	
Twin mode	Number -	Rel. freq. (%)	Rel. twinned area (%)	Number -	Rel. freq. (%)	Rel. twinned area (%)
All	211	10.7	3.9	22	4.3	4.9
T_1	180	55.2	43.7	14	3.3	0.6
T_2	20	11.2	8.4	7	7.7	19.5
C_1	8	0.5	0.2	1	33.3	68.2

Twin growth

Twin growth is considered to be the last step in the twinning process, consisting in twin lamella thickening. The influence of grain orientation, grain size and twin-twin junctions is investigated via histograms presenting twin thickness distributions with respect to grain area and Schmid factor. Following the same approach as the one used for twin nucleation, Figure 4.20 shows statistics of twin true thicknesses as a function of grain size. Figures 4.20a and 4.20b are histograms displaying average twin true thicknesses sorted by twinning mode. In the case of the TT compression, T_1 twin thickness average is always close to 0.5 μm. The value of C_1 average twin thickness appears to first increase until grain size reaches 928 μm^2 and then to decrease ; the values corresponding to the first and last bin are 0.64 and 0.71 μm, respectively. In the case of the IP compression, the T_1 twin thickness average oscillates around 0.75 μm. As a result, it is not possible to identify a correlation between twin thickness, twinning mode and twinned grain area. However, Figure 4.20 also reveals that the average thickness of twins belonging to the most active mode is always greater than the average thickness of twins belonging to the second most active mode. Figures 4.20c and 4.20d consist of scattergraphs that display all true thicknesses of twins observed in samples loaded along the TT and IP directions. The spread is significant and does not follow any pattern. Fluctuations may be associated with neighbor effects on twin

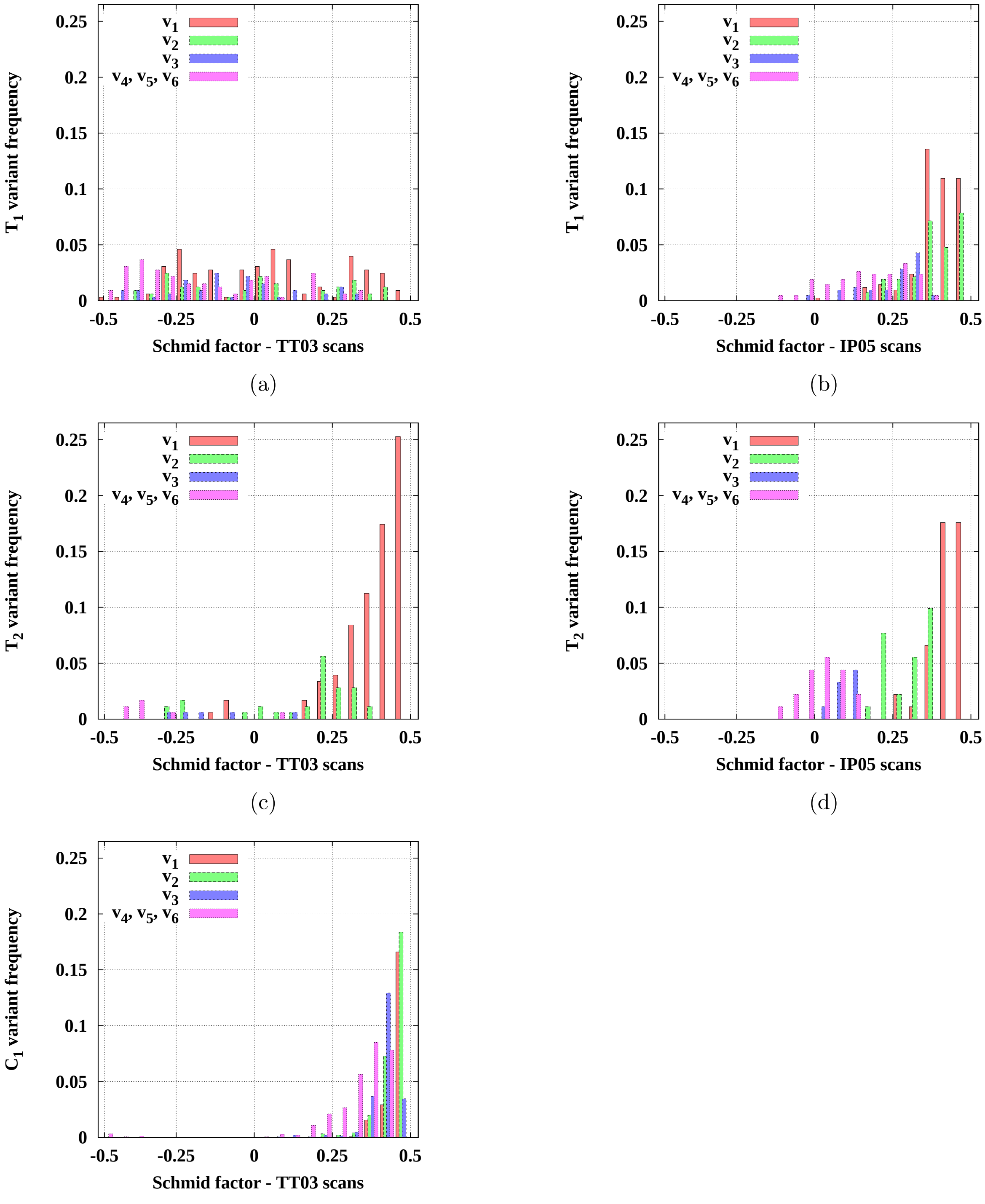

(a)

(b)

(c)

(d)

(e)

FIGURE 4.19 – Distribution of variant frequencies of T_1 (a), T_2 (c) and C_1 (e) twins in TT03 scans and of T_1 (b) and T_2 (d) in IP05 scans, respectively, with respect to their Schmid factor. Variant frequencies consist of the ratio of the number of twins of a given SF variant and of a given twinning mode to the total population of twins belonging to the considered twinning mode.

growth. Numerical support for such effects is provided by Kumar et al. [152] and based on shear accommodation and stress considerations. Large thickness values observed in small grains also suggest that using 2D variables to describe spatial phenomena introduces a bias in grain size effect statistics. The same comment was made in the paragraph dealing with twin nucleation.

Disregarding negative Schmid factor twins (Figure 4.18), the influence of the crystallographic orientation on growth of twins belonging to the predominant mode is clearly shown in Figure 4.21. Figure 4.21 presents the distribution of twin thickness sorted by twinning mode with respect to Schmid factor. The average true twin thickness of C_1 and T_1 twins increases with increasing Schmid factor values in TT03 and P05 specimens, respectively. This indicates that the macroscopic stress is the major driving force for twin growth in the case of first most active twinning modes. However, similar to observations made about twin nucleation, the influence of grain orientation and macroscopic stress direction is reduced for twins belonging to the second and third most active twinning modes. As a result, mechanisms involved in the growth of twins belonging to the predominant twinning mode are likely to be different from those responsible for the growth of other twins. Beyerlein et al. [110] and Capolungo et al. [109] argue that if backstresses induced by neighboring grains in reaction to the localized twin shear are independent of orientation, then twins with higher SF, and hence with higher resolved shear stress, have an advantage to overcome this shear reaction.

Finally, to highlight the influence of twin-twin junctions on twin thickening in a statistically meaningful manner, the comparison of twin thicknesses between single twinned (also referred to as mono-twinned grains in Figures 4.22 and 4.23) and multi-twinned grains is performed for C_1 twins in TT03 specimens. A multi-twinned grain is, here, defined as a twinned grain containing several twins. In the TT03 scans, 102 and 1369 twins in single twinned and multi-twinned grains were observed, respectively (see Tables 4.7 and 4.9). Figures 4.22b and 4.23b show the distribution of twins embedded in single twinned and multi-twinned grains as a function of grain area and Schmid factor. They are aimed at indicating the statistical relevance of data about twins contained by single twinned grains. Figure 4.23a presents the distribution of averaged twin thicknesses embedded in both single twinned and multi-twinned grains as a function of Schmid factor values. Figure 4.23a clearly shows that the average twin thickness of twins embedded in single twinned grains is greater than or equal to the average twin thickness of twins contained by multi-twinned grains irrespective of grain orientation. This phenomenon appears more clearly for high and mid-high Schmid factor values, i.e. $SF > 0.25$. As previoulsy mentioned, Figure 4.23b shows that bars associated with negative Schmid factors apply to only a few single twinned grains. Moreover, Figure 4.23a shows that similar to multi-twinned grains, the thickness of twins contained in single twinned grains does not depend on grain area. However, the latter is generally greater than the average twin thickness of twins in multi-twinned grains. Figure 4.22b also shows that almost all the single twinned grain areas are smaller than 664 μm^2. Such a result was expected due to the influence of grain size on twin nucleation.

4.4 Conclusion

The statistical analyses performed on Mg AZ31alloy EBSD scans were aimed at determining activation criteria of two distinct types of "unlikely twins", i.e. low Schmid factor twins, defined as twins with either a negative Schmid factor or a Schmid factor smaller than 0.3 and a ratio of the Schmid factor to the highest twin variant Schmid factor possible in the considered twinned grain lower or equal to 0.6, and double extension twins. As implied by their designation, the

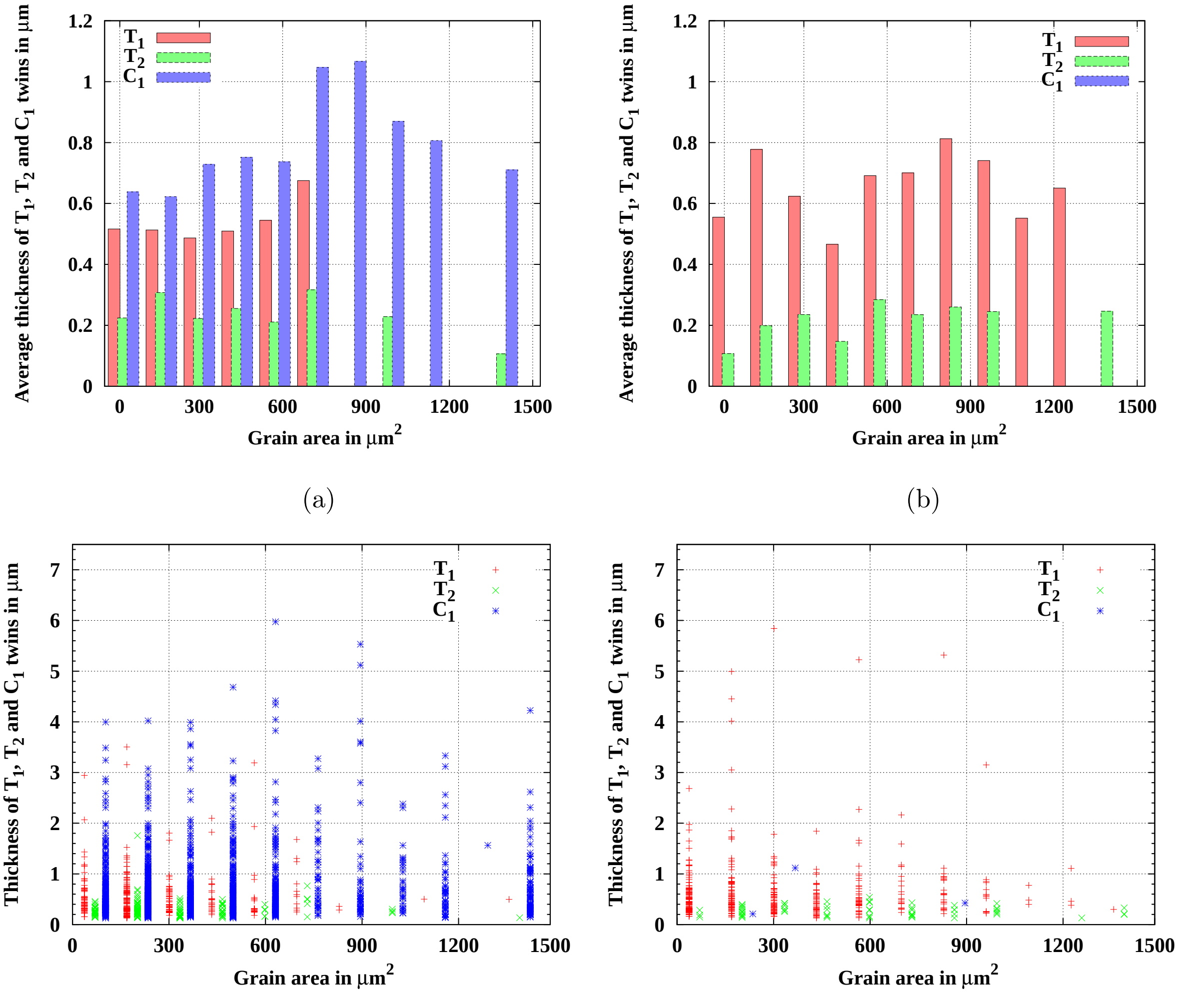

(a)

(b)

(c)

(d)

FIGURE 4.20 – Distribution of average twin thicknesses as a function of grain size in samples loaded along the TT (a) and the IP (b) directions and scattergraphs displaying twin thickness values with respect to grain size in samples loaded along the TT (c) and the IP (d) directions. Each cross represents one twin.

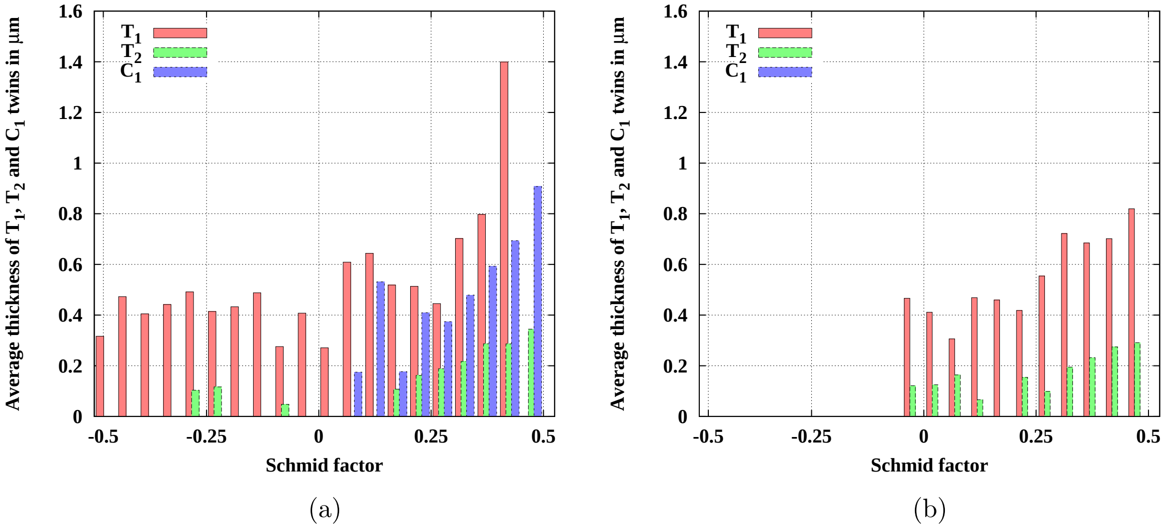

(a)

(b)

FIGURE 4.21 – Distribution of average twin thicknesses as a function of SF values in samples loaded along the TT (a) and the IP (b) directions.

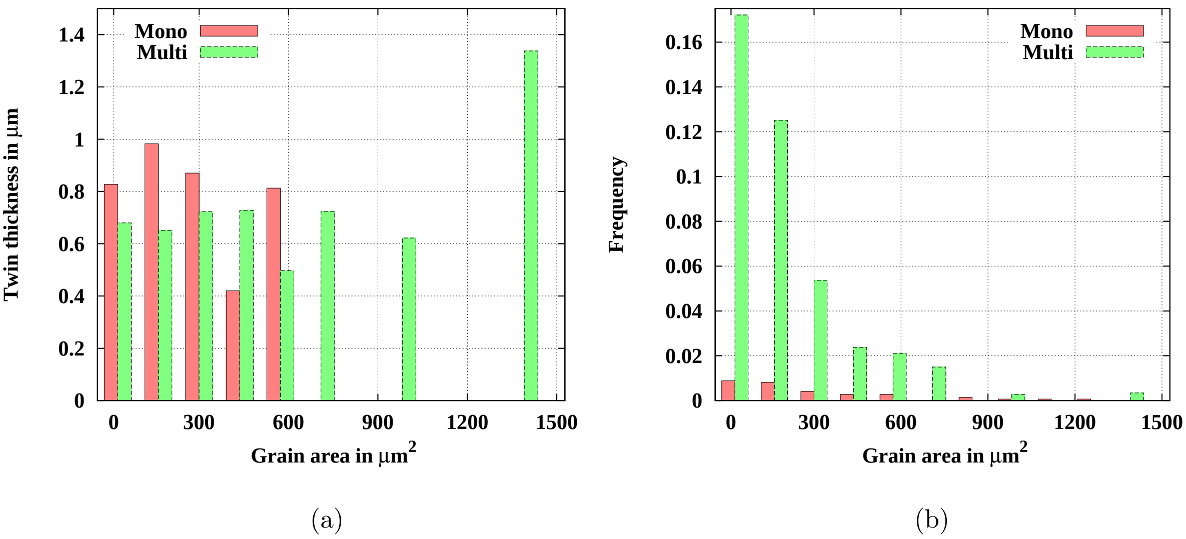

(a)

(b)

FIGURE 4.22 – Distribution of the twin thickness (a) and the frequency (b) of C_1 twins with respect to grain area in samples loaded along the TT direction.

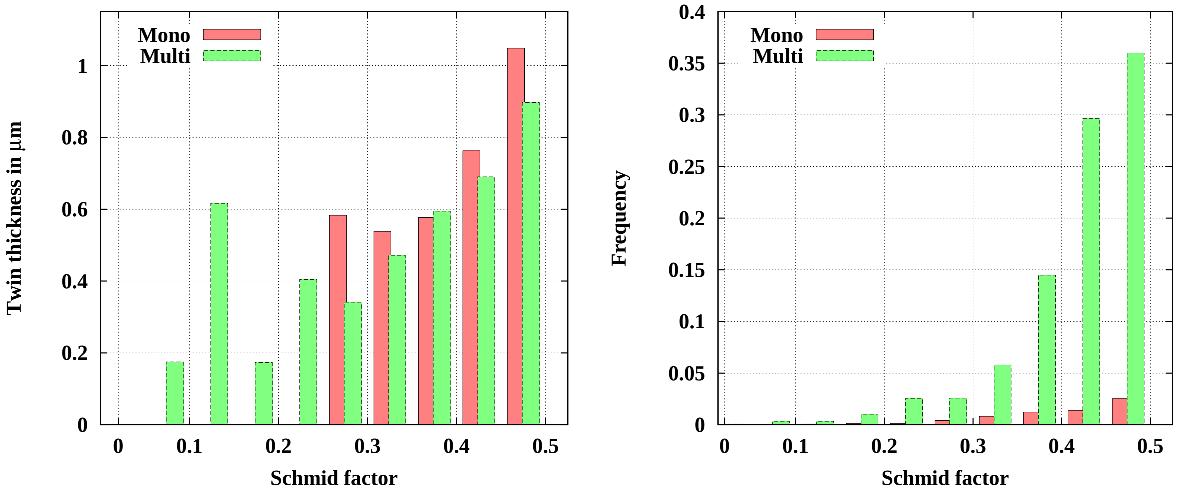

(a) (b)

FIGURE 4.23 – Distribution of the twin thickness (a) and the frequency (b) of C_1 twins with respect to SF values in samples loaded along the TT direction.

nucleation of both low Schmid factor and double extension can be considered as a rare event since low Schmid factor and double extension twins represent 6.7 % and 5.7 % of all twins, respectively. Note also that double extension twins occupy less than 0.5% of the total twinned area. Relying on the value of the distortion induced by a twin that has to be accommodated by the potential other deformation modes, it was found that group 1 low Schmid factor twins, i.e. twin in contact with a grain boundary, require the most accommodation through basal slip with the lowest CRSS and the least accommodation through pyramidal slip with the highest CRSS. Group 2 low Schmid factor twins, i.e. twins forming a cross-boundary twin pair, require the least pyramidal slip or contraction twinning accommodations with high CRSS but the most accommodation through prismatic slip and tensile twinning, of which CRSSs are higher than basal slip and lower than pyramidal slip and compressive twinning. The second study highlights that, contrary to primary twins, secondary tensile twins obey the Schmid's law. It also showed that the use of a micromechanical double-inclusion model is an accurate way to predict the activation of the right twin variant. The fact that the activation of double extension twin variant obeys the Schmid's law also implies that purely deterministic approaches as those used in classical polycrystalline model should be able to predict the nucleation of such twins.

The statistical study performed on a large set of EBSD scans of high purity Zr discusses the influence of twin-twin junctions between first generation twins, grain size and crystallographic orientation on nucleation and growth of twins. Samples were loaded in compression at liquid nitrogen temperature along the through-thickness and one of the in-plane directions in order to favor C_1 and T_1 twins, respectively. This study is the first to establish the statistical relevance of twin-twin junctions by collecting and processing data about all twinning modes and all twin-twin junctions in Zr. Six different types of twin-twin junctions ,i.e. $T_1 - T_1$, $T_1 - T_2$, $T_1 - C_1$, $T_2 - T_2$, $T_2 - C_1$ and $C_1 - C_1$, are observed. Twin-twin junctions occurring between twins belonging to different modes, and more particularly between twins belonging to the first and second most active twinning modes, appear very frequently and cannot be neglected. Depending on the loading configuration, they may represent more than half of all twin-twin junctions. The comparison between the average twin thickness of twins embedded in single twinned and multi-twinned grains reveals that twin-twin junctions hinder twin growth. In addition, only nucleation and growth of twins belonging to the predominant twinning mode seem to be strongly sensitive to grain orientation and loading direction. These differences can probably be explained by the presence of localized high stress levels allowing the nucleation of any twinning mode. In agreement with previous studies, it is also found that the probability of twin nucleation and the average number of twins per twinned grain increase with grain size.

Chapitre 5

Conclusion

Three types of interactions, i.e. slip/slip, slip/twin, and twin/twin interactions, are key to the mechanical response and strain hardening in h.c.p. metals. The work presented here clearly focused on the twinning process in general and, more specifically on understanding the means of internal stress development within the twin domain from inception to the final shape and on quantifying the statistical relevance of twin/twin interactions (i.e. double/sequential twinning and twin intersection). To this end, novel micromechanical models were introduced, specimens were experimentally characterized by means of mechanical testing, XRD and EBSD techniques, and these results were analyzed in light of a new freeware developed along the course of the work to extract quantified links between twins, initial microstructure and loading directions. The key findings of each of those initiatives are presented in what follows, and guidance for future developments is proposed.

To study internal stress development during twinning, a new micromechanical approach based on a double inclusion topology and the use of the Tanaka-Mori theorem was first adopted in the form an elasto-static Tanaka-Mori scheme in heterogeneous elastic media with plastic incompatibilities. This first model was introduced to study the evolution of internal stresses in both parent and twins during first and second-generation twinning in h.c.p materials. The model was first applied to the case of pure Mg to reproduce the average internal resolved shear stresses in the parent and twin phases. While the study is limited to anisotropic heterogeneous elasticity with eigenstrains representing the twinning shears, it is suggested that the magnitude of the back-stresses is sufficient to induce plastic deformation within the twin domains. Moreover, the predominant effect on the magnitude and the direction of the back-stresses appears to be due to heterogeneous elasticity because of large induced misorientations between the parent and the twin domains. It is also found that the stress state within twin domains is largely affected by the shape of the parent phase. Using the same notations as Martin et al. [67] to refer to as "secondary" any $\{10\bar{1}2\}$ tensile twin variants embedded in $\{10\bar{1}1\}$ compressive twins, application of the model shows that only three (i.e. A, B, D) of the six tensile twin variants have a positive resolved shear stress on the twin plane. Two of those correspond to the most experimentally observed variants. In addition, variants A and D2 are found to exhibit the largest elastic energy decrease during secondary twin growth. Interestingly, it is also found that variant A can also grow to larger volume fractions than variant D. Clearly, all results shown here are limited to static configurations and neglect internal variable evolutions. Nonetheless, these first results suggest that application of the generalized Tanaka-Mori scheme to mean-field self-consistent methods will yield more accurate predictions of the internal state within twin domains for real polycrystalline hexagonal metals like magnesium and associated alloys.

Consequently, a second model called the double inclusion elasto-plastic self-consistent scheme (DI-EPSC) and consisting of an extension of the elasto-static Tanaka-Mori scheme to elasto-plasticity and polycrystalline media, was proposed. Similar to the previous model, the original Tanaka-Mori result is used to derive new concentration relations including average strains in twins and twinned grains. Then, twinned and non-twinned grains are embedded in an HEM, with effective behavior determined in an implicit nonlinear iterative self-consistent procedure called the "DI-EPSC" model. Contrary to the existing EPSC scheme, which only considers single ellipsoidal inclusions, new strain concentration relations account for a direct coupling between parent and twin phases. Using the same Voce's law coefficients and the same hardening parameters as in Clausen et al. [4], comparison between the EPSC, the DI-EPSC and experimental data leads to three main results with respect to twinning and associated plasticity mechanisms. First, it appears that, by introducing a new topology for twinning, latent effects induced by twinning in the parent phases are capable of predicting the influence of plasticity on hardening and hardening rates in the twin phases. Second, because twins are now directly embedded in the parent phases, new concentration relations lead to more scattered shear strain distributions in the twin phases. Twin stress states are strongly controlled by the interaction with their associated parent domains. Third, the study clearly shows the importance of appropriately considering the initial twin stress state at twin inception.

During this study, it was found that most numerical instabilities can be traced back to the choice of hardening matrix [40, 41]. Although such matrix was chosen to be positive semi-definite, the EPSC scheme would have been more stable if all eigenvalues of the hardening matrix were strictly positive, i.e. if the hardening matrix was positive definite. However, the hardening matrix associated with Mg single crystals computed by Bertin et al. [55] from dislocation dynamics is definitely not positive semi-definite and even less positive definite. As a result, the easiest way to overcome such an issue, inherent in the EPSC algorithm, is either to use hardening laws with strictly positive definite hardening matrices or to use visco-plastic self-consistent or elasto-visco-plastic self-consistent schemes.

In order to process EBSD scans and extract twinning statistics automatically, a new EBSD analysis software based on graph theory and quaternion algebra was developed. Quaternions allow an easy computation of disorientations between pixels and areas of consistent orientation. The subsequent use of graph and group structures allows grain identification, twin recognition and statistics extraction.

The newly introduced software is distinguished from pre-existing commercial softwares or academic codes by combining visualization with automated analysis of the EBSD map. The built-in graphical user interface enables an immediate and direct access to microstructural and twinning data such as orientation and size of twins and grains, mode and system of twins; it also allows the user to correct or complete, if necessary, the analysis performed by the software. In addition, all raw and processed data are saved in a relational database. Consequently, all experimental parameters, microstructural data and twinning statistics are easily accessible via SQL requests. The database also enables us to quantify systematically the influence of a very large number of parameters. The construction of such a database makes a significant difference compared to other pre-existing analysis tools.

Moreover, although the tool was initially developed to perform statistical analyses on Mg and Zr scans, the software is not limited to these two h.c.p. metals. Its algorithm is capable of identifying any twin occurring in h.c.p. materials on condition that the user writes in the code the value of the c/a ratio and the theoretical disorientation quaternions corresponding to all potentially active twinning systems. For the analysis of other crystallographic structures, the user has to adapt the cell characteristics, add or remove quaternions corresponding to the different twinning orientation relations and modify the symmetry quaternions.

The two first statistical studies were performed from rolled AZ31 Mg alloy EBSD scans in order to explain the activation of low Schmid factor $\{10\bar{1}2\}$ tensile twins and successive $\{10\bar{1}2\}$-$\{10\bar{1}2\}$ double extension twins. The first study revealed that low Schmid factor $\{10\bar{1}2\}$ tensile twins only represent 6.8 % of all twins. Based on purely deterministic constitutive laws, polycrystalline schemes such as EPSC or EVPSC will not be able to predict the formation of low Schmid factor twins. However, consequences on predicted mechanical responses are expected to be small because of their low statistical relevance. The second study revealed that $\{10\bar{1}2\}$-$\{10\bar{1}2\}$ double extension twins obey the Schmid's law in general. It also showed that considering internal energy changes computed from a micromechanical double-inclusion model, even simplified, results in very accurate predictions of double extension twin variant activation. The study also pointed out that such double twins are extremely rare and have a negligible effect on the mechanical properties of the material.

Another statistical study performed from Zr EBSD scans was carried out in order to discuss the influence of twin-twin junctions between first generation twins, grain size and crystallographic orientation on nucleation and growth of twins. Samples were loaded in compression at liquid nitrogen temperature along the through-thickness and one of the in-plane directions in order to favor C_1 and T_1 twins, respectively. Abbreviations T_1, T_2 and C_1 stand for $\{10\bar{1}2\}$, $\{11\bar{2}1\}$ and $\{11\bar{2}2\}$ twins, respectively. This study is the first to establish the statistical relevance of twin-twin junctions by collecting and processing data about all twinning modes and all twin-twin junctions in Zr. Six different types of twin-twin junctions ,i.e. $T_1 - T_1$, $T_1 - T_2$, $T_1 - C_1$, $T_2 - T_2$, $T_2 - C_1$ and $C_1 - C_1$, are observed. Twin-twin junctions occurring between twins belonging to different modes, and more particularly between twins belonging to the first and second most active twinning modes, appear very frequently and cannot be neglected. Depending on the loading configuration, they may represent more than half of all twin-twin junctions. The comparison between the average twin thickness of twins embedded in single twinned and multi-twinned grains reveals that twin-twin junctions hinder twin growth. In addition, only nucleation and growth of twins belonging to the predominant twinning mode seem to be strongly sensitive to grain orientation and loading direction. These differences can probably be explained by the presence of localized high stress levels allowing the nucleation of any twinning mode. In agreement with previous studies, it is also found that the probability of twin nucleation and the average number of twins per twinned grain increase with grain size.

The logical continuation of this work consists of 1) a more user-friendly integration of post-processing capabilities in the EBSD software and 2) the development and implementation of stochastic models taking into account all new statistically meaningful data into the DI-EPSC scheme scheme. For example, the software could become more user-friendly if SQL requests were directly implemented in the software and if the software would display and output tables with information about twins, twin junctions, twinned grains, etc. One can also imagine an interface allowing the user to choose the microstructural features he desires to obtain. Regarding the development of stochastic models, Beyerlein et al. [34] and then Niezgoda et al. [108] proposed models dealing with nucleation of $\{10\bar{1}2\}$ tensile twins in Mg. These models could be extended so as to be capable of predicting the nucleation of any type of twinning mode in h.c.p. metals.

Results of the statistical study on Zr presented in Chapter 4 are a starting point. In addition, performing EBSD measurements on more Mg and Zr samples loaded either monotonically or cyclically along different directions at different temperatures and strain rates would represent an incredible additional source of data for the modeling community.

Annexe A

Graphical User Interface of the EBSD map analysis software and SQL Requests for automated twin statistics extraction

A.0.1 Graphical User Interface

To assist the EBSD map analysis, 9 distinct visualization modes and 8 color mappings of the EBSD data are provided by the software. The color mappings correspond to two different color mappings of the rotation space, three stereographic projections ; and displayed in grey levels, the image quality, confidence index and fitness value reported by the acquisition software. The 9 visualization modes are the following :

1. Raw mode : displays the raw EBSD measurement points as shown in Figure 3.23, left.
2. Twinning editor : displays twinning relations between fragments and allows the user to enable or disable them. Fragments identified as parent phases, first, second, third and higher generation twins are marked with yellow, light blue, dark blue and red discs, respectively. Discs indicating high order twins, i.e. second, third and higher order, appear larger in order to be more visible. Likely being the result of incorrectly enabled relations, these twinning relations have to be inspected in priority (Figure 3.23, center).
3. Grain neighbors : displays grains with their neighbors. The user, here, is able to mark a fragment as parent or twin phase.
4. Clusters : displays phases grouped by twinning order. Colors used to indicate twinning modes are also the same as those used in the twinning editor visualization mode. However, it emphasizes twinning order. For example, it was previously mentioned that first generation twins are marked with a light blue disc in the twinning editor mode. Here, first generation twins are not only marked by a light blue disc but their boundaries appear in light blue (Figure 3.23, right).
5. Twinning statistics : exactly like the twinning editor mode except that only intragranular relations are displayed. The interest of this mode lies in the possibility for the user to obtain information about pairs of twins and grains or pairs of twins just by clicking on the edges linking two connected parts. The user has then access to a list of information about

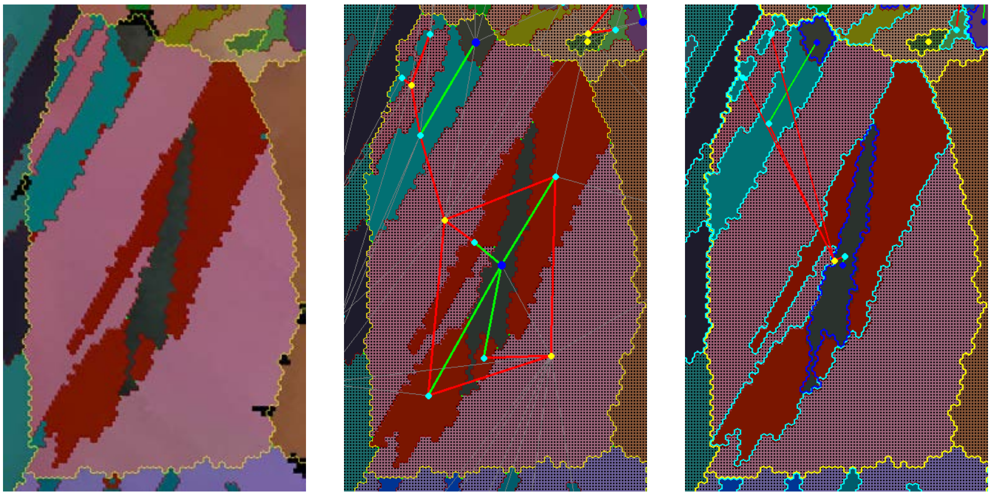

Raw measurements Twinning editor Phases

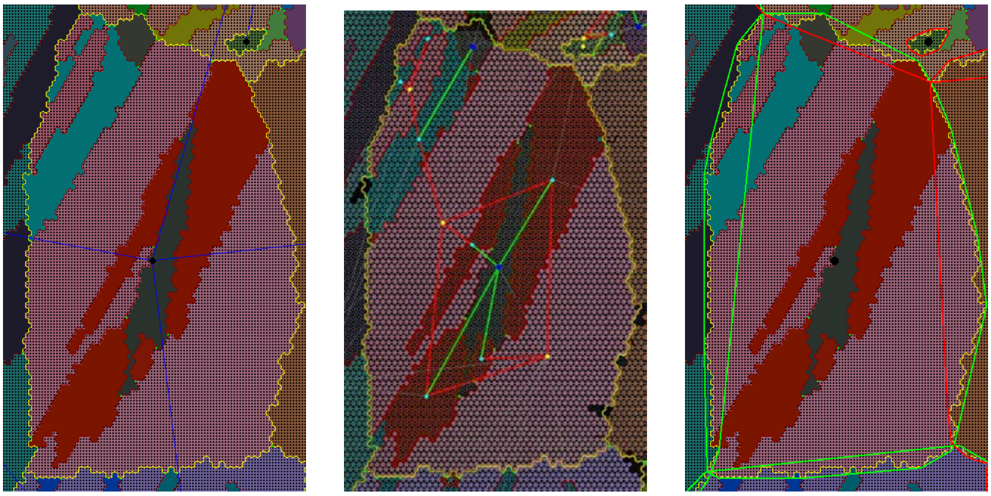

Grains Individual measurements Convex hulls

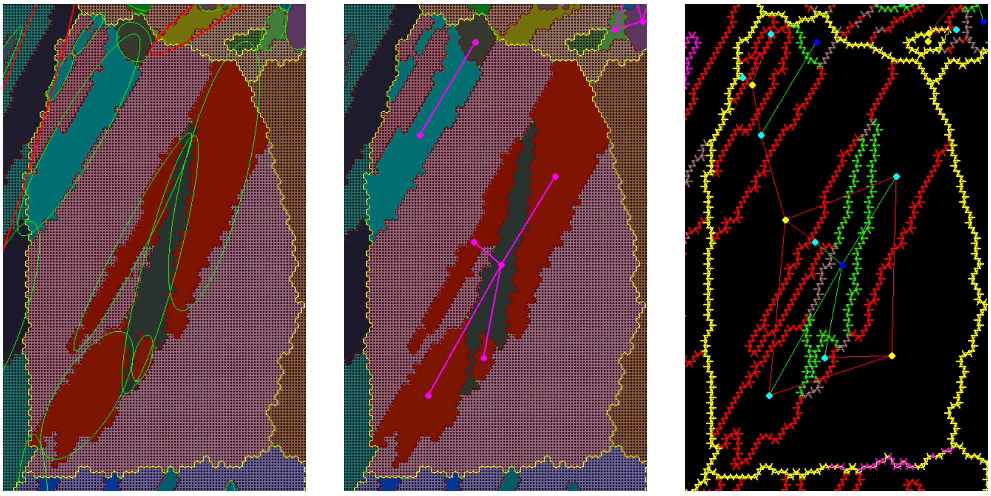

Ellipses Twin interactions Twin boundaries

FIGURE A.1 – Visualization modes for a single grain these two connected parts such as the disorientation existing between the twin and the parent phases, the twinning mode corresponding to the disorientation, etc.

6. Convex hulls : displays the convex hull of detected grains. The polygons are drawn in green if their area is close to the enclosed grain area, in red otherwise.
7. Ellipses : displays a fitted ellipse around every detected twins. Twins whose shape does not fit an ellipse very well are drawn in red because they are likely to be the result of the merging of two (or more) twins (Figure 3.24, left). This mode allows the user to have access to grain and twin properties such as orientation and size.
8. Connected twins : displays detected twin-twin junctions. The user can also mark manually undetected twin-twin junctions.
9. Twin joints : displays identified twinning relations between measurement points located along twin boundaries. Even though measurement points along twin boundaries are not very reliable, this mode might be useful to visualize how strong the disorientation appears along the boundary.

In addition to these visualization modes, options are available to highlight grain or twin boundaries, exclude grains in contact with the map edge, replace twins in a twin strip by their union (Figure 3.24, right), display connected part ids and zoom in or out and pan. When zooming in to a level where individual measurement can be separated, local disorientation is also displayed as shown in figure 3.17. Figure A.1 summarizes all available modes.

A.0.2 SQL Requests

All SQL requests used for statistics extraction are listed in the following.

- Request 1 :

```sql
select g.id,g.area,g.qx,g.qy,g.qz,g.qw
from grains as g
where not g.map_edge
order by g.id;
```

- Request 2 :

```sql
drop view Twins;
create view Twins as
select C1.id as P, C2.id,c2.grain,S2.area,C2.size,S2.length,
S2.thickness,c2.x,c2.y,s2.qx,s2.qy,s2.qz,s2.qw,
e.twinning,e.variant
from ConnectedEdges as E
    inner join Fragments as c1 on c1.id=e.i
    inner join Fragments as c2 on c2.id=e.j
    inner join FragmentStatistics as s1 on c1.id=s1.id
    inner join FragmentStatistics as s2 on c2.id=s2.id
    inner join Grains as G on G.id = C2.grain
and C1.is_parent
and E.twinning>1
and C1.grain=C2.grain
and not G.map_edge
and c1.twinstrip<=0 and c2.twinstrip<=0
and c2.twinning_order=1
order by C2.id;
```

- Request 3 :

```
select C1.grain, C1.id, C2.id,
    T1.twinning, T1.variant, T2.twinning, T2.variant
from FragmentEdges as E
    inner join Fragment as C1 on C1.id = E.i
    inner join Fragment as C2 on C2.id = E.j
    inner join Twins as T1 on C1.id = T1.id
    inner join Twins as T2 on C2.id = T2.id
where E.i > E.j
    and not C1.is_parent and not C2.is_parent
    and C1.is_valid and C2.is_valid
    and C1.grain=C2.grain
    and C1.twinstrip <= 0 and C2.twinstrip <= 0
order by C1.grain;
```

— Request 4 :

```
select t.grain,d.i,d.j,d.dist,d.xi,d.yi,d.xj,d.yj
from twins as t, IngrainDistances as d
where (t.id=d.i or t.id=d.j)
group by d.dist*d.xi*d.xj order by t.grain;
```

— Request 5 :

```
select MAP_ID,g.id, g.area,g.border_length,
avg(t.area),sum(t.area),count(t.id),avg(t.thickness)
from grains as g,  Twins as t
where G.id = t.grain
group by g.id order by g.id;
```

Annexe B

Stress-strain curve correction method and mechanical testing parameters

Measuring the evolution of the distance existing between the current and the initial positions of the upper compression plate is an accurate way to estimate the deformation of the sample. However, during a compression test, the distance measured by LVDT sensors evolves not only because of the deformation of the sample but also because of the deformation of the machine. Initially, the stiffness of the machine was measured experimentally by compressing square tungsten samples. Correction parameters were then directly derived from the measured machine stiffness. Unfortunately, tungsten samples cracked. As a result, it was decided to correct the measured strain in such a way that the Young's modulus, during the loading phase, is equal to 45 GPa. To calculate the corrective parameters, a MATLAB code was written to extract the stress and strain values as well as to output the stress-strain curves, and another was written to calculate the corrective parameters and Young,s modulus for both loading and unloading regimes. The reason why many Young,s moduli for unloading regimes are missing in Table B.1 is that measurement points corresponding to unloading phases were not recorded initially. The procedure was then adapted in order to save them. This is also why the elastic regime of the loading phase was used to determine the correction parameters. The following equations describe the method used to correct the measured strain.

First, the measured strain, ϵ^m, is corrected by a term denoted by ϵ^{corr} linearly proportional to the force applied and, as a result, to the engineering stress, σ^m :

$$\epsilon^c = \epsilon^m - \epsilon^{corr} \tag{B.1}$$

where ϵ^c denotes the measured strain after correction and ϵ^{corr} the correction term expressed as follows :

$$\epsilon^{corr} = a.\sigma^m + b \tag{B.2}$$

Correction parameters a and b are determined from the desired theoretical Young,s modulus value, i.e. $E^{th} = 45$ GPa, and two measurement points, $P_1(\epsilon_1^m, \sigma_1^m)$ and $P_2(\epsilon_2^m, \sigma_2^m)$, picked such that both σ_1^m and σ_2^m belong to the elastic regime of the loading. For all corrections, points P_1 and P_2 were chosen to have σ_1^m and σ_2^m equal to about 30 MPa and 60 MPa, respectively.

Consequently, parameters a and b can be expressed as follows :

$$a = \frac{\epsilon_2^m - \epsilon_1^m}{\sigma_2^m - \sigma_1^m} - \frac{1}{E^{th}} \tag{B.3}$$

$$b = \epsilon^i - \frac{\sigma^i}{E^{th}}(1 + a.E^{th}) \tag{B.4}$$

with $i = \{1, 2\}$.

Table B.1 lists the measured Young,s moduli and correction parameters for compression tests whose characteristics are described in Table B.2. Abbreviations RD, TD and ND stand for rolling direction, transverse direction and normal direction, respectively.

Table B.1 – Young's moduli measured for both the loading and unloading regimes before correction and correction parameters

Sample Label	Young's modulus loading (GPa)	Young's modulus unloading (GPa)	Corr. Param. a (MPa^{-1})	Corr. Param. b
RD1		-	7.8511e-05	5.2016e-04
RD2		-	3.0803e-05	7.7801e-04
RD3		-	5.2416e-05	6.6649e-04
TD2	15.6	-	4.5699e-05	7.8436e-04
ND2	21.4	73.2	2.4145e-05	-6.34e-04
ND3	25.9	69.7	1.6109e-05	-7.043e-04
ND5	18.1	15.0	3.3402e-05	1.02751e-03
ND6	19.6	14.9	2.9008e-05	1.03421e-03
RD1TD1	19.7	-	1.9934e-05	1.39418e-03
-	14.1	-	/4.88218e-05	/1.20736e-03
RD2TD2	17.9	-	3.4792e-05	7.7543e-03
-	16.3	-	/3.9626e-05	/9.511e-04
RD3TD3	17.4	-	3.669e-05	7.9274e-03
-	13.7	-	/5.11435e-05	/1.0106e-03

Table B.2 – Description of loading conditions

Sample Label	Loading Direction	Strain Rate (/s)	Temperature (K)
RD1	RD	0.001	25
RD2	RD	0.001	25
RD3	RD	0.001	25
TD2	TD	0.001	25
ND2	ND	0.001	75
ND3	ND	0.001	75
ND5	ND	0.1	25
ND6	ND	0.1	25
RD1TD1	RD thenTD	0.001	25
RD2TD2	RD thenTD	0.001	25
RD3TD3	RD thenTD	0.001	25

Bibliographie

[1] S. I. Kurukuri, M. J. Worswick, D. Ghaffari-Tari, R. K. Mishra, and J. T. Carter, "Rate sensitivity and tension–compression asymmetry in az31b magnesium alloy sheet," *Philosophical Transactions of the Royal Society of London A : Mathematical, Physical and Engineering Sciences*, vol. 372, no. 2015, 2014.

[2] G. C. Kaschner, J. F. Bingert, C. Liu, M. L. Lovato, P. J. Maudlin, M. G. Stout, and C. N. Tomé, "Mechanical response of zirconium—ii. experimental and finite element analysis of bent beams," *Acta Materialia*, vol. 49, no. 15, pp. 3097 – 3108, 2001.

[3] J. W. Christian and S. Mahajan, "Deformation twinning," *Progress in Materials Science*, vol. 39, no. 1-2, pp. 1 – 157, 1995.

[4] B. Clausen, C. N. Tomé, D. W. Brown, and S. R. Agnew, "Reorientation and stress relaxation due to twinning : Modeling and experimental characterization for mg," *Acta Materialia*, vol. 56, no. 11, pp. 2456 – 2468, 2008.

[5] W. Zhou and Z. L. Wang, *Scanning Microscopy for Nanotechnology.* Springer-Verlag, 2007.

[6] H. Boersch, "About bands in electron diffraction," *Physikalische Zeitschrift*, vol. 38, pp. 1000–1004, 1937.

[7] J. A. Venables and C. J. Harland, "Electron back-scattering patterns - a new technique for obtaining crystallographic information in the scanning electron microscope," *Philosophical Magazine*, vol. 27, pp. 1193–1200, 1973.

[8] R. J. McCabe, G. Proust, E. K. Cerreta, and A. Misra, "Quantitative analysis of deformation twinning in zirconium," *International Journal of Plasticity*, vol. 25, no. 3, pp. 454 – 472, 2009.

[9] B. Fultz and J. Howe, *Transmission Electron Microscopy and Diffractometry of Materials.* Springer - Verlag Berlin Weidelberg, 2013.

[10] S. I. Wright and B. L. Adams, "Automatic-analysis of electron backscatter diffraction patterns," *Metallurgical Transactions A - Physical Metallurgy and Materials Science*, vol. 23, no. 3, pp. 759–767, 1992.

[11] P.-A. Juan, C. Pradalier, S. Berbenni, R. J. McCabe, C. N. Tomé, and L. Capolungo, "A statistical analysis of the influence of microstructure and twin-twin junctions on nucleation and growth of twins in zr," *Acta Materialia*, vol. 95, pp. 399–410, 2015.

[12] K. D. Kreuer, "Proton conductivity : Materials and applications," *Chemistry of Materials*, vol. 8, no. 3, pp. 610–641, 1996.

[13] K. D. Maglic, N. L. Perovic, and A. M. Stanimirovic, "Calorimetric and transport properties of zircalloy-2, zircalloy-4 and inconel-625," *International Journal of Thermophysics*, vol. 15, no. 4, pp. 741–755, 1994.

[14] W. Kreher and A. Molinari, “Residual stresses in polycrystals influenced by grain shape and texture,” *Journal of the Mechanics and Physics of Solids*, vol. 41, no. 12, pp. 1955–1977, 1993.

[15] H. R. V. Carrillo, C. R. Martinez, L. L. Q. Torres, N. E. Hertel, and F. Y. Iskander, “Nuclear characterization of zinalco and zircalloy-4,” *International Journal of Radiation Applications and Instrumentation. Part C. Radiation Physics and Chemistry*, vol. 38, no. 2, pp. 263 –, 1991.

[16] B. L. Mordike and T. Ebert, “Magnesium. properties - applications - potential,” *Materials Science and Engineering A*, vol. 301, pp. 37 – 45, 2001.

[17] P. G. Partridge, “The crystallography and deformation modes of hexagonal close-packed metals,” *Metallurgical Review*, vol. 12, no. 118, pp. 168 – 192, 1967.

[18] R. W. Cahn, “Plastic deformation of alpha-uranium ; twinning and slip,” *Acta Metallurgica*, vol. 1, no. 1, pp. 49 – 70, 1953.

[19] A. G. Crocker, “The crystallography of deformation twinning in alpha-uranium,” *Journal of Nuclear Materials*, vol. 16, no. 3, pp. 306 – 326, 1965.

[20] G. I. Taylor, “Plastic strain in metals.,” *Journal of the Institute of Metals*, vol. 62, pp. 307–324, 1938.

[21] L. Capolungo and I. J. Beyerlein, “Nucleation and stability of twins in hcp metals,” *Physical Review B*, vol. 78, no. 2, 2008.

[22] J. Wang, J. P. Hirth, and C. N. Tomé, “((1)over-bar0 1 2) Twinning nucleation mechanisms in hexagonal-close-packed crystals,” *Acta Materiala*, vol. 57, no. 18, pp. 5521–5530, 2009.

[23] J. Wang, R. G. Hoagland, J. P. Hirth, L. Capolungo, I. J. Beyerlein, and C. N. Tomé, “Nucleation of a twin in hexagonal close-packed crystals,” *Scripta Materialia*, vol. 61, no. 9, pp. 903 – 906, 2009.

[24] A. Serra, D. J. Bacon, and R. C. Pond, “The crystallography and core structure of twinning dislocations in HCP metals,” *Acta Metallurgica*, vol. 36, no. 12, pp. 3183–3203, 1988.

[25] M. H. Yoo, J. R. Morris, K. M. Ho, and S. R. Agnew, “Nonbasal deformation modes of HCP metals and alloys : Role of dislocation source and mobility,” *Metallurgical and Materials Transactions A-Physical Metallurgy and Materials Science*, vol. 33, no. 3, SI, pp. 813–822, 2002.

[26] E. O. Hall, *Twinning.* Butterworth, 1954.

[27] B. A. Bilby and A. G. Crocker, “Theory of crystallography of deformation twinning,” *Proceedings of the Royal Society of London Series A - Mathematical and Physical Sciences*, vol. 288, no. 1413, pp. 240–&, 1965.

[28] M. Bevis and A. G. Crocker, “Twinning shears in lattices,” *Proceedings of the Royal Society of London Series A - Mathematical and Physical Sciences*, vol. 304, no. 1476, pp. 123–&, 1968.

[29] M. Bevis and A. G. Crocker, “Twinning modes in lattices,” *Proceedings of the Royal Society of London Series A - Mathematical and Physical Sciences*, vol. 313, no. 1515, pp. 509–&, 1969.

[30] A. A. Salem, S. R. Kalidindi, and S. L. Semiatin, “Strain hardening due to deformation twinning in titanium : Constitutive relations and crystal-plasticity modeling,” *Acta Materialia*, vol. 53, no. 12, pp. 3495 – 3502, 2005.

[31] G. Proust, C. N. Tomé, and G. C. Kaschner, “Modeling texture, twinning and hardening evolution during deformation of hexagonal materials,” *Acta Materialia*, vol. 55, no. 6, pp. 2137 – 2148, 2007.

[32] G. Proust, C. N. Tomé, A. Jain, and S. R. Agnew, “Modeling the effect of twinning and detwinning during strain-path changes of magnesium alloy {AZ31},” *International Journal of Plasticity*, vol. 25, no. 5, pp. 861 – 880, 2009.

[33] H. Abdolvand, M. R. Daymond, and C. Mareau, “Incorporation of twinning into a crystal plasticity finite element model : Evolution of lattice strains and texture in zircaloy-2,” *International Journal of Plasticity*, vol. 27, no. 11, pp. 1721 – 1738, 2011.

[34] I. J. Beyerlein, R. J. McCabe, and C. N. Tomé, “Effect of microstructure on the nucleation of deformation twins in polycrystalline high-purity magnesium : A multi-scale modeling study,” *Journal of the Mechanics and Physics of Solids*, vol. 59, no. 5, pp. 988 – 1003, 2011.

[35] A. Khosravani, J. Scott, M. P. Miles, D. Fullwood, B. L. Adams, and R. K. Mishra, “Twinning in magnesium alloy {AZ31B} under different strain paths at moderately elevated temperatures,” *International Journal of Plasticity*, vol. 45, no. 0, pp. 160 – 173, 2013.

[36] C. C. Aydiner, J. V. Bernier, B. Clausen, U. Lienert, C. N. Tomé, and D. W. Brown, “Evolution of stress in individual grains and twins in a magnesium alloy aggregate,” *Physical Review B*, vol. 80, no. 2, 2009.

[37] E. Kr´oner *Z. Phys*, vol. 151, p. 504, 1958.

[38] E. Kr´oner *Acta Metallurgica*, vol. 9, p. 155, 1961.

[39] B. Budiansky, “On the elastic moduli of some heterogeneous materials,” *Journal of the Mechanics and Physics of Solids*, vol. 13, no. 4, pp. 223 – 227, 1965.

[40] R. Hill, “A self-consistent mechanics of composite materials,” *Journal of the Mechanics and Physics of Solids*, vol. 13, no. 4, pp. 213–&, 1965.

[41] J. W. Hutchinson, “Elastic-plastic behaviour of polycrystalline metals and composites,” *Proceedings of the Royal Society of London Series A-Mathematical and Physical sciences*, vol. 319, no. 1537, pp. 247–&, 1970.

[42] Z. Hashin and S. Shtrikman, “A variational approach to the theory of the elastic behaviour of multiphase materials,” *Journal of the Mechanics and Physics of Solids*, vol. 11, no. 2, pp. 127 – 140, 1963.

[43] T. Mori and K. Tanaka, “Average stress in matrix and average elastic energy of materials with misfitting inclusions,” *Acta Metallurgica*, vol. 21, no. 5, pp. 571 – 574, 1973.

[44] M. Berveiller and A. Zaoui, “An extension of the self-consistent scheme to plastically-flowing polycrystals,” *Journal of the Mechanics and Physics of Solids*, vol. 26, no. 5-6, pp. 325 – 344, 1978.

[45] M. Berveiller, O. Fassi-Fehri, and A. Hihi, “The problem of two plastic and heterogeneous inclusions in an anisotropic medium,” *International Journal of Engineering Science*, vol. 25, no. 6, pp. 691 – 709, 1987.

[46] P. Lipinski and M. Berveiller, “Elastoplasticity of micro-inhomogeneous metals at large strains,” *International Journal of Plasticity*, vol. 5, no. 2, pp. 149 – 172, 1989.

[47] A. Molinari, G. R. Canova, and S. Ahzi, “A self consistent approach of the large deformation polycrystal viscoplasticity,” *Acta Metallurgica*, vol. 35, no. 12, pp. 2983 – 2994, 1987.

[48] H. Sabar, M. Berveiller, V. Favier, and S. Berbenni, “A new class of micro-macro models for elastic-viscoplastic heterogeneous materials,” *International Journal of Solids and Structures*, vol. 39, no. 12, pp. 3257 – 3276, 2002.

[49] H. Wang, P. D. Wu, C. N. Tomé, and Y. Huang, “A finite strain elastic-viscoplastic self-consistent model for polycrystalline materials,” *Journal of the Mechanics and Physics of Solids*, vol. 58, no. 4, pp. 594 – 612, 2010.

[50] T. Mura, *Micromechanics of defects in solids.* Martinus Nijhoff Publishers, 1982.

[51] G. W. Groves and A. Kelly, “Independent slip systems in crystals,” *Philosophical Magazine*, vol. 8, no. 89, pp. 877–&, 1963.

[52] M. H. Yoo, “Slip, twinning and fracture in hexagonal close-packed metals,” *Metallurgical and Materials Transactions A-Physical Metallurgy and Materials Science*, vol. 12, no. 3, pp. 409–418, 1981.

[53] U. F. Kocks and D. G. Westlake, “Importance of twinning for ductility of CPH polycrystals,” *Transactions of the Metallurgical Society of AIME*, vol. 239, no. 7, pp. 1107–&, 1967.

[54] J. W. Hutchinson, “Creep and plasticity of hexagonal polycrystals as related to single-crystal slip,” *Metallurgical Transactions A - Physical Metallurgy and Materials Science*, vol. 8, no. 9, pp. 1465–1469, 1977.

[55] N. Bertin, C. N. Tomé, I. J. Beyerlein, M. R. Barnett, and L. Capolungo, “On the strength of dislocation interactions and their effect on latent hardening in pure magnesium,” *International Journal of Plasticity*, vol. 62, no. 0, pp. 72 – 92, 2014.

[56] S. R. Agnew, L. Capolungo, and C. A. Calhoun, “Connections between the basal {I1} “growth” fault and <c+a> dislocations,” *Acta Materialia*, vol. 82, no. 0, pp. 255 – 265, 2015.

[57] A. Serra and D. J. Bacon, “Computer-simulation of twin boundaries in the HCP metals,” *Philosophical Magazine A - Physics of condensed matter structure defects and mechanical properties*, vol. 54, no. 6, pp. 793–804, 1986.

[58] A. Serra, D. J. Bacon, and R. C. Pond, “Dislocations in interfaces in the h.c.p. metals. defects formed by absorption of crystal dislocations,” *Acta Materialia*, vol. 47, no. 5, pp. 1425 – 1439, 1999.

[59] H. Fan, S. Aubry, A. Arsenlis, and J. A. El-Awady, “The role of twinning deformation on the hardening response of polycrystalline magnesium from discrete dislocation dynamics simulations,” *Acta Materialia*, vol. 92, no. 0, pp. 126 – 139, 2015.

[60] Q. Yu, J. Wang, Y. Jiang, R. J. McCabe, N. Li, and C. N. Tomé, “Twin-twin interactions in magnesium,” *Acta Materialia*, vol. 77, no. 0, pp. 28 – 42, 2014.

[61] H. El Kadiri, J. Kapil, A. L. Oppedal, L. G. Hector, S. R. Agnew, M. Cherkaoui, and S. C. Vogel, “The effect of twin-twin interactions on the nucleation and propagation of twinning in magnesium,” *Acta Materialia*, vol. 61, no. 10, pp. 3549 – 3563, 2013.

[62] Q. Yu, J. Wang, Y. Jiang, R. J. McCabe, and C. N. Tomé, “Co-zone $\{10-12\}$ twin interaction in magnesium single crystal,” *Materials Research Letters*, vol. 2, no. 2, pp. 82–88, 2014.

[63] M. Hori and S. Nemat-Nasser, “Double-inclusion model and overall moduli of multi-phase composites,” *Mechanics of Materials*, vol. 14, no. 3, pp. 189 – 206, 1993.

[64] S. Nemat-Nasser and M. Hori, *Micromechanics : overall properties of heterogeneous materials.* 2nd revised edition. Elsevier, 1999.

[65] M. R. Barnett, Z. Keshavarz, A. G. Beer, and X. Ma, “Non-schmid behaviour during secondary twinning in a polycrystalline magnesium alloy,” *Acta Materialia*, vol. 56, no. 1, pp. 5 – 15, 2008.

[66] I. J. Beyerlein, J. Wang, M. R. Barnett, and C. N. Tomé, “Double twinning mechanisms in magnesium alloys via dissociation of lattice dislocations,” *Proceedings of the Royal Society A - Mathematical Physical and Engineering Sciences*, vol. 468, no. 2141, pp. 1496–1520, 2012.

[67] E. Martin, L. Capolungo, L. Jiang, and J. J. Jonas, “Variant selection during secondary twinning in mg-3%al,” *Acta Materialia*, vol. 58, no. 11, pp. 3970 – 3983, 2010.

[68] J. E. Dorn and J. B. Mitchell, *High-Strength Materials.* John Wiley and Sons, 1964.

[69] H. Kiho, “The crystallographic aspect of the mechanical twinning in metals,” *Journal of the Physical Society of Japan*, vol. 9, no. 5, pp. 739–747, 1954.

[70] H. Kiho, “The crystallographic aspect of the mechanical twinning in Ti and alpha-U,” *Journal of the Physical Society of Japan*, vol. 13, no. 3, pp. 269–272, 1958.

[71] M. A. Jaswon and D. B. Dove, “Twinning properties of lattice planes,” *Acta Crystallographica*, vol. 9, no. 7, pp. 621–626, 1956.

[72] M. A. Jaswon and D. B. Dove, “The prediction of twinning modes in metal crystals,” *Acta Crystallographica*, vol. 10, no. 1, pp. 14–18, 1957.

[73] M. A. Jaswon and D. B. Dove, “The crystallography of deformation twinning,” *Acta Crystallographica*, vol. 13, no. 3, pp. 232–240, 1960.

[74] R. E. Reed-Hill, “A study of the (1011) and (1013) twinning modes in magnesium,” *Transactions of the American Institute of Mining and Metallurgical Engineers*, vol. 218, no. 3, pp. 554–558, 1960.

[75] H. El Kadiri, C. D. Barrett, and M. A. Tschopp, “The candidacy of shuffle and shear during compound twinning in hexagonal close-packed structures,” *Acta Materialia*, vol. 61, no. 20, pp. 7646 – 7659, 2013.

[76] A. Serra, R. C. Pond, and D. J. Bacon, “Computer-simulation of the structure and mobility of twinning dislocations in hcp metals,” *Acta Metallurgica et Materialia*, vol. 39, no. 7, pp. 1469–1480, 1991.

[77] K. V. Vladimirskij *Zh. Eksper. Teor. Fiz.*, vol. 17, p. 530, 1947.

[78] F. C. Frank and J. H. Van der Merwe, “One-dimensional dislocations .1. Static theory,” *Proceedings of the Royal Society of London Series A - Mathematical and Physical Sciences*, vol. 198, no. 1053, pp. 205–216, 1949.

[79] N. Thompson and D. J. Millard, “Twin formation in Cadmium,” *Philosophical Magazine*, vol. 43, no. 339, pp. 422–440, 1952.

[80] S. Mendelson, *Fundamental Aspects of Dislocation Theory.* National Bureau of Standard Publications, 1970.

[81] B. Xu, L. Capolungo, and D. Rodney, “On the importance of prismatic/basal interfaces in the growth of twins in hexagonal close packed crystals,” *Scripta Materialia*, vol. 68, no. 11, pp. 901 – 904, 2013.

[82] J. S. Koehler, F. Seitz, W. T. Read, W. Shockley, and E. Orowan, *Dislocations in Metals.* The Institute of Metals Division - The American Institute of Mining and Metallurgical Engineers, 1954.

[83] P. B. Price, “Pyramidal glide and the formation and climb of dislocation loops in nearly perfect zinc crystals,” *Philosophical Magazine*, vol. 5, no. 57, pp. 873–&, 1960.

[84] P. B. Price, “Nucleation and growth of twins in dislocation-free zinc crystals,” *Proceedings of the Royal Society of London. Series A. Mathematical and Physical Sciences*, vol. 260, no. 1301, pp. 251–262, 1961.

[85] P. B. Price, “Non-basal glide in dislocation-free cadmium crystals,” *Journal of Applied Physics*, vol. 32, no. 9, pp. 1746–&, 1961.

[86] J. K. Lee and M. H. Yoo, “Elastic strain-energy of deformation twinning in tetragonal crystals,” *Metallurgical Transactions A - Physical Metallurgy and Materials Science*, vol. 21, no. 9, pp. 2521–2530, 1990.

[87] M. H. Yoo and J. K. Lee, “Deformation twinning in hcp metals and alloys,” *Philosophical Magazine A-Physics of condensed matter structure defects and mechanical properties*, vol. 63, no. 5, pp. 987–1000, 1991.

[88] R. L. Bell and R. W. Cahn, “The nucleation problem in deformation twinning,” *Acta Metallurgica* , vol. 1, no. 6, pp. 752–753, 1953.

[89] R. L. Bell and R. W. Cahn, “The dynamics of twinning and the interrelation of slip and twinning in zinc crystals,” *Proceedings of the Royal Society of London Series A - Mathematical and Physical Sciences*, vol. 239, no. 1219, pp. 494–&, 1957.

[90] J. W. Christian and A. G. Crocker, *Dislocations in Solids.* F.R.N. Nabarro, 1980.

[91] B. A. Bilby, “On the mutual transformation of lattices,” *Philosophical Magazine*, vol. 44, no. 354, pp. 782–785, 1953.

[92] A. H. Cottrell and B. A. Bilby, “A mechanism for the growth of deformation twins in crystals,” *Philosophical Magazine*, vol. 42, no. 329, pp. 573–581, 1951.

[93] B. A. Bilby and J. W. Christian, *The Mechanism of Phase Transformations in Metals.* The Institute of Metals, 1956.

[94] J. A. Venables, “Dislocation pole models for twinning,” *Philosophical Magazine*, vol. 30, no. 5, pp. 1165–1169, 1974.

[95] J. P. Hirth and J. Lothe, *Theory of Crystal Dislocations.* John Wiley and Sons, 1982.

[96] A. Izadbakhsh, K. Inal, and R. K. Mishra, “Numerical formability assessment in single crystals of magnesium,” *Computational Materials Science*, vol. 50, no. 2, pp. 571 – 585, 2010.

[97] M. N. Shiekhelsouk, V. Favier, K. Inal, and M. Cherkaoui, “Modelling the behaviour of polycrystalline austenitic steel with twinning-induced plasticity effect,” *International Journal of Plasticity*, vol. 25, no. 1, pp. 105 – 133, 2009.

[98] H. Moulinec and P. Suquet, “A numerical method for computing the overall response of nonlinear composites with complex microstructure,” *Computer Methods in Applied Mechanics and Engineering*, vol. 157, no. 1-2, pp. 69–94, 1998.

[99] H. Moulinec and P. Suquet, “Intraphase strain heterogeneity in nonlinear composites : a computational approach,” *European Journal of Mechanics - A/Solids*, vol. 22, no. 5, pp. 751 – 770, 2003.

[100] C. N. Tomé, R. A. Lebensohn, and U. F. Kocks, “A model for texture development dominated by deformation twinning : Application to zirconium alloys,” *Acta Metallurgica et Materialia*, vol. 39, no. 11, pp. 2667 – 2680, 1991.

[101] R. A. Lebensohn and C. N. Tomé, “A self-consistent anisotropic approach for the simulation of plastic deformation and texture development of polycrystals : Application to zirconium alloys,” *Acta Metallurgica et Materialia*, vol. 41, no. 9, pp. 2611 – 2624, 1993.

[102] P. Van Houtte, “Simulation of the rolling and shear texture of brass by the taylor theory adapted for mechanical twinning,” *Acta Metallurgica*, vol. 26, no. 4, pp. 591 – 604, 1978.

[103] H. Wang, P. D. Wu, C. N. Tomé, and J. Wang, “A constitutive model of twinning and detwinning for hexagonal close packed polycrystals,” *Materials Science and Engineering : A*, vol. 555, no. 0, pp. 93 – 98, 2012.

[104] H. Wang, W. P. D., J. Wang, and C. N. Tomé, “A crystal plasticity model for hexagonal close packed (hcp) crystals including twinning and de-twinning mechanisms,” *International Journal of Plasticity*, vol. 49, no. 0, pp. 36 – 52, 2013.

[105] L. Balogh, S. R. Niezgoda, A. K. Kanjarla, D. W. Brown, B. Clausen, W. Liu, and C. N. Tomé, “Spatially resolved in situ strain measurements from an interior twinned grain in bulk polycrystalline {AZ31} alloy,” *Acta Materialia*, vol. 61, no. 10, pp. 3612 – 3620, 2013.

[106] R. A. Lebensohn and C. N. Tomé, “A study of the stress state associated with twin nucleation and propagation in anisotropic materials,” *Philosophical Magazine A*, vol. 67, no. 1, pp. 187–206, 1993.

[107] R. A. Lebensohn, A. K. Kanjarla, and P. Eisenlohr, “An elasto-viscoplastic formulation based on fast fourier transforms for the prediction of micromechanical fields in polycrystalline materials,” *International Journal of Plasticity*, vol. 32-33, no. 0, pp. 59 – 69, 2012.

[108] S. R. Niezgoda, A. K. Kanjarla, I. J. Beyerlein, and C. N. Tomé, “Stochastic modeling of twin nucleation in polycrystals : An application in hexagonal close-packed metals,” *International Journal of Plasticity*, vol. 56, no. 0, pp. 119 – 138, 2014.

[109] L. Capolungo, P. Marshall, R. McCabe, I. Beyerlein, and C. Tomé, “Nucleation and growth of twins in zr : A statistical study,” *Acta Materialia*, vol. 57, no. 20, pp. 6047 – 6056, 2009.

[110] I. J. Beyerlein, L. Capolungo, P. E. Marshall, R. J. McCabe, and C. N. Tome, “Statistical analyses of deformation twinning in magnesium,” *Philosophical Magazine*, vol. 90, no. 16, pp. 2161–2190, 2010.

[111] P. E. Marshall, G. Proust, J. T. Rogers, and R. J. McCabe, “Automatic twin statistics from electron backscattered diffraction data,” *Journal of Microscopy*, vol. 238, no. 3, pp. 218–229, 2010.

[112] K. Tanaka and T. Mori, “Note on volume integrals of the elastic field around an ellipsoidal inclusion,” *Journal of Elasticity*, vol. 2, no. 3, pp. 199–200, 1972.

[113] P.-A. Juan, S. Berbenni, and L. Capolungo, “Prediction of internal stresses during growth of first- and second-generation twins in mg and mg alloys,” *Acta Materialia*, vol. 60, no. 2, pp. 476 – 486, 2012.

[114] P.-A. Juan, S. Berbenni, M. Barnett, C. Tomé, and L. Capolungo, “A double inclusion homogenization scheme for polycrystals with hierarchal topologies : application to twinning in mg alloys,” *International Journal of Plasticity*, no. 0, pp. –, 2014.

[115] J. D. Eshelby, “The determination of the elastic field of an ellipsoidal inclusion and related problems,” *Proceedings of the Royal Society of London Series A-Mathematical and Physical sciences*, vol. 241, no. 1226, pp. 376–396, 1957.

[116] S. Berbenni, M. Berveiller, and T. Richeton, “Intra-granular plastic slip heterogeneities : Discrete vs. mean field approaches,” *International Journal of Solids and Structures*, vol. 45, no. 14-15, pp. 4147 – 4172, 2008.

[117] C. Collard, V. Favier, S. Berbenni, and M. Berveiller, “Role of discrete intra-granular slip bands on the strain-hardening of polycrystals,” *International Journal of Plasticity*, vol. 26, no. 2, pp. 310 – 328, 2010.

[118] P. Dederich and R. Zeller *Z Physics*, vol. 259, pp. 103–116, 1973.

[119] H. M. Shodja and A. S. Sarvestani, “Elastic fields in double inhomogeneity by the equivalent inclusion method,” *Journal of Applied Mechanics*, vol. 68, no. 1, pp. 3–10, 2001.

[120] P. A. Turner and C. N. Tomé, “A study of residual stresses in zircaloy-2 with rod texture,” *Acta Metallurgica et Materialia*, vol. 42, no. 12, pp. 4143 – 4153, 1994.

[121] R. Hill, “Elastic properties of reinforced solids : some theoretical principles,” *Journal of the Mechanics and Physics of Solids*, vol. 11, no. 5, pp. 357–&, 1963.

[122] J. Mandel, *Cours de Mécanique des Milieux Continus.* Gauthier-Villars, 1966.

[123] U. F. Kocks, C. N. Tomé, and H. R. Wenk, *Texture and anisotropy.* Cambridge University Press, 1998.

[124] R. Hill, “Generalized constitutive relations for incremental deformation of metal crystals by multislip,” *Journal of the Mechanics and Physics of Solids*, vol. 14, no. 2, pp. 95 – 102, 1966.

[125] O. Muránsky, M. R. Barnett, V. Luzin, and V. Vogel, “On the correlation between deformation twinning and l´uders-like deformation in an extruded mg alloy : in situ neutron diffraction and epsc4 modeling,” *Materials Science and Engineering : A*, vol. 527, no. 6, pp. 1383 – 1394, 2010.

[126] L. Capolungo, I. J. Beyerlein, and C. N. Tomé, “Slip-assisted twin growth in hexagonal close-packed metals,” *Scripta Materialia*, vol. 60, no. 1, pp. 32 – 35, 2009.

[127] C. Pradalier, P.-A. Juan, and L. Capolungo, “A graph theory based automated twin recognition technique for Electron Backscatter Diffraction analysis,” *to be submitted to Journal of Microscopy*, 2015.

[128] S. Kikuchi, “Diffraction of cathode rays by mica,” *Japan Journal of Physics*, vol. 5, p. 83, 1928.

[129] S. Nishikawa and S. Kikuchi, “The diffraction of cathode rays by calcite,” *Proceedings of the Imperial Academy (Japan)*, vol. 4, pp. 475–477, 1928.

[130] M. N. Alam, M. Blackman, and D. W. Pashley, “High-angle kikuchi patterns,” *Proceedings of the Royal Society of London Series A - Mathematical and Physical Sciences*, vol. 221, no. 1145, pp. 224–242, 1954.

[131] D. C. Joy, *Electron channeling patterns in the SEM, in : Quantitative Scanning Electron Microscopy.* Academic Press London, 1974.

[132] D. J. Dingley and S. Biggin, “A general method for locating the x-ray source point in kossel diffraction,” *Journal of Applied Crystallography*, vol. 10, p. 173, 1977.

[133] J. A. Venables, A. Bin-Jaya, and C. J. Harland, *Crystallographic orientation determination in the SEM using electron backscattering patterns and channel plates, in : Developments in Electron Microscopy and Analysis.* Academic Press London, 1976.

[134] D. J. Dingley, “Diffraction from sub-micron areas using electron backscattering in a scanning electron microscope,” *Scanning Electron Microscopy*, vol. 2, pp. 569–575, 1984.

[135] N. C. Krieger Lassen, D. Juul Jensen, and K. Conradsen, “Image processing procedures for analysis of electron back-scattering patterns,” *Scanning Microscopy*, vol. 6, pp. 115–121, 1992.

[136] P. V. C. Hough, “Method and means for recognizing complex patterns,” *US Patent 3, 069, 654*, 1962.

[137] B. L. Adams, S. L. Wright, and K. Kunze, "Orientation imaging : the emergence of a new microscopy," *Metallurgical Transactions A*, vol. 24, pp. 819–831, 1993.

[138] N. C. Krieger Lassen, D. Juul Jensen, and K. Conradsen, "Automated crystal lattice orientation mapping using a computer-controlled sem," *Micron*, vol. 28, pp. 249–265, 1997.

[139] J. R. Michael and R. P. Goehner, "Advances in backscattered electron kikuchi patterns for crystallographic phase identification," *Proceedings of the 52nd annual meeting of the microscopy society of America*, pp. 596–597, 1994.

[140] N. H. Schmidt and N. O. Olesen, "Computer aided determination of crystal orientation from electron channeling patterns in the sem," *Canadian Mineralogist*, vol. 27, p. 15, 1989.

[141] C. Davisson and L. H. Germer, "Diffraction of electrons by a crystal of nickel," *Phys. Rev.*, vol. 30, pp. 705–740, 1927.

[142] E. B. Dam, M. Koch, and M. Lillholm, *Quaternions, interpolation and animation.* Datalogisk Institut, Københavns Universitet, 1998.

[143] do Carmo, M.P., *Riemannian geometry.* Birkhäuser Boston, 1992.

[144] G. C. Kaschner, C. N. Tomé, I. J. Beyerlein, S. C. Vogel, D. W. Brown, and R. J. McCabe, "Role of twinning in the hardening response of zirconium during temperature reloads," *Acta Materialia*, vol. 54, no. 11, pp. 2887 – 2896, 2006.

[145] B. Fulkerson, A. Vedaldi, and S. Soatto, "Class segmentation and object localization with superpixel neighborhoods," in *Computer Vision, 2009 IEEE 12th International Conference on*, pp. 670–677, IEEE, 2009.

[146] Achanta, R. and Shaji, A. and Smith, K. and Lucchi, A. and Fua, P. and Süsstrunk, S., "SLIC Superpixels compared to state-of-the-art of Superpixel Methods," *IEEE Transactions on Pattern Analysis and Machine Intelligence*, vol. 34, no. 11, pp. 2274–2282, 2012.

[147] J. A. Bondy and U. S. R. Murty, *Graph theory with applications*, vol. 290. Macmillan London, 1976.

[148] S. Burtsev and Y. P. Kuzmin, "An efficient flood-filling algorithm," *Computers & graphics*, vol. 17, no. 5, pp. 549–561, 1993.

[149] Z. Shi, Y. Zhang, F. Wagner, P.-A. Juan, S. Berbenni, L. Capolungo, J.-S. Lecomte, and T. Richeton, "On the selection of extension twin variants with low schmid factors in a deformed mg alloy," *Acta Materialia*, vol. 83, no. 0, pp. 17 – 28, 2015.

[150] Z. Shi, Y. Zhang, F. Wagner, T. Richeton, P.-A. Juan, J.-S. Lecomte, L. Capolungo, and S. Berbenni, "Double extension twinning in a magnesium alloy : combined statistical and micromechanical analyses," *Acta Materialia*, vol. 96, pp. 333–343, 2015.

[151] D. Scott, "On optimal and data-based histograms," *Biometrika*, vol. 66, pp. 605–610, 1979.

[152] M. A. Kumar, A. K. Kanjarla, S. R. Niezgoda, R. A. Lebensohn, and C. N. Tomé, "Numerical study of the stress state of a deformation twin in magnesium," *Acta Materialia*, vol. 84, no. 0, pp. 349 – 358, 2015.

Abstract

The main objective of this thesis is to investigate and quantify the influence of parent-twin and twin-twin interactions on the mechanical response of hexagonal close-packed metals. To study parent-twin interactions, a mean-field continuum mechanics approach has been developed based on a new twinning topology in which twins are embedded in twinned grains. A first model generalizing the Tanaka-Mori scheme to heterogeneous elastic media is applied to first and second generation twinning in magnesium. In the case of first generation twinning, the model is capable of reproducing the trends in the development of backstresses within the twin domain as observed experimentally. Applying the methodology to the case of second-generation twinning allows the identification, in exact agreement with experimental observations, of the most likely second-generation twin variants to grow in a primary twin domain. Because the elastic behavior assumption causes internal stress level magnitudes to be excessively high, the first model is extended to the case of elasto-plasticity. Using a self-consistent approximation, the model, referred to as the double inclusion elasto-plastic self-consistent (DI-EPSC) scheme, is applied to Mg alloy polycrystals. The comparison of results obtained from the DI-EPSC and EPSC schemes reveals that deformation system activities and plastic strain distributions within twins drastically depend on the interaction with parent domains.

The influence of twin-twin interactions on nucleation and growth of twins is being statistically studied from zirconium and magnesium electron back-scattered diffraction scans. A new twin recognition software relying on graph theory analysis has been developed to extract all microstructural and crystallographic data. It is capable of identifying all twinning modes and all twin-twin interaction types occurring in hexagonal close-packed materials. The first results obtained from high purity Zr electron back-scattered diffraction maps reveal that twin-twin interactions hinder subsequent twin nucleation. They also show that mechanisms involved in twin growth may differ significantly for each twinning mode. A second study performed on AZ31 Mg presents statistics about low Schmid factor $\{10\bar{1}2\}$ tensile twins and about $\{10\bar{1}2\}$-$\{10\bar{1}2\}$ sequential double twins coupled with a simplified version of the Tanaka-Mori scheme generalized to heterogeneous elasticity with plastic incompatibilities.

Keywords: twinning, magnesium, zirconium, twin-twin junctions, micromechanics, EBSD.